Measurement of the angle gamma of the Unitarity Triangle with BaBar experiment

D. Derkach

LAL 10-96
Juin 2010

Université Paris-sud 11

THÈSE

présentée pour obtenir le grade de

Docteur en Sciences de l'Université Paris-Sud 11

Spécialité : physique des particules

par

Denis DERKACH

Mesure de l'angle γ du triangle d'unitarité avec le détecteur *BABAR*

Soutenue le 25 juin 2010 devant le Jury composé de :

M.	A. Bevan	
Mme	E. Kou	
M.	J.-P. Lees	Rapporteur
M.	S. Monteil	Rapporteur
M.	A. Stocchi	Directeur de thèse
M.	G. Wormser	Président du Jury

Contents

Résume de la thèse

Dans cette thèse nous présentons des études sur les mésons B effectués en utilisant les données enregistrées par l'expérience *BABAR* auprès de PEP-II à SLAC.

D'abord nous présentons la recherche des désintégrations rare $B^+ \to D^+ K^{(*)0}$. Ces modes de désintégration sont intéressants car il s'agit de processus d'annihilation qui fournit des informations importantes sur la dynamique de la désintégration des mésons beaux et les éléments de la matrice CKM , V_{ij}. Les résultats obtenus sur ces modes de désintégration peuvent être utilisés dans des ajustements phénoménologiques. Cela permet de traduire les mesures sur les amplitudes chargées $B^+ \to D^+ K^{(*)0}$ en estimations sur les amplitudes $B^0 \to D^0 K^{(*)0}$ supprimées par V_{ub}. L'analyse expérimentale est effectuée en utilisant plusieurs modes de désintégration du méson D chargé. Nous n'avons obtenu aucune évidence significative de signal et les limites supérieures sur les rapports d'embranchement suivants ont été établies

$$\mathcal{B}(B^+ \to D^+ K^0) < 2.9 \times 10^{-6} \text{ à } 90\% \text{ prob.},$$
$$\mathcal{B}(B^+ \to D^+ K^{*0}) < 3.0 \times 10^{-6} \text{ à } 90\% \text{ prob.}$$

Dans la deuxième partie de la thèse nous présentons des études sur la violation de *CP* dans le système des mésons B et en particulier la mesure de l'angle γ du Triangle d'Unitarité. L'angle γ est la phase relative entre les éléments V_{ub} et V_{cb} de la matrice CKM. Un paramètre crucial qui détermine la sensibilité à γ est le rapport r entre les amplitudes de transition $b \to u$ et $b \to c$. Dans cette thèse nous présentons une analyse du canal de désintégration des mésons B chargés: $B^+ \to D^0 K^+$. Ces désintégrations sont étudiées en utilisant la méthode ADS et le méson neutre D est reconstruit dans son état final $K\pi\pi^0$. En combinant cette analyse avec une analyse similaire qui utilise l'état final $K\pi$ des D^0 le rapport $r(DK)$ et l'angle γ ont été déterminés

$$\begin{aligned} r(DK) &= 0.083^{+0.028}_{-0.043}\,, \\ \gamma &= 86^{\circ}{}^{+51^{\circ}}_{-45^{\circ}}\,. \end{aligned} \tag{1}$$

Si les résultats expérimentaux contenus dans cette thèse sont utilisées dans les systèmes exprimant les amplitudes de désintégrations des $B \to DK$ et $B \to DK*$ des résultats intéressants peuvent tre obtenus. La précision sur le rapport $r(DK^*)$ pour les mésons B charges est améliorée d'un facteur trois : $r(DK^*) = 0.08 \pm 0.03$. Le rapport entre les modules des amplitudes V_{ub} d'annihilation (A) et supprimée de couleur (C) est $|A/C| < 0.6$ (à 90% du probabilité). Finalement le rapport $r(DK^0)$ pour les mésons neutres vaut 0.27 ± 0.09. La grande valeur de ce rapport est particulièrement intéressante pour les analyses futures qui ont eu but de mesurer la quantité $2\beta + \gamma$ en utilisant ces modes de désintégrations.

Abstract

In this thesis, we present studies of the B mesons system performed using the full dataset collected by the *BABAR* experiment at the PEP-II collider at SLAC.

The first analysis presented is the search of the rare V_{ub} mediated decays $B^+ \to D^+ K^{(*)0}$. These decays are particularly interesting because they are expected to be dominated by the annihilation processes and can provide insight to the internal dynamics of the B mesons. Another point of interest is coming from the fact that the rates of these decays can be used to constrain the annihilation amplitudes in phenomenological fits. This allows the translation of the measurements of the charged $B^+ \to D^+ K^{(*)0}$ amplitudes into estimations of the V_{ub} suppressed amplitudes of $B^0 \to D^0 K^{(*)0}$. The experimental analysis is performed looking at several D^+ decay modes. No signals have been found and upper limits have been set to be:

$$\mathcal{B}(B^+ \to D^+ K^0) < 2.9 \times 10^{-6} \text{à } 90\% \text{ prob.},$$
$$\mathcal{B}(B^+ \to D^+ K^{*0}) < 3.0 \times 10^{-6} \text{à } 90\% \text{ prob.}.$$

In the second part of the thesis we present the *CP* violation studies in the B-meson system, and in particular measurements of the angle γ of the Unitarity Triangle. The angle γ is the relative weak phase between the V_{ub} and V_{cb} elements of the CKM matrix. A crucial parameter, which drives the sensitivity to γ, is the ratio r between $b \to u$ and $b \to c$ transition amplitudes. We present and describe the analysis using the charged B meson decays: $B^+ \to D^0 K^+$. These decays are studied through the ADS method, where the neutral D mesons are reconstructed into $K\pi\pi^0$ final states. Combining this analysis with a similar one that used $K\pi$ as a D^0 final state the ratio $r(DK)$ and the angle have been obtained to be

$$\begin{aligned} r(DK) &= 0.083^{+0.028}_{-0.043}\,, \\ \gamma &= 86^{\circ\,+51^\circ}_{\quad -45^\circ}\,. \end{aligned} \tag{2}$$

If the results of this thesis are used in the full system of the $B \to DK$ and $B \to DK^*$ decay amplitudes, other interesting results can be obtained. The error on the ratio $r(DK^*)$ for the

charged B decays is improved by a factor of three resulting in $r(DK*) = 0.08 \pm 0.03$. The ratio between the V_{ub} mediated annihilation (A) and the color suppressed (C) amplitudes is obtained to be $|A/C| < 0.6$ (at 90% probability). Finally, the ratio $r(DK^0)$ for neutral B decays is found to be 0.27 ± 0.09. The large value for this ratio is particularly interesting for future analyses aiming at the measurement of $2\beta + \gamma$ using these decays modes.

Chapter 1

Introduction

The Standard Model of elementary particles (SM) has given a good effective description of the physical processes that have been tested until 2010. This model has provided well confirmed predictions of the effects connected to three out of the four fundamental interactions in a coherent framework.

The comprehensive test of the Standard Model is the main goal of current physical experiments in the particle physics. These experiments can use different approaches: elementary particle collisions at different energies, heavy ion collisions, astroparticle experiments, etc. One of the way to explore SM in the part describing *CP* violation is to develop experiments aimed at study B meson decays, where a multitude of *CP* violating effects are expected. For these reasons the two "B factory experiments" were constructed: *BABAR*, based in SLAC, Menlo Park, California, USA and Belle, based in KEK, Tsukuba, Japan. These B factories have jointly collected data sample with more than 10^9 $B\overline{B}$ meson pairs for about 10 years of running.

The results of these experiments have played a crucial role in the study of *CP* violation, which is described in the SM with the use of the CKM matrix (as described in Chapter 2). This thesis is dedicated to the study of *CP* violation effects and in particular the measurements of the angle γ of the Unitarity triangle (Chapter 3) using the final dataset collected with the *BABAR* detector (described in Chapter 5).

Since this angle is the relative phase between V_{ub} and V_{cb} elements of the CKM matrix, its value can be accessed studying processes that involve $b \to u$ and $b \to c$ transitions. The simplest way to access these transitions is to study in details the $B \to DK$ decays (as described in Chapters 3 and 4). In the recent years, different methods to measure the angle γ were developed and a lot of efforts of scientific community were concentrated on the experimental determination of this parameter. Despite the experimental efforts, γ is not known precisely. The reason for

it is that the sensitivity to γ is driven by the value of the ratios r between $b \to u$ and $b \to c$ amplitudes. The numerical values of these ratios are decay dependent. They are expected to be small and have to be determined on data.

The experimental work presented in this thesis is composed of two analyses. The first analysis (described in Chapters 6 and 7) describes the search for the rare decays $B^+ \to D^+ K^{(*)0}$. These decays have never been observed before and are quite interesting since they allow to access annihilation amplitudes that enter in the determination of the ratios r.

The second analysis concerns the measurements of the $B^+ \to D^0(\overline{D}^0)K^+$ decays analyzed through the ADS method allowing the determination of r and the angle γ (Chapter 8).

In Chapter 9 the phenomenological impacts of the measurements presented in the thesis are discussed.

Chapter 2

CKM Matrix and *CP* Violation in the Standard Model

In the past decade, one of the major challenges of particle physics has been to gain an in-depth understanding of the role of quark flavor. In this time frame, measurements and the theoretical interpretation of their results have advanced tremendously. A much broader understanding of flavor particles has been achieved, apart from their masses and quantum numbers, there now exist detailed measurements of the characteristics of their interactions allowing stringent tests of Standard Model predictions.

The Standard Model (SM) [2] has a rich structure in its flavor sector, mainly because it contains three generations of quarks and leptons. In the quark sector, it is well established that the misalignment between the weak interaction eigenstates and mass eigenstates leads to the Cabibbo-Kobayashi-Maskawa (CKM) matrix [3], which is the source of the transitions between different generations. Even more importantly, it offers the source of the *CP* violation. This flavor structure has been confirmed by many experimental measurements to a good precision.

The SM is a low energy effective theory and one of the main tasks of modern high-energy physics is the search for contradictions of measurements with the SM predictions. The existence of such a difference would imply the presence of "new physics" (NP) effects. The flavor sector is one of the main frontiers in the NP effects search [4].

This Chapter is devoted to a brief introduction to flavor physics. The current status of the flavor sector measurements is given in Section 2.3

2.1 Symmetries

Symmetries play an important role in the modern physics. The symmetry properties of a physical system are intimately related to the conservation laws characterizing that system. Noether's theorem gives a precise description of this relation [1]. The theorem states that each continuous symmetry of a physical system implies that some physical property of that system is conserved.

The particle physics has three related discrete symmetries. These state that the space is indistinguishable from one under the following transformations:

- parity transformation P, which is the flip in the sign of one of spatial coordinates;
- time reversal transformation T, which reverses the time variables of the system;
- charge-conjugation transformation C, which inverses all the charges of particles to opposite (i.e. changing particles and anti-particles).

The CPT theorem requires the preservation of the discrete CPT symmetry by all physical phenomena. The violation of this rule is being searched but, until the time of this thesis publication, all observation are consistent with exact CPT symmetry. The strong and electromagnetic interactions show no experimental evidence for C, P or T violation, while weak interactions violate C and P separately, conserving, in first approximation, their product CP. The first evidence of CP violation was found in 1964 in rare processes in the kaon system [5]. In 2001 this was confirmed in B meson decays [6] studied in the dedicated experiments.

2.2 CP Violation and the CKM Matrix

The Standard Model is based on $SU(3)_C \otimes SU(2) \otimes U(1)$ gauge symmetry, where $SU(3)_C$ describes the color symmetry of strong interactions, $SU(2)$ the weak isospin symmetry, and $U(1)$ the symmetry under hypercharge transformations. CP violation in weak processes arises from a single irremovable complex phase in the mixing matrix for quarks, which governs the charged W gauge boson interaction with the quarks: this is called the Cabibbo-Kobayashi-Maskawa (CKM) mechanism [3]. Such charged current weak interaction can be written as:

$$\mathcal{L}_W = -\frac{g}{\sqrt{2}}(\overline{u}, \overline{c}, \overline{t})_L \gamma^\mu \begin{pmatrix} d \\ s \\ b \end{pmatrix}_L W_\mu^+ + \text{h.c.}, \tag{2.1}$$

where g is the $SU(2)_L$ coupling constant, W_μ^+ is the W boson field operator, and $(u, c, t)_L$ and $(d, s, b)_L$ are the left-handed quark field flavor eigenstates, with charges $Q = 2/3$ and

$Q = -1/3$, respectively. The matrix of the couplings, V, called Cabibbo-Kobayashi-Maskawa (CKM) matrix [3] is in principle a unitary, 3×3 complex matrix. The matrix elements are normally notated according to the quarks they correspond to:

$$V = \begin{pmatrix} V_{ud} & V_{us} & V_{ub} \\ V_{cd} & V_{cs} & V_{cb} \\ V_{td} & V_{ts} & V_{tb} \end{pmatrix}. \tag{2.2}$$

This CKM matrix thus depends on nine parameters, three real angles and six phases. It can always be parameterized with three Euler angles (real parameters) and six phases (complex parameters). Five of these six phases disappear under transformations that redefine the phase of the quark fields in the quark mass eigenstate basis and leave the diagonal mass matrix unchanged. One of the six phases is irreducible. The presence of this phase accounts for the *CP* violation in the Standard Model.

An explicit parameterization in terms of three mixing angles θ_{12}, θ_{13}, θ_{23}, and a phase δ [8], with a particular quark fields phase convention can be written:

$$V_{\mathrm{CKM}} = \begin{pmatrix} c_{12}c_{13} & s_{12}c_{13} & s_{13}e^{-i\delta} \\ -s_{12}c_{23} - c_{12}s_{23}s_{13}e^{i\delta} & c_{12}c_{23} - s_{12}s_{23}s_{13}e^{i\delta} & s_{23}c_{13} \\ s_{12}s_{23} - c_{12}c_{23}s_{13}e^{i\delta} & -s_{23}c_{12} - s_{12}c_{23}s_{13}e^{i\delta} & c_{23}c_{13} \end{pmatrix}, \tag{2.3}$$

where $c_{ij} = \cos\theta_{ij}$ and $s_{ij} = \sin\theta_{ij}$ $(i, j = 1, 2, 3,\ j > i)$. The experimental values suggest that $\theta_{13} \ll \theta_{23} \ll \theta_{12}$.

Considering that the mixing angles are small, the Wolfenstein parametrization [9] can be introduced for the description of the V matrix elements magnitude. In this parametrization, the matrix elements are the result of an expansion in terms of a small parameter $\lambda = |V_{us}| \approx 0.22$. The four independent real parameters can be defined:

$$\begin{aligned} s_{12} &= \lambda, \\ s_{23} &= A\lambda^2, \\ \rho &= \frac{s_{13}}{s_{12}s_{23}}\cos\delta, \\ \eta &= \frac{s_{13}}{s_{12}s_{23}}\sin\delta. \end{aligned} \tag{2.4}$$

For these variables, the CKM matrix can be expressed

$$V_{\mathrm{CKM}} = \begin{pmatrix} 1 - \frac{\lambda^2}{2} & \lambda & A\lambda^3(\rho - i\eta) \\ -\lambda & 1 - \frac{\lambda^2}{2} & A\lambda^2 \\ A\lambda^3(1 - \rho - i\eta) & -A\lambda^2 & 1 \end{pmatrix} + \mathcal{O}(\lambda^4). \tag{2.5}$$

A more accurate expression of the Wolfenstein parametrization, including $\mathcal{O}(\lambda^4)$ and $\mathcal{O}(\lambda^5)$ terms, gives [10]:

$$\begin{pmatrix} 1-\frac{1}{2}\lambda^2-\frac{1}{8}\lambda^4 & \lambda & A\lambda^3(\bar{\rho}-i\eta) \\ -\lambda+\frac{1}{2}A^2\lambda^5[1-2(\bar{\rho}+i\eta)] & 1-\frac{1}{2}\lambda^2-\frac{1}{8}\lambda^4(1+4A^2) & A\lambda^2 \\ A\lambda^3(1-\bar{\rho}-i\bar{\eta}) & -A\lambda^2+\frac{1}{2}A\lambda^4[1-2(\bar{\rho}+i\eta)] & 1-\frac{1}{2}A^2\lambda^4 \end{pmatrix} + \mathcal{O}(\lambda^6) \quad (2.6)$$

where $\bar{\rho}$ and $\bar{\eta}$ are related to ρ and η by:

$$\begin{aligned} \bar{\rho} &= \rho\,(1-\frac{\lambda^2}{2}), \\ \bar{\eta} &= \eta\,(1-\frac{\lambda^2}{2}). \end{aligned} \quad (2.7)$$

The unitarity of the V matrix implies several relations between its elements,

$$\sum_{i=1}^{3} V_{ij}V_{ik}^* = \delta_{jk} \text{ and } \sum_{i=1}^{3} V_{ij}V_{kj}^* = \delta_{ik}. \quad (2.8)$$

Six of them are particularly interesting

Each of these relations can be represented as a triangle in the $(\bar{\rho},\bar{\eta})$ plane, where the ones obtained by product of neighboring rows or columns are nearly degenerated. The areas of all these triangles are equal to half of the Jarlskog invariant J [14] defined by:

$$J \equiv c_{12}c_{23}c_{13}^2 s_{12}s_{23}s_{13}\sin\delta. \quad (2.9)$$

The value of J can estimate the amount of CP Violation. The maximum value J, $1/(6\sqrt{3}) \approx 0.1$, gives the fully violated *CP* symmetry. The recent value of determinant is $J = (3.0 \pm 0.1) * 10^{-5}$ [17].

The interest is driven by equation

$$V_{ud}V_{ub}^* + V_{cd}V_{cb}^* + V_{td}V_{tb}^* = 0, \quad (2.10)$$

with each item approximately proportional to λ^3. This equation is connected to the B meson decays due to the presence of V_{ub} and V_{cb} matrix elements. Dividing all the terms of the relation by $V_{cd}V_{cb}^*$, one obtains

$$\frac{V_{ud}V_{ub}^*}{V_{cd}V_{cb}^*} + 1 + \frac{V_{td}V_{tb}^*}{V_{cd}V_{cb}^*} = 0. \quad (2.11)$$

This equation can be graphically represented on the $\bar{\rho}-\bar{\eta}$ plane. Figure 2.1 shows the triangle, which sides, usually noted R_b and R_t, can be calculated as:

$$\begin{aligned} \overline{CA} = R_b &= \frac{|V_{ud}V_{ub}^*|}{|V_{cd}V_{cb}^*|} = \sqrt{\bar{\rho}^2+\bar{\eta}^2} = (1-\frac{\lambda^2}{2})\frac{1}{\lambda}\left|\frac{V_{ub}}{V_{cb}}\right|, \\ \overline{BA} = R_t &= \frac{|V_{td}V_{tb}^*|}{|V_{cd}V_{cb}^*|} = \sqrt{(1-\bar{\rho})^2+\bar{\eta}^2} = \frac{1}{\lambda}\left|\frac{V_{td}}{V_{cb}}\right|. \end{aligned} \quad (2.12)$$

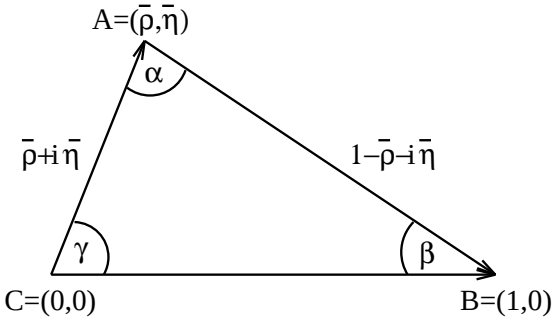

Figure 2.1: Unitarity Triangle in the $\bar{\rho} - \bar{\eta}$ plane.

The three angles, denoted by α, β, and γ, are[1]:

$$\begin{aligned} \alpha &= \arg\left(\frac{V_{td}V_{tb}^*}{V_{ud}V_{ub}^*}\right), \\ \beta &= \arg\left(\frac{V_{cd}V_{cb}^*}{V_{td}V_{tb}^*}\right), \\ \gamma &= \arg\left(\frac{V_{ud}V_{ub}^*}{V_{cd}V_{cb}^*}\right) = \pi - \alpha - \beta \end{aligned} \tag{2.13}$$

In the Wolfenstein parametrization the only complex elements, up to terms of order $\mathcal{O}(\lambda^5)$, are V_{ub} and V_{td} and the phases γ and β can be directly related to them:

$$V_{td} = |V_{td}|e^{-i\beta}, \tag{2.14}$$

$$V_{ub} = |V_{ub}|e^{-i\gamma}. \tag{2.15}$$

2.3 Current Status of the Unitarity Triangle Measurements

Among experimental tests of the *CP* violation, measurements of the mixing induced *CP* violation in the neutral B meson system played a central role at the present B factories. The angle β of the unitarity triangle has been measured very precisely, and precision measurement of the angle α is also possible by accumulating more statistics at the future B factories. The present B factories have also demonstrated the sensitivity in other measurements investigating the flavor structure. Direct *CP* violation in B meson decays has been measured in the decay modes such as $B \to \pi\pi$ and $B \to K\pi$. The angle γ can be measured through the interference of decay

[1] Another notation for angles, which is also used, is $\phi_1 \equiv \alpha$, $\phi_2 \equiv \beta$, and $\phi_3 \equiv \gamma$. The latter notation is commonly used by Belle experiment.

amplitudes involving intermediate D mesons. Several other Flavor Changing Neutral Current (FCNC) processes that are sensitive to possible new heavy particles exchanged in the loops of Feynman diagrams have also been investigated.

Several methods have been developed for the data statistical treatment. By the time of this thesis, the most active groups are CKMfitter [15] that uses frequentist approach, and UTfit [17] using Bayesian approach. The aim of each method is to obtain the constraints in the $(\bar{\rho} - \bar{\eta})$ plane.

The Bayesian approach of the UT triangle fit developed by the UTfit collaboration relies on the following arguments. Each observable gives rise to the equation that relates a constraint c_j to the CKM triangle parameters $\bar{\rho} - \bar{\eta}$ via the set of ancillary parameters x, where $x = x_1, x_2, ..., x_N$ stands for all experimentally determined or theoretically calculated quantities from which the various c_j depend.

In an ideal case of exact knowledge of c_j and x, each of the constraints provides a curve in the $\bar{\rho} - \bar{\eta}$ plane. In such a case, there would be no reason to favor any of the points on the curve, unless we have some further information or physical prejudice, which might exclude points outside a determined physical region, or, in general, assign different weights to different points. In the real experimental case we deal with the parameters, which are known with some precision, which in general leads to assigning different weights to different points. This means that, instead of a single curve in the $\bar{\rho} - \bar{\eta}$ plane, we have a family of curves which depends on the distribution of the set $\{c_j, x\}$. As a result, the points in the $\bar{\rho} - \bar{\eta}$ plane get different weights (even if they were taken to be equally probable a priori) and our confidence on the values of $\bar{\rho}$ and $\bar{\eta}$ clusters in a region of the plane becomes different.

One of the methods that takes into account the experimental and theoretical uncertainties and describes them in terms of a probability density function f (PDF), which quantifies our confidence on the values of a given quantity, is the Bayesian approach. The inference of $\bar{\rho}$ and $\bar{\eta}$ becomes then a straightforward application of probabilities theory.

The probabilistic approach can be implemented defining an idealized PDF for each constraint:

$$f(\bar{\rho}, \bar{\eta} | c_j, \mathbf{x}) \sim \delta(c_j - c_j(\bar{\rho}, \bar{\eta}, \mathbf{x})), \tag{2.16}$$

where δ is Dirac delta function.

The pdf which takes into account the full uncertainty of knowledge about c_j and x is then

obtained by making use of the standard probability rules:

$$\begin{aligned} f(\bar{\rho},\bar{\eta}) &= \int f(\bar{\rho},\bar{\eta}|c_j,\mathbf{x})\cdot f(c_j,\mathbf{x})\,dc_j\,d\mathbf{x} \\ &\propto \int \delta(c_j - c_j(\bar{\rho},\bar{\eta},\mathbf{x}))\cdot f(c_j)\cdot f(\mathbf{x})\,dc_j\,d\mathbf{x} \\ &\propto \int \delta(c_j - c_j(\bar{\rho},\bar{\eta},\mathbf{x}))\cdot \frac{1}{\sqrt{2\pi}\sigma(c_j)}\exp\left(-\frac{(c_j-\hat{c}_j)^2}{2\sigma^2(c_j)}\right)\cdot f(\mathbf{x})\,dc_j\,d\mathbf{x} \\ &\propto \int \frac{1}{\sqrt{2\pi}\sigma(c_j)}\exp\left(-\frac{(c_j(\bar{\rho},\bar{\eta},\mathbf{x})-\hat{c}_j)^2}{2\sigma^2(c_j)}\right)\cdot f(x_1)\cdot f(x_2)\cdots f(x_N)\,d\mathbf{x} \end{aligned} \tag{2.17}$$

where $\hat{c}_j$ is the experimental best estimate of c_j , with uncertainty $\sigma(cj)$. The joint pdf $f(c_j;\mathbf{x})$ has been splitted as a product of the individual pdf assuming the independence of the different quantities, which is a very good approximation for the case under study.

This formula may be represented in a different approach introducing a global interference relating $\bar{\rho}$, $\bar{\eta}$, c_j, and $\mathbf{x}$ (integrating over not interesting parameters). In this case, with the help of Bayes' theorem, one can obtain

$$\begin{aligned} f(\bar{\rho},\bar{\eta}|\hat{c}_j) &\propto f(\hat{c}_j|c_j,\bar{\rho},\bar{\eta})\cdot f(c_j,\bar{\rho},\bar{\eta},\mathbf{x}) \\ &\propto f(\hat{c}_j|c_j)\cdot f(c_j|\bar{\rho},\bar{\eta},\mathbf{x})\cdot f(\bar{\rho},\bar{\eta},\mathbf{x}) \\ &\propto f(\hat{c}_j|c_j)\cdot \delta(c_j - c_j(\bar{\rho},\bar{\eta},\mathbf{x}))\cdot f(\mathbf{x})\cdot f_\circ(\bar{\rho},\bar{\eta}), \end{aligned} \tag{2.18}$$

where $f_\circ(\bar{\rho},\bar{\eta})$ denotes the prior distribution.

The extension of relation 2.18 to several constraints, assuming these constraints are uncorrelated, can be written as

$$f(\bar{\rho},\bar{\eta}|\hat{c}_1,...,\hat{c}_M) \propto \prod_{j=1,M} f_j(\hat{c}_j|\bar{\rho},\bar{\eta},\mathbf{x}) \times \prod_{j=1,M} f_i(x_i) \times f_\circ(\bar{\rho},\bar{\eta}). \tag{2.19}$$

Integrating this equation over $\mathbf{x}$ we can rewrite the interference scheme in the following way:

$$f(\bar{\rho},\bar{\eta}|\hat{\mathbf{c}},\mathbf{f}) \propto \mathcal{L}(\hat{\mathbf{c}},\bar{\rho},\bar{\eta},\mathbf{f}) \times f_\circ(\bar{\rho},\bar{\eta}), \tag{2.20}$$

where $\hat{\mathbf{c}}$ stands for the set of measured constraints, and

$$\mathcal{L}(\hat{\mathbf{c}},\bar{\rho},\bar{\eta},\mathbf{f}) = \int \prod_{j=1,M} f_j(\hat{c}_j|\bar{\rho},\bar{\eta},\mathbf{x}) \times \prod_{j=1,M} f_i(x_i) \tag{2.21}$$

is the effective overall likelihood, which takes into account all possible values of x_j, properly weighted.

Whereas a priori all values for $(\bar{\rho},\bar{\eta})$ are taken to be equally likely, a posteriori the probability clusters around the point which maximizes the likelihood.

In conclusion, the final (unnormalized) pdf is obtained starting from a flat distribution of $(\bar{\rho}, \bar{\eta})$ is

$$f(\bar{\rho}, \bar{\eta}) \propto \int \prod_{j=1,M} f_j(\hat{c}_j|\bar{\rho}, \bar{\eta}, \mathbf{x}) \times \prod_{j=1,M} f_i(x_i), \tag{2.22}$$

The integration can be done by Monte Carlo methods.

The following measurements, resulting in different constraints on the $\bar{\rho}-\bar{\eta}$ plane, are included in the Unitarity Triangle analysis:

- $|V_{ub}|$ and $|V_{cb}|$. Their values measured in inclusive or exclusive semileptonic $B \to X_{u,c} l \nu_l$. The relative rate of charmless over charmed B meson semileptonic decays is proportional to the square of the ratio:

$$\frac{|V_{ub}|}{|V_{cb}|} = \frac{\lambda}{1 - \frac{\lambda^2}{2}} \sqrt{\overline{\rho}^2 + \overline{\eta}^2}. \tag{2.23}$$

  This corresponds in the $(\bar{\rho}, \bar{\eta})$ plane to a ring centered in $(0, 0)$ with radius $R_b = \sqrt{\overline{\rho}^2 + \overline{\eta}^2}$.

- Δm_d. The box diagram with the exchange of a top quark gives the dominant contribution to the $B^0 - \overline{B}^0$ oscillations. The time oscillation frequency can be related in the SM to the mass difference between the light and heavy mass eigenstates of the $B^0 - \overline{B}^0$ system:

$$\Delta m_d = \frac{G_F^2}{6\pi^2} m_W^2 \eta_b S(x_t) m_{B_d} f_{B_d}^2 \hat{B}_{B_d} |V_{cb}|^2 \lambda^2 ((1-\bar{\rho})^2 + \bar{\eta}^2. \tag{2.24}$$

  where $S(x_t)$ is the Inami-Lim function [11] and $x_t = m_t^2/M_W^2$, m_t is the top quark mass and η_b is the perturbative QCD short-distance NLO correction. The scale for the evaluation of those corrections entering into η_b and the running of the t quark mass have to be defined in a consistent way. The value of $\eta_b = 0.55 \pm 0.01$ has been obtained in [12] and, in order to be consistent, the measured value of the pole top quark mass, obtained by CDF and D0 collaborations, $m_t = (172.6 \pm 1.4)$ GeV/c^2 , has to be corrected downwards by (7 ± 1) GeV/c^2. The remaining factor, $f_{B_d}^2 \hat{B}_{B_d}$, encodes the information of non-perturbative QCD. The constant $f_{B_d}^2$ translates the size of the B meson wave function at the origin. The bag factor $\hat{B}_{B_d}$ is also introduced to take into account all possible deviations from vacuum.

  The Δm_d constraint can be represented by a ring centered at (1,0).

- $\Delta m_d / \Delta m_s$. The ratio between Δm_d defined in previous bullet and Δm_s, which is defined in the same way like Δm_d but for $B_s - \overline{B}_s$ system.

- ϵ_K, the phenomenological parameter describing "indirect" *CP* violation in the $K^0 \bar{K}^0$ system being the fraction of *CP*-violating component in the mass eigenstates.

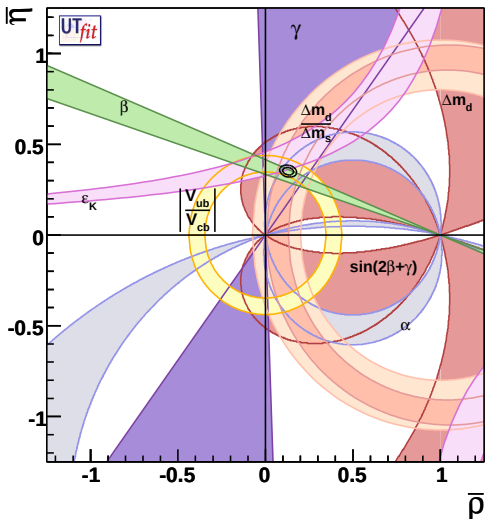

Figure 2.2: Allowed regions for $(\bar{\rho}-\bar{\eta})$. The closed contours at 95% probability are shown. The full lines correspond to 95% probability regions for the constraints, given by the measurements of $|V_{ub}|/|V_{cb}|$, ϵ_K, Δm_d,$\Delta m_d/\Delta m_s$, γ, α, β, $2\beta+\gamma$.

- α, β, and γ (or the $2\beta+\gamma$ combination. Information on the angles can be obtained from the measurement of CP violating B^+ and B^0 decays. Methods to extract γ are described in Chapter 3.

The fit is performed assuming the validity of the Standard Model. Figure 2.2 shows the graphical results of the fit in using the approach described in [17]. With the recent precision on inputs the SM predictions are in good agreement with the experimental data.

The results for $\bar{\rho}$ and $\bar{\eta}$ parameters are:

$$\begin{aligned} \overline{\rho} &= 0.130 \pm 0.019, \\ \overline{\eta} &= 0.351 \pm 0.012, \end{aligned} \tag{2.25}$$

with errors giving 68% probability regions.

The new physics models (i.e. the models describing the processes not included in SM) usually predict the deviations from SM scenarios in the processes that can be described by Feynmann diagrams with at least one loop. Thus, one can separate the contributions from the observables that can be determined from the "tree-level" processes (γ and $|V_{ub}|$) from the ones that can be determined only from the study of the "loop-level" processes (all other quantities listed before).

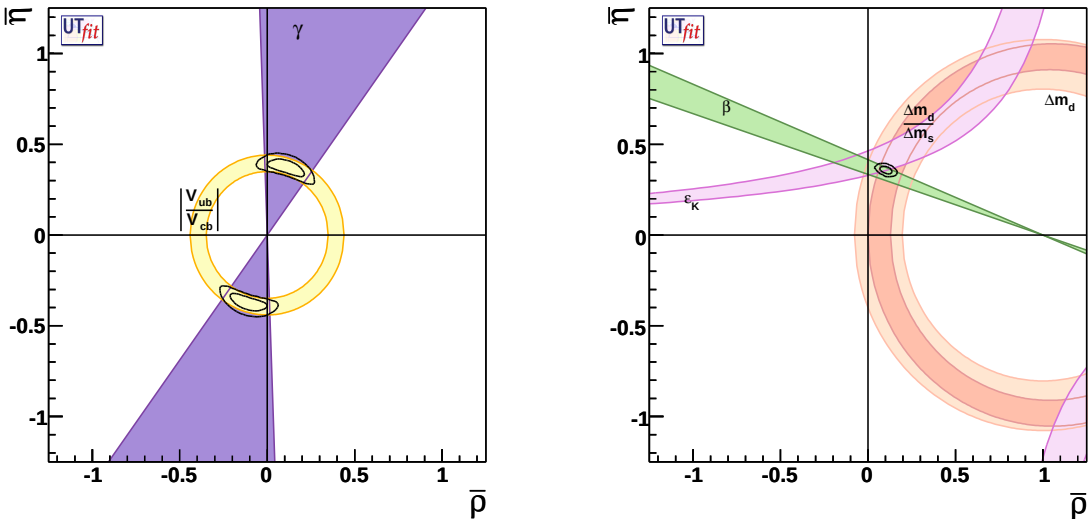

Figure 2.3: Allowed regions for $(\bar{\rho} - \bar{\eta})$ from the "tree-level" (left) and "loop-level" (right) variables. The closed contours at 68% and 95% probability are shown.

The resulting fits are shown in Figure 2.3. The resulting fits from the tree-level processes:

$$\begin{aligned} \overline{\rho} &= 0.116^{+0.060}_{-0.077}, \\ \overline{\eta} &= 0.374^{+0.031}_{-0.029}. \end{aligned} \tag{2.26}$$

which has got high relative error, since the "tree-level" contribution is constrained only by two measurements. The precision of these measurements thus plays a crucial role in the search for new physics.

Another way to perform the search for the new physics is the comparison of the input values of the fit (i.e. observables obtained experimentally) with the predictions obtained after the fit (i.e. predictions assuming the validity of SM). The predictions can be also obtained without inserting this particular measurement in the fit. Any contradiction between these measurements would imply the NP effects. The results of this study is shown in Table 2.1.

The fit also produces the predictions of the elements of the CKM matrix.

$$V_{CKM} = \begin{pmatrix} 0.97408 \pm 0.00031 & 0.2261 \pm 0.0013 & 0.00358 \pm 0.00011 \\ 0.2259 \pm 0.0013 & 0.97326 \pm 0.00030 & 0.04121 \pm 0.00044 \\ 0.00875 \pm 0.00019 & 0.04042 \pm 0.00043 & 0.999145 \pm 0.000015 \end{pmatrix} \tag{2.27}$$

These predictions are well compatible with the SM expectations.

Parameter	Input value	Full fit	Prediction
$\bar{\rho}$	—	0.130 ± 0.019	—
$\bar{\eta}$	—	0.351 ± 0.012	—
A	—	0.806 ± 0.013	—
λ	—	0.2261 ± 0.0013	—
$\lvert V_{ub}\rvert$	0.00367 ± 0.00020	0.00358 ± 0.00011	0.00358 ± 0.00011
$\lvert V_{cb}\rvert$	0.04082 ± 0.00045	0.04121 ± 0.00044	—
Δm_s, ps^{-1}	17.77 ± 0.12	17.76 ± 0.11	17.4 ± 1.3
$\alpha, [^\circ]$	91.4 ± 6.1	88.2 ± 2.9	86.3 ± 3.7
$\beta, [^\circ]$	—	21.97 ± 0.75	24.2 ± 1.4
$\sin(2\beta)$	0.654 ± 0.026	0.694 ± 0.018	—
$\cos(2\beta)$	0.86 ± 0.12	0.720 ± 0.018	—
$2\beta + \gamma, [^\circ]$	94 ± 52	113.8 ± 3.1	114.0 ± 3.1
$\gamma, [^\circ]$	74 ± 11	69.6 ± 3.0	69.2 ± 3.1
$\lvert\varepsilon_K\rvert$	0.002355 ± 0.000049	0.002340 ± 0.000047	0.002359 ± 0.000049

Table 2.1: The input values used in the fit, their value after the fit and the predictions of these values assuming the validity of SM.

Chapter 3

Measurement of the Unitarity Triangle Angle γ

The angle γ is defined as the weak phase of the CKM element $V_{ub} = |V_{ub}|e^{-i\gamma}$. Various methods related to $B^+ \to D^{(*)0}K^{(*)+}$ decays have been proposed to determine the UT angle γ. These methods exploit the fact that the neutral D meson decay product can be either a D^0 (from a $\bar{b} \to c\bar{u}s$ transition), or a $\bar{D}^0$ (from a $\bar{b} \to u\bar{c}s$ transition; or vice versa for b decays). If the final state is chosen such that both D^0 and $\bar{D}^0$ can contribute, the interference between these amplitudes is sensitive to the phase γ, allowing γ to be determined with essentially no theoretical assumptions. Choices for the final state include D^0 meson decaying to:

- a singly Cabibbo-suppressed *CP* eigenstate, like $D^0 \to h^+h^-$ $(h = \pi, K)$ for Gronau-London-Wyler (GLW) method [60];
- a doubly Cabibbo-suppressed flavor eigenstate, like $D^0 \to K^+\pi^-$ for Atwood-Dunietz-Soni (ADS) method [61];
- a Cabibbo-allowed self-conjugate 3-body state, like $D^0 \to K^0_S\pi^+\pi^-$ for Giri-Grossman-Soffer-Zupan (GGSZ) method [62].

If we now consider the counterpart of neutral meson decays the situation is different. In fact, since neutral B mesons mix, interference effects between $b \to c$ and $b \to u$ decay amplitudes in B^0 decays (for instance into $D^{(*)\pm}\pi^{\mp}$ final states) are studied for the determination of the combination of UT angles $2\beta + \gamma$. In this case the tagging technique and a time dependent analysis are required [20]. In contrast, $B^0 \to D^{(*)0}K^{*0}$ decay modes can be used to directly measure γ. In fact, in this case, tagging is not needed and we can unambiguously identify if a B^0 or $\bar{B}^0$ has decayed through the sign of the electric charge of the kaon from the $K^{*0} \to K\pi$

decay[1].

An example of such processes is shown in Figure 3.1. γ is the relative weak phase between the two diagrams, and can be accessed by measuring *CP* violating effects in B decays where the two amplitudes interfere. This type of interference can be seen in both charged an neutral B meson decays.

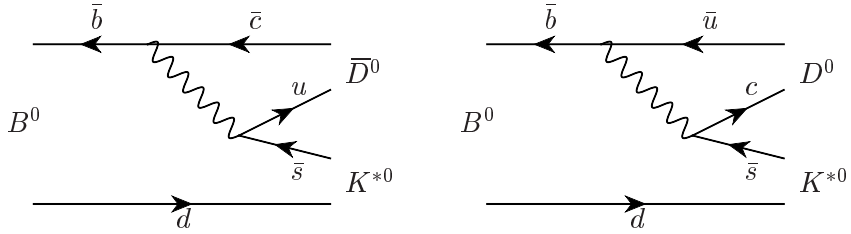

Figure 3.1: Feynman diagrams for $B^0 \to \overline{D}^0 K^{*0}$ and $B^0 \to D^0 K^{*0}$. The relative phase between these decays is proportional to the CKM angle γ.

3.1 General Formalism

Keeping in mind that $V_{ub} = |V_{ub}|e^{-i\gamma}$ one can define the following amplitudes for B meson to two body decays :

$$\begin{aligned} A(B^- \to D^0 K^-) &= |A_B| e^{i\Delta_B}, \\ A(B^- \to \overline{D}^0 K^-) &= |\bar{A}_B| e^{i\bar{\Delta}_B} e^{-i\gamma}, \\ A(B^+ \to \overline{D}^0 K^+) &= |A_B| e^{i\Delta_B}, \\ A(B^+ \to D^0 K^+) &= |\bar{A}_B| e^{i\bar{\Delta}_B} e^{i\gamma}, \end{aligned} \tag{3.1}$$

with Δ_B and $\bar{\Delta}_B$ being the strong phase of the B decay. The same can be done for the decays $D^0 \to f$:

$$\begin{aligned} A(D^0 \to f) &= |A_D| e^{i\Delta_D}, \\ A(D^0 \to \bar{f}) &= |\bar{A}_D| e^{i\bar{\Delta}_D}, \\ A(\overline{D}^0 \to \bar{f}) &= |A_D| e^{i\Delta_D}, \\ A(\overline{D}^0 \to f) &= |\bar{A}_D| e^{i\bar{\Delta}_D}, \end{aligned} \tag{3.2}$$

with Δ_D and $\bar{\Delta}_D$ being the strong phase of the D decay.

[1]Some analyses also try to measure γ from charmless B decay, where $b \to u$ transitions appear in penguin diagrams, making use of the SU(3) symmetry. These methods will not be discussed here.

Thus, the amplitude of the decay $B^- \to [f]_{D^0} K^-$ (with $[f]_{D^0}$ notating the fact that the f can come either from D^0 or from $\overline{D}^0$) can be presented (neglecting the $D^0 - \overline{D}^0$ mixing):

$$\begin{aligned} A(B^- \to [f]_{D^0} K^-) =& A(B^- \to D^0 K^-) A(D^0 \to f) \\ &+ A(B^- \to \overline{D}^0 K^-) A(\overline{D}^0 \to f) \\ &= |A_B||A_D| e^{i(\Delta_B + \Delta_D)} + |\bar{A}_B||\bar{A}_D| e^{i(\bar{\Delta}_B + \bar{\Delta}_D - \gamma)}, \\ A(B^+ \to [\bar{f}]_{D^0} K^+) =& A(B^+ \to \overline{D}^0 K^+) A(\overline{D}^0 \to \bar{f}) \\ &+ A(B^+ \to D^0 K^+) A(D^0 \to \bar{f}) \\ &= |A_B||A_D| e^{i(\Delta_B + \Delta_D)} + |\bar{A}_B||\bar{A}_D| e^{i(\bar{\Delta}_B + \bar{\Delta}_D + \gamma)}. \end{aligned} \tag{3.3}$$

Thus, the partial widths of the decays can be written as:

$$\begin{aligned} \Gamma(B^- \to [f]_{D^0} K^-) &= |A_B|^2 |A_D|^2 + |\bar{A}_B|^2 |\bar{A}_D|^2 + 2|A_B||A_D||\bar{A}_B||\bar{A}_D| \cos(\delta - \gamma), \\ \Gamma(B^+ \to [\bar{f}]_{D^0} K^+) &= |A_B|^2 |A_D|^2 + |\bar{A}_B|^2 |\bar{A}_D|^2 + 2|A_B||A_D||\bar{A}_B||\bar{A}_D| \cos(\delta + \gamma), \end{aligned} \tag{3.4}$$

where

$$\begin{aligned} \delta &= \delta_{\mathrm{B}} + \delta_{\mathrm{D}}, \\ \delta_{\mathrm{B}} &= \bar{\Delta}_B - \Delta_B, \\ \delta_{\mathrm{D}} &= \bar{\Delta}_D - \Delta_D. \end{aligned} \tag{3.5}$$

One can define:

$$r_{\mathrm{B}} \equiv \frac{|A(B^- \to \overline{D}^0 K^-)|}{|A(B^- \to D^0 K^-)|} = \frac{|\bar{A}_B|}{|A_B|}, \tag{3.6}$$

$$r_{\mathrm{D}}(f) \equiv \frac{|A(D^0 \to f)|}{|A(D^0 \to \bar{f})|} = \frac{|A_D|}{|\bar{A}_D|}. \tag{3.7}$$

These quantities play an important role in the determination of γ. The value and the relative error of ratio r_{B} drives the precision on γ. The values of $r_{\mathrm{D}}(f)$ are determined with B or charm factories data (for example, [58, 59]).

Introducing the definitions of Equations 3.6 and 3.7 into partial width expressions (Equation 3.4) one gets:

$$\begin{aligned} \Gamma(B^- \to [f]_{D^0} K^-) &= |A_B|^2 |\bar{A}_D|^2 (r_{\mathrm{D}}^2(f) + r_{\mathrm{B}}^2 + 2 r_{\mathrm{B}} r_{\mathrm{D}} \cos(\delta - \gamma)), \\ \Gamma(B^+ \to [\bar{f}]_{D^0} K^+) &= |A_B|^2 |\bar{A}_D|^2 (r_{\mathrm{D}}^2(f) + r_{\mathrm{B}}^2 + 2 r_{\mathrm{B}} r_{\mathrm{D}} \cos(\delta + \gamma)). \end{aligned} \tag{3.8}$$

More generally, in case of multibody D meson decays for the point p in the phase space:

$$\begin{aligned} A(D^0 \to f)_p &= |A_D(p)| e^{i\Delta_D(p)}, \\ A(D^0 \to \bar{f})_p &= |\bar{A}_D(p)| e^{i\bar{\Delta}_D(p)}, \\ A(\overline{D}^0 \to \bar{f})_p &= |A_D(p)| e^{i\Delta_D(p)}, \\ A(\overline{D}^0 \to f)_p &= |\bar{A}_D(p)| e^{i\bar{\Delta}_D(p)}. \end{aligned} \tag{3.9}$$

Following the same steps as in case of 2-body D meson decay the partial widths can be written:

$$\begin{aligned}\Gamma(B^- \to [f]_{D^0} K^-) &= |A_B|^2 \int |(\bar{A}_D)_p|^2 \, dp (r_{\rm D}^2(f) + r_{\rm B}^2 + 2 r_{\rm B} r_{\rm D} k_{\rm D} \cos(\delta - \gamma)), \\ \Gamma(B^+ \to [\bar{f}]_{D^0} K^+) &= |A_B|^2 \int |(\bar{A}_D)_p|^2 \, dp (r_{\rm D}^2(f) + r_{\rm B}^2 + 2 r_{\rm B} r_{\rm D} k_{\rm D} \cos(\delta + \gamma)),\end{aligned} \tag{3.10}$$

with

$$k_{\rm D} e^{i\delta_{\rm D}^s} \equiv \frac{\int dp \, A_D(p) \bar{A}_D(p) e^{i\delta(p)}}{\sqrt{\int dp \, A_D^2(p) \int dp \, \bar{A}_D^2(p)}}, \tag{3.11}$$

$$r_{\rm D} = \frac{\int dp \, |\bar{A}_D(p)|}{\int dp \, |A_D(p)|}. \tag{3.12}$$

These partial widths are the main constructing elements of the observables used in different methods. All the formulas can be easily generalized to the $B^+ \to D^0 K^{*+}$, $B^+ \to D^{*0} K^+$, and $B^0 \to D^0 K^{*0}$. In case of the $B \to DK^*$ channel the same formalism as the one used for the three body D decays should be introduced for B:

$$r_S = \frac{\int dp \, |\bar{A}_B(p)|}{\int dp \, |A_B(p)|}, \tag{3.13}$$

in this case, we use r_S instead of $r_{\rm B}$ since the value of this ratio is different depending on the portion of the $DK\pi$ phase space analyzed. $\delta_{\rm B}$ should be redefined accordingly:

$$k_S e^{i\delta_B^s} \equiv \frac{\int dp \, A_B(p) \bar{A}_B(p) e^{i\delta(p)}}{\sqrt{\int dp \, A_B^2(p) \int dp \, \bar{A}_B^2(p)}}, \tag{3.14}$$

where $|\bar{A}_B(p)|$ is the amplitude for the suppressed decay of the B meson, $|A_B(p)|$ is the amplitude for the allowed mode. Since the choice of the K^* introduces a cut on the Dalitz plane, the value of r_S is different from the value of $r_{\rm B}$. The study presented in [19] shows that $k_S = (0.95 \pm 0.03)$.

In the following we will describe the methods in details.

3.1.1 The Gronau-London-Wyler Method

The Gronau-London-Wyler (GLW) method [60] is based on the reconstruction of the B decay to $D^0 K$ where D^0 and $\overline{D}^0$ decay to CP-even (like K^+K^-) or CP-odd (like $K_S^0\pi^0$) eigenstates. These eigenstates can be written as:

$$|D_\pm^0\rangle = \frac{1}{\sqrt{2}} \left(|D^0\rangle \pm |\overline{D}^0\rangle \right), \tag{3.15}$$

where the subscript $\pm$ indicates the *CP*-even and *CP*-odd eigenstate, respectively. In this case, the $f = \bar{f}$ implies $\bar{A}_D = A_D$ and $\bar{\Delta}_D = \Delta_D$ or $\bar{\Delta}_D = \Delta_D + \pi$, which leads to $r_{\rm D}(CP) = 1$, and $\delta_{\rm D} = 0$ or $\delta_{\rm D} = \pi$.

The D^0 decay modes normally used are:

- *CP*+: K^+K^-, $\pi^+\pi^-$;
- *CP*−: $K^0_S\pi^0$, ϕK^0_S, ηK^0_S, ρK^0_S, and ωK^0_S.

The four observables for this method are formed in the following way:

$$\begin{aligned} R_{CP\pm} &= \frac{\Gamma(B^+ \to D^0_\pm K^+) + \Gamma(B^- \to D^0_\pm K^-)}{\Gamma(B^+ \to D^0 K^+) + \Gamma(B^- \to \overline{D}^0 K^-)} = 1 + r_{\rm B}^2 \pm 2 r_{\rm B} \cos\gamma \cos\delta_{\rm B}, \\ A_{CP\pm} &= \frac{\Gamma(B^+ \to D^0_\pm K^+) - \Gamma(B^- \to D^0_\pm K^-)}{\Gamma(B^+ \to D^0_\pm K^+) + \Gamma(B^- \to D^0_\pm K^-)} = \frac{\pm 2 r_{\rm B} \sin\gamma \sin\delta_{\rm B}}{R_{CP\pm}}, \end{aligned} \tag{3.16}$$

with $r_{\rm D} = 1$ due to two body decay of the D^0 meson.

By construction, the $R_{CP\pm}$ and $A_{CP\pm}$ are invariant under the following operations:

- $\{\gamma, \delta_{\rm B}\} \leftrightarrow \{-\gamma, -\delta_{\rm B}\}$;
- $\{\gamma, \delta_{\rm B}\} \leftrightarrow \{\gamma + \pi, \delta_{\rm B} + \pi\}$;
- $\{\gamma, \delta_{\rm B}\} \leftrightarrow \{\delta_{\rm B}, \gamma\}$.

These symmetries give rise to the 8-fold ambiguity which represents the weakness of the method. This ambiguity can be reduced to 4-fold in case of simultaneous analysis of two different B decays such as $B^+ \to D^{*0}_{CP} K^+$ and $B^+ \to D^0_{CP} K^{*+}$.

Another limitation of the method is the low branching fractions of the overall decay chain. The final branching fraction including secondary decays is less than 10^{-6}.

The GLW method is useful in measuring $r_{\rm B}$, but has typically a low sensitivity to γ.

3.1.2 The Atwood-Dunietz-Soni Method

In the ADS method [61], γ is measured from the study of $B \to DK$ decays, where D mesons decay into non *CP* eigenstate final states. The suppression of $b \to u$ transition with respect to the $b \to c$ one is partly overcome by the study of decays of the B meson in final states which can

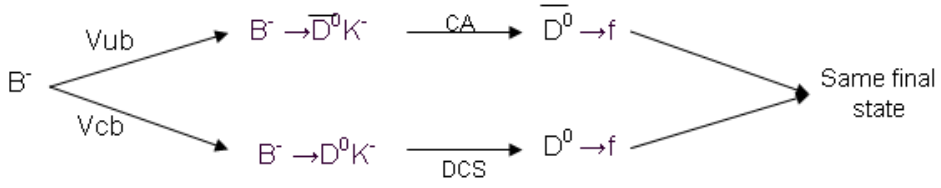

Figure 3.2: Scheme for the ADS method: B^+ mesons decaying to the same final state, through two different decay chains, for "opposite sign" events (top) and for "same sign" events (bottom).

proceed in two ways: either through a favored $b \to c$ B decay followed by a doubly-Cabibbo-suppressed D decay, or through a suppressed $b \to u$ B decay followed by a Cabibbo-favored D decay. The decay chains studied are sketched in Figure 3.2.

In the ADS method the "classical" set observables are:

$$\begin{aligned} R_{\rm ADS} &= \frac{\Gamma(B^- \to [f]_{D^0} K^-) + \Gamma(B^+ \to [\bar{f}]_{D^0} K^+)}{\Gamma(B^+ \to [f]_{D^0} K^+) + \Gamma(B^- \to [\bar{f}]_{D^0} K^-)}, \\ A_{\rm ADS} &= \frac{\Gamma(B^- \to [f]_{D^0} K^-) - \Gamma(B^+ \to [\bar{f}]_{D^0} K^+)}{\Gamma(B^- \to [f]_{D^0} K^-) + \Gamma(B^+ \to [\bar{f}]_{D^0} K^+)}. \end{aligned} \tag{3.17}$$

Keeping in mind the definition that were introduced in Equations 3.9 and neglecting higher order contributions one readily receives:

$$\begin{aligned} R_{\rm ADS} &= r_{\rm S}^2 + r_{\rm D}^2 + 2 r_{\rm S} k_{\rm B} r_{\rm D} k_{\rm D} \cos\gamma \cos(\delta_{\rm B}^s + \delta_{\rm D}^s), \\ A_{\rm ADS} &= \frac{2 r_{\rm S} r_{\rm D} k_{\rm D} \sin\gamma \sin(\delta_{\rm B}^s + \delta_{\rm D}^s)}{R_{\rm ADS}}. \end{aligned} \tag{3.18}$$

In the case of the two body D decays $\delta_{\rm D}^s \to \delta_{\rm D}$ and $k_{\rm D} \to 1$ and in the case of the two body B decays $\delta_{\rm B}^s \to \delta_{\rm B}$.

The following parameters can be extracted from the observables:

- $r_{\rm S}$, $\delta_{\rm B}^s$, $k_{\rm B}$(B sector);
- $r_{\rm D}$, $\delta_{\rm D}$, $k_{\rm D}$(D sector);
- γ.

Each parameter in the B sector depends on the studied B decays, whereas the parameters of the D sector depend on the D-meson channel.

The D decay parameters can be extracted from the separate study of the D mesons. In particular, the $\{\delta_{\rm D}, k_{\rm D}\}$ likelihood can be measured using quantum-correlated measurements at

CLEO-c experiment [59]. The results of the study for $D^0 \to K^+\pi^-\pi^0$ and $D^0 \to K^+\pi^-\pi^+\pi^-$ are shown in Figure 3.3. The value of $r_{\rm D}$ is normally taken from the world average (with the leading sensitivity at B factories). The magnitude of $r_{\rm D}$ controls the sensitivity on γ in the way the value of $r_{\rm B}$ does. That is why the most sensitive D^0 channel is the two-body $D^0 \to K\pi$ decay ($r_{\rm D} = 1$ in this case). However, it has been argued that other decay channels (with $r_{\rm D} < 1$) can give competitive results on γ.

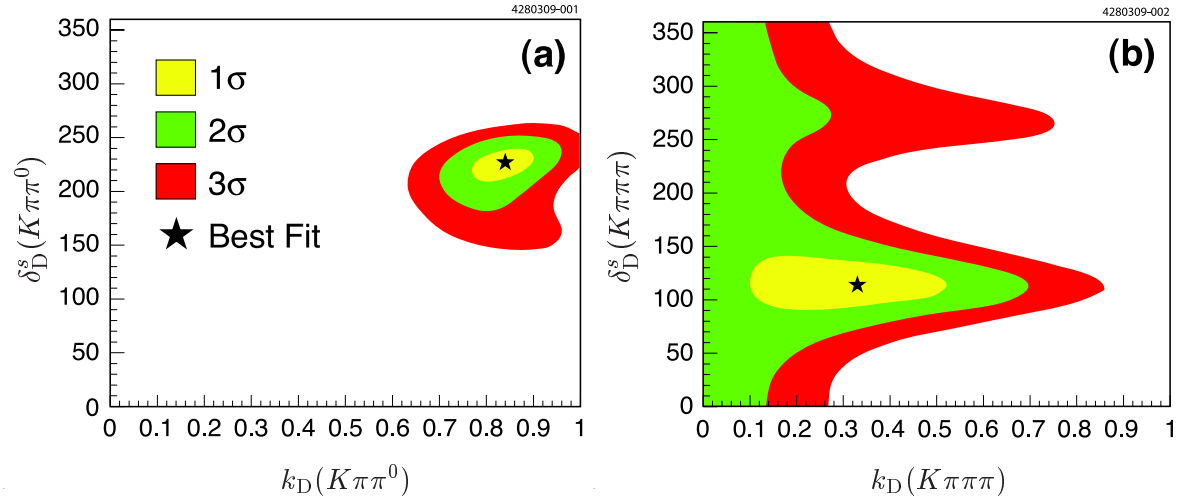

Figure 3.3: The 1σ, 2σ, and 3σ allowed regions in the plane $\{\delta_{\rm D}, k_{\rm D}\}$ for (a) $D^0 \to K^+\pi^-\pi^0$ and (b) $D^0 \to K^+\pi^-\pi^+\pi^-$.

The ratio $A_{\rm ADS}$ is usually either not measured (like the analysis in [63]) or reconstructed from charge-specific ratios $R^{\pm}$ (like analysis in [64]):

$$\begin{aligned} R^+ &= \frac{\Gamma(B^+ \to [\bar{f}]_{D^0} K^+)}{\Gamma(B^+ \to [f]_{D^0} K^+)} = r_{\rm B}^2 + r_{\rm D}^2 + 2 r_{\rm B} r_{\rm D} k_{\rm D} \cos(\gamma + \delta), \\ R^- &= \frac{\Gamma(B^- \to [f]_{D^0} K^-)}{\Gamma(B^+ \to [\bar{f}]_{D^0} K^+)} = r_{\rm B}^2 + r_{\rm D}^2 + 2 r_{\rm B} r_{\rm D} k_{\rm D} \cos(\gamma - \delta), \end{aligned} \tag{3.19}$$

that are connected with the $R_{\rm ADS}$ and $A_{\rm ADS}$ by simple relations:

$$\begin{aligned} R_{\rm ADS} &= \frac{R^+ + R^-}{2}; \\ A_{\rm ADS} &= \frac{R^- - R^+}{R^- + R^+}. \end{aligned} \tag{3.20}$$

Since R^+ and R^- are two independent observables, while $R_{\rm ADS}$ and $A_{\rm ADS}$ are correlated we prefer to extract the physical parameters from (R^+, R^-) rather than $(R_{\rm ADS}, A_{\rm ADS})$.

However, some analyses were performed with the fit extraction of $A_{\rm ADS}$ [65]. The discussion of the strategy choice can be found in Chapter 8 that is devoted to the description of analysis done with this method.

This type of analysis observables definition gives rise to following symmetries:

- $\{\gamma;\delta\} \leftrightarrow \{-\gamma;-\delta\}$;
- $\{\gamma,\delta\} \leftrightarrow \{\delta,\gamma\}$;
- $\{\gamma,\delta\} \leftrightarrow \{\gamma+\pi,\delta+\pi\}$.

The D^0 final states reconstructed in this method are usually: $K^+\pi^-$ (essentially), $K^+\pi^-\pi^0$, $K^+\pi^+\pi^-\pi^-$. Also it has been argued that a cut in the Dalitz plane of these decays can increase the sensitivity. However such a cut complicates the combination with the results of the charm factories that study the D meson decay.

To explicitly show the characteristics of the ADS method we use the relations 3.19 to extract $r_{\rm B}$, $\delta_{\rm B}$, and γ. We follow the Bayesian approach extracting $(r_{\rm D};\delta_{\rm D};k_{\rm D})$ according to their experimental distributions, while for $(r_{\rm B};\delta_{\rm B};\gamma)$ the flat priors are used. R^+ and R^- are generated Gaussian. We perform the extraction with fixed and not fixed value of $r_{\rm B}$ building each time the 2D-likelihood $\{\delta_{\rm B};\gamma\}$. The plots generated with fixed $r_{\rm B}$ (Figure 3.4) show expected 8-fold ADS ambiguity for a single channel, which is solved after application of the D sector measurements and combination with the other channel. The impact of charm sector measurement has got more impact due to the absence of π ambiguity in the $\delta_{\rm D}$. More details of the extraction procedure are described in Chapter 9.

The plots with $r_{\rm B}$ allowed to vary in the fit (Figure 3.5) show that in reality a (less probable) solution still exists. This ambiguity can probably be resolved in case of combining with the $D^0 \to K\pi\pi\pi$ channel, which has never been measured.

3.1.3 The Giri-Grossman-Soffer-Zupan Method

The Giri-Grossmann-Soffer-Zupan (GGSZ) method (often called Dalitz plot method) is based on the reconstruction of $B \to D^0K$ and $B \to \overline{D}^0K$ decays with the D^0 and $\overline{D}^0$ reconstructed into a multi-body *CP* eigenstate. We consider here, as an example, the decay $D^0 \to K^0_S\pi^+\pi^-$, but all the relations can be easily generalized to any multibody D^0 decay.

The decays of D^0 meson are studied in the Dalitz plane (s_{12}, s_{13}), where $s_{ij} = (P_i + P_j)^2$ is the invariant mass of the couple M_iM_j of the D decay products. If one denotes the point in the Dalitz plot as $(m^2_-;m^2_+)$ then the amplitude for $D^0 \to K^0_S\pi^+\pi^-$ in this point can be written as:

$$f(m^2_-,m^2_+) = |f(m^2_-,m^2_+)|e^{i\Delta(m^2_-,m^2_+)}. \tag{3.21}$$

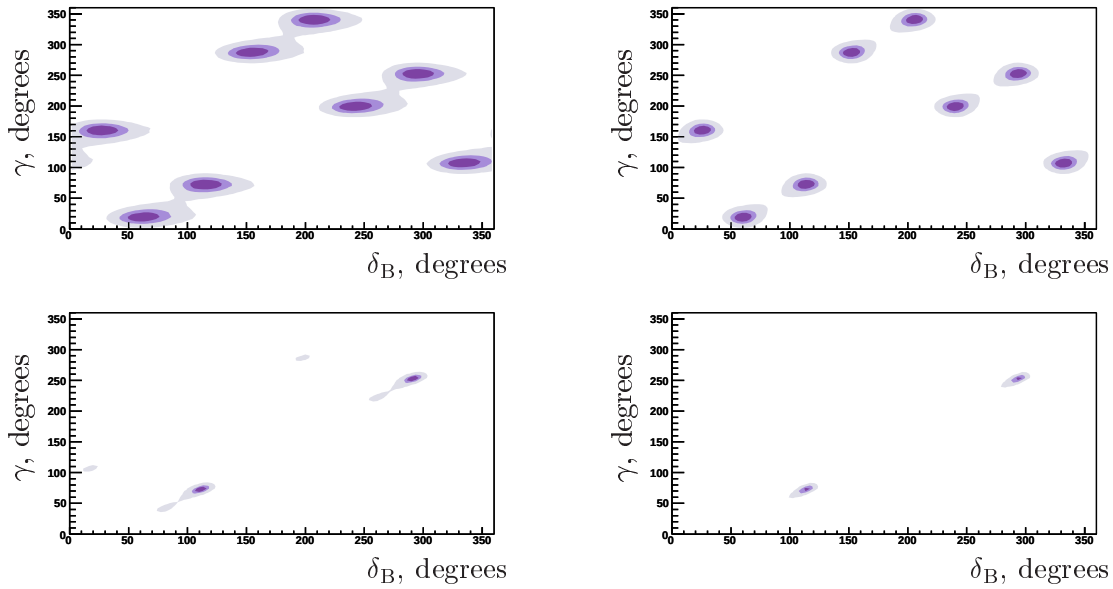

Figure 3.4: The plots show the extracted 2D likelihoods $\{\delta_B; \gamma\}$ for ADS method. Left plots are obtained using recent charm sector measurements, right plots are for the same extraction obtained with δ_D and k_D fixed. The upper line show the results when only the $K\pi\pi^0$ is used, the bottom line shows the results for the combination of the $K\pi$ and $K\pi\pi^0$ channels. The colored zones represent the 39%, 68%, and 95% probability regions. The generated values are $(\gamma; \delta_B) = (73^\circ; 114^\circ)$, the reconstructed values are compatible with the generated ones. For all these analyses r_B is fixed to 0.1.

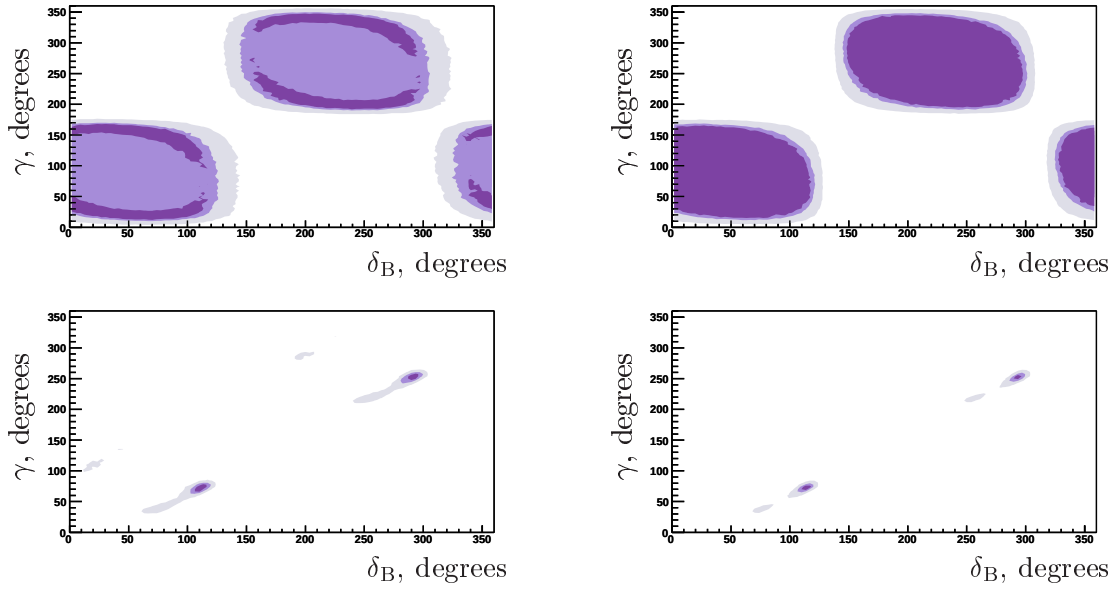

Figure 3.5: The plots show the extracted 2D likelihoods $\{\delta_B; \gamma\}$. Left plots show the results when the recent charm sector measurements are used, right plots obtained with δ_D and k_D fixed. The upper line shows the results using the $K\pi\pi^0$ channel only, whereas the bottom line shows the results obtained combining the $K\pi$ and $K\pi\pi^0$ channels. The colored zones represent the 39%, 68%, and 95% probability regions. The generated values are $(\gamma; \delta_B; r_B) = (73°; 114°; 0.1)$, the reconstructed values are compatible with the generated ones.

The amplitude for the same point of Dalitz plot for $\overline{D}^0 \to K^0_S\pi^+\pi^-$ can be expressed then:

$$f(m^2_+, m^2_-) = |f(m^2_+, m^2_-)|e^{i\Delta(m^2_+, m^2_-)}. \tag{3.22}$$

The total amplitudes for B^- and B^+ decays for the (m^2_+, m^2_-) point of the Dalitz plane can thus be written:

$$\begin{aligned} A_-(m^2_+, m^2_-) &= A(B^- \to D^0K^-)\left(f(m^2_-, m^2_+) + r_{\rm B}e^{i(\delta_{\rm B}-\gamma)}f(m^2_+, m^2_-)\right), \\ A_+(m^2_+, m^2_-) &= A(B^+ \to \overline{D}^0K^+)\left(f(m^2_+, m^2_-) + r_{\rm B}e^{i(\delta_{\rm B}+\gamma)}f(m^2_-, m^2_+)\right). \end{aligned} \tag{3.23}$$

These formulae are indeed just a generalization of the expressions for the two-body decays. The dependence of $f(m^2_-, m^2_+)$ on the point in the Dalitz plane is usually described by the isobar model, in which the decay amplitude is written as a sum of amplitudes with quasi two-body intermediate states, i.e. the decay $D^0 \to M_1M_2M_3$ is considered to be the sum of decays $D^0 \to M_rM_3$ (or $D^0 \to M_rM_2$), where M_r is the resonant state of particles M_1 and M_2 (or M_1 and M_3).

We thus can write the following expression:

$$|f(m^2_-, m^2_+)|e^{i\Delta(m^2_-, m^2_+)} = \sum_j a_j e^{i\delta_j} BW^j_{(m^2_-, m^2_+)}(m, \Gamma, s) + a_{nr}e^{i\delta_{nr}}. \tag{3.24}$$

where $BW^j_{(m^2_-, m^2_+)}(m, \Gamma, s)$ is the expression for the relativistic Breit-Wigner describing the decay through an intermediate j^{th} resonance characterized by its spin s, its mass m and decay width Γ; a_j and δ_j are the amplitude and the decay phase of this resonance; nr marks the non-resonant part of the D^0 decay. Another possibility to know $f(m^2_-, m^2_+)$ is to study this distribution in the separate analyses and use it as an input for the Dalitz analysis at the B factories. The Dalitz method suffers of the ambiguity: $\{\gamma, \delta\} \leftrightarrow \{\gamma + \pi, \delta + \pi\}$.

This method's main limiting factor is the precision of $f(m^2_-, m^2_+)$ knowledge, which can lead to a systematic uncertainty in the γ determination. As shown later the GGSZ method, however, gives the most precise determination of γ.

A usual set of observables for this method is:

$$\begin{aligned} x_+ &= r_{\rm B}\cos(\delta_{\rm B} + \gamma), \\ x_- &= r_{\rm B}\cos(\delta_{\rm B} - \gamma), \\ y_+ &= r_{\rm B}\sin(\delta_{\rm B} - \gamma), \\ y_+ &= r_{\rm B}\sin(\delta_{\rm B} - \gamma). \end{aligned} \tag{3.25}$$

3.2 State-of-the-art in the γ Measurements

The present knowledge of the UT angle γ comes from the combination of several measurements. The following experimental results are available:

- GLW analyses of $B^+ \to D^0_{CP\pm}K^+$, $B^+ \to D^{*0}_{CP\pm}K^+$, and $B^+ \to D^0_{CP\pm}K^{*+}$, (performed both by the *BABAR* [21, 24, 26] and Belle [22, 25] collaborations), the $B^+ \to D^0_{CP\pm}K^+$ mode was studied also by the CDF collaboration [23].
- ADS analyses of $B^+ \to \overline{D}^0(D^0)K^+$ with $\overline{D}^0(D^0) \to K^+\pi^-$ (performed by *BABAR* [27] and Belle [28]) and with $\overline{D}^0(D^0) \to K^+\pi^-\pi^0$ (performed by *BABAR* only [97]), ADS analyses of $B^+ \to \overline{D}^{*0}(D^{*0})K^+$ [27] and for $B^+ \to \overline{D}^0(D^0)K^{*+}$ [29] (*BABAR* collaboration).
- ADS analyses in the neutral B meson decay $B^0 \to \overline{D}^0(D^0)K^{*0}$ with D^0 ($\overline{D}^0$) going to $K^+\pi^-$, $K^+\pi^-\pi^0$, and $K^+\pi^-\pi^+\pi^-$ final states (*BABAR* [63]).
- GGSZ analyses of $B^+ \to D^0_{CP\pm}K^+$, $B^+ \to D^{*0}_{CP\pm}K^+$, and $B^+ \to D^0_{CP\pm}K^{*+}$, with the neutral D reconstructed in $K^0_S\pi^+\pi^-$ (Belle [31, 32], *BABAR* [30]) and $K^0_SK^+K^-$ (*BABAR* [30]). GGSZ analyses of $B^+ \to D^0_{CP\pm}K^+$ with neutral D going to $\pi^+\pi^-\pi^0$ final state [34].
- GGSZ analysis of $B^0 \to D^0_{CP\pm}K^{*0}$, with D reconstructed in $K^0_S\pi^+\pi^-$ was performed by *BABAR* [33].

The results of the measurements summarized by HFAG collaboration [18] can be seen in Figures 3.6, 3.7, 3.8.

The pdf for γ obtained in Bayesian approach using all the measurements presented at the winter 2010 conference are shown in Figure 3.9, giving the result

$$\gamma = (74 \pm 11)^\circ. \tag{3.26}$$

The pdf obtained for the $r_{\rm B}$ ratio, which drives the sensitivity on γ, are shown in Figure 3.10 and the results of the combination are:

$$\begin{aligned} r_{\rm B}(B^+ \to D^0K^+) &= 0.106 \pm 0.016, \\ r_{\rm B}(B^+ \to D^0K^{*+}) &= 0.11 \pm 0.07, \\ r_{\rm B}(B^+ \to D^{*0}K^+) &= 0.113 \pm 0.0025, \\ r_{\rm B}(B^0 \to D^0K^{*0}) &= 0.26 \pm 0.0076. \end{aligned} \tag{3.27}$$

It can be noted that the Dalitz analyses give the most important contribution for the determination of γ, while the GLW and ADS analyses are important for the precise determination of the $r_{\rm B}$ ratios.

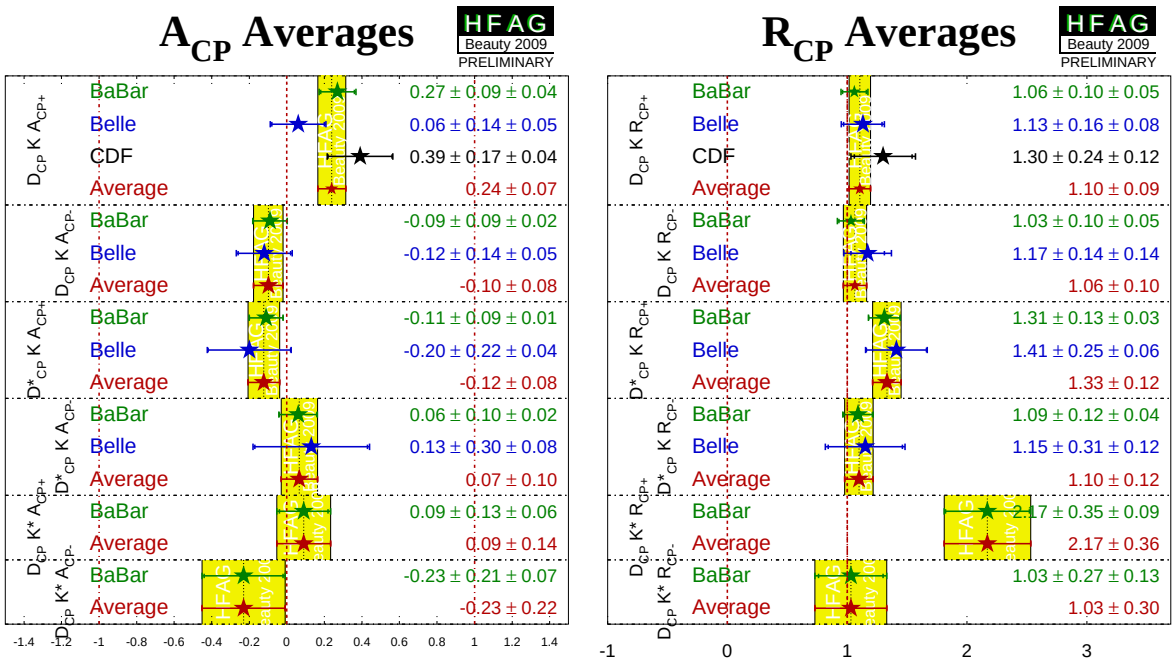

Figure 3.6: The summary of the GLW method results obtained by different experiments, as described in the text. The observables are described in Section 3.1.1

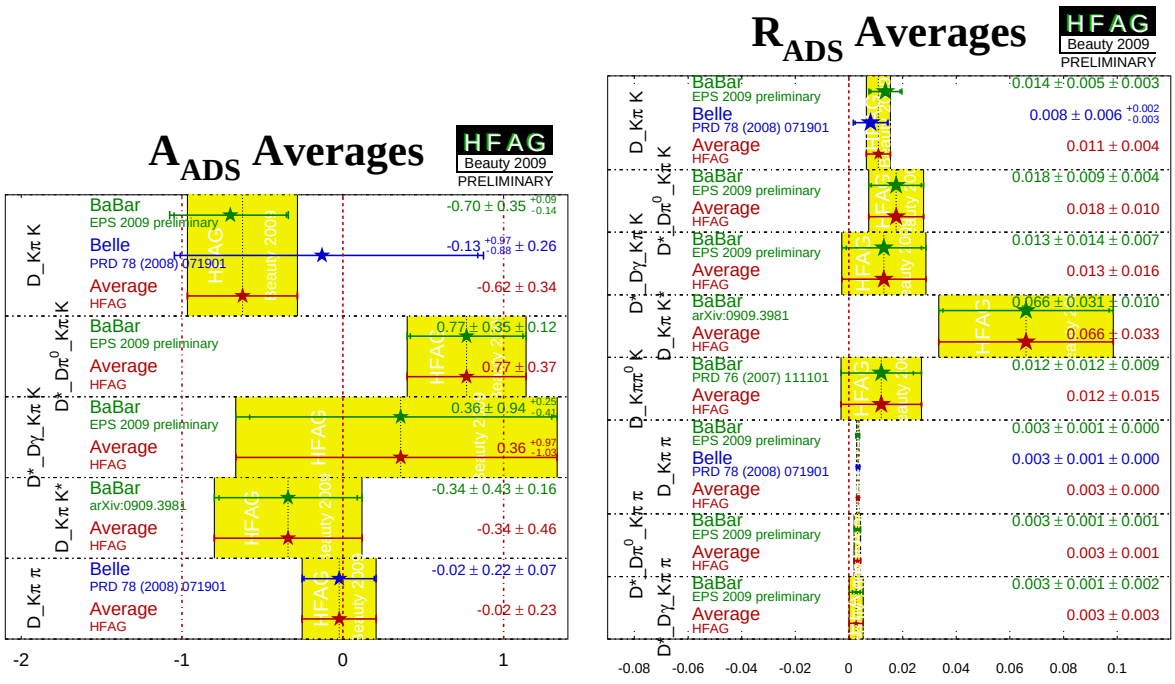

Figure 3.7: The summary of the ADS method results obtained by different experiments, as described in the text. The observables are described in Section 3.1.2

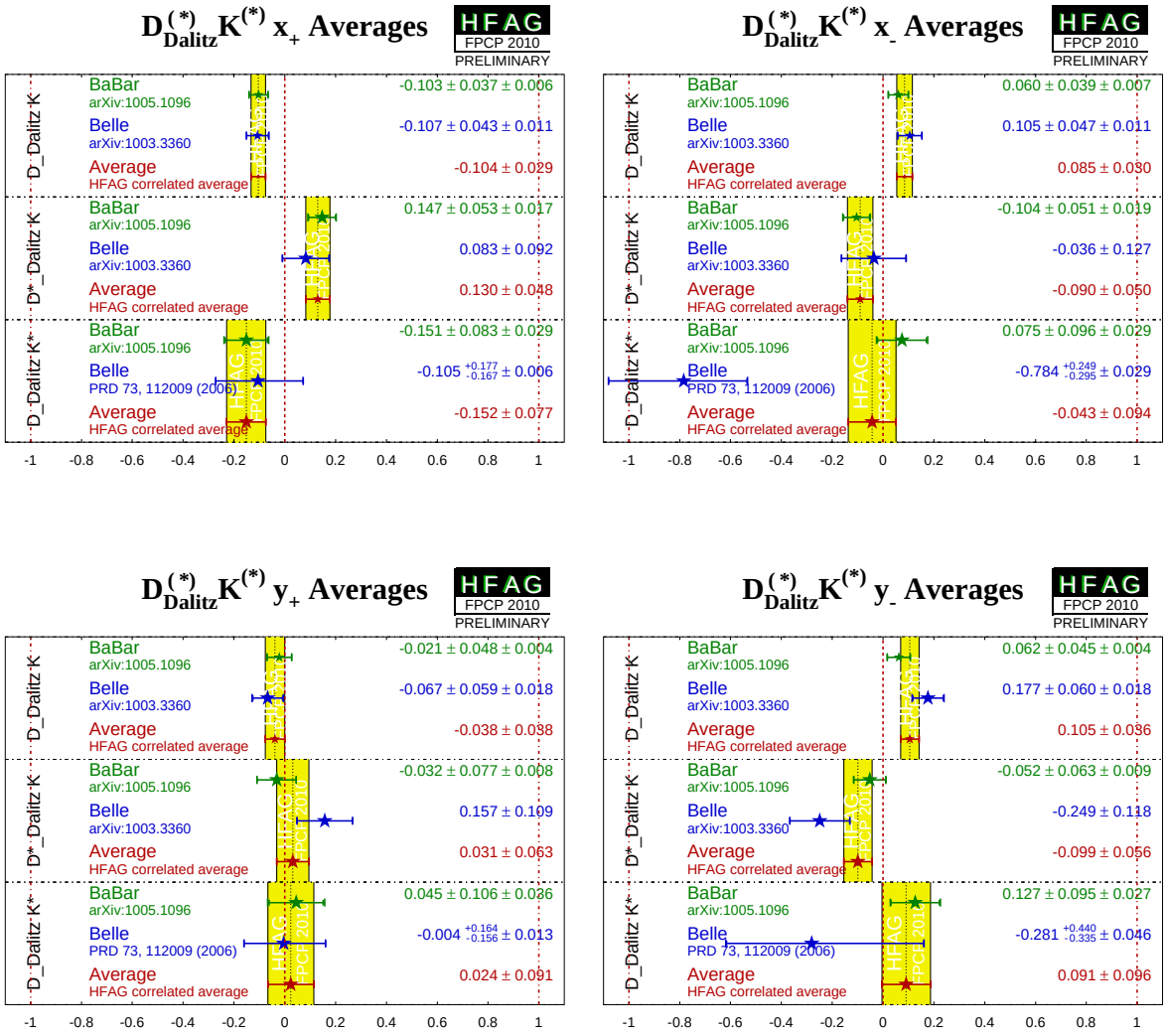

Figure 3.8: The summary of the GGSZ method results obtained by different experiments, as described in the text. The observables are described in Section 3.1.3

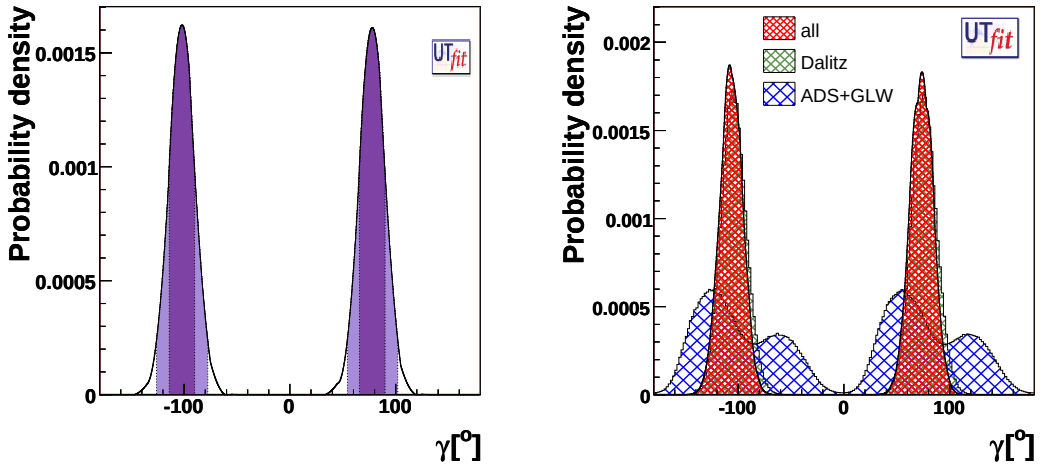

Figure 3.9: One-dimensional pdf for γ from the combination of all the analyses in the charged B meson modes (left). The dark and light colored zones show the 68% and 95% probability regions respectively. In the right plot pdfs are shown separately for γ from GLW and ADS and from Dalitz analyses separately. The combination is also shown, but is barely visible since it is almost coinciding with the result from Dalitz analysis alone. These results are obtained using experimental data available for the 2010 winter conferences.

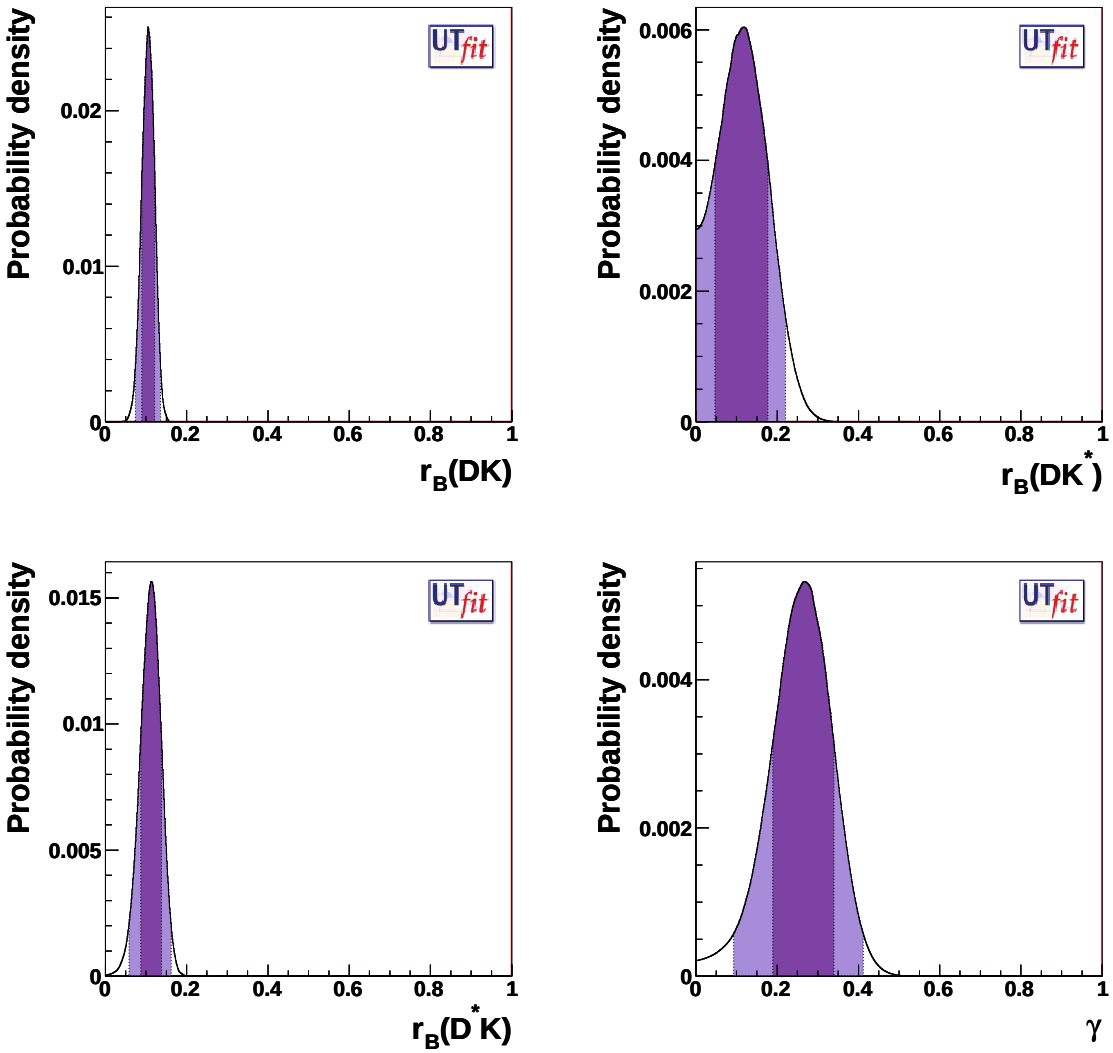

Figure 3.10: One-dimensional pdfs for r_B from the combination of all the analyses for the $B^+ \to DK$, the $B^+ \to DK^*$, the $B^+ \to D^*K$, and the $B^0 \to DK^*$ modes, respectively. The dark and light colored zones show the 68% and 95% probability regions respectively. These results are obtained using experimental data available for the 2010 winter conferences.

Chapter 4

The DK system

The accurate study of the open charm decays, $B \to DK$, allows tests for understanding of the B decay dynamics and represents a privileged tool to precisely determine γ. Different approaches using these decays are described in Chapter 3. The precision of the γ determination is controlled by the $r_{\rm B}$ parameter, which is different depending on the type of decay and the charge of the B meson. The possible way to describe these decays is shown in this Chapter. The outcome of such a description is discussed in the end of the Chapter and in Chapter 9.

Description of the $B \to DK$ decays is frequently done in terms of the operator product expansion (OPE) described in [74, 76]. In this formalism B decays (both charged and neutral) are described with an effective hamiltonian and the process amplitude final state is expressed by matrix element:

$$A(B \to DK) = \langle DK|H_{\rm eff}|B\rangle, \tag{4.1}$$

where H_{eff} is an effective weak Hamiltonian. For the decay of interest we can write only the part of the Hamiltonian:

$$\begin{aligned} H_{\rm eff} =& \frac{G_F}{\sqrt{2}}(|V_{ub}^* V_{cs}|[C_1(\mu)Q_1^{scu}(\mu) + C_2(\mu)Q_2^{scu}(\mu)]+ \\ &+ |V_{cb}^* V_{us}|[C_1(\mu)Q_1^{suc}(\mu) + C_2(\mu)Q_2^{suc}(\mu)]+ \\ &+ |V_{ub}^* V_{cd}|[C_1(\mu)Q_1^{dcu}(\mu) + C_2(\mu)Q_2^{dcu}(\mu)]+ \\ &+ |V_{cb}^* V_{cd}|[C_1(\mu)Q_1^{dcu}(\mu) + C_2(\mu)Q_2^{dcu}(\mu)]), \end{aligned} \tag{4.2}$$

where V_{ij} is the CKM matrix element; $G_F\ (\hbar c)^3 = \frac{\sqrt{2}g_w^2}{8M_W^2} = 1.16637(1) \times 10^{-5}$ GeV^{-2} is the Fermi constant; $C_i(\mu)$ are Wilson coefficients; the Q_1 and Q_2 operators are the so called current-current operators and are defined by:

$$Q_1^{d_i u_j u_k} = (\bar{b}u_k)_{V-A}(\bar{u}_j d_i)_{V-A}, \tag{4.3}$$

$$Q_2^{d_i u_j u_k} = (\bar{b}d_i)_{V-A}(\bar{u}_j u_k)_{V-A}. \tag{4.4}$$

The Q operators can be regarded as effective vertices with coupling $C_i(\mu)$. The μ scale is arbitrary, but its value is normally assumed to be of the order of the b quark mass ($m_b = 4.3$ GeV/c^2). The μ-dependence of $C_i(\mu)$ has to cancel the μ-dependence of $< Q_i(\mu) >$ so that the physical amplitude $A(B \to DK)$ is μ-independent. In the same way the renormalization scheme dependence should be canceled out. It should be stressed that these cancelations involve generally several terms in the expansion.

The contributions to the matrix elements of the relevant operators are classified in terms of different topologies of Wick contractions. In this case the amplitudes for the decays can be expressed in terms of renormalization scheme and scale independent parameters, that are linear combinations of Wick contractions for different operators, weighted with their Wilson coefficients. The topologies of interest for $B \to DK$ decays are shown in Figure 4.1. These are Disconnected Emission (DE), Connected Emission (CE), Disconnected Annihilation (DA) and Connected Annihilation (CA).

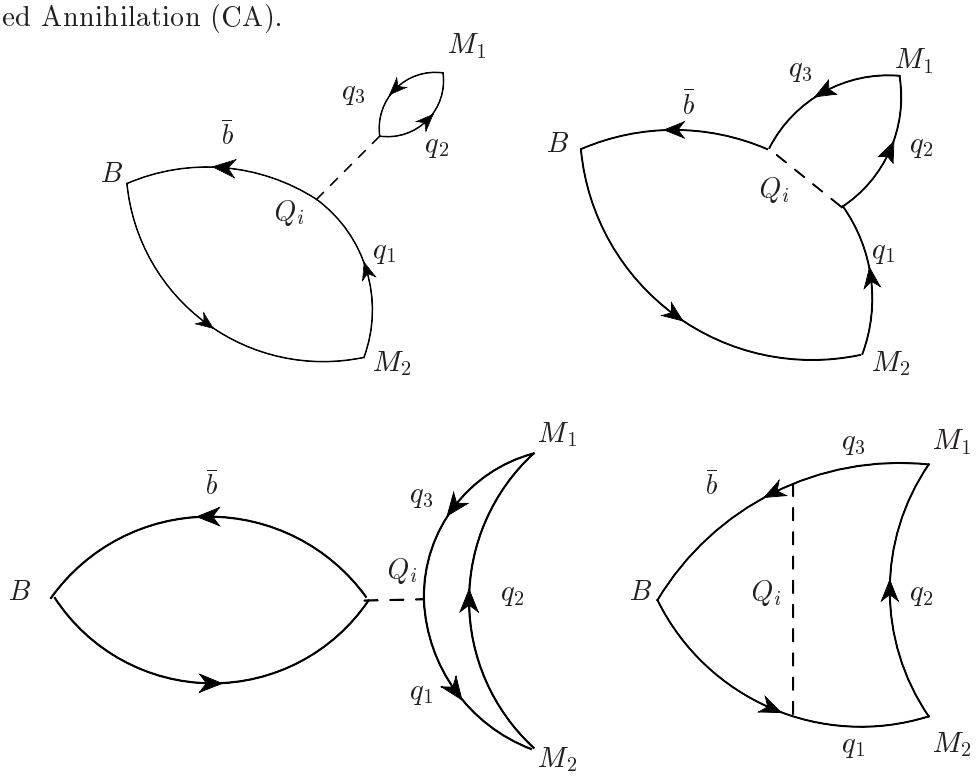

Figure 4.1: Topologies used to describe $B \to DK$ decays amplitudes

In this way the emission and annihilation parameters can be defined as

$$\begin{aligned}
E_1(q_1, q_2, q_3; B, M_1, M_2) &= C_1 DE(q_1, q_2, q_3; B, M_1, M_2) + C_2 CE(q_1, q_2, q_3, M1, M2), \\
E_2(q_1, q_2, q_3; B, M_1, M_2) &= C_1 DE(q_1, q_2, q_3; B, M_1, M_2) + C_2 CE(q_1, q_2, q_3; B, M1, M2), \\
A_1(q_1, q_2, q_3; B, M_1, M_2) &= C_1 DA(q_1, q_2, q_3; B, M_1, M_2) + C_2 CA(q_1, q_2, q_3; B, M1, M2),
\end{aligned} \tag{4.5}$$

with q_i being different quarks that contribute to the process of $B \to M_1 M_2$.

The amplitudes of $B_{\text{charged}} \to DK$ decays can be expressed as following:

$$\begin{aligned} A(B^+ \to \overline{D}^0 K^+) &= V_{us} V_{cb}^* (E_1(s,u,c;B^+,K^+,\overline{D}^0) + E_2(c,u,s;B^+,\overline{D}^0,K^+)), \\ A(B^+ \to D^0 K^+) &= V_{cs} V_{ub}^* (E_2(u,c,s;B^+,D^0,K^+) + A_1(s,u,c;B^+,K^+,D^0)), \\ A(B^+ \to D^+ K^0) &= V_{cs} V_{ub}^* (A_1(s,d,c;B^+,K^0,D^+)). \end{aligned} \tag{4.6}$$

The similar relations hold for neutral sector:

$$\begin{aligned} A(B^0 \to D^- K^+) &= V_{us} V_{cb}^* E_1(s,u,c;B^0,K^+,D^-); \\ A(B^0 \to \overline{D}^0 K^0) &= V_{us} V_{cb}^* E_2(c,u,s;B^0,\overline{D}^0,K^0); \\ A(B^0 \to D^0 K^0) &= V_{cs} V_{ub}^* E_2(u,c,s;B^0,D^0,K^0); \end{aligned} \tag{4.7}$$

These relations are commonly rewritten using the definitions:

$$\begin{aligned} \bar{T}_{\text{charged}} &= V_{us} V_{cb}^* E_1(s,u,c;B^+,K^+,\overline{D}^0), \\ \bar{C}_{\text{charged}} &= V_{us} V_{cb}^* E_2(s,u,c;B^+,K^+,D^0), \\ C_{\text{charged}} &= V_{cs} V_{ub}^* E_2(u,c,s;B^+,D^0,K^+), \\ A_{\text{charged}} &= V_{cs} V_{ub}^* A_1(s,u,c;B^+,K^+,D^0), \\ A'_{\text{charged}} &= V_{cs} V_{ub}^* A_1(s,d,c;B^+,D^+,K^0), \end{aligned} \tag{4.8}$$

that gives a clear (although not completely correct) link between topological and diagrammatic descriptions: the $\bar{T}_{\text{charged}}$ stays for "tree contribution", $\bar{C}_{\text{charged}}$ and C_{charged} are "color-suppressed contributions", and A_{charged} and A'_{charged} is "annihilation contributions". Substituting Equations 4.8 into Equations 4.6 one gets

$$\begin{aligned} A(B^+ \to \overline{D}^0 K^+) &= (\bar{T}_{\text{charged}} + \bar{C}_{\text{charged}}), \\ A(B^+ \to D^0 K^+) &= (C_{\text{charged}} + A_{\text{charged}}), \\ A(B^+ \to D^+ K^0) &= A'_{\text{charged}}, \end{aligned} \tag{4.9}$$

giving the possibility to associate the diagrams shown in Figure 4.2 with the corresponding diagram[1]

The same definitions can be written in case of neutral B mesons (substituting charged particles to the neutral ones):

$$\begin{aligned} \bar{T}_{\text{neutral}} &= V_{us} V_{cb}^* E_1(s,u,c;B^0,K^+,D^-), \\ \bar{C}_{\text{neutral}} &= V_{us} V_{cb}^* E_2(c,u,s;B^0,K^0,\overline{D}^0), \\ C_{\text{neutral}} &= V_{cs} V_{ub}^* E_2(u,c,s;B^0,D^0,K^0), \end{aligned} \tag{4.10}$$

[1] Indeed the diagrammatic approach in case of a B meson decaying into the DK system gives a good approximation of OPE approach. However it is quite important to follow the OPE in description of any other decay mode.

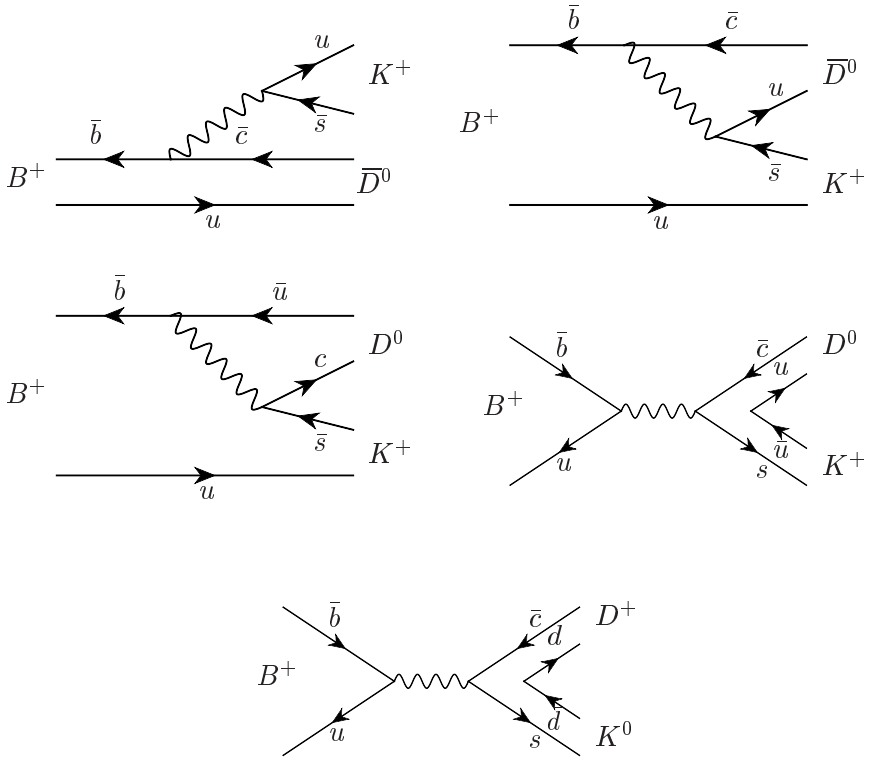

Figure 4.2: The charged B mesons decays. $B^+ \to \overline{D}^0 K^+$ proceeding through $\bar{T}_{\text{charged}}$ (top left), $\bar{C}_{\text{charged}}$ (top right); $B^+ \to D^0 K^+$ proceeding through C_{charged} (middle left) and A_{charged} (middle right); $B^+ \to D^+ K^0$ proceeding through A'_{charged} (bottom).

which gives

$$\begin{aligned} A(B^0 \to D^- K^+) &= \bar{T}_{\text{neutral}}, \\ A(B^0 \to \overline{D}^0 K^0) &= \bar{C}_{\text{neutral}}, \\ A(B^0 \to D^0 K^0) &= C_{\text{neutral}}, \end{aligned} \tag{4.11}$$

with the diagrammatic description shown in Figure 4.3.

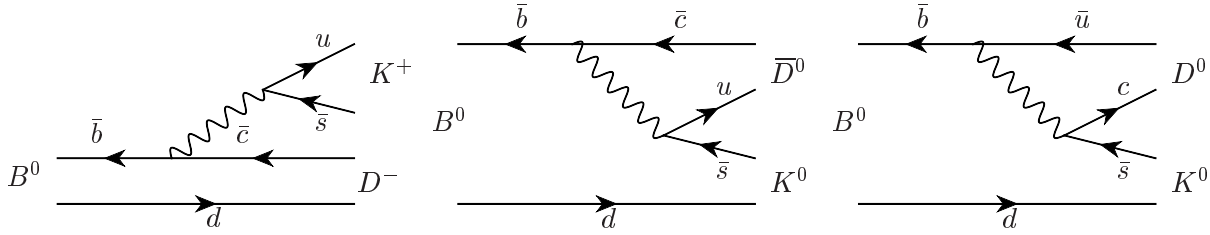

Figure 4.3: The neutral B mesons decays. The diagrams represent $B^0 \to D^- K^+$: $\bar{T}_{\text{neutral}}$ (left); $B^0 \to \overline{D}^0 K^0$: $\bar{C}_{\text{neutral}}$ (middle); $B^0 \to D^0 K^0$: C_{neutral} (bottom).

If one assumes the validity of the isospin SU(2) symmetry, the charged and neutral sector

variables defined in Equations 4.8 and 4.10 degenerate:

$$\begin{aligned} \bar{T}_{\text{charged}} &= \bar{T}_{\text{neutral}}, \\ \bar{C}_{\text{charged}} &= \bar{C}_{\text{neutral}}, \\ C_{\text{charged}} &= C_{\text{neutral}}, \\ A_{\text{charged}} &= A'_{\text{charged}}. \end{aligned} \tag{4.12}$$

The "charged" and "neutral" subscripts are omitted in the following.

Setting $\bar{T}$ real and defining ϕ the relative to $\bar{T}$ strong phase we get (from Equations 4.8 and 4.10):

$$\begin{aligned} A(B^+ \to \overline{D}^0 K^+) &= (|\bar{T}| + |\bar{C}|e^{i\phi_{\bar{C}}}), \\ A(B^0 \to D^- K^+) &= |\bar{T}|, \\ A(B^0 \to \overline{D}^0 K^0) &= |\bar{C}|e^{i\phi_{\bar{C}}}, \\ A(B^+ \to D^0 K^+) &= (|C|e^{i\phi_C} + |A|e^{i\phi_A})e^{i\gamma}, \\ A(B^+ \to D^+ K^0) &= (|A|)e^{i\phi_A}e^{i\gamma}, \\ A(B^0 \to D^0 K^0) &= (|C|)e^{i\phi_C}e^{i\gamma}, \end{aligned} \tag{4.13}$$

where the weak phase γ coming from the V_{ub} matrix element is written explicitly. The same system of amplitudes can be written for $B \to DK^*$ and $B \to D^*K$ systems.

The amplitudes described in Equation 4.13 are proportional either to $|V_{cb}|$ (first three equations) or $|V_{ub}|$ (last three equations) matrix element. We first concentrate on the former part of the system. The values of $|\bar{T}|$, $|\bar{C}|$, and $\phi_{\bar{C}}$ can be extracted from the $|V_{cb}|$ part of the system using:

$$\begin{aligned} \mathcal{B}(B^+ \to \overline{D}^0 K^+) &= (|\bar{T}|^2 + |\bar{C}|^2 + 2|\bar{T}||\bar{C}|\cos(\phi_{\bar{C}})), \\ \mathcal{B}(B^0 \to D^- K^+) &= |\bar{T}|^2, \\ \mathcal{B}(B^0 \to \overline{D}^0 K^0) &= |\bar{C}|^2, \end{aligned} \tag{4.14}$$

These branching fractions are measured and can be taken from the PDG [77]. Their values are listed in Table 4.1.

The results are shown in Figure 4.4 (the same results for the $B \to DK^*$ and $B \to D^*K$ modes are shown in Figures 4.5 and 4.6, respectively) and summarized in Table 4.2.

We now consider the three last relations in Equations 4.13. We first recall the definitions of the r_{B} ratio for charged and neutral B meson decays:

$$r_{\text{B}}^+ \equiv \frac{|A(B^0 \to D^0 K^+)|}{|A(B^0 \to \overline{D}^0 K^+)|}. \tag{4.15}$$

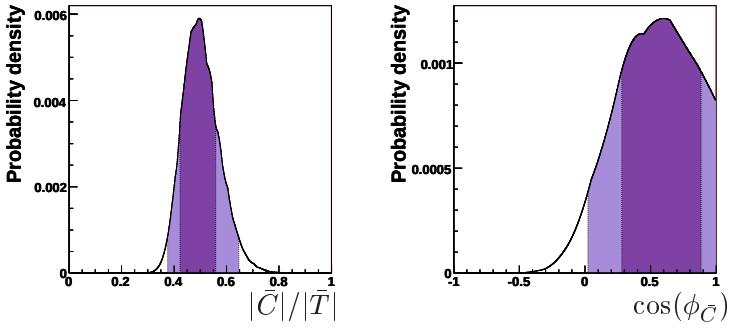

Figure 4.4: PDFs for $|\bar{C}/\bar{T}|$, and $\cos(\phi_{\bar{C}})$ obtained using the relations 4.14 for the $B \to DK$ mode.

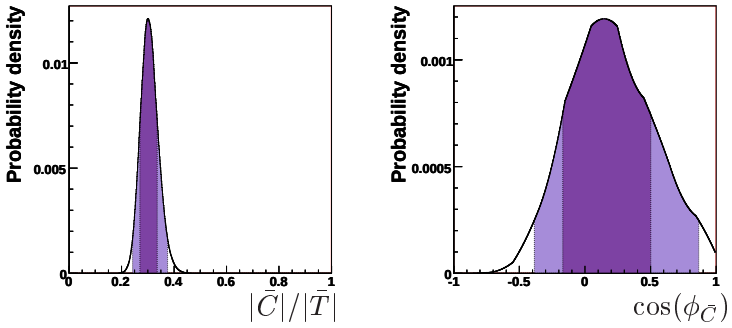

Figure 4.5: PDFs for $|\bar{C}/\bar{T}|$, and $\cos(\phi_{\bar{C}})$ obtained using the relations 4.14 for the $B \to DK^*$ mode.

$$r_{\mathrm{B}}^0 \equiv \frac{|A(B^0 \to D^0 K^0)|}{|A(B^0 \to \overline{D}^0 K^0)|}. \tag{4.16}$$

Using Equations 4.13 one gets:

$$\begin{aligned} \left(r_{\mathrm{B}}^+\right)^2 &= \frac{|C+A|^2}{|\bar{C}+\bar{T}|^2} = \frac{|C|^2+|A|^2+2|C||A|\cos(\phi_C-\phi_A)}{|\bar{T}|^2+|\bar{C}|^2+2|\bar{T}||\bar{C}|\cos(\phi_{\bar{C}})}, \\ \left(r_{\mathrm{B}}^0\right)^2 &= \frac{|C|^2}{|\bar{C}|^2}. \end{aligned} \tag{4.17}$$

The ratios r_{B}^+ and r_{B}^0 are correlated (as was pointed out in [73]). It can be noted that since

$$|C|^2 = \left(r_{\mathrm{B}}^0\right)^2 \mathcal{B}(B^0 \to \overline{D}^0 K^0), |C+A|^2 = \left(r_{\mathrm{B}}^+\right)^2 \mathcal{B}(B^+ \to \overline{D}^0 K^+), \tag{4.18}$$

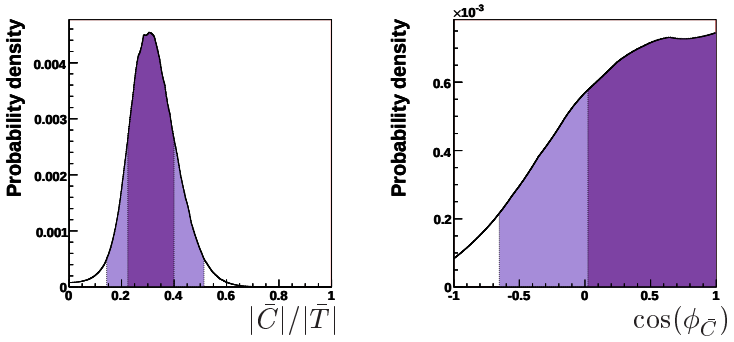

Figure 4.6: PDFs for $|\bar{C}/\bar{T}|$, and $\cos(\phi_{\bar{C}})$ obtained using the relations 4.14 for the $B \to D^*K$ mode.

System	$Br(B^+ \to \overline{D}^{neut.} K^{charg.})$	$Br(B^0 \to \overline{D}^{charg.} K^{charg.})$	$Br(B^0 \to \overline{D}^{neut.} K^{neut.})$
DK	$(4.02 \pm 0.33) \times 10^{-4}$	$(2.0 \pm 0.6) \times 10^{-4}$	$(5.2 \pm 0.7) \times 10^{-5}$
D^*K	$(4.16 \pm 0.33) \times 10^{-4}$	$(2.14 \pm 0.16) \times 10^{-4}$	$(3.2 \pm 1.2) \times 10^{-5}$
DK^*	$(5.3 \pm 0.4) \times 10^{-4}$	$(4.5 \pm 0.7) \times 10^{-4}$	$(4.2 \pm 0.6) \times 10^{-5}$

Table 4.1: Branching fractions of the $b \to c$ mediated processes used in the description of the $B \to DK$ system.

In case of $|C| \gg |A|$ all the terms containing $|A|$ can be neglected, thus giving

$$r_{\rm B}^{+} = \frac{\mathcal{B}(B^0 \to \overline{D}^0 K^0)}{\mathcal{B}(B^+ \to \overline{D}^0 K^+)} \left(r_{\rm B}^{0}\right). \tag{4.19}$$

The annihilation amplitude $|A|$ can be determined by the measurement of $B^+ \to D^+ K^{(*)0}$ decays since (Equations 4.13)

$$\mathcal{B}(B^+ \to D^+ K^0) = |A|^2. \tag{4.20}$$

In this case the relation between $r_{\rm B}^{+}$ and $r_{\rm B}^{0}$ of Equation 4.19 becomes

$$\left(r_{\rm B}^{+}\right)^2 = \frac{\mathcal{B}(B^0 \to \overline{D}^0 K^0)}{\mathcal{B}(B^+ \to \overline{D}^0 K^+)} \left(r_{\rm B}^{0}\right)^2 + 2\frac{\sqrt{\mathcal{B}(B^0 \to \overline{D}^0 K^0)}}{\mathcal{B}(B^+ \to \overline{D}^0 K^+)} r_{\rm B}^{0} |A| \cos(\phi_C - \phi_A) + \frac{1}{\mathcal{B}(B^+ \to \overline{D}^0 K^+)} |A|^2. \tag{4.21}$$

In Chapter 7 of this thesis we present the search for the $B^+ \to D^+ K^{(*)0}$ decays. The phenomenological impact of such a measurement will be shown in Chapter 9.

B decay	$\frac{\lvert\overline{C}\rvert}{\lvert\overline{T}\rvert}$	$cos(\phi_{\bar{C}})$
$B \to DK$	0.49 ± 0.07	0.6 ± 0.3
$B \to D^*K$	0.32 ± 0.08	0.5 ± 0.5
$B \to DK^*$	0.31 ± 0.04	0.2 ± 0.3

Table 4.2: Results obtained on $|\overline{C}|/|\overline{T}|$ and $cos(\phi_{\bar{C}})$ using relations 4.14.

Chapter 5

The *BABAR* experiment

The main goal of the *BABAR* experiment is the systematic study of *CP* violation in the neutral B meson system. The design of the detector is optimized for this purpose. The accelerator machine PEP-II and the *BABAR* detector are described in the following Sections, focussing on the requirements they satisfy and the performance achieved.

5.1 The PEP-II Accelerator

PEP-II [35] is a high-luminosity two-ring asymmetric e^+e^- collider at the Stanford Linear Accelerator Center (now SLAC National Accelerator Laboratory, SLAC) that uses three-kilometer linear accelerator complex as injector (Fig. 5.1).

The energies of the colliding beams are tuned to sum up to a center-of-mass energy of 10.58 GeV, corresponding to the mass of the $\Upsilon(4S)$ vector meson resonance. The effective cross section for the production of the $\Upsilon(4S)$ at $\sqrt{s} = 10.58$ GeV is of about 1.1 nb. This resonance decays nearly with 100% probability into a pair of B mesons, $B^0\overline{B}^0$ or B^+B^-. The design peak luminosity was foreseen to be $\mathcal{L} = 3\times10^{33}$ cm^{-2}s^{-1} but in the final PEP-II machine run (Run 6) a stable $\mathcal{L} = 1.2 \times 10^{34}$ cm^{-2}s^{-1} has been achieved. With this luminosity PEP-II produces of 100 million $B\overline{B}$ pairs in one year of continuous operation providing an ideal laboratory for the study of B mesons.

If the $\Upsilon(4S)$ is produced at rest, then the B mesons would have an average residual momentum such that the average distance covered by a B meson would be of the order of 30 μm and it would be experimentally very difficult to measure the separation between the decay points of the two B mesons. To avoid this problem electron and positron beams are accelerated at the energies of 9.0 GeV (HER, high-energy ring, in which the electrons circulate) and 3.1 GeV

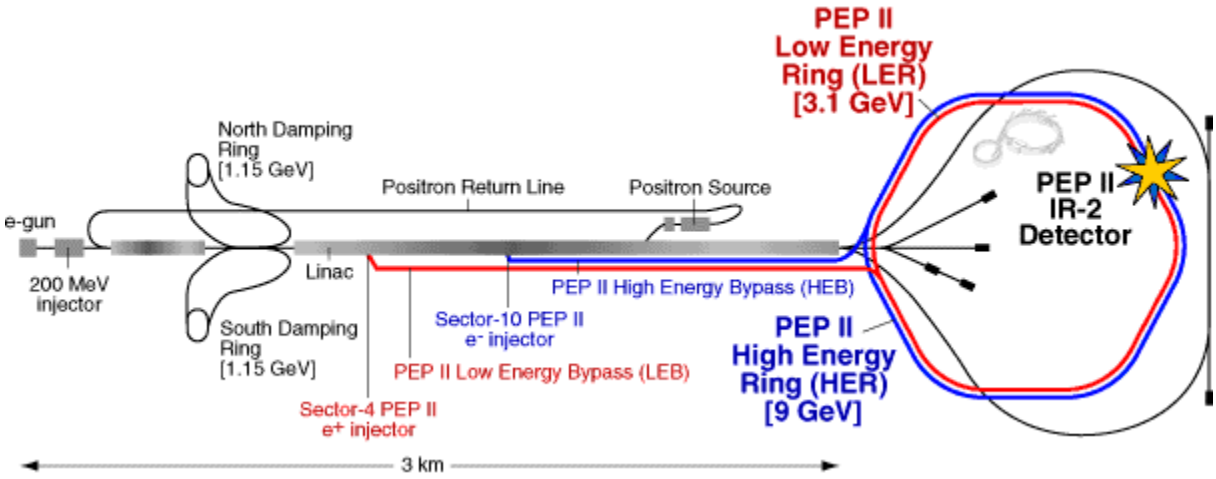

Figure 5.1: Overview of the PEP-II accelerator. The *BABAR* detector is installed in the IR2 point.

(LER, low-energy ring, in which the positrons, produced in the linac by collisions of 30 GeV electrons on a target, circulate), respectively. This energy provides the Lorentz boost of the $\Upsilon(4S)$ to be $\beta\gamma = \frac{E_{e^-} - E_{e^+}}{E_{\rm cm}}$ (with $E_{\rm cm}$ being energy of center of mass), resulting in an average separation between the two B mesons of the order of 250 μm. The measurement of this distance is possible in an experiment, provided a precise tracking device is placed close to the interaction point.

Approximately 8% of data is taken at 40 MeV below the $\Upsilon(4S)$ mass. This set of events is used for the studies of the combinatorial backgrounds originating from u, d, s, c quark- and tau-pair production. This part is referred to as "off-resonance" data in the following.

Construction of the PEP-II, a joint project between SLAC (the electron ring) and the Lawrence Berkeley and Lawrence Livermore National Laboratories (the positron ring) was started in early 1994; first collisions took place in July 1998, and colliding beams were delivered to *BABAR* in May 1999. The designed instantaneous luminosity of 3×10^{33} cm^{-2}s^{-1} for PEP-II has been improved by a factor of four, 12×10^{33} cm^{-2}s^{-1}, a peak-luminosity record achieved in August 2006. A 50% improvement to the integrated luminosity has been achieved between December 2003 and March 2004 with the implementation of a novel mode of operation of PEP-II, called "trickle injection". With this technique, the *BABAR* detector can keep taking data virtually uninterrupted while the linac continuously injects electron and positron bunches (at a rate up to 10 Hz in the HER and 20Hz in the LER) into the two PEP-II storage rings.

The luminosity is measured by PEP-II with radiative Bhabha scattering, while *BABAR* mea-

sures it offline, taking advantage of QED processes, like $e^+e^-, \mu^+\mu^-$ pairs. *BABAR* has recorded an integrated luminosity of about 531 fb^{-1}, including about 54 fb^{-1} of off-resonance data, 433 fb^{-1} recorded at the $\Upsilon(4S)$ and 44 fb^{-1} at other Υ resonances. The *BABAR* recorded luminosity until the end of data taking is shown in Fig. 5.2.

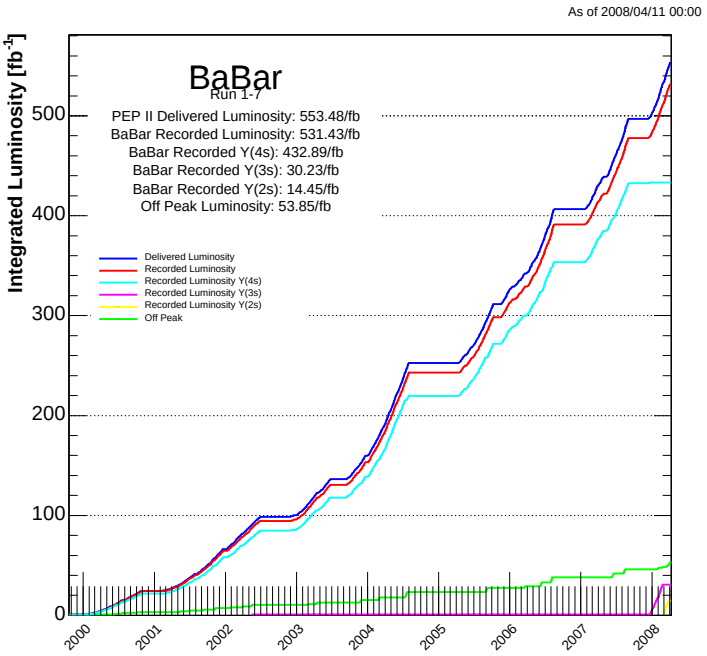

Figure 5.2: The integrated PEP-II luminosity delivered to and recorded by *BABAR*.

5.2 The *BABAR* Detector

The design of the *BABAR* detector is optimized for *CP* violation studies, but it is also well suited to do precision measurements in other B and non B physics. To achieve the goal of performing accurate measurements there are many requirements:

- a large and uniform acceptance in the center-of-mass system. Although the boost originated by the asymmetric beams is not a big one, optimizing the detector acceptance leads to an asymmetric detector;
- an excellent vertex resolution, in particular along the collision axis, since the B mesons travel almost parallel to it;

- an excellent detection efficiency and an excellent precision on the momentum measurement for charged particles with transverse momentum ranging between 60 MeV/c and 4 GeV/c;
- an excellent energy and angular resolution for photons and π^0 with energy down to 20 MeV and up to 5 GeV;
- a good discrimination between e, μ, π, K, p over a wide kinematic range;
- neutral hadrons identification capability.

Furthermore, since the average momentum of B decay products is less than 1 GeV/c, the precision of the measured track parameters is primarily influenced by multiple Coulomb scattering, rather than by the intrinsic devices resolutions. Similarly, for low energy photons, the detection efficiency and energy resolution are impacted by the amount of material traversed before the calorimetry system. For these reasons, the material in the active volume of the detector has been kept at the minimum.

A schematic view of the detector is shown in Figures 5.3 and 5.4. The major subsystems are indicated. A Silicon Vertex Tracker (SVT) provides precise position information for charged tracks, and contributes to charged tracks identification and momentum measurement together with a central Drift Chamber (DCH). A Detector of Internally Reflected Cherenkov light (DIRC) is optimized for charged hadrons identification. An Electromagnetic Calorimeter (EMC) provides electron and neutral particle identification. These detectors are located inside a 1.5 T magnetic field supplied by a superconducting solenoid. The yoke for the flux return of the magnetic field is highly segmented and instrumented with Resistive Plate Chambers (RPCs) and Limited Streamer Tubes (LSTs) for muon identification and long-living neutral hadron detection. The next Sections are dedicated to a detailed description of each subsystem.

The convention adopted in *BABAR* for the coordinate system follows a standard spherical-polar coordinate system centered in the interaction point (IP), the z axis being parallel to the beam direction, and θ and ϕ being the usual polar and azimuthal angles. The cartesian axes form a right-handed system with the x axis pointing outwards from the PEP-II ring and the y axis pointing upwards.

5.2.1 The Silicon Vertex Tracker

The main task of the *BABAR* vertex detector is the reconstruction of the decay vertices of the two B mesons with a precision of better than one half their mean separation, in order to allow the determination of the B mesons decay times for the measurement of time-dependent *CP*-asymmetries. In addition, the charged particles with a transverse momentum (p_T) smaller than

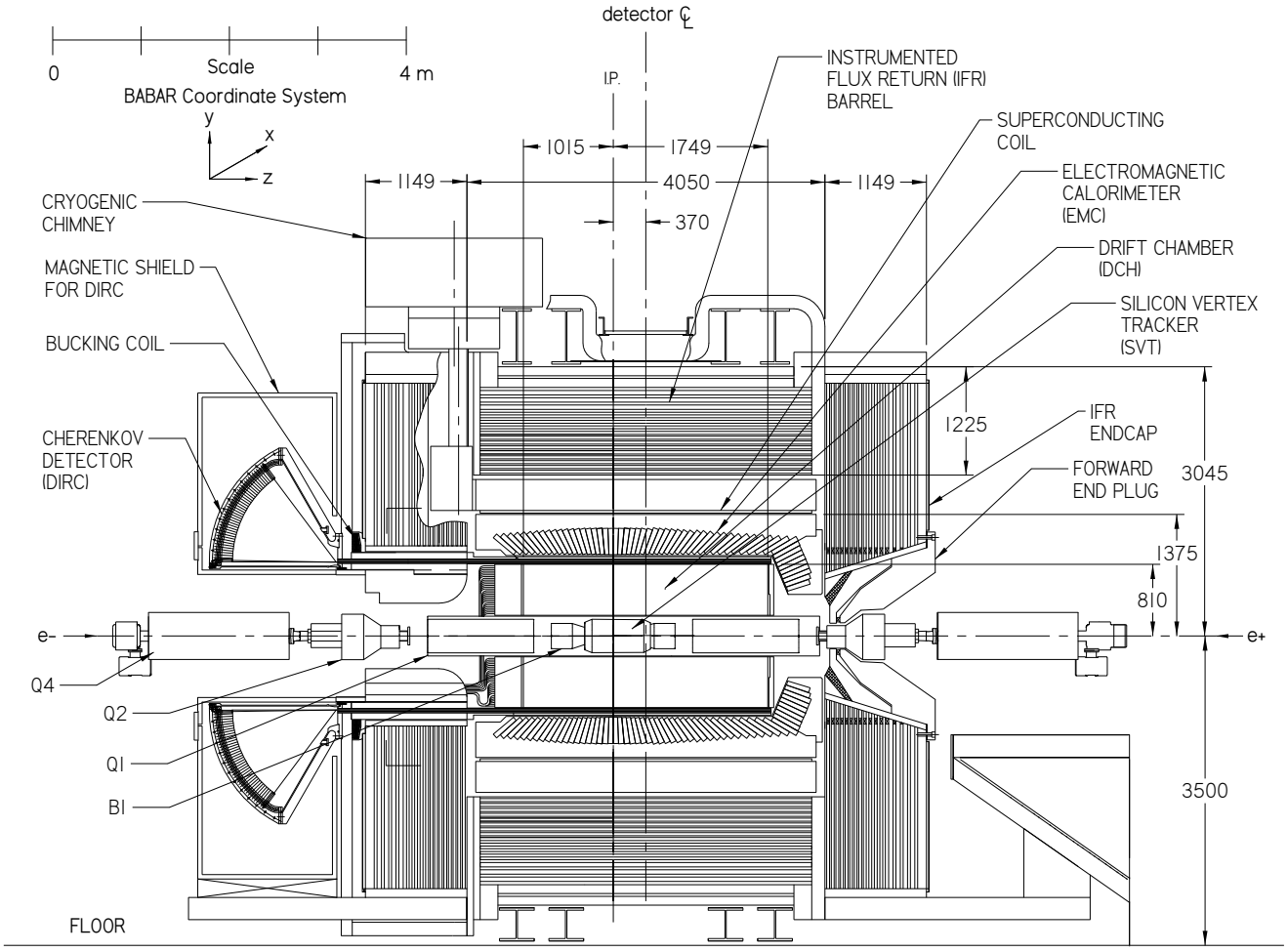

Figure 5.3: *Longitudinal view of the BABAR detector.*

100 MeV/c do not reach the drift chamber and the SVT provides the only tracking information for them. Finally, the SVT also plays a role in particle identification through its own measurements of the rate of energy loss, and by giving the best determination of the polar angle of high momentum tracks, which is a necessary input to fully exploit the DIRC.

The SVT is located just outside the beam pipe, at around 3 cm from its center. To achieve the necessary resolution in Δt, a resolution of 80 μm must be attained in z for single-vertex measurements. In the xy plane, distances of approximately 100 μm must be resolved for the correct reconstruction of secondary vertices such as those from D and τ decays.

The SVT is composed of five layers of double-sided silicon strips (see Figure 5.5), with the strips on the outside being parallel to the beam and on the inside perpendicular, thus providing

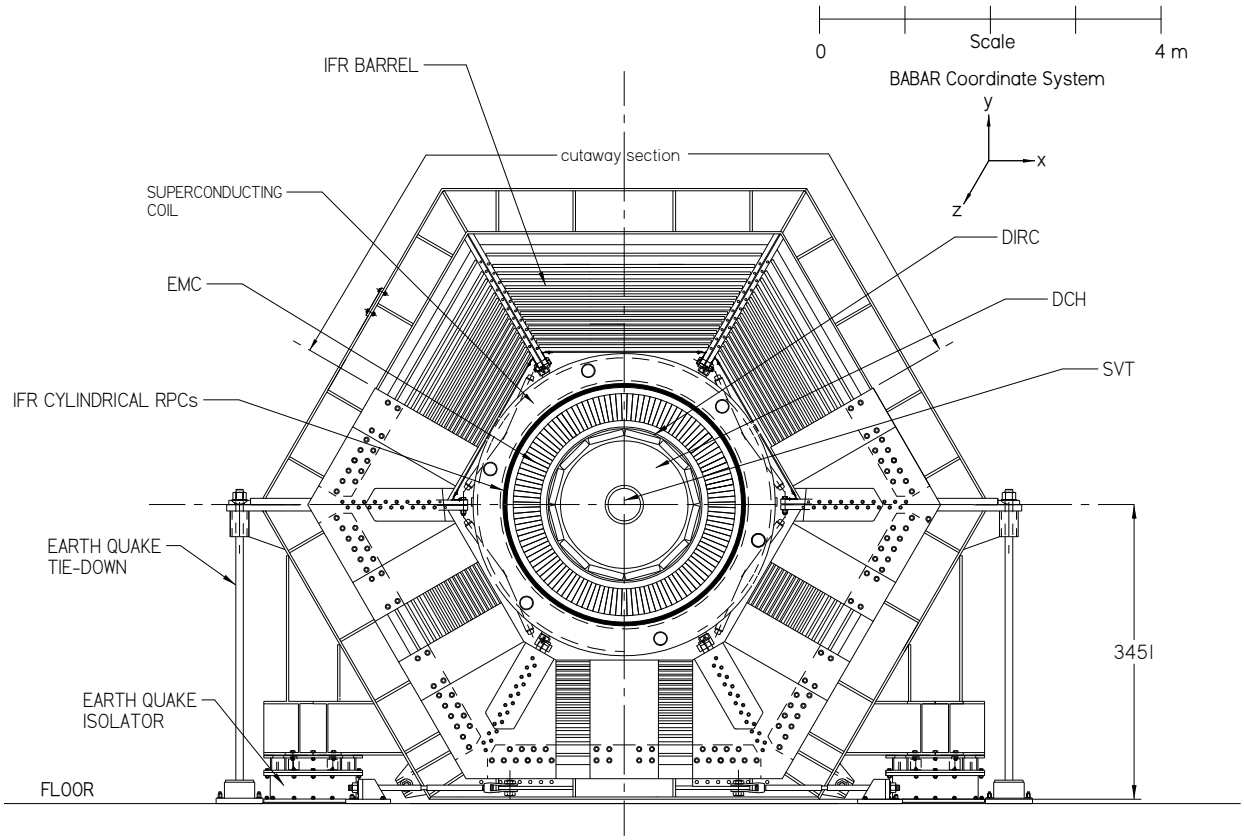

Figure 5.4: *Transverse view of the BABAR detector.*

simultaneous measurements of ϕ and z, respectively, for each hit.

The modules of the inner layers are tilted in ϕ by 5° to provide a full azimuthal coverage. The modules of the outer layers cannot be tilted, due to their arch geometry: to have a suitable overlap and avoid gaps, layers 4 and 5 are divided into two sublayers (labelled 4a, 4b, 5a, 5b in Figure 5.5), placed at slightly different radii.

The total active silicon area is 0.96 m^2 and the geometrical acceptance is 90% of the solid angle in the center-of-mass frame. The material traversed by particles corresponds to approximately 4% of a radiation length. The spatial resolution of the SVT hits can be evaluated by fitting high momentum tracks without the hit in the layer under inspection and comparing the hit with the intersection of the fitted track. The residuals are divided by the uncertainty on the track determination to get the resolution. This is found to be better than 40 μm, implying a vertex resolution better than 70 μm.

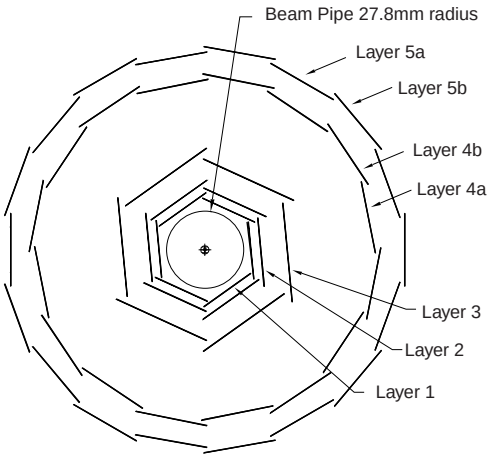

Figure 5.5: Schematic view of the SVT (transverse section).

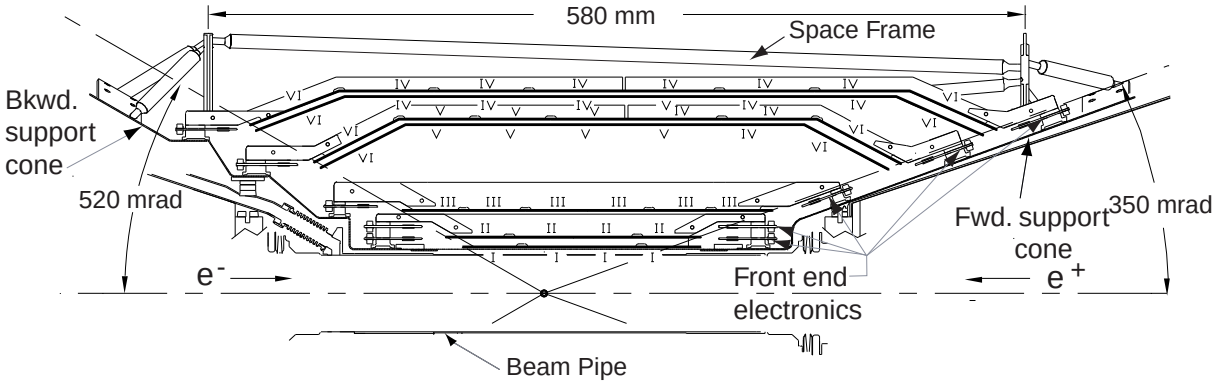

Figure 5.6: Schematic view of the SVT (longitudinal section).

5.2.2 The Drift Chamber

The drift chamber is the main tracking system in the *BABAR* detector and it is therefore expected to measure the momenta and polar angles of the tracks efficiently and precisely over a wide range of momenta, $0.12 < p_T < 5.00$ GeV/c. It provides one of the main inputs to the Level 1 trigger and plays a key role in the extrapolation of tracks into the DIRC, EMC and IFR. The DCH also contributes to particle identification by measurement of $\mathrm{d}E/\mathrm{d}x$, especially for low momentum particles.

The inner wall of the Drift Chamber is placed close to the SVT outer wall to facilitate track-matching between the two devices. The chamber is 2.8 m long and has 40 cylindrical layers of 12 mm by 19 mm hexagonal cells, each containing six field wires at the corners and one field wire in the center as shown in Figure 5.7. Each cell consists of one sense wire surrounded by six field wires. The sense wires are 20 μm-diameter Rh-W gold-plated wires operating nominally in the range 1900-1960 V; the field wires are 120 μm in diameter. All wires grounded to the rear end-plate. Within a given superlayer, the sense and field wires are organized with the same orientation. For measuring also the z coordinate, the superlayers alternate in orientation: first an axial view, then a pair of small angle stereo views (one with positive, one with negative angle), as indicated in Figure 5.8.

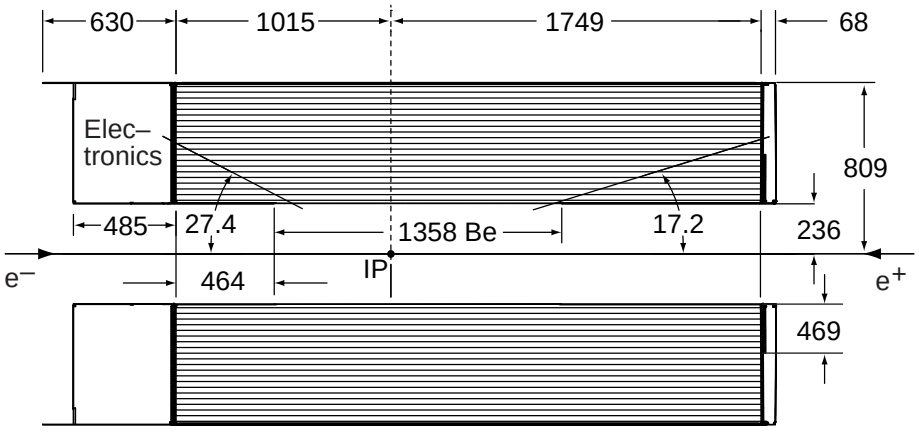

Figure 5.7: Schematic view of the DCH (longitudinal section).

The drift chamber reconstruction efficiency has been measured on data in selected samples of multi-track events by exploiting the fact that tracks can be reconstructed independently in the SVT and the DCH. The absolute drift chamber tracking efficiency is determined as the fraction of all tracks detected in the SVT which are also reconstructed by the DCH when they fall within its acceptance. Its dependency on the transverse momentum and polar angle is shown in Figure 5.9 [36]. At the design voltage of 1960V the reconstruction efficiency of the drift chamber averages $98 \pm 1\%$ for tracks above 200 MeV/c and polar angle $\theta > 500$ mrad (29°).

The p_T resolution is measured as a function of p_T in cosmic ray studies:

$$\frac{\sigma p_T}{p_T} = (0.13 \pm 0.01)\% \cdot \frac{p_T}{1 \text{ GeV}/c} + (0.45 \pm 0.03)\%, \tag{5.1}$$

where p_T is expressed in GeV/c. The first contribution, dominating at high p_T, comes from the curvature error due to finite spatial measurement resolution; the second contribution, dominating at low momenta, is due to multiple Coulomb scattering. The specific ionization loss dE/dx for

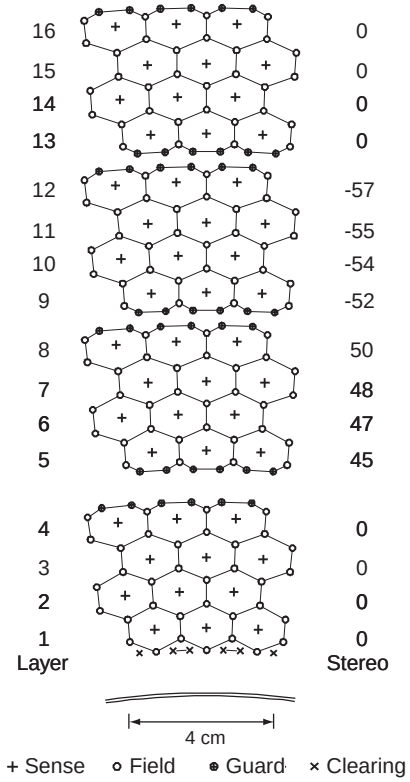

Figure 5.8: Schematic layout of the drift cells for the four innermost superlayers.

charged particles traversing the drift chamber is derived from the total charge deposited in each drift cell. The resolution achieved to date is typically about 7.5%. A 3σ separation between kaons and pions can be achieved up to momenta of about 700 MeV/c.

5.2.3 The Čerenkov Detector

The particle identification (PID) at low momenta exploits primarily the dE/dx measurements in the DCH and SVT (see Chapter 6 for details). More specifically, above 700 MeV/c, the DCH is no longer able to distinguish kaons from pions. The Detector of Internally Reflected Čerenkov radiation (DIRC) is employed primarily for the separation of pions and kaons from about 500 MeV/c to the kinematic limit of 4 GeV/c reached in rare B decays like $B \to \pi^+\pi^-/K^+K^-$. For the muons, the DIRC must complement the IFR, whose effectiveness falls for momenta below 750 MeV/c.

The DIRC consists of 144 fused silica quartz bars with rectangular cross section; each bar is

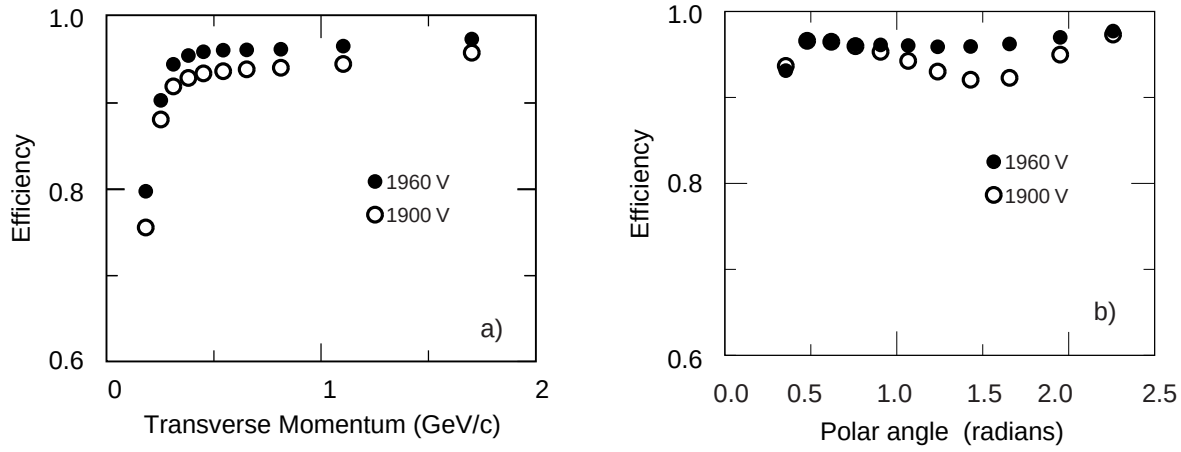

Figure 5.9: Track reconstruction efficiency in the DCH at operating voltages of 1900 V and 1960 V, as a function of transverse momentum (a) and polar angle (b).

approximately 17 mm thick, 35 mm wide and 4.9 m long. When a charged particle crosses the quartz bar, it generates Čerenkov photons at an angle θ_C with respect to its direction such that $\cos\theta_C = 1/(\beta n)$, where β is the velocity of the particle and n is the refraction index of the quartz ($n = 1.473$). The photons are internally reflected in the bar and transported to either one of the ends; those going forward are reflected by a mirror, so that all arrive at the (instrumented) rear end of the bar. Figure 5.10 illustrates the principles of light production, transport, and imaging in the DIRC.

5.2.4 The Electromagnetic Calorimeter

The *BABAR* electromagnetic calorimeter (EMC) is designed to detect and measure electromagnetic showers with high efficiency and very good energy and angular resolution over a wide energy range: from 20 MeV to 9 GeV. This allows the reconstruction of $\pi^0 \to \gamma\gamma$ and $\eta \to \gamma\gamma$ decays where the photons can have very low energy, as well as the reconstruction of Bhabha events and processes like $e^+e^- \to \gamma\gamma$, important for luminosity monitoring and calibration, where electron and photon energies can be very large. The EMC also provides the primary information for electron identification and electron-hadron separation.

Energy deposit clusters in the EMC with lateral shape consistent with the expected pattern from an electromagnetic shower are identified as photons when they are not associated to any charged tracks extrapolated from the SVT and the drift chamber, and as electrons if they are matched to a charged track and if the ratio between the energy E measured in the EMC and the momentum p measured by the tracking system is $E/p \approx 1$.

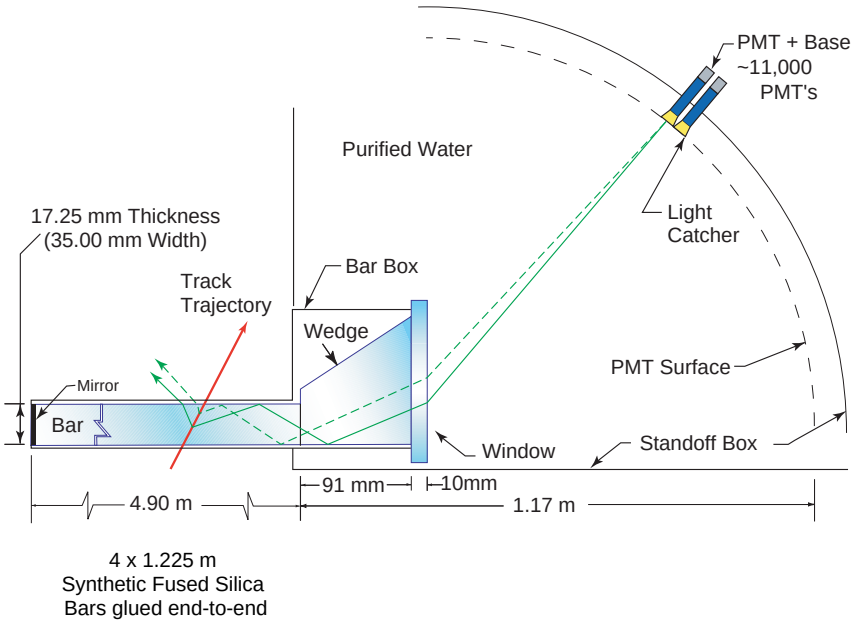

Figure 5.10: Schematic view of the DIRC fused silica radiator bar and imaging region. In this scheme the forward region is to the left and the backward region is to the right.

The EMC contains 6580 CsI crystals doped with Tl (Figure 5.11). CsI(Tl) has a high light yield (50000 photons/ MeV) and a small Molière radius (3.8 cm), which provide the required energy and angular resolution; its radiation length of 1.86 cm guarantees complete shower containment at the *BABAR* energies.

Each crystal is a truncated trapezoidal pyramid and ranges from 16 to 17.5 radiation lengths in thickness. The front faces are typically about 5 cm in each dimension. The crystals are arranged to form a barrel and a forward endcap giving a 90% solid-angle coverage in the center-of-mass frame. The barrel has 48 rows of crystals in θ and 120 in ϕ; the forward endcap contains 8 rings in θ. Overall the EMC extends from an inner radius of 91 cm to an outer radius of 136 cm and is displaced asymmetrically with respect to the interaction point.

The crystals are read out by two independent 1 cm^2 PIN photodiodes, glued to their rear faces, which are connected to low-noise preamplifiers that shape the signal with a short shaping time (400 ns) so to reduce soft beam-related photon backgrounds.

For the purpose of precise calibration and monitoring, use is made of a neutron activated fluorocarbon fluid, which produces a radioactive source (^{16}N) originating a 6.1 MeV photon peak in each crystal. A light pulser system injecting light into the rear of each crystal is also used. In addition, signals from data, including π^0 decays and $e^+e^- \to e^+e^-/\gamma\gamma/\mu^+\mu^-$ events,

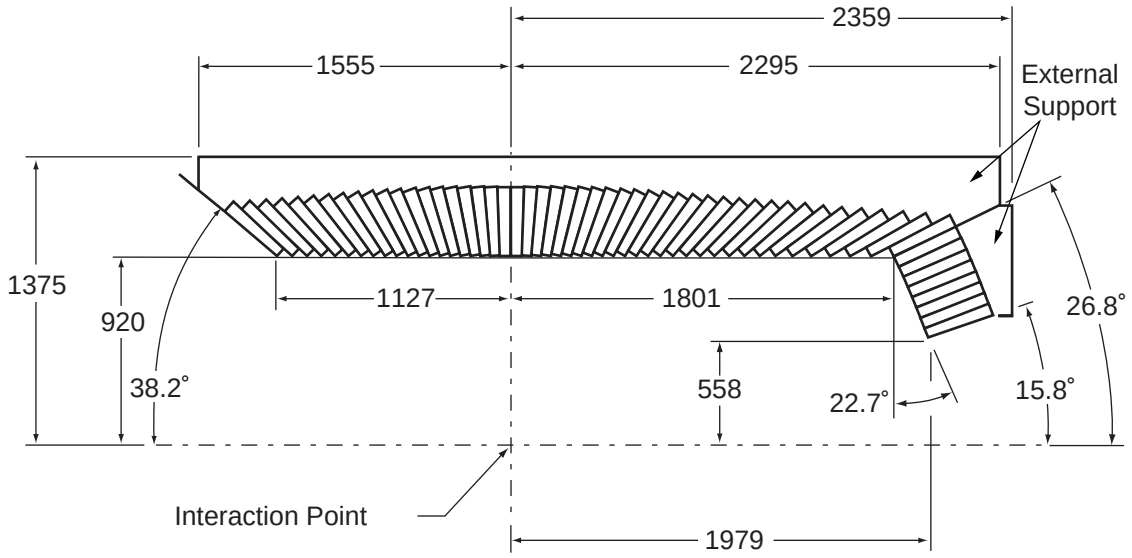

Figure 5.11: Longitudinal section of the top half of the EMC (barrel and forward). Dimensions are in mm.

provide energy calibration and resolution determination.

The efficiency of the EMC exceeds 96% for the detection of photons with energy above 20 MeV. The energy resolution is usually parameterized by

$$\frac{\sigma_E}{E} = \frac{\sigma_1}{E^{1/4}(\,\mathrm{GeV})} \oplus \sigma_2, \tag{5.2}$$

where $\sigma_1 = 2.32 \pm 0.30\%$ and $\sigma_2 = 1.85 \pm 0.12\%$, as determined using the above mentioned sources. The first term in Equation 5.2 arises from fluctuations in photon statistics and is dominant for energies below about 2.5 GeV, while the constant term takes into account several effects, such as fluctuations in shower containment, non-uniformities, calibration uncertainties and electronic noise.

The decays of π^0 and η candidates in which the two photons have approximately equal energy are used to infer angular resolution. It varies between about 12 mrad at low energies and 3 mrad at high energy. The data fit the empirical parameterization:

$$\sigma_{\theta,\phi} = \left(\frac{(3.87 \pm 0.07)}{\sqrt{E(\,\mathrm{GeV})}} + (0.00 \pm 0.04) \right) \text{ mrad} \tag{5.3}$$

Figure 5.12 shows the energy and angular resolution measured as a function of the photon energy.

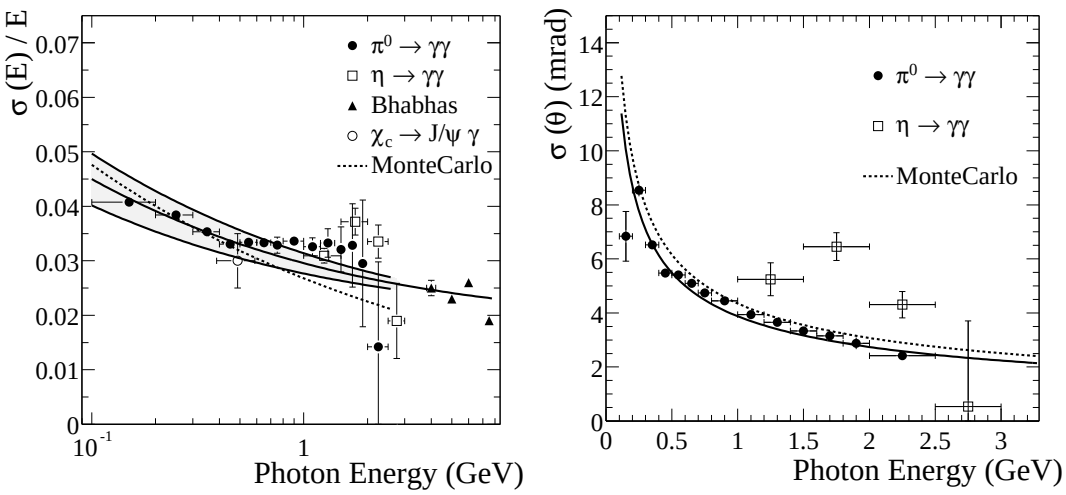

Figure 5.12: Energy (left) and angular (right) resolutions measured using a variety of data. The solid curves represent a fit to the data using Equation 5.2 and 5.3 respectively.

5.2.5 The Instrumented Flux Return

The Instrumented Flux Return (IFR) is designed to identify muons and neutral hadrons (primarily K_L and neutrons). Muons are important for tagging the flavor of neutral B mesons via semi-leptonic decays, for the reconstruction of vector mesons, like the J/ψ, and the study of semi-leptonic and rare decays involving leptons from B and D mesons and τ leptons. K_L detection allows for the study of exclusive B decays, in particular CP eigenstates. The principal requirements for IFR are large solid angle coverage, good efficiency and high background rejection for muons down to momenta below 1 GeV/c. For neutral hadrons, high efficiency and good angular resolution are most important.

The IFR uses the steel flux return of the magnet as muon filter and hadron absorber, limiting pion contamination in the muon identification. Originally single gap resistive plate chambers (RPC) with two-coordinate readout, operated in limited streamer mode constituted the active part of the detector, with 19 layers in the barrel and 18 in each endcap. The RPC were installed in the gaps of the finely segmented steel of the six barrel sectors and the two end-doors of the flux return, as illustrated in Figure 5.13. The steel segmentation has been optimized on the basis of Monte Carlo studies of muon penetration and charged and neutral hadron interactions. In addition, two layers of cylindrical RPCs were installed between the EMC and the magnet cryostat to detect particles exiting the EMC. RPCs contain a 2 mm Bakelite gap with approximately 8 kV across it. Ionizing particles which cross the gap create streamers of ions and electrons in the gas mixture (Argon, freon and isobutane), which in turn creates signals via capacitive

coupling on the strips mounted on each side of the RPC. Soon after the installation (which took

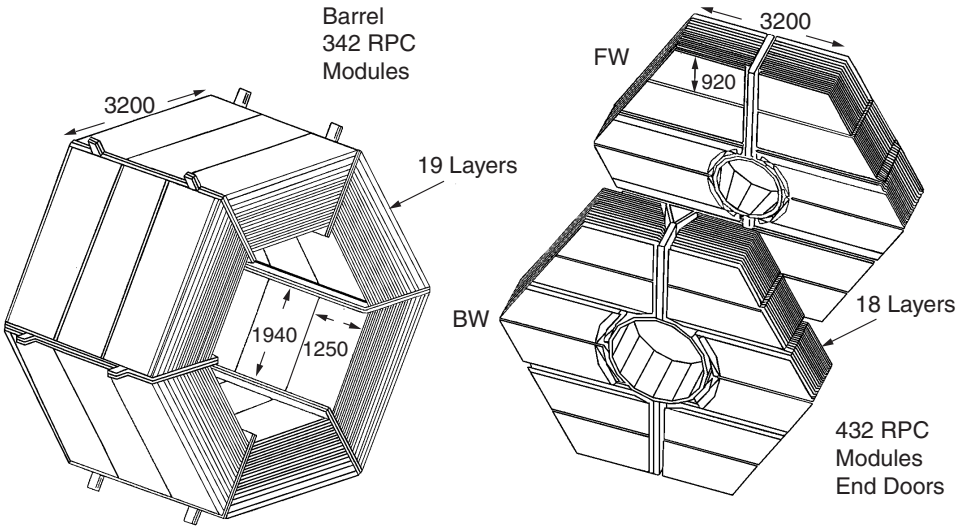

Figure 5.13: Overview of the IFR Barrel sectors and forward and backward end-doors; the shape of the RPC modules and the way they are stratified is shown.

place in Summer 1999), the efficiency of a significant fraction of the chambers (initially greater than 90%) has started to deteriorate at a rate of 0.5-1%/month. In order to solve some of the inefficiency problems, an extensive improvement program has been developed. The forward endcap was retrofitted with new improved RPCs in 2002, their efficiency has not significantly decreased since then. In the barrel, the RPCs have been replaced in 2004 and 2006 by 12 layers of limited streamer tube (LST) detectors and 6 layers of brass have been added to improve hadron absorption. The tubes have performed well since their installation with an efficiency of all layers at the geometrically expected level of 90%. The pion rejection versus muon efficiency is shown in Figure 5.14 for the LSTs and RPCs. The LSTs efficiency is better than the efficiency that the RPCs had, even during the Run 1.

5.2.6 The *BABAR* Trigger

The *BABAR* trigger is designed to select a large variety of physics processes (efficiency greater than 99% for $B\bar{B}$ events) while keeping the output rate below 400 Hz to satisfy computing limitations of the offline processing farms (beam induced background rates with at least one track with $p_T > 120$ MeV/c or at least one EMC cluster with $E > 100$ MeV are typically 20 kHz). The trigger accepts also 95 % of continuum hadronic events and more than 90 % of $\tau^+\tau^-$ events. It is implemented as a two level hierarchy, the hardware Level 1 (L1) followed by the

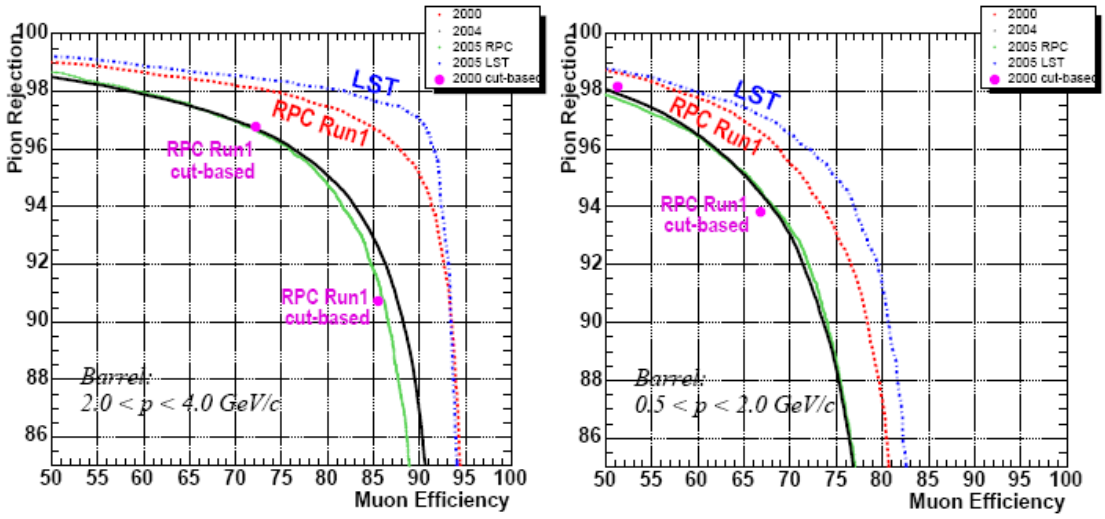

Figure 5.14: Pion rejection versus muon efficiency for two different momentum ranges (left: $2 < p < 4$ GeV/c, right $0.5 < p < 2$ GeV/c). The LST efficiency (blue) is compared with the RPC one for different Runs. We see the deterioration of the RPC performance between 2000 (red) and 2005 (green).

software Level 3 (L3).

The L1 trigger has an output rate of the order of 1 kHz to 3 kHz, depending on the luminosity and background conditions. It is based on charged tracks in the DCH above a preset transverse momentum, showers in the EMC, and track detected in the IFR. L3 operates by refining and augmenting the selection methods used in L1. Based on both the complete event and L1 trigger information, the L3 software algorithm selects events of interest allowing them to be transferred to mass storage data for further analysis. It uses an algorithm based on the drift chamber tracking, which rejects beam-induced charged particle background produced in the material close to the IP, and a second algorithm based on the calorimeter clustering. Then, based on the L3 tracks and clusters, a variety of filters perform event classification and background reduction. Table 5.1 shows the L3 and L1+L3 trigger efficiency for some relevant physics processes, derived from simulated events.

L3 Trigger	$\epsilon_{b\overline{b}}$	$\epsilon_{B\to\pi^0\pi^0}$	$\epsilon_{B\to\tau\nu}$	$\epsilon_{c\overline{c}}$	ϵ_{uds}	$\epsilon_{\tau\tau}$
Combined DCH filters	99.4	89.1	96.6	97.1	95.4	95.5
Combined EMC filters	93.5	95.7	62.3	87.4	85.6	46.3
Combined DCH+EMC filters	> 99.9	99.3	98.1	99.0	97.6	97.3
Combined L1+L3	> 99.9	99.1	97.8	98.9	95.8	92.0

Table 5.1: L3 trigger efficiency (%) for various physics processes, derived from Monte Carlo simulation.

Chapter 6

Event Reconstruction and Background Characterization

The analyses presented in this thesis concern the decays of B mesons, that originate from the $\Upsilon(4S)$ decays. These events are selected from a large data sample produced in e^+e^- collisions at a center-of-mass energy corresponding to the $\Upsilon(4S)$ resonance. Only a fraction of the e^+e^- collisions actually produces a $\Upsilon(4S)$ and thus a $B\overline{B}$ pair. Other processes are $e^+e^- \to u\overline{u}$, $d\overline{d}$, $s\overline{s}$, $c\overline{c}$ (continuum events in the following), $e^+e^- \to l\overline{l}$, where $l = e$, μ or τ. While the latter type of decays can be easily distinguished from the $e^+e^- \to q\overline{q}$ events by looking at the number of tracks and the visible energy in each event, while the former ($e^+e^- \to u\overline{u}$, $d\overline{d}$, $s\overline{s}$, $c\overline{c}$) are more similar to $e^+e^- \to b\overline{b}$ events and can be a potential source of background due to their large cross sections (given in Table 6.1). The characterization of the continuum events is performed with the help of a special sample of e^+e^- collisions collected with the *BABAR* detector at a center-of-mass energy 40 MeV below the $\Upsilon(4S)$ resonance where the production of a $B\overline{B}$ meson pair is kinematically forbidden. This sample is called off-resonance data in the following.

$e^+e^- \to$	$b\overline{b}$	$c\overline{c}$	$s\overline{s}$	$d\overline{d}$	$u\overline{u}$	$\tau^+\tau^-$	$\mu^+\mu^-$	e^+e^-
Cross Section, [nb]	1.05	1.3	0.35	0.35	1.39	0.94	1.16	40

Table 6.1: Cross section for different processes for e^+e^- collisions at an energy $\sqrt{s} = M(\Upsilon(4S))$.

In this Chapter, charged and neutral particles reconstruction with *BABAR* detector is described. Typically, the process of reconstruction starts with charged tracks and calorimeter clusters using hits in the Drift Chamber and the Silicon Vertex Tracker and eventually in the Instrumented Flux Return, and energy deposits in the electromagnetic calorimeter. Čerenkov angle of photons and dE/dx information are also processed at this stage to provide particle iden-

tification. Algorithms are constructed to identify pions, kaons, protons, electrons, and muons (described in Section 6.1 and 6.3). Then the "composite" particles (all the particles that decay inside detector) are combined from the appropriate amount of charged tracks and (or) photon candidates (described in Section 6.4). Finally, the fit of the B meson candidate decay of interest is performed (as described in Section 6.4.6). If an event has more then one candidate then a special selection criteria is applied in order to find the best candidate for this decay chain.

6.1 Charged Track Reconstruction and Identification

The *BABAR* detector inner part (as described in Chapter 5) operates in an axial magnetic magnetic field. The charged particles are deflected by this field and this effect is used in the identification. Charged particle tracks are reconstructed from the spacial hits in the SVT and the DCH and fitted using a Kalman filter technique [78]. This algorithm performs pattern recognition and determines five parameters characterizing each track:

- d_0, the distance in the xy plane to the z axis;
- z_0, the coordinate along the z axis;
- ϕ_0, the azimuthal angle of the POCA (position of the closest approach);
- λ, the dip angle of the track with respect to the transverse (xy) plane. It is related to the cylindrical polar angle θ via $\theta = \frac{\pi}{2} - \lambda$;
- ω, the (signed) curvature of the track, whose sign and magnitude are related, respectively, to the charge of the associated particle and its transverse momentum.

All the quantities are defined at the POCA to the z axis. The fit procedure starts form the DCH hits constrained to belong to one track, and further checks the track consistency with SVT hits. The low momentum tracks are searched in SVT.

Two lists of charged tracks are used:

- `GoodTracksVeryLoose` is built on the following requirements:
  - transverse momentum of the track, $p_T > 0.1$ GeV/c;
  - momentum of the track, $p < 10$ GeV/c;
  - position of the closest approach, $POCA < 1.5$ cm
  - the coordinate along the z axis, $-10 < z_0 < 10$ cm

- For `GoodTracksLoose` an extra condition is added requiring for more than 12 hits in the DCH.

6.2 Charged Tracks Identification

There are five types of charged, long-lived particles that can be "tracked" in *BABAR* detector: electrons, muons, pions, kaons, and protons. Most of the tracks produced in an event are pions.

"Selectors" are used to perfrom the particle identification. The selectors combine the information coming from the *BABAR* detector and provide various points ranked in purity and efficiency.

The selectors discriminating between charged protons, kaons, and pions make use of the loss of energy $\mathrm{d}E/\mathrm{d}x$, as measured by the SVT and the DCH and the Čerenkov angle θ_C as measured by the DIRC. The discriminating power of these variables can be estimated from Figures 6.1 and 6.2. The three sub-detectors are to a large extent complementary and give good separation of proton from kaons and pions. In order to identify a track a probability density function (pdf) for each particle hypothesis is built. These pdfs are used to construct a likelihood for the particle identification (PID) hypothesis ($\mathcal{L}_K$, $\mathcal{L}_\pi$, $\mathcal{L}_\mu$ etc.). The selectors are defined by the different cuts applied on the likelihood ratios ($\mathcal{L}_\pi/\mathcal{L}_K$ etc.) The likelihood is built using the following information:

- for track momenta $p < 500$ MeV/c, $\mathrm{d}E/\mathrm{d}x$ measurements from the SVT and DCH are combined;
- for track momenta $500 < p < 600$ MeV/c, $\mathrm{d}E/\mathrm{d}x$ measurements from the DCH only is used;
- for track momenta $p > 600$ MeV/c, θ_C measurements form the DIRC is added in addition to the previous information.

In both analyses presented in this thesis, the `KLHLoose` selector criteria is used, which has a average efficiency on kaons of about 90% and an efficiency of reconstructing a pion as a kaon of about 2%. In the ADS analysis, `KLHTight` selector is also used, which has an average efficiency on kaons of about 85% and an efficiency of reconstructing a pion as a kaon of about 1%. The efficiencies of the PID selection for kaons as a function of the momentum, as well as pions and protons misidentified as kaons, are shown in Figure 6.3 for `KLHLoose` list and in Figure 6.4 for `KLHTight`. The efficiency of the selectors obtained on data and on simulated events are in good agreement.

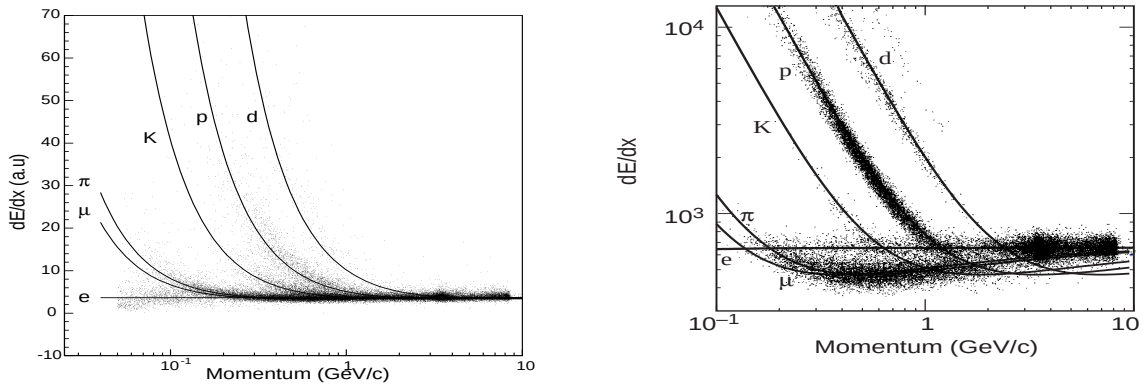

Figure 6.1: Energy loss $\mathrm{d}E/\mathrm{d}x$ (in arbitrary units), as a function of the track momentum, in the SVT (left) and in the DCH (right) for different types of particles. The curves are the theoretical behaviors following the Bethe-Bloch formula.

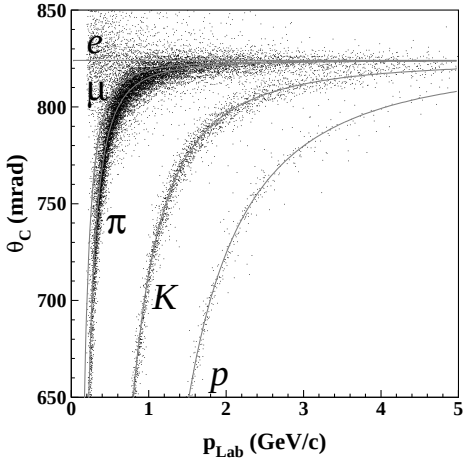

Figure 6.2: The fitted Cherenkov angle θ_C of tracks from an inclusive sample of multi-hadron events plotted against the momentum of the tracks at the entrance to the DIRC bar box. The grey lines are the predicted values of the θ_C for the different particle species.

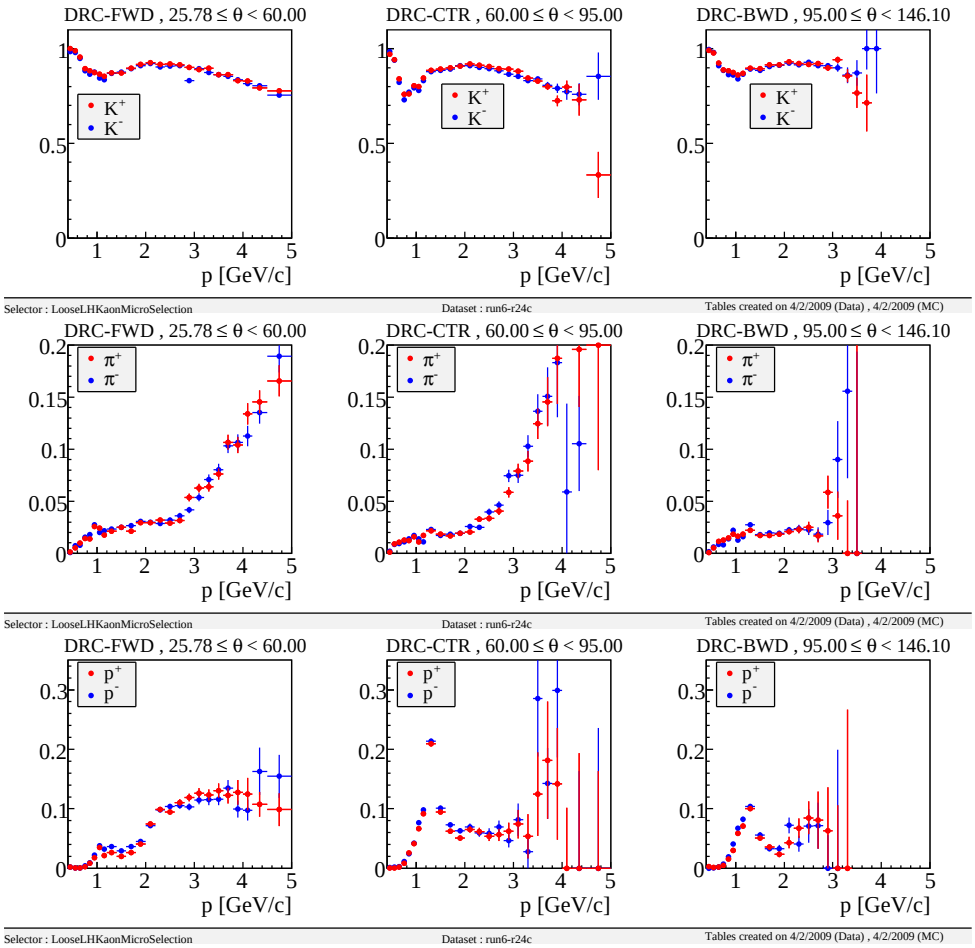

Figure 6.3: Kaon identification efficiency for the KLHLoose kaon selector list as a function of momentum, for three different angular regions (top), same for pions (middle) and protons (bottom) contributing to this list.

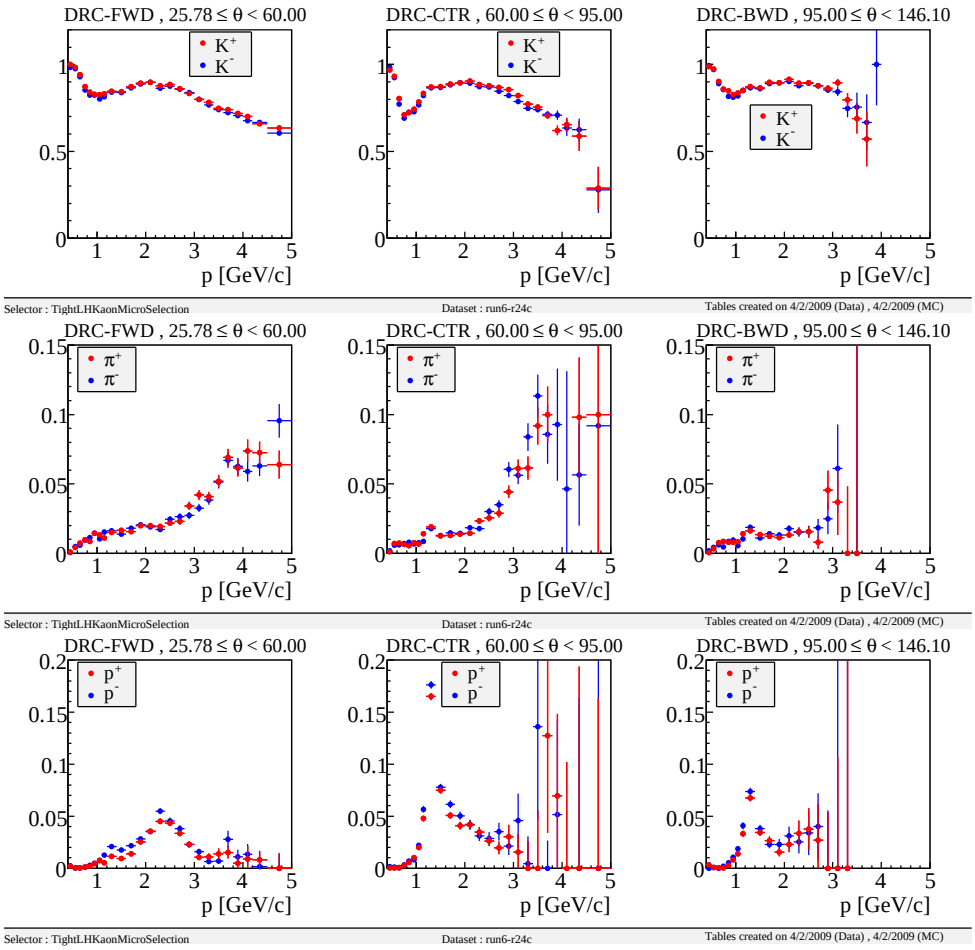

Figure 6.4: Kaon identification efficiency for the KLHTight kaon selector list as a function of momentum, for three different angular regions (top), same for pions (middle) and protons (bottom) contributing to this list.

Electron identification is based on the EMC information on the lateral shower profile and energy deposit. Since the electrons that reach the calorimeter produce electromagnetic showers depositing their energy in the crystals, which can be easily distinguished from hadrons (using condition on the lateral energy distribution). To ensure that the electromagnetic shower was generated by an electron and not by a photon, the charged track pointing to the direction of the energy deposit in the EMC is searched. If this track is found, a candidate is considered not to be a photon.

The detector dedicated to the muon identification in *BABAR* is the IFR. In order to associate the DCH information to each energy deposit in the IFR, all the charged tracks reconstructed in the DCH are extrapolated to the IFR, taking into account the bending due to the magnetic field. Only tracks that intersect the layers close to a hit are associated with a charged cluster.

6.3 Photon Selection

Photon candidates are reconstructed in the EMC. Each photon produces an electromagnetic shower in the calorimeter, distinguishable from an hadronic shower because of the different shape. One can define a variable connected to the lateral shower shape:

$$LAT = \frac{\sum_{i=3}^{N} E_i r_i^2}{\sum_{i=3}^{N} E_i r_i^2 + E_1 r_0^2 + E_2 r_0^2}, \tag{6.1}$$

where N is the number of crystals touched by the shower, E_i the energy of the i-th crystal (with $E_i > E_{i+1}$), r_i the distance between the i-th crystal and the shower axis, and r_0 is the average distance between the two most energetic crystals (typically, $r_0 = 5$ cm). In order to select photons the requirement $LAT < 0.8$ is applied.

To ensure that the electromagnetic shower was generated by a photon and not by an electron, photon candidates for which the DCH has detected a charged track pointing to the direction of the energy deposit in the EMC are rejected.

6.4 Composite Particle Reconstruction

In this Section, the reconstruction of short-lived particles (that decay before reaching the outer calorimeters), such as π^0, K_S^0, D^+ etc. is presented. This reconstruction is performed by means of their charged and neutral decay products, selected with the criteria defined in the previous

Sections. Background from random combinations of charged tracks or photons in the event is typically suppressed by selecting only the combinations which emerge from a common space-point (decay vertex) and whose invariant mass is sufficiently close to the known mean mass of the particle. Additional information such as, for instance, angular correlations due to the spin of the particles, can be used to further suppress background events.

Candidates for composite (not observable) particles are first formed from all the possible combinations of tracks and neutral objects matching the decay products of the particle. These candidates are then required to meet some kinematic criteria, and are subsequently vertexed.

Once a kinematic candidate has been found, its decay vertex is calculated by means of a geometric fit, in which the tracks of the decay products are required to emerge from a common vertex. The decay point of a particle is determined by finding the best intersection of the tracks using a χ^2 minimization. Since the track trajectories are bent by the magnetic field, the problem is not linear and the iterative search for local solutions is performed until the χ^2 difference between one iteration and the next one is below 0.01. The maximum number of possible iterations is six. The χ^2 is minimized by varying the position and four-momentum components of the decay products. In addition, the energy and momentum conservation is applied by use of the Lagrange multipliers and the mass of the decaying particle can be fixed to its nominal mass.

In this Section we describe the composite particles used in analyses performed. More details on the selection criteria can be found in the Chapters 7 and 8.

6.4.1 π^0 Reconstruction

Any pair of two photons, each one with energy higher that 30 MeV and with a total energy sum larger than 200 MeV makes a candidate π^0, provided that its invariant mass is in the interval 110 MeV/c^2 $< \pi^0 <$ 160 MeV/c^2 (the π^0 nominal mass being 135 MeV/c^2 [77]). The π^0 four-momentum is determined from a fit to the two photons, in which the π^0 reconstructed mass is constrained to be equal to the nominal π^0 mass [77]. The "unconstrained" mass is obtained from the same tracks without fixing the mass of the candidate and it is used in selection and referred as M_{π^0} in the following Sections. The distribution of M_{π^0} is shown in Figure 6.5.

6.4.2 K^0_S Reconstruction

The K^0_S candidates are taken from the `KsDefault` list, which implies the K^0_S is reconstructed from pairs of oppositely charged pions originating from a common vertex. The K^0_S four-momentum is

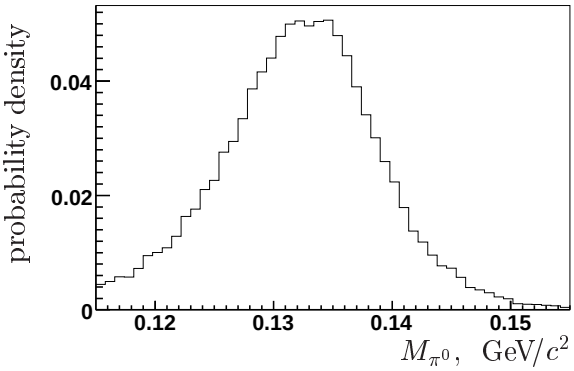

Figure 6.5: Distribution of the unconstrained π^0 invariant mass for π^0 decaying to $\gamma\gamma$ correctly identified MC signal events.

obtained from its decay products through a fit in which the K_S^0 reconstructed mass is constrained to be equal to the nominal K_S^0 mass. The unconstrained K_S^0 mass is referred to as $M_{K_S^0}$ in the following Sections. The distributions of the unconstrained mass $M_{K_S^0}$ is shown in Figure 6.6.

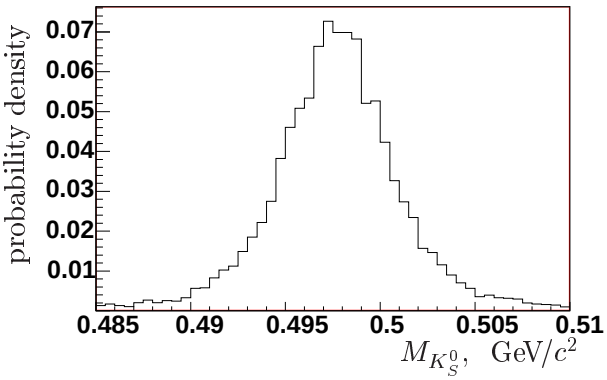

Figure 6.6: Distribution of the unconstrained K_S^0 invariant mass for K_S^0 decaying to $\pi^+\pi^-$ correctly identified MC signal events.

6.4.3 K^{*0} Reconstruction

The reconstruction of $K^{*0}(892)$ is used in the $B^+ \to D^+ K^{*0}$ analysis presented in Chapter 7. The $K^{*0}(892)$ candidates are reconstructed in the final state $K^+\pi^-$. In the following we will refer $K^{*0}(892)$ as K^{*0}.

The K^{*0} candidate is reconstructed by combining two oppositely-charged tracks belonging to the list `GoodTracksVeryLoose`. The K^{*0} candidates are selected using the K^{*0} invariant mass [77] and the cosine of the helicity angle of the K^{*0} products, $\cos\theta^{\rm H}$, which is defined as the angle between the direction of flight of the charged K and the direction of flight of the B in the K^{*0} rest frame. The probability distribution of $\cos\theta_{\rm H}$ is proportional to $\cos^2\theta^{\rm H}$ for longitudinally polarized K^{*0} mesons from $B^+ \to D^+K^{*0}$ decays, due to angular momentum conservation, and is approximately flat for fake (random combinations of tracks) or unpolarized background K^{*0} candidates. The invariant K^{*0} mass and $\cos\theta^{\rm H}$ obtained from the simulated events are shown in Figure 6.7.

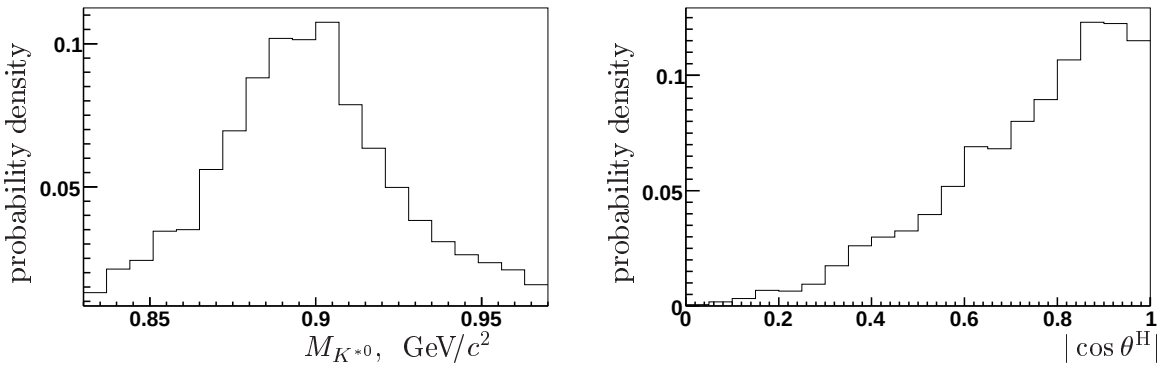

Figure 6.7: Distribution of the K^{*0} invariant mass (left) and $|\cos\theta^{\rm H}|$ (right) for $B^+ \to D^+K^{*0}$ correctly identified MC generated signal events. The D^- meson is reconstructed into $K^0_S\pi^-$ final state.

6.4.4 D^+ Reconstruction

In the Chapter dedicated to the $B^+ \to D^+K^{(*)0}$ analysis, the D^+ are reconstructed in the following subchannels: $K^-\pi^+\pi^+$, $K^-\pi^+\pi^+\pi^0$, $K^0_S\pi^+$, and $K^0_S\pi^+\pi^0$. The charged kaon is requested not to pass the pion identification (cutting exhibitively on the likelihood), while no particular constraints are put on π^+. The π^0 candidates are selected according to the discussion above. The unconstrained D^+ mass is referred as M_{D^+} in the following Sections. The distributions of this variable depending on the channel are shown in Figure 6.8. The mass resolutions of the D^+ meson mass for different decay channels are shown in Table 6.2. The charged D four-momentum is determined from a fit to its decay products in which the D reconstructed mass is constrained to be equal to the nominal D^+ mass.

$D^+ \to$	$K\pi\pi$	$K\pi\pi\pi^0$	$K^0_S\pi$	$K^0_S\pi\pi^0$
σ, [MeV/c^2]	6.8 ± 0.1	12.5 ± 0.3	8.3 ± 0.1	15.1 ± 0.2

Table 6.2: The mass resolution of the mass for D^+ reconstructed candidates for the different decay modes studied in this thesis.

6.4.5 D^0 Reconstruction

In Chapter 8 we describe the reconstruction of $B^+ \to D^0 K^+$ with the subsequent D^0 decaying to $K^-\pi^+\pi^0$ final state. For this channel the K^- and π^+ candidates are taken from `GoodTracksVeryLoose` list, while π^0 are selected according to the discussion given above. The distribution of the unconstrained D^0 mass is shown in Figure 6.9. The mass resolution for the D^0 meson in this channel is of 14.6 ± 0.1 MeV/c^2.

6.4.6 The Reconstruction of the B charged mesons

The charged B meson is reconstructed from a (mass constrained) D and a K^0_S, a K^{*0} or a K^+, depending on the channel. A kinematic fit, in which the D and the K are constrained to originate from the interaction point (`beamspot`), is applied to the B. In the `beamspot` constrained fit, the error on the determination of the interaction point, which is about 10 μm in y, 200 μm in x and 8 mm in z, is taken into account.

6.5 Kinematic Variables: $m_{\rm ES}$ and ΔE

One of the advantages of studying B physics in an e^+e^- collider at the $\Upsilon(4S)$ resonance is the kinematic constraint provided by the initial state. The energy of each B meson in the $\Upsilon(4S)$ frame must be equal to $\sqrt{s}/2$, where $\sqrt{s}$ is the total e^+e^- CM energy. This constraint is exploited by introducing two almost uncorrelated kinematical variables:

- the energy-substituted mass

$$m_{\rm ES} \equiv \sqrt{(E^{*2}_0/2 + \vec{p_0} \cdot \vec{p_B})^2/E^2_0 - p^2_B} \tag{6.2}$$

- the energy difference

$$\Delta E \equiv E^*_B - E^*_0/2, \tag{6.3}$$

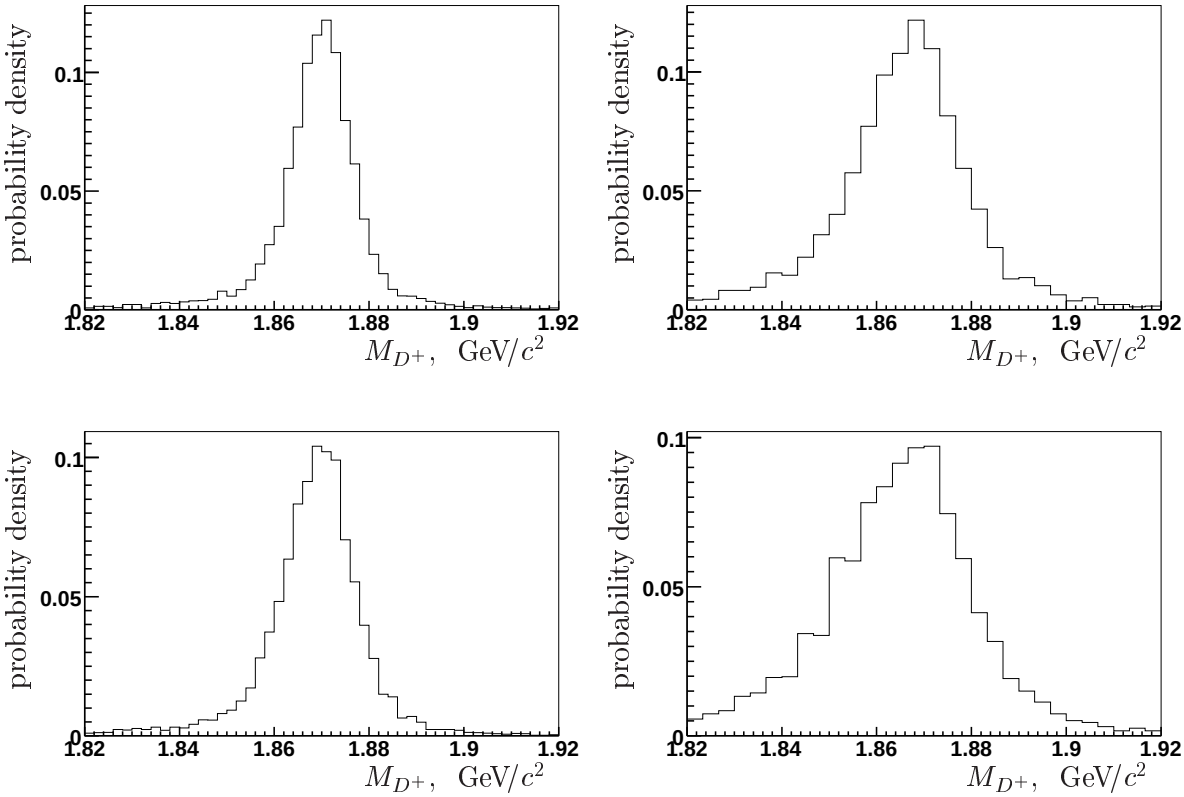

Figure 6.8: Distribution of the unconstrained D^+ invariant mass for D^+ decaying to $K^-\pi^+\pi^+$ (top left), $K^-\pi^+\pi^+\pi^0$ (top right), $K^0_S\pi^+$ (bottom left), and $K^0_S\pi^+\pi^0$ (bottom right) correctly identified MC generated signal events.

where E and p are the energy and the momentum respectively, the subscripts B and 0 refer to the candidate B and to the e^+e^- system respectively and the asterisk denotes the e^+e^- CM frame.

For correctly reconstructed B decays $m_{\rm ES}$ peaks at the B mass, as shown in Figure 6.10, while ΔE peaks at zero, as shown in Figure 6.11.

The $m_{\rm ES}$ resolution $\sigma_{m_{\rm ES}}$ is determined by the B meson true energy spread, which depends on event-by-event beam energy variations, $\sigma_{E^*_{\rm beam}} \approx 2.6$ MeV [36], and by the B momentum measurement error in the $\Upsilon(4S)$ frame, $\sigma_{p^*_B} \approx 16$ MeV/c:

$$\sigma^2_{m_{\rm ES}} \approx \sigma^2_{E^*_{\rm beam}} + \left(\frac{p^*_B}{M_B}\right)\sigma^2_{p^*_B}. \tag{6.4}$$

Since in the $\Upsilon(4S)$ frame $p^*_B/M_B \simeq 0.06$, $\sigma^2_{m_{\rm ES}}$ is dominated by the beam energy fluctuations: the $m_{\rm ES}$ distribution of correctly reconstructed B decays is therefore independent on the de-

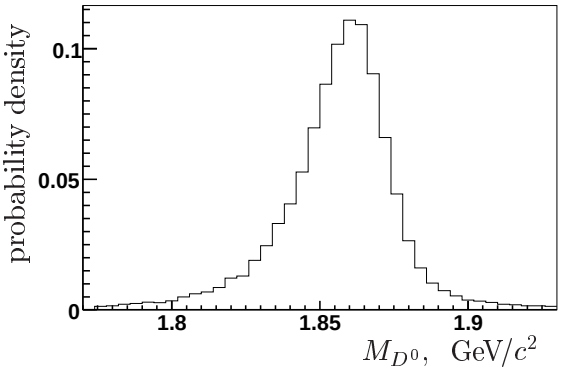

Figure 6.9: Distribution of the unconstrained D^0 invariant mass for D^0 decaying to $K^-\pi^+\pi^0$ correctly identified MC generated signal events.

cay mode, as observed in simulated signal events. The typical resolution for $m_{\rm ES}$ of correctly reconstructed B decay is 2.6 MeV.

The r.m.s. spread of the ΔE distribution depends on the B energy measurement resolution $\sigma_{E_b^*}$ and on the spread in E^*_{beam}

$$\sigma^2_{\Delta E} = \sigma^2_{E^*_{beam}} + \sigma^2_{E^*_B}. \tag{6.5}$$

Since $\sigma^2_{E^*_B} \approx 17$ MeV for B mesons reconstructed in the decay modes studied in the analysis, while $\sigma^2_{E^*_{beam}} \approx 2.6$ MeV, $\sigma^2_{\Delta E}$ is dominated by the energy measurement error. The experimental resolutions of ΔE for the channels described in this thesis are shown in Table 6.3. $m_{\rm ES}$ and ΔE are not correlated, as shown in Figure 6.12.

B decay	$B^+ \to D^+ K^0_S$				$B^+ \to D^+ K^{*0}$		$B^+ \to D^0 K^+$
D decay	$K\pi\pi$	$K\pi\pi\pi^0$	$K^0_S\pi$	$K^0_S\pi\pi^0$	$K\pi\pi$	$K^0_S\pi$	$K\pi\pi^0$
σ, [MeV]	16.8 ± 0.1	19.7 ± 0.1	17.4 ± 0.1	19.2 ± 0.1	16.8 ± 0.1	20.7 ± 0.1	20.7 ± 0.1

Table 6.3: The resolution for the ΔE variable.

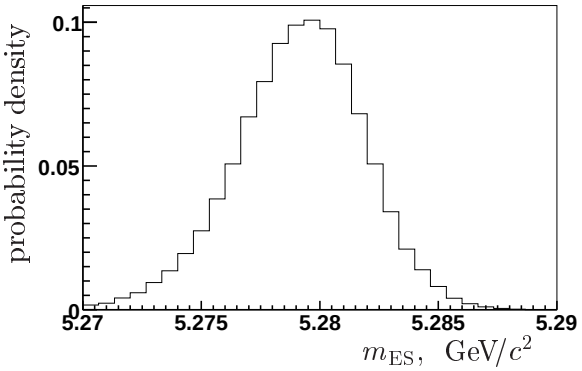

Figure 6.10: Distribution of $m_{\rm ES}$ for $B^+ \to D^0 K^+$ correctly identified MC generated signal events. The D^0 meson is reconstructed into $K^+\pi^-\pi^0$ final state.

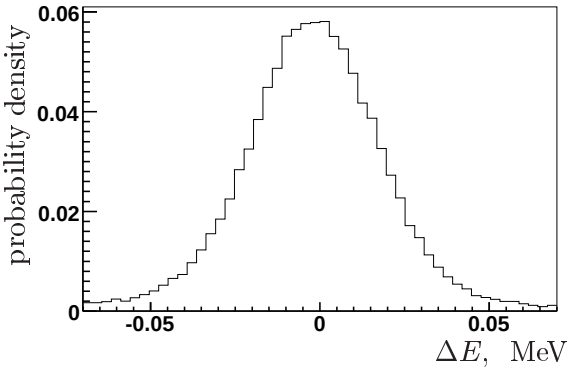

Figure 6.11: Distribution of ΔE for $B^+ \to D^0 K^+$ correctly identified MC generated signal events. The D^0 meson is reconstructed into $K^+\pi^-\pi^0$ final state.

Background events have a different $m_{\rm ES}$ distribution (except for some decay channels, that are discussed in details in the following Chapters).

The $m_{\rm ES}$ distributions for $q\overline{q}$ backgrounds usually have form of threshold function, while some decays contributing to the $B\overline{B}$ background can have the $m_{\rm ES}$ distribution that can be fitted by the Crystal Ball function. These distributions are shown in Figure 6.13.

The threshold (ARGUS) function [95] is expressed as follows:

$$A(x) = x\sqrt{1-\left(\frac{x}{x_0}\right)^2}\cdot e^{c\left(1-\left(\frac{x}{x_0}\right)^2\right)}, \tag{6.6}$$

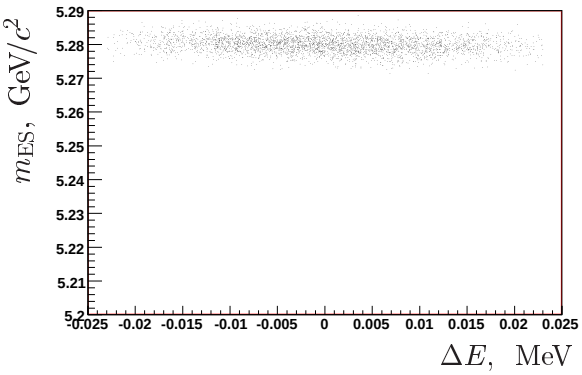

Figure 6.12: 2-dimensional $\{m_{\rm ES}, \Delta E\}$ distribution of correctly identified MC generated signal events for $B^- \to D^- K^0$ with $D^- \to K^+\pi^-\pi^-$ channel.

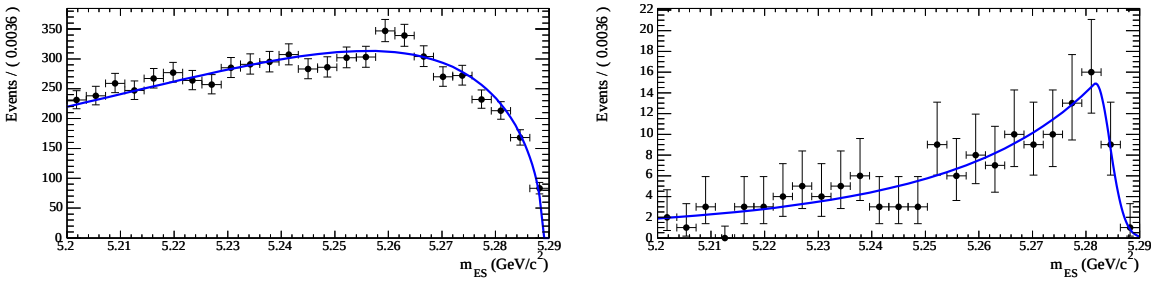

Figure 6.13: Distribution of $m_{\rm ES}$ for $B^+ \to D^+ K^{*0}$ with $D^+ \to K^-\pi^+\pi^+$ continuum (left) and selected decays of $B\overline{B}$ (right) background events. The superimposed curves are the results of the fits with the threshold and Crystal Ball functions, respectively.

where x_0 represents the maximum allowed value for the variable x described by $A(x)$ and c accounts for the shape of the distribution (usually the function is used for $x = m_{\rm ES}$). All the PDF parameterizations are derived from the simulated events. The Crystal ball (CB) [96] function is a Gaussian modified to have an extended power-law tail on the low (left) side.

6.6 Event Shape Variables

Since e^+e^- collide at $\sqrt{s} \simeq M(\Upsilon(4S))$, the $\Upsilon(4S)$ resonance is produced almost at rest. Given the mass of the $\Upsilon(4S)$, $M(\Upsilon(4S)) = 10.58$ GeV/c^2, the mass of the B, $M_B = 5.279$ GeV/c^2, and the $\Upsilon(4S)$ boost, the B mesons have a very low momentum (of the order of 330 MeV/c) in the CM frame. On the other hand, $q\overline{q}$ pairs are produced with large momenta because the quark q is lighter than the quark b; the two quarks are emitted in opposite directions and hadronize

independently. For this reason, $q\overline{q}$ events have a jet-like spatial shape, while the $B\overline{B}$ events have a spherical distributed shape.

This shape difference is reflected in several variables that can be used to distinguish continuum events from $B\overline{B}$ ones. These variables contain global information on the event shape and normally use all the tracks and energy clusters in the event, not only the ones used to reconstruct the B candidates. The variables used in the analyses presented in this thesis are (other variables have been tried, but are not used because they do not give significant gain in sensitivity):

- **Event Shape Moments**, L_0 and L_2.

$$L_0 = \sum_{i=0}^{roe} p_i,$$
$$L_2 = \sum_{i=0}^{roe} p_i \cdot \cos^2(\theta_i),$$

  where p_i is the momentum of the considered particle evaluated in the e^+e^- CM frame and θ_i is the polar angle of the considered particle with respect to the thrust axis of the B candidate. The index i runs on all the charged tracks and neutrals coming from the rest of the events (roe) i.e. that do not come from the reconstructed B.

- $|\cos(\theta_{\rm thrust})|$. The absolute value of the cosine of the angle between the B direction and the rest of the event thrust axis (where the thrust axis is defined as the direction that maximizes the sum of the longitudinal momenta of all particles). Since continuum events have a jet-like topology, the $|cos(\theta_{\rm thrust})|$ distribution is peaked at 1, while for $B\bar{B}$ events (that are spherically distributed in the space) it is distributed uniformly.

Analyses that are described in this thesis use also the following global variables to distinguish between signal and background events:

- $|\mathbf{\Delta t}|$. Proper time difference calculated from the difference between the decay vertex z coordinates of the two B mesons in the event. In true $B\bar{B}$ events, this variable has a decreasing exponential shape due to the B lifetime convoluted with the Δz detector resolution and is then wider than in the case of continuum events, in which we just observe the resolution.

- **Distance of the closest approach** (DOCA). The distance between the two K meson flight directions, in the point of their closest approach (used for $B^+ \to D^0K$ with $D^0 \to K\pi\pi^0$ analysis).

- **Distance between the B and the D** The distance between the decay vertices of the B and of the D.

The distributions of these variables can be found in the Chapters dedicated to a particular analyses (Chapters 7 and 8).

Each of these variables can be used to discriminate signal and background events in the selected sample. Instead, a unique variable may be defined which takes full advantage of all the discriminating variables and their correlations to maximize the separation power.

The Fisher discriminant [79] is a technique allowing to discriminate between two classes of events in a given sample. Starting from an ensemble of discriminating variables an iterative procedure (training) calculates the linear combination of the variables which maximizes the separation between the background and signal classes. Each event in a sample is characterized with n_{var} variables $\{x_k\}$. The classification of the events in signal and background classes relies on the following characteristics: the sample means $\bar{x}_k$ for each variable $k = 1, ..., n_{var}$, the class-specific sample means $\bar{x}_{S(B)}, k$, and the total covariance matrix C of the sample.

The covariance matrix can be decomposed into the sum of a within- (W) and a between-class matrix (B). They respectively describe the dispersion of events relative to the means of their own class (within-class matrix),

$$W_{kl} = \sum_{U=S,B} \langle x_{U,k} - \bar{x}_{U,k} \rangle \langle x_{U,l} - \bar{x}_{U,l} \rangle, B_{kl} = \frac{1}{2} \sum_{U=S,B} (\bar{x}_{U,k} - \bar{x}_k)(\bar{x}_{U,l} - \bar{x}_l), \tag{6.7}$$

The Fisher coefficients, F_k, are then given by

$$F_k = \frac{\sqrt{N_S N_B}}{N_S + N_B} \sum_{l=1}^{n_{var}} W_{kl}^{-1} (\bar{x}_{S,l} - \bar{x}_{B,l}), \tag{6.8}$$

where $N_{S(B)}$ are the number of signal (background) events in the training sample. The Fisher discriminant $\mathcal{F}$ for event i is given by

$$\mathcal{F}(i) = F_0 + \sum_{l=1}^{n_{var}} F_k x_k(i). \tag{6.9}$$

The offset F_0 centers the sample mean $\mathcal{F}$ of all $N_S + N_B$ events at zero.

The Fisher discriminant for $B^+ \to D^+ K^{(*)0}$ analysis was trained by the previously developed package based on Fortran, while $B^+ \to D^+ K^{(*)0}$ analysis profited from the TMVA package [81].

Chapter 7

Search for Rare $B^+ \to D^+ K^{(*)0}$ Decays

In this Chapter the search for $B^+ \to D^+ K^{(*)0}$ decays performed on 426 fb^{-1} is reported. This amount of data corresponds to the full data sample of 467×10^6 $B\overline{B}$ pairs collected by *BABAR* at the $\Upsilon(4S)$ center of mass energy.

Candidates for D^+ mesons are reconstructed in the $D^+ \to K^-\pi^+\pi^+$ ($DK_{K\pi\pi}$ in the following), $D^+ \to K^0_S\pi^+$ ($DK_{K^0_S\pi}$), $D^+ \to K^-\pi^+\pi^+\pi^0$ ($DK_{K\pi\pi\pi^0}$) and $D^+ \to K^0_S\pi^+\pi^0$ ($DK_{K^0_S\pi\pi^0}$) modes for the $B^+ \to D^+K^0$ decay mode. Only the first two modes were used for $B^+ \to D^+K^{*0}$ decay mode ($DK^*_{K\pi\pi}$ and $DK^*_{K^0_S\pi}$).

The aim of this search is to measure the branching fraction of these decay modes, which allow to constrain the annihilation amplitude, as explained in Chapter 4.

7.1 Introduction to the Analysis

Charged B meson decays in which neither constituent quark appears in the final state, such as $B^+ \to D^+K^{(*)0}$, are expected to be dominated by weak annihilation diagrams with the $\overline{b}u$ pair annihilating into a W^+ boson. Such processes therefore can provide insight into the internal dynamics of B mesons, in particular the overlap between the b and the u quark wave functions. Annihilation amplitudes cannot be evaluated with the commonly-used factorization approach [86]. As a consequence, there are no reliable estimates for the corresponding decay rates. Annihilation amplitudes are expected to be proportional to f_B/m_B where m_B is the mass of the B meson and f_B is the pseudoscalar B meson decay constant. The quantity f_B represents the probability amplitude for the two quark wave functions to overlap. Numerically, f_B/m_B

is approximately equal to λ^2, where λ is the sine of the Cabibbo angle [87, 86]. In addition, these amplitudes are also suppressed by the CKM factor $|V_{ub}| \sim \lambda^3$. So far, there has been no observation of a hadronic B meson decay that proceeds purely through weak annihilation diagrams, although evidence for the leptonic decay $B \to \tau\nu$ has been found [72]. In theoretical calculations of nonleptonic decays, the assumption is often made that these amplitudes may be neglected.

Some studies indicate that the branching fractions of weak-annihilation processes could be enhanced by so-called rescattering effects, in which long-range strong interactions between B decay products, rather than the decay amplitudes, lead to the final state of interest [87]. Figure 7.1 shows the Feynman diagram for the decays $B^+ \to D^+ K^{(*)0}$ and $B^+ \to D_s^+ \pi^0$ [88], and the hadron-level diagram for the rescattering of $D_s^+ \pi^0$ into $D^+ K^{(*)0}$. Significant rescattering could thus mimic a large weak annihilation amplitude. It has been argued [87] that rescattering effects might be suppressed by only λ^4, compared to λ^5 for the weak annihilation amplitudes, rendering the $B^+ \to D^+ K^{(*)0}$ decay rate with rescattering comparable to the isospin-related color-suppressed $B^0 \to D^0 K^{(*)0}$ decay rate of order 5×10^{-6}.

$B^+ \to D^+ K^{(*)0}$ decays are also of interest because their decay rates can be used to constrain the annihilation amplitudes in phenomenological fits (see Chapter 4 for details). This allows the translation of the estimation of the $B^+ \to D^0 K^{(*)+}$ amplitudes into estimations of the Cabibbo-suppressed decay $B^0 \to D^0 K^{(*)0}$ [73, 90] (see Equation 4.21). None of the modes studied here has been observed so far, and a 90% confidence level upper limit on the branching fraction $\mathcal{B}(B^+ \to D^+ K^0) < 5 \times 10^{-6}$ has been established by *BABAR* [91].

7.2 Data and Monte Carlo Samples

The analysis is based on the data sample collected with the *BABAR* detector from 1999 to 2008 (Runs 1-6). As described in the introduction of this Chapter different D decay modes are studied. In Table 7.1 the branching fractions and the number of expected events within 426 fb^{-1} are shown assuming the branching fractions for both $B^+ \to D^+ K^0$ and $B^+ \to D^+ K^{*0}$ decays to be 5×10^{-6} (which is inside the limits put by previous analysis [91]).

The data and MC samples used for the analysis are shown in Table 7.2 (using the signal branching fractions estimated in Table 7.1).

mode	Branching fraction	Number of events expected
$DK_{K\pi\pi}$	1.6×10^{-7}	77.0
$DK_{K^0_S\pi}$	1.8×10^{-8}	8.2
$DK_{K^0_S\pi\pi^0}$	8.4×10^{-8}	39.2
$DK_{K\pi\pi\pi^0}$	1.0×10^{-7}	48.6
$DK^*_{K\pi\pi}$	3.2×10^{-7}	148.4
$DK^*_{K^0_S\pi}$	3.4×10^{-8}	15.8

Table 7.1: The overall branching fractions (including secondary D, K^{*0} and K^0_S branching fractions) and the number of expected events within 426 fb^{-1} assuming branching fractions for both $B^+ \to D^+K^0$ and $B^+ \to D^+K^{*0}$ decays to be 5×10^{-6}. All the other values for branching fractions were taken from PDG 2008 [77].

Sample	Number of Events	L_{eq}
On-resonance data	-	426 fb^{-1}
Off-resonance data	-	44.4 fb^{-1}
Signal $DK_{K^0_S\pi}$	20K	1032 ab^{-1}
Signal $DK_{K^0_S\pi\pi}$	20K	217 ab^{-1}
Signal $DK_{K\pi\pi}$	20K	110 ab^{-1}
Signal $DK_{K\pi\pi\pi}$	20K	175 ab^{-1}
Signal $DK^*_{K^0_S\pi}$	20K	535 ab^{-1}
Signal $DK^*_{K\pi\pi}$	20K	57 ab^{-1}
Generic B^+B^-	731M	1329 fb^{-1}
Generic $B^0\overline{B}^0$	736M	1337 fb^{-1}
Generic $c\overline{c}$	1132M	871 fb^{-1}
Generic uds	938M	449 fb^{-1}

Table 7.2: Data and MC samples used for the analysis in terms of equivalent integrated luminosity and number of events. The luminosity of a signal MC sample is estimated taking the branching fractions of $B^+ \to D^+K^0$ and $B^+ \to D^+K^{*0}$ to be 5×10^{-6}.

7.3 Event Selection and Background Characterization

7.3.1 Event Reconstruction and Preselection Criteria

In addition to reconstruction process described in Chapter 6 some selection criteria (named "preselection cuts") are also used. The rationale for that is to reduce the size of the background sample with very loose selection criteria keeping almost all the signal events which have passed the reconstruction. The list of the preselection cuts which are common to all the analyses presented in this Chapter is the following:

- $|\Delta t| < 10$ ps (the values of RMS for this variable vary from 2 ps to 2.4 ps for different D channels).
- $|\Delta E| < 0.07$ GeV (the values of RMS for this variable vary from 0.015 GeV to 0.017 GeV for different D channels, see Chapter 6).
- $|M_D - M_{D,PDG}| < 0.09$ GeV/c^2 (the values of RMS for this variable vary from 0.008 GeV/c^2 to 0.0015 GeV/c^2 for different D channels, see Chapter 6).
- $m_{\rm ES} > 5.2$ GeV/c^2 and $m_{ES} < 5.3$ GeV/c^2.
- $P_{\pi^0} > 0.25$ GeV/c, if π^0 is present in current channel.
- $|M_{\pi^0} - M_{\pi^0,PDG}| < 0.016$ GeV/c^2, if π^0 is present in current channel (the values of RMS for this variable is about 0.006 GeV/c^2 for different D channels).

7.3.2 Selection Criteria Optimization

The preselection cuts are followed by an optimization procedure which is applied on the remaining events. For the optimization procedure the ratio

$$S = \frac{N_S}{\sqrt{N_S + N_B}}, \tag{7.1}$$

is maximized, where N_S is the number of signal events and N_B is the number of background events. The optimization is done for events with $m_{\rm ES} > 5.27$ GeV/c^2(in order to have correct estimation of background that will mostly contaminate the signal).

The optimization procedure is divided into two steps:

- optimization against all backgrounds, here $N_B = N_{\rm cont} + N_{B\overline{B}}$;
- optimization against "peaking" background, here $N_B = N_{\rm peakingbkg}$ (see below).

The number of signal and background events are all rescaled to the data luminosity of 426 fb^{-1}. In order to rescale the signal MC the branching fractions of $B^+ \to D^+ K^0$ and $B^+ \to D^+ K^{*0}$ are taken to be equal to 5×10^{-6} (inside the limits put by previous *BABAR* analysis [91]).

The optimization procedure was applied to the following set of variables:

- $|\Delta E|$, the energy difference, defined as described is Section 6.5;
- $|M_D - M_{D,PDG}|$, D meson reconstructed mass M_D difference to the nominal one taken from PDG [77];

- $|\cos(\Theta_{B^+})|$, cosine of the B polar angle with respect to the beam axis in the CM frame;
- $|M_{K^0_S,B} - M_{K^0_S,B,PDG}|$, prompt K^0_S meson reconstructed mass $M_{K^0_S,B}$ difference to the nominal one taken from PDG $M_{K^0_S,B,PDG}$ [77];
- $|M_{K^0_S,D} - M_{K^0_S,D,PDG}|$, the same as previous but for K^0_S daughter coming form the D^+ decay;
- $|M_{K^{*0}} - M_{K^{*0},PDG}|$, prompt K^{*0} meson reconstructed mass $M_{K^{*0}}$ difference to the nominal one taken from PDG $M_{K^{*0},B,PDG}$ [77];
- $|P_{\pi^0}|$ momentum of the π^0 from the D^+ decay;
- $|\cos\theta^H(K^{*0})|$ the cosine of the helicity angle of K^{*0} (as described in Section 6.4.3).

Figure 7.2 shows the variation of the ratio S as a function of the cut position in case of the $DK_{K\pi\pi}$ mode for variables specific for this channel. As it was said, the optimum selection criterion corresponds to the value, which maximizes S. The distributions of the variable for the different components (signal and background) for this channel are shown in Figure 7.3.

The distributions of the selection variables for the other decay modes are shown in Appendix A. The summary of the applied selection criteria is given in Table 7.7.

7.3.3 Continuum Background Rejection

After having reconstructed and selected the candidate events as described in previous Sections, surviving background candidates arise primarily from $e^+e^- \to q\overline{q}$ ($q = u,\ d,\ s,\ c$) events, in which random combinations of tracks and photons in the event are picked up in the reconstruction.

The Fisher discriminant (defined in 6.6) is constructed using four variables: event shape moments L_0, L_2, the angle between thrust axes of the event $|cos(\theta_{\rm thrust})|$, and the proper time difference $|\Delta t|$ (defined in Section 6.6). The coefficients of the Fisher discriminant are optimized for maximum statistical separation using MC samples of true signal events and $q\overline{q}$ events. The optimization is performed for each channel separately applying all selection criteria and also selecting only events with $m_{\rm ES} > 5.27$ GeV/c^2. These selection criteria have been applied in order to perform the continuum rejection studies on a sample similar to the final selected sample of this analysis.

Figure 7.4 shows the distributions of the different variables for a signal and $q\overline{q}$ background. In the same plots we show the comparison for the $q\overline{q}$ background distributions, as obtained from

Channel	$DK_{K\pi\pi}$	$DK_{K\pi\pi\pi^0}$	$DK_{K^0_S\pi}$	$DK_{K^0_S\pi\pi^0}$	$DK^*_{K\pi\pi}$	$DK^*_{K^0_S\pi}$
F_0	1.3587	1.6989	1.7763	1.7349	1.3595	2.4712
F_1	0.1402	0.1783	0.0099	0.1161	0.1583	0.0089
F_2	-0.1842	-0.7540	-0.0289	-0.4161	-0.2402	-0.5506
F_3	0.2096	0.1081	0.1715	0.1568	0.2234	0.1373
F_4	-2.7758	-1.5167	-2.8547	-2.2613	-2.6730	-2.1900

Table 7.3: Coefficients of the Fisher discriminant constructed using Equation 7.2

MC sample and from off-resonance data.

The resulting Fisher is constructed (according to Section 6.6):

$$F = F_0 + F_1 \cdot L_0 + F_2 \cdot L_2 + F_3 \cdot |cos(\theta_{\rm thrust})| + F_4 \cdot |\Delta t|. \tag{7.2}$$

The values for the different coefficients are shown in Table 7.3. The comparison of Fisher discriminants is shown in Figure 7.5.

7.3.4 The Peaking Background Studies

A special attention has been put, within the $B\overline{B}$ background, on possible sources of peaking background, which can occur when one or several particles of a background channel are replaced by a soft charged π^+ or π^0 and the resulting candidate still contributes to the signal region (i.e. the distributions of the $m_{\rm ES}$ variables "peaks" at the mass of the B meson). This can happen due to the close kinematics of the described B decay to the signal one, or due the high branching fraction of the process.

The possible sources of peaking $B\overline{B}$ background have been identified from a study of generic $B\overline{B}$ MC sample after general selection criteria described in the previous Section are applied. These modes are then studied on the additional samples of dedicated MC. The decay modes identified and the MC samples generated are shown in Tables 7.4 and 7.5 for $B^+ \to D^+ K^0$ and $B^+ \to D^+ K^{*0}$ modes, respectively. The probability distributions of $m_{\rm ES}$ for the identified sources of peaking background are shown in Appendix A.

In order to reduce the influence of the peaking $B\overline{B}$ background additional selection criteria were introduced. As it can be noticed, for most of the peaking background K^0_S are not present on the final state. We thus define $\alpha_{K^0_S}(B^+)$ as the angle between the momentum vector of the K^0_S and the vector connecting the B^+ and K^0_S decay vertices. A sketch of of the $K^0_S \to \pi^+\pi^-$ decay is shown in Figure 7.6. Similarly $\alpha_{K^0_S}(D^+)$ can be defined for K^0_S candidates from the D^+ decays.

Sample	Number of events	approximate luminosity, ab^{-1}
$B^0 \to D^-\rho, D \to K\pi\pi$	1.2M	1.7
$B^0 \to D^-\rho, D \to K\pi\pi\pi^0$	1.1M	2.5
$B^0 \to D^-\rho, D \to K^0_S\pi$	0.9M	12
$B^0 \to D^-\rho, D \to K^0_S\pi\pi^0$	1.1M	1.5
$B^0 \to \overline{D}^0 K^0$	698K	28
$B^0 \to \overline{D}^{*0} K^0$	1.1M	66

Table 7.4: $[B^+ \to D^+K^0]$ List of the decays identified as peaking $B\overline{B}$ background events. The number of events generated and the approximate luminosities (calculated assuming the nominal values for the different branching fractions) are shown

Sample	Number of events	approximate luminosity, ab^{-1}
$B^0 \to D^-\rho, D \to K\pi\pi$	1.2M	1.7
$B^0 \to D^-\rho, D \to K^0_S\pi$	0.9M	12
$B^0 \to D^-a_1^+, D \to K\pi\pi$	1.2M	12
$B^0 \to D^-a_1^+, D \to K^0_S\pi$	1.2M	2
$B^0 \to D^-K^{*+}, D \to K\pi\pi$	1.2M	15
$B^0 \to D^-K^{*+}, D \to K^0_S\pi$	0.6M	187

Table 7.5: $[B^+ \to D^+K^{*0}]$ List of the decays identified as peaking $B\overline{B}$ background events. The number of events generated and the approximate luminosities (calculated assuming the nominal values for the different branching fractions) are shown.

	$DK_{K\pi\pi}$	$DK_{K\pi\pi\pi^0}$	$DK_{K_S\pi}$	$DK_{K_S\pi\pi^0}$
No. events passing selection	3706	1205	4278	1316
No. of events with more than one candidate	11	27	33	28
No. misidentified events	8	10	10	9

Table 7.6: Number of events passing all selection criteria, number of events with multiple B candidates per channel, number of events with misidentified B candidate.

To further reduce the contribution from the $B^0 \to D^- \rho^+$ background, the variable $|\cos\theta^{\rm H}_{K^0_S}|$ is introduced, where $\theta^{\rm H}_{K^0_S}$ is the K^0_S helicity angle, i.e., the angle between one of the two pions from the K^0_S and the D^+ in the K^0_S rest frame. The distributions for the variables are shown in Figure 7.7 and in Appendix A. The selection criteria on $\theta^{\rm H}_{K^0_S}$, $\log(\cos(\alpha_{K^0_S}(B^+)) + 1)$, and $\log(\cos(\alpha_{K^0_S}(D^+)) + 1)$ are optimized using the same optimization procedure as before with $N_B = N_{peak}$. The summary of channel dependent selection criteria is given in Table 7.7.

7.3.5 The Best Candidate Choice

If after all the selection criteria applied, more that one B candidate is found in an event the candidate with the lowest $\chi^2(M_{D^-}) = \frac{(M_{D^-} - M_{D^-,PDG})^2}{\sigma^2_{D^-}}$ is chosen. Here σ_{D^-} is the experimental resolution on Monte Carlo signal events for the reconstructed channel.

In case the candidates have the same D^- mass the candidate with ΔE closest to zero is chosen (this can happen in the $B^+ \to D^+ K^{*0}$ analysis). The amount of events with multiple candidates after all the selection criteria as well as the number of events with misidentified B candidate are shown in Table 7.6.

7.3.6 Final Selected Sample

The summary of the selection criteria used is shown in Table 7.7. The overall reconstruction and selection efficiencies for signal events, as well as the number of expected events in each background species, are given in Tables 7.8 and 7.9.

We denote two regions: the fit region, defined as $5.2 < m_{\rm ES} < 5.29$ GeV/c^2 and $-5 < \mathcal{F} < 5$, and the signal region, defined as $5.27 < m_{\rm ES} < 5.29\,{\rm GeV}/c^2$ and $0 < \mathcal{F} < 5$.

Selection criteria	$DK_{K\pi\pi}$	$DK_{K\pi\pi\pi^0}$	$DK_{K^0_S\pi}$	$DK_{K^0_S\pi\pi^0}$	$DK^*_{K\pi\pi}$	$DK^*_{K^0_S\pi}$
$\lvert\Delta E\rvert$ [MeV]	< 20	< 23	< 25	< 24	< 19	< 19
$\lvert M_D - M_{D.PDG}\rvert$ [MeV/c^2]	< 12	< 18	< 14	< 22	< 10	< 10
$\lvert\cos(\Theta_{B_{cm}}\rvert$	< 0.76	< 0.77	< 0.87	< 0.85	< 0.82	< 0.84
$\lvert M_{K^0_S,B} - M_{K^0_S,PDG}\rvert$ [MeV/c^2]	< 6	< 6	< 7	< 6	-	-
$\ln(\cos(\alpha_{K^0_S,B}) + 1)$	< -8	< -8	< -8	< -8	-	-
$\lvert cos(\Theta^H(K^0_S))\rvert$	< 0.8	< 0.94	-	< 0.97	-	-
$\lvert cos(\Theta^H(K^{*0}))\rvert$	-	-	-	-	> 0.5	> 0.5
$\lvert M_{K^0_S,D} - M_{K^0_S.PDG}\rvert$ [MeV/c^2]	-	-	< 6	< 7	-	-
$\ln(\cos(\alpha_{K^0_S,D}) + 1)$	-	-	< -6.7	< -6	-	-
P^0_π [GeV/c2]	-	> 0.4	-	> 0.4	-	-
$\lvert M_{\pi^0} - M_{\pi^0,PDG}\rvert$ [MeV/c^2]	-	< 10	-	< 12	-	-
$\lvert M^{*0}_K - M_{K^{*0},PDG}\rvert$ [MeV/c^2]	-	-	-	-	< 40	< 40

Table 7.7: The summary of the selection criteria used for selecting $B^+ \to D^+K^0$ and $B^+ \to D^+K^{*0}$.

7.4 Maximum Likelihood Fit

7.4.1 The Fit Model

An extended unbinned maximum likelihood for the set of variables $\{m_{ES}, \mathcal{F}\}$ is built [94] to perform a fit to the yield. The likelihood $\mathcal{L}$ is defined as:

$$\mathcal{L} = \frac{e^{-N'}}{N!} \cdot N'^N \cdot \prod_{j=1}^{N} f(\mathbf{x}_j \mid \theta, N') \,,$$
$$\text{with } f(\mathbf{x} \mid \theta, N') = \frac{N_{sig} f_{sig}(\mathbf{x}|\theta) + \sum_i N_{B_i} f_{B_i}(\mathbf{x}|\theta)}{N'} \,,$$

where $f_{sig}(\mathbf{x}|\theta)$ (and $f_{B_i}(\mathbf{x}|\theta)$) are the probability density functions (PDFs) for the hypothesis that the event is a signal (background) event, N is the number of events in the selected sample, N' is the expectation value for the total number of events, and B_i indicates the different background categories used in the fit. The correlations between these variables are checked using MC samples and are found to be negligible. The variables are indicated by the vector $\mathbf{x}$ and θ indicates a set of parameters. N_{sig} is the number of signal events, whereas N_{B_i} is the total number for each background species events (see the list below). Thus we write the pdf as the product of the 1-dimensional PDFs for the single variables.

We consider three background categories:

- continuum background;

	region	$B^+ \to D^+ K^0$			
		$DK_{K\pi\pi}$	$DK_{K\pi\pi\pi^0}$	$DK_{K^0_S\pi}$	$DK_{K^0_S\pi\pi^0}$
Signal efficiency	fit	18.4%	5.2%	21.3%	6.2%
	signal	12.4%	3.8%	14.7%	4.9%
Signal	fit	14.1 ± 0.2	2.5 ± 0.1	1.81 ± 0.03	2.4 ± 0.1
	signal	9.6 ± 0.2	1.8 ± 0.1	1.21 ± 0.03	1.9 ± 0.1
Combinatorial $B\overline{B}$ background	fit	67 ± 4	157 ± 4	12 ± 2	36 ± 3
	signal	7 ± 2	20 ± 2	3 ± 1	8 ± 2
Peaking $B\overline{B}$ background	fit	2.0 ± 0.2	3.3 ± 0.4	1.1 ± 0.2	1.8 ± 0.5
	signal	0.3 ± 0.1	1.0 ± 0.2	0.3 ± 0.1	0.6 ± 0.2
Continuum background	fit	2840 ± 40	4860 ± 50	640 ± 20	1600 ± 30
	signal	63 ± 6	104 ± 8	12 ± 3	45 ± 5

Table 7.8: $[B^+ \to D^+ K^0]$ The reconstruction efficiency and expected number of events, assuming $\mathcal{B}(B^+ \to D^+ K^0) = 5 \times 10^{-6}$, in the fit and signal regions as defined in the text.

- $B\overline{B}$ background (excluding $B\overline{B}$ peaking background).
- $B\overline{B}$ peaking background (see the discussion in Section 7.3.4).

We leave the following parameters free in the fit:

- $N_{\rm sig}$ number of signal events in the sample.
- N_{BB} number of $B\overline{B}$ background events in the sample.
- N_{cont} number of continuum background events in the sample.
- a_{cont} shape of the Argus function parameterizing $m_{\rm ES}$ distribution for continuum background events.

The fit is done in the region $(m_{\rm ES}, \mathcal{F})$ which is defined by $5.2 < m_{\rm ES} < 5.3$ GeV/c^2 and $-5 < \mathcal{F} < 5$.

7.4.2 Parameterizations of the Distributions Used in the Fit

The $m_{\rm ES}$ and $\mathcal{F}$ distributions are parameterized on MC events using the functions listed in Table 7.10. An example of parameterization (on the $DK_{K\pi\pi}$ decay mode) is shown in Figure 7.8. The plots for the other channels are collected in Appendix A.5. The final parameterization coefficients are also listed in Appendix A.5. The parameterization for the $q\overline{q}$ background events is also performed on the off-resonance data and compared with the one obtained on MC events.

	region	$B^+ \to D^+K^{*0}$	
		$DK^*_{K\pi\pi}$	$DK^*_{K^0_S\pi}$
Signal efficiency	fit	10.6%	10.5%
	signal	7.6%	7.4%
Signal	fit	15.8 ± 0.3	1.70 ± 0.04
	signal	11.3 ± 0.3	1.20 ± 0.03
Combinatorial $B\overline{B}$ background	fit	400 ± 10	42.8 ± 4
	signal	30 ± 2	6.4 ± 1
Peaking $B\overline{B}$ background	fit	26 ± 2	2.4 ± 0.3
	signal	5.4 ± 1	0.7 ± 0.2
Continuum background	fit	6100 ± 50	630 ± 20
	signal	129 ± 8	13 ± 3

Table 7.9: $[B^+ \to D^+K^{*0}]$ The reconstruction efficiency and expected number of events, assuming $\mathcal{B}(B^+ \to D^+K^{*0}) = 5 \times 10^{-6}$ in the fit and signal region as defined in the text.

mode	signal		$B\overline{B}$ background		$q\overline{q}$ background		$B\overline{B}$ peaking background	
	$m_{\rm ES}$	$\mathcal{F}$	$m_{\rm ES}$	$\mathcal{F}$	$m_{\rm ES}$	$\mathcal{F}$	$m_{\rm ES}$	$\mathcal{F}$
$DK_{K\pi\pi}$	Gaussian	DBG	ARGUS	Gaussian	ARGUS	DBG	CB	Gaussian
$DK_{K\pi\pi\pi^0}$	Gaussian	DBG	ARGUS	Gaussian	ARGUS	DBG	CB	Gaussian
$DK_{K^0_S\pi}$	Gaussian	DBG	ARGUS	Gaussian	ARGUS	DBG	CB	Gaussian
$DK_{K^0_S\pi\pi^0}$	Gaussian	DBG	ARGUS	Gaussian	ARGUS	DBG	CB	Gaussian
$DK^*_{K\pi\pi}$	Gaussian	DBG	ARGUS	DBG	ARGUS	DBG	CB	Gaussian
$DK^*_{K^0_S\pi}$	Gaussian	DBG	ARGUS	DBG	ARGUS	DBG	CB	Gaussian

Table 7.10: Functions used for the parameterization of signal and background events. DBG stands for Double Bifurcated Gaussian, CB stands means Crystal Ball function. Definitions of Crystal ball and ARGUS functions are given in Section 6.5.

The agreement is found to be satisfactory (as shown in Appendix A.5) and the differences in the fitted parameters are taken into account in the systematic errors evaluation.

7.4.3 Fit Validation Using Parameterized Pseudo-experiments

The fit procedure is validated using an ensemble of simulated experiments (toy MC studies), where the yields of the fit are generated according to a Poisson distribution using the values obtained in the pdf parameterization procedure. The number of generated events is chosen following the results on MC reported in Tables 7.8 and 7.9. The non-floating parameters of the fit as well as the shape of the $q\overline{q}$ background threshold function are fixed to the values obtained from the MC sample.

	10 combined 1d-likelihoods	1d-likelihood with 10× stat
68% prob.	[20.9, 44.6]	[17.0, 37.6]
95% prob.	[10.7, 55.9]	[8.7, 48.9]
99% prob.	[6.2, 60.5]	[4.5, 55.8]

Table 7.11: Comparison between the selected probability regions for the number of signal event on $DK_{K^0_S\pi}$ channel obtained by combining 10 likelihood with the same statistics as the one expected on data and the regions obtained if the fit is performed on a sample with all the events together.

In Figure 7.9 the distribution of $N_{\rm sig}$, its errors (symmetric and asymmetric), and its pulls for the $DK_{K\pi\pi}$ mode are shown. The pull for a variable x is defined as the difference between the fitted $x_{\rm fit}$ and the mean generated value $\langle x_{\rm gen}\rangle$, divided by the error $\sigma_{\rm err}$, $x_{\rm pull} = (x_{\rm fit} - \langle x_{\rm gen}\rangle)/\sigma_{\rm err}$.

We show the negative and the positive errors obtained for N_{sig}, when we fit it with asymmetric errors, and the corresponding pull distributions. When calculating the pull with asymmetric errors, the negative error is used for fitted values that are smaller than the generated ones, while the positive error is used in case we find higher fitted values than the generated ones. The asymmetric errors are obtained from MINOS [82] estimation.

The likelihood for N_{sig} from the toy MC experiment is not Gaussian and thus the pull distribution for N_{sig}, calculated using the Gaussian errors, have no mean consistent with unity. One can notice that the asymmetric pull distribution shows a good behavior, which means that the result for N_{sig} can be described by a bifurcated Gaussian.

In Figure 7.10 we show the asymmetric pulls for all other modes studied. It is clear that for the $DK^{(*)}_{K^0_S\pi}$ modes the shape of the likelihood is not Gaussian and in this case the likelihood cannot be described by a bifurcated Gaussian either. This behavior can be explained by the fact that the amount of events in these channels is very low. In order to decide if this channel can be included in the combined likelihood two sanity checks are performed.

For the first test, 10 toys with the same statistics as for the data are generated. These 10 likelihoods are then combined and compared with the likelihood obtained by performing the fit on the single sample obtained using all together the events of the 10 samples. The result is shown in table 7.11.

We also generated 10000 toy MC experiments with the same parameterization functions as for $DK_{K^0_S\pi}$ but with 100 times more events. The pull obtained is shown in Figure 7.11. These two tests are considered satisfactory and 1d-likelihood for $DK_{K^0_S\pi}$ is used for the measurement.

7.4.4 Fit Validation Using Fully Simulated Samples

We perform the fit to the generic Monte Carlo sample constructed by making fully simulated signal and background events. The rationale for this test is to check the impact of the possible correlations between the variables, which have been assumed uncorrelated in the fit. In the MC sample a branching fraction $\mathcal{B}(B^+ \to D^+ K^0_S) = 1.1 \times 10^{-5}$ was used for generation, which is 2.2 times larger than current experimental limit. The results of the fit depending on the channel are shown in Table 7.12. The likelihood projections obtained in the fits are shown in Figure 7.12. In Figure 7.13 we also show the same distribution after having applied a cut on $\mathcal{F} > 0$ to visually enhance the signal.

Parameter	fitted value ± error	number of events in sample
$DK_{K\pi\pi}$ channel		
N_{BB}	75 ± 27	
N_{cont}	2826 ± 58	
N_{sig}	$42^{+9.8}_{-10.2}$	38
N_{peak} (fixed in the fit)	2.0	
Shape of Argus	-42 ± 3	
$DK_{K\pi\pi\pi^0}$ channel		
N_{BB}	187 ± 50	
N_{cont}	4834 ± 54	
N_{sig}	19 ± 11	8
N_{peak} (fixed in the fit)	3.3	
Shape of Argus	-34 ± 1.5	
$DK_{K^0_S\pi}$ channel		
N_{BB}	26 ± 13	
N_{cont}	430 ± 24	
N_{sig}	$5.1^{+4.7}_{-3.4}$	5
N_{peak} (fixed in the fit)	0.9	
Shape of Argus	-31 ± 6	
$DK_{K^0_S\pi\pi^0}$ channel		
N_{BB}	49 ± 35	
N_{cont}	1582 ± 49	
N_{sig}	$0.4^{+4.0}_{-5.3}$	2
N_{peak} (fixed in the fit)	1.8	
Shape of Argus	-33 ± 3	

Table 7.12: $[B^+ \to D^+ K^0]$ Results of the fit to the MC sample with integrated of luminosity 426 fb^{-1}.

Same exercise has been made for the $B^+ \to D^+ K^{*0}$ analysis. Due to the fact that signal events were not generated in the generic MC we insert into each generic sample the amount

of events which is equivalent to $BR(B^+ \to D^+ K^{*0}) = 11 \times 10^{-6}$. The results are shown in Table 7.13 and in Figure 7.14. In Figure 7.15 the same distributions after having applied a cut on $\mathcal{F} > 0$ to visually enhance the signal are shown.

Parameter	fitted value ± error	number of events in sample
$DK^*_{K\pi\pi}$ channel		
N_{BB}	414±65	
N_{cont}	6108±98	
N_{sig}	23±13	35
N_{peak} (fixed in the fit)	26	
Shape of Argus	-39±1	
$DK^*_{K^0_S\pi}$ channel		
N_{BB}	42±18	
N_{cont}	630±30	
N_{sig}	1.4 ± 4.7	4
N_{peak} (fixed in the fit)	2.4	
Shape of Argus	-40±5	

Table 7.13: [$B^+ \to D^+ K^{*0}$ decay channel] Results for the fit to the MC sample of luminosity 426 fb^{-1} for $B \to DK^*$ decay channel.

7.4.5 Flavor Tagging

To reduce the importance of the continuum background in the final sample we divide the events according to their flavor-tagging category [92]. We define the following exclusive tagging categories:

- *lepton category,* events containing at least one lepton in the decay of the other B meson;
- *kaon category,* events containing at least one kaon in the decay of the other B meson, which do not belong to the first category;
- *other category* contains all the events not included in the two previous categories.

The first two categories are expected to be less contaminated by continuum background (as shown in Table 7.14). We fit all three categories simultaneously. Studies of simulated events show that using the tagging categories reduces the statistical uncertainty on the measured branching fraction for the $K\pi\pi$ mode by 5%, but leads to little gain for the other modes (which are less statistically significant themselves). Hence, we use tagging information only for the $K\pi\pi$ channel.

The results of the fit to the generic MC sample are shown in Table 7.15.

tagging category	species	region	$DK_{K\pi\pi}$	$DK^*_{K\pi\pi}$
lepton	Signal	fit	1.39 ± 0.1	1.66 ± 0.04
		signal	0.89 ± 0.05	1.17 ± 0.03
	Combinatorial $B\overline{B}$ background	fit	1.9 ± 0.3	10.8 ± 1
		signal	0.0 ± 0.3	0.3 ± 0.1
	Peaking $B\overline{B}$ background	fit	0.0 ± 0.1	1.0 ± 0.1
		signal	0.0 ± 0.1	0.1 ± 0.1
	Continuum background	fit	19.4 ± 0.5	32 ± 0.6
		signal	0.0 ± 0.2	5.3 ± 0.2
kaon	Signal	fit	4.2 ± 0.1	4.7 ± 0.1
		signal	2.9 ± 0.1	3.4 ± 0.1
	Combinatorial $B\overline{B}$ background	fit	14 ± 3	78 ± 5
		signal	30 ± 2	6.1 ± 2.0
	Peaking $B\overline{B}$ background	fit	0.4 ± 0.1	7.3 ± 1.4
		signal	0.0 ± 0.1	1.4 ± 0.3
	Continuum background	fit	592 ± 19	1270 ± 22
		signal	10 ± 2	16 ± 3
other	Signal	fit	8.55 ± 0.07	9.5 ± 0.3
		signal	5.81 ± 0.03	6.8 ± 0.2
	Combinatorial $B\overline{B}$ background	fit	51.1 ± 4.0	314.8 ± 9.1
		signal	7.3 ± 2	23.9 ± 2.1
	Peaking $B\overline{B}$ background	fit	1.6 ± 0.2	2.4 ± 0.3
		signal	0.2 ± 0.1	0.7 ± 0.2
	Continuum background	fit	2231 ± 36	4805 ± 40
		signal	52 ± 6	112 ± 8

Table 7.14: The expected number of events per tagging categories, assuming $\mathcal{B}(B^+ \to D^+K^0) = \mathcal{B}(B^+ \to D^+K^{*0}) = 5 \times 10^{-6}$. Numbers correspond to signal and fit regions.

Parameter	value ± error tagged	number of events in sample
$DK_{K\pi\pi}$ channel		
N_{BB}	76 ± 26	
N_{cont}	2826 ± 57	
N_{sig}	$42^{+9.5}_{-10.5}$	38
N_{peak} (fixed in the fit)	2.0	
Shape of Argus	-42 ± 3	
$DK^*_{K\pi\pi}$ channel		
N_{BB}	420 ± 60	
N_{cont}	6100 ± 100	
N_{sig}	25^{+11}_{-10}	36
N_{peak} (fixed in the fit)	26	
Shape of Argus	-39 ± 1.5	

Table 7.15: Results for the fit to the MC sample rescaled to 426 fb^{-1} for $DK_{K\pi\pi}$ and $DK^*_{K\pi\pi}$ channels in the tagged case.

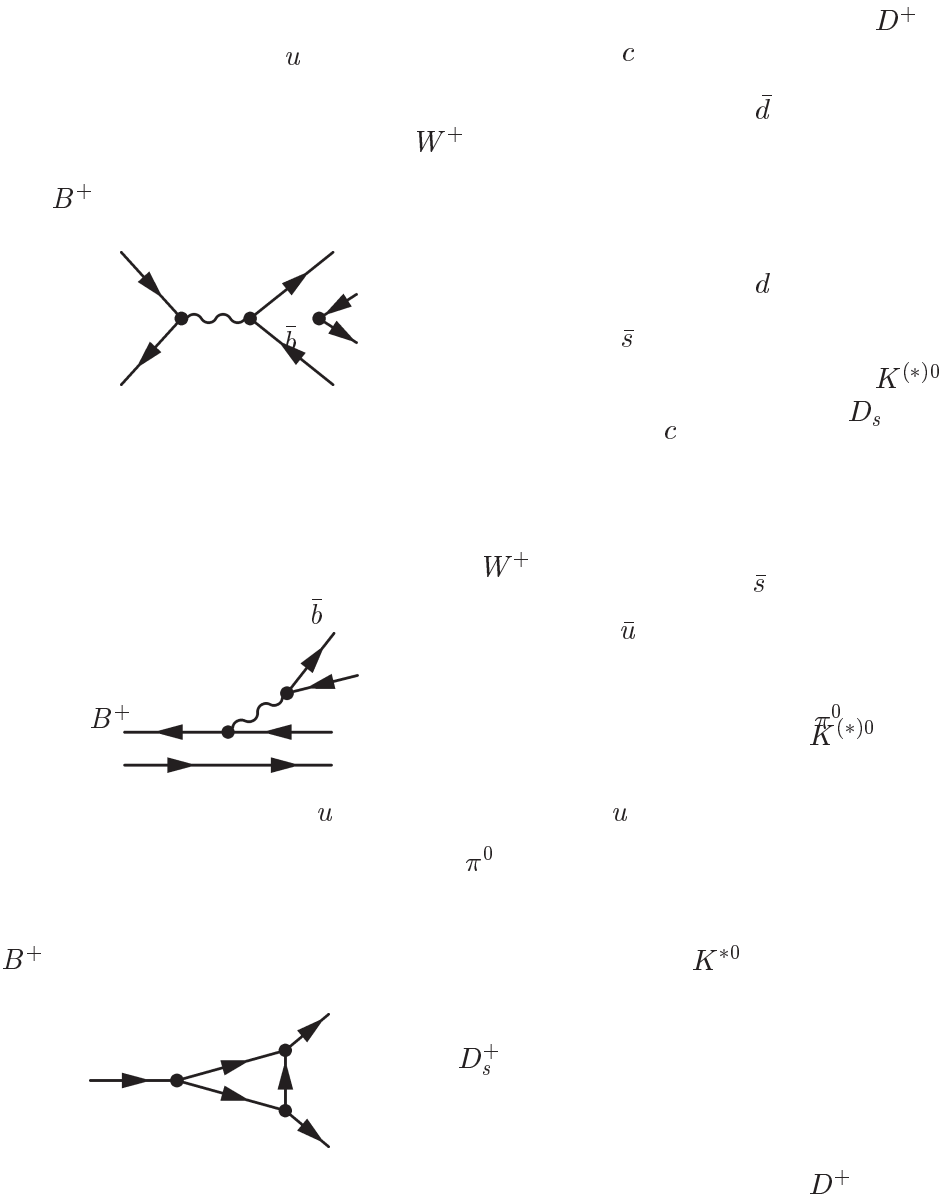

Figure 7.1: Annihilation diagram for the decay $B^+ \to D^+ K^{(*)0}$ (left). Tree diagram (middle) for the decay $B^+ \to D_S^+ \pi^0$ and hadron-level diagram (right) for the rescattering contribution to $B^+ \to D^+ K^{(*)0}$ via $B^+ \to D_s^+ \pi^0$.

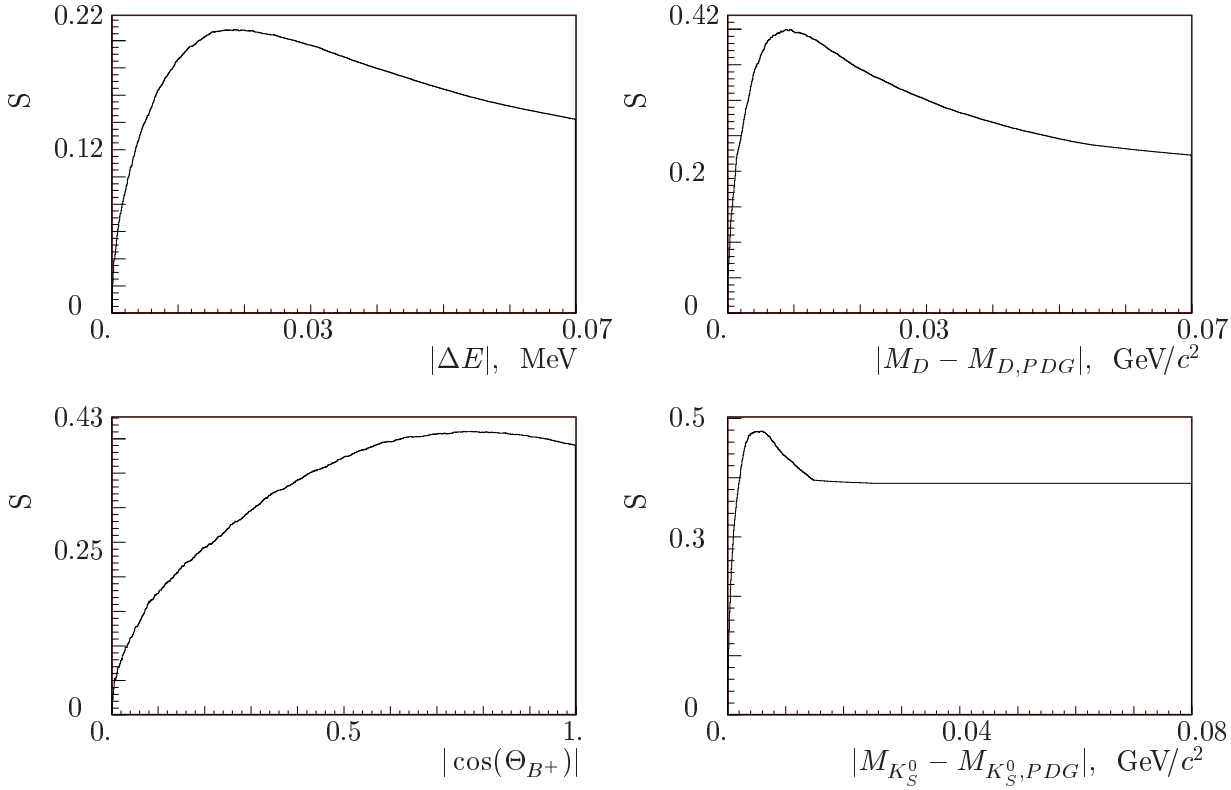

Figure 7.2: [$DK_{K\pi\pi}$ decay channel] $S = \dfrac{N_S}{\sqrt{N_S + N_B}}$ as a function of the applied selection criteria for $|\Delta E|$ (top left), $|M_D - M_{D,PDG}|$ (top right), $|\cos(\Theta_{B^+})|$ (bottom left), and $|M_{K^0_S} - M_{K^0_S,PDG}|$ (bottom right), respectively.

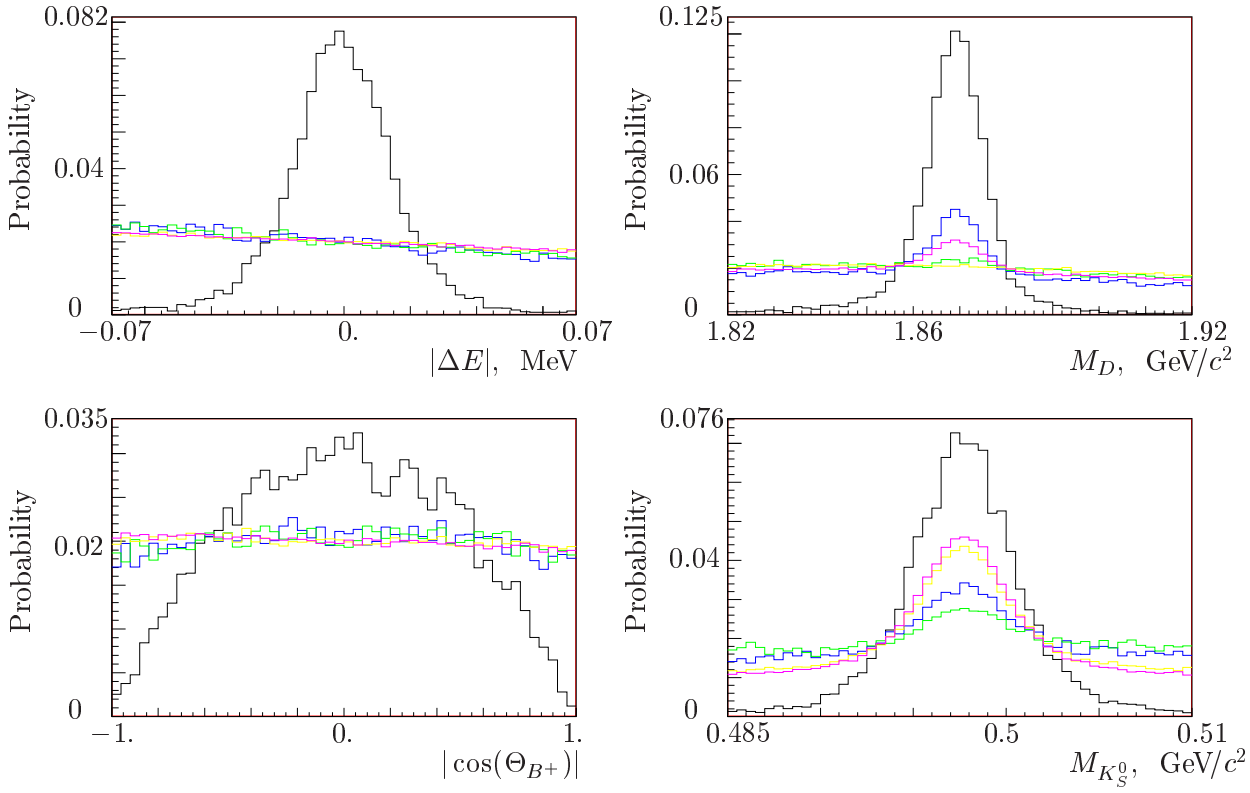

Figure 7.3: [$DK_{K\pi\pi}$ decay channel] Distributions of ΔE (top left), M_D (top right), $\cos(\Theta_{B^+})$ (bottom left), and $M_{K^0_S}$ (bottom right). The color codes for histogram corresponds to $c\overline{c}$ background (magenta), *uds* background (yellow), $B^0\overline{B}^0$ background (blue), B^+B^- background (green), and signal (black).

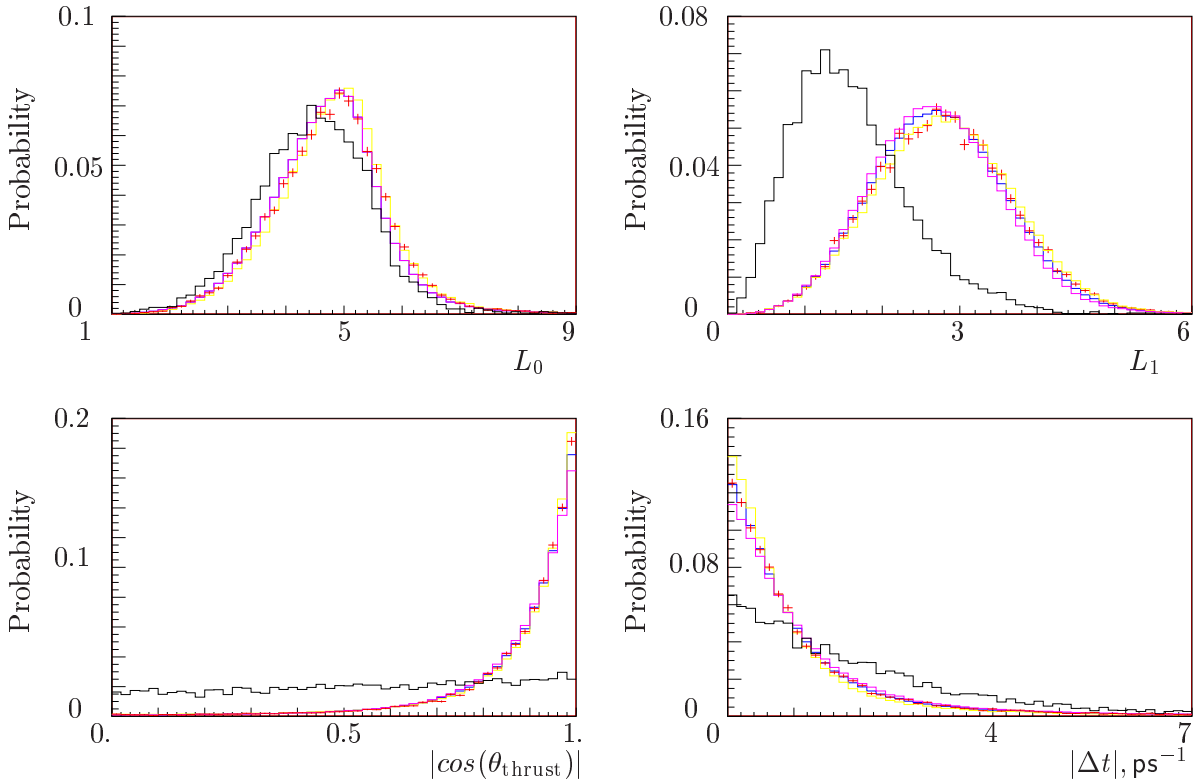

Figure 7.4: $[DK_{K\pi\pi}]$. Distributions of the variables Comparison between *uds* MC (yellow), $c\bar{c}$ MC (magenta), a weighted sum of the two (blue), off-resonance data for the variables (red dots with errors) and signal MC (black) chosen to construct the Fisher discriminant. The variables are: L_0 (top left), L_1 (top right), $|cos(\theta_{\rm thrust})|$ (bottom left), and $|\Delta t|$ (bottom right).

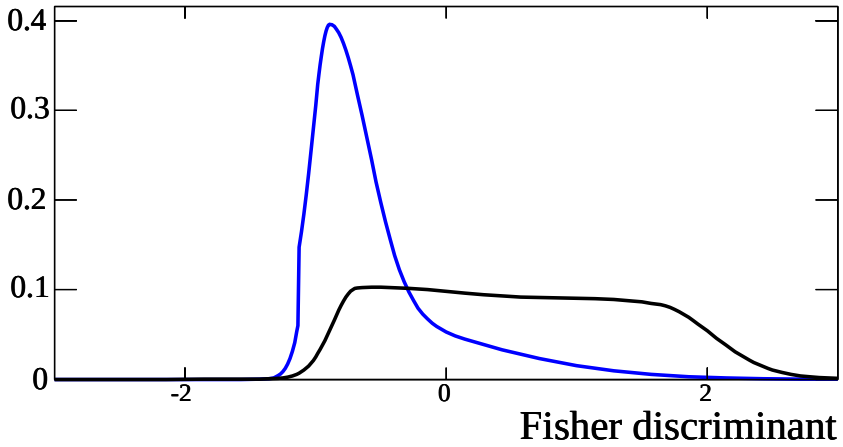

Figure 7.5: $[DK_{K\pi\pi}]$. The Fisher discriminant distributions for continuum background (blue) and signal (black).

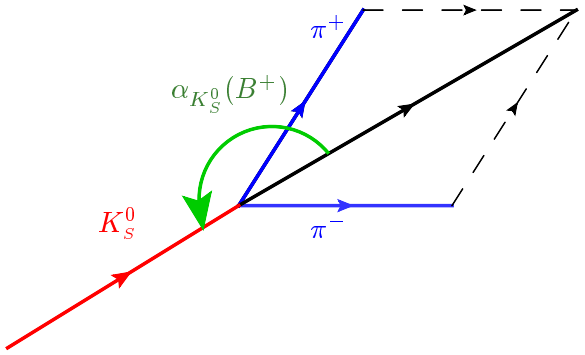

Figure 7.6: Sketch of the K^0_S decay into $\pi^+\pi^-$. Red vector indicates the direction of K^0_S defined from the decay vertices. Black vector is the K^0_S momentum vector defined as a sum of $\pi^\pm$ momenta. $\alpha_{K^0_S}(B^+)$ is the angle between these two vectors defined as shown in Figure.

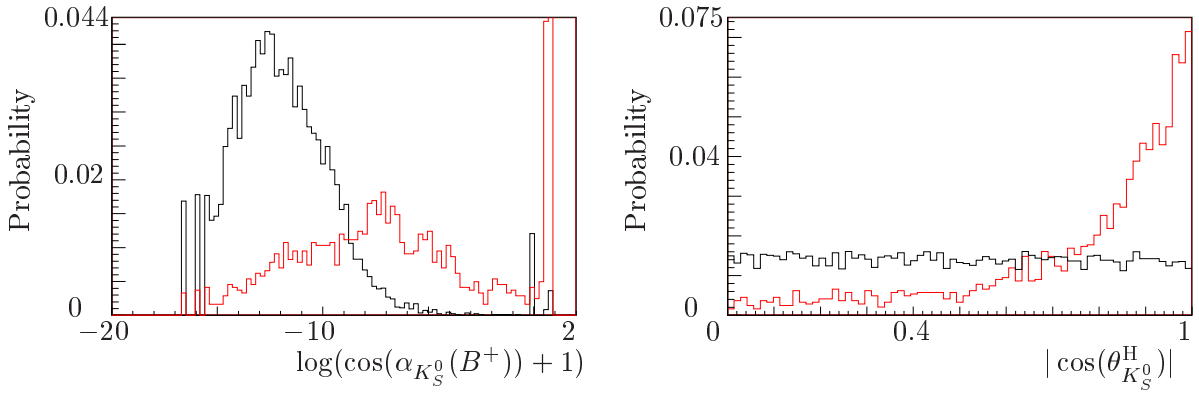

Figure 7.7: [$DK_{K\pi\pi}$ mode]. Comparison of signal (black) and peaking $B\overline{B}$ background (red) distributions for $|cos\Theta^{\rm H}_{K^0_S}|$ (left plot), $\log(\cos(\alpha_{K^0_S}(B^+)) + 1)$ (right plot) for the $DK_{K\pi\pi}$ mode. Same distributions for other modes are shown in Appendix A.

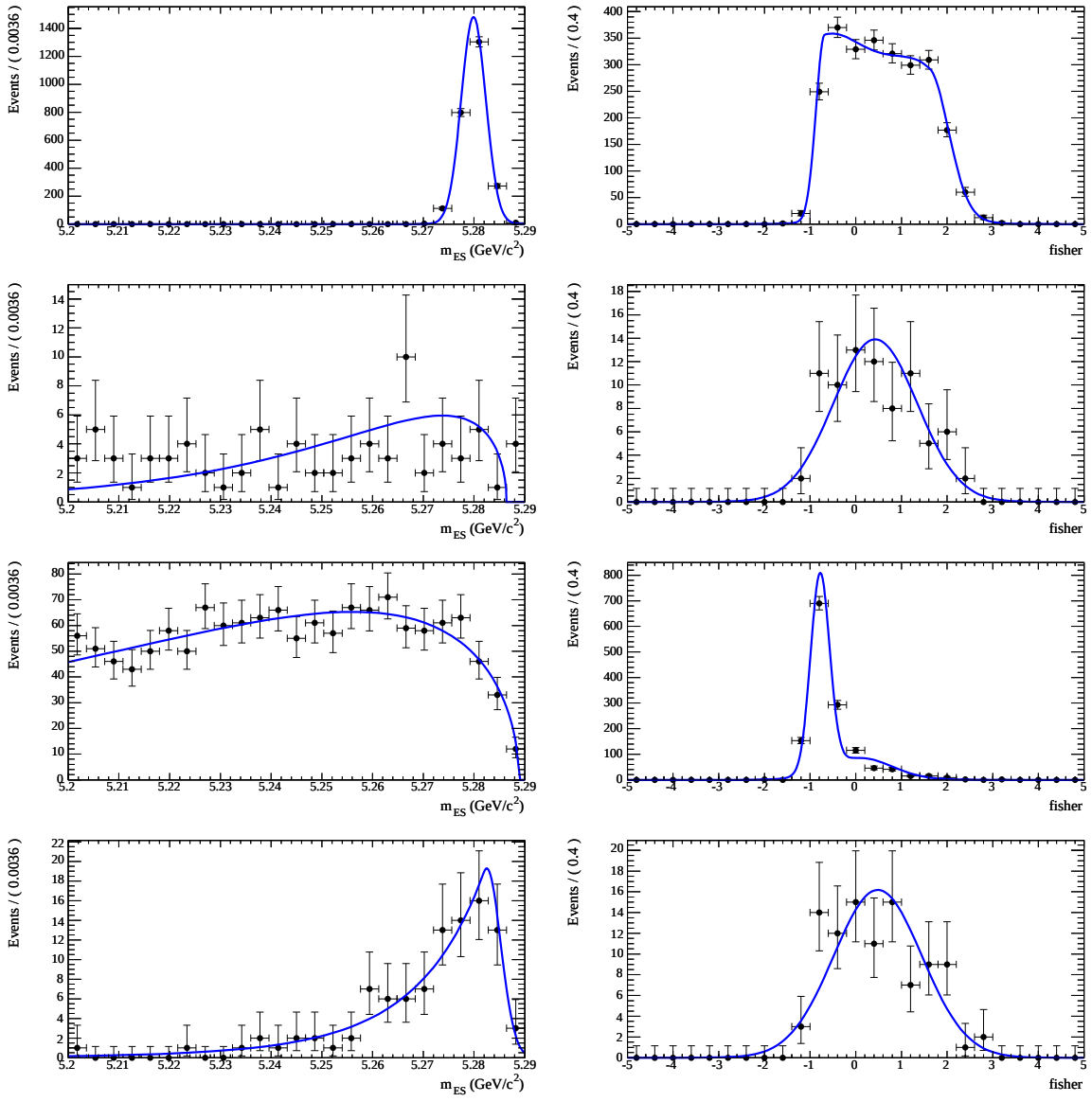

Figure 7.8: $m_{\rm ES}$ (left) and Fisher (right) distributions for the $DK_{K\pi\pi}$ mode for signal (top), $B\overline{B}$ background (2nd row), $q\overline{q}$ background (3rd row), and peaking $B\overline{B}$ background (bottom row). The superimposed curves are the results of the fits.

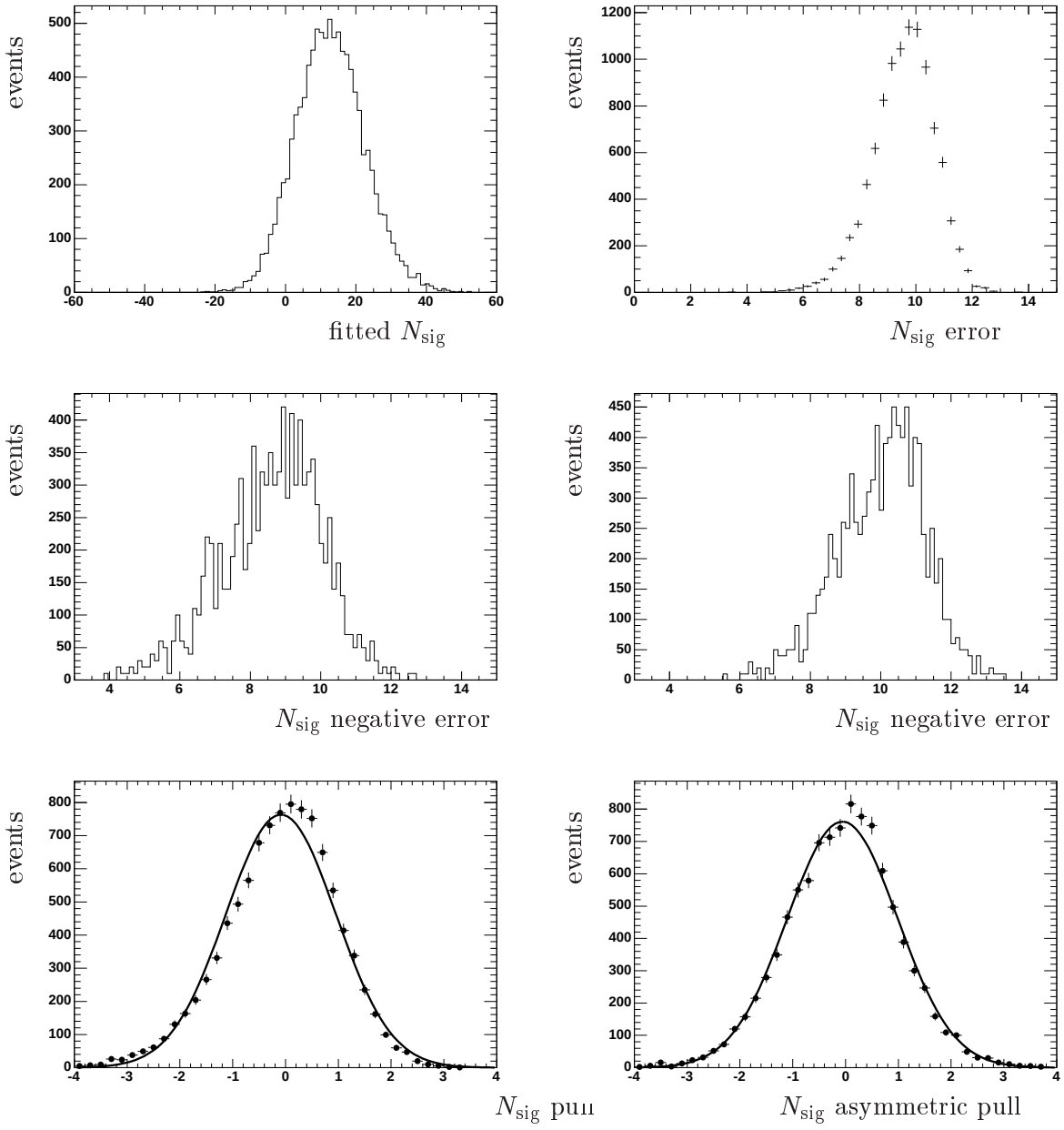

Figure 7.9: [$DK_{K\pi\pi}$ decay channel]. Distributions of the fitted value for $N_{\rm sig}$ and its symmetric error (upper plots), its lower and higher errors (middle plots) and the symmetric and asymmetric pulls(lower plots) obtained from the toy MC described in the text.

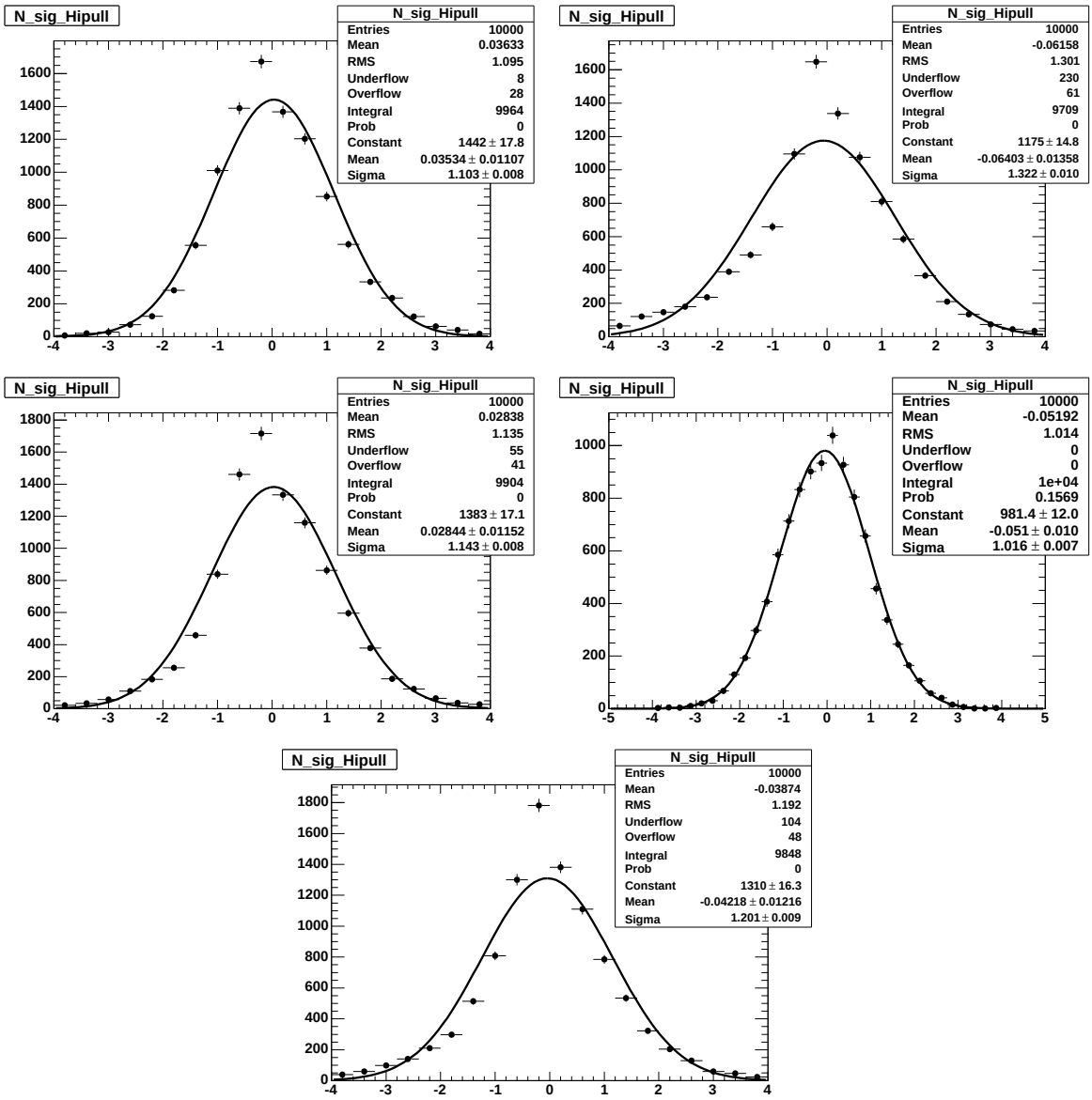

Figure 7.10: Distributions of the asymmetric pulls for the $DK_{K\pi\pi\pi^0}$ (top left), $DK_{K^0_S\pi}$ (top right), $DK_{K^0_S\pi\pi^0}$ (center left), $DK^*_{K\pi\pi}$ (center right), $DK^*_{K^0_S\pi}$ (bottom) obtained from the toy MC described in the text.

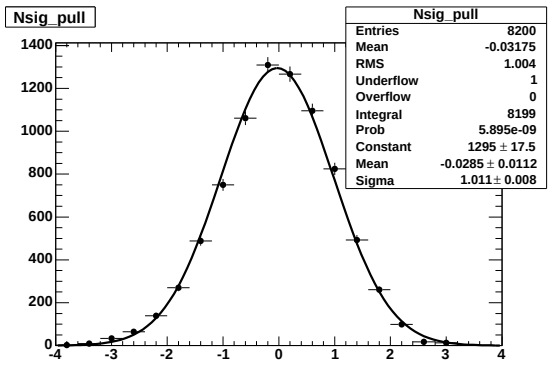

Figure 7.11: [$DK_{K^0_S\pi}$ decay channel]. Pull distribution for N_{sig} with 100 times the statistics (see text for more explanations).

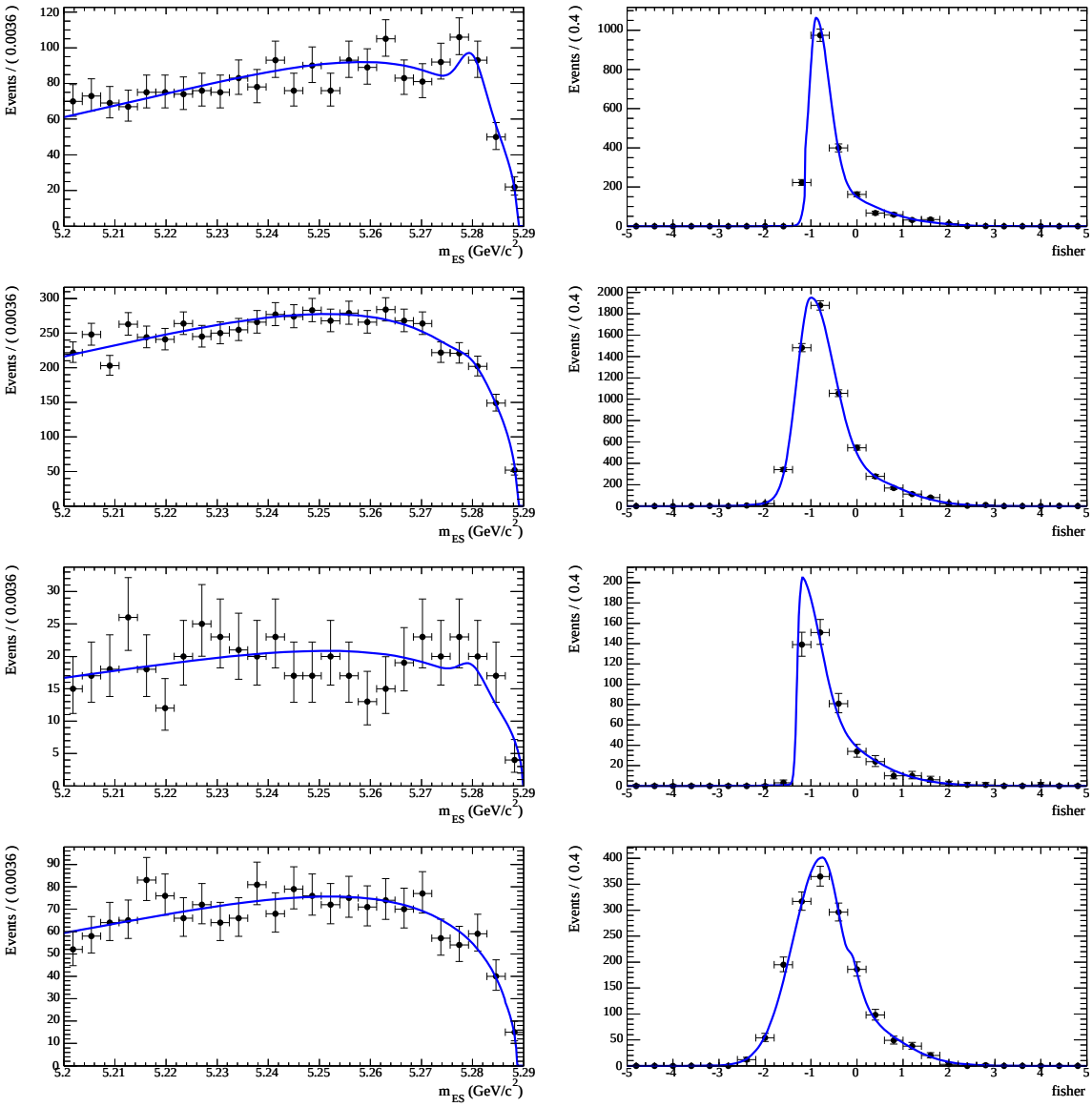

Figure 7.12: [$B^+ \to D^+ K^0$ decay channel] Projections of the 2D likelihood fit to the $m_{\rm ES}$ (left) and $\mathcal{F}$ (right) variables performed on the generic MC sample for $DK_{K\pi\pi}$, $DK_{K\pi\pi\pi^0}$, $DK_{K^0_S\pi}$, $DK_{K^0_S\pi\pi^0}$ decay channels (from top to bottom), respectively.

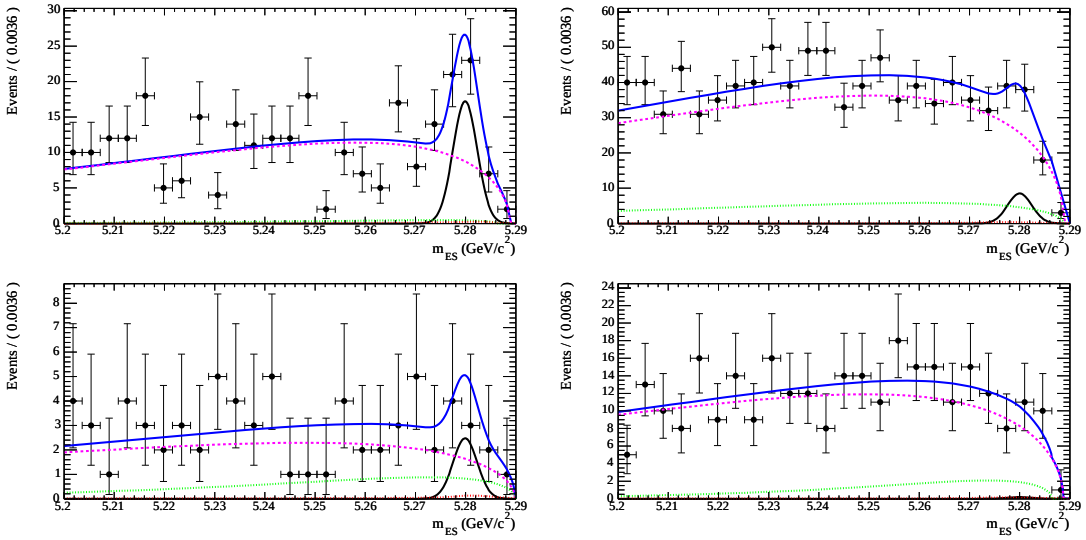

Figure 7.13: [$B^+ \to D^+K^0$ decay channel] Projection of the 2D likelihood fit to the $m_{\rm ES}$ distributions after having applied a cut on $\mathcal{F} > 0$. Blue line shows the result of the fit . Magenta, green, red and black lines show the results of the fit for continuum, $B\overline{B}$, peaking and signal components respectively. Plots for $DK_{K\pi\pi}$ (top left), $DK_{K\pi\pi\pi^0}$ (top right), $DK_{K^0_S\pi}$ (bottom left), $DK_{K^0_S\pi\pi^0}$ (bottom right) decay channels are shown.

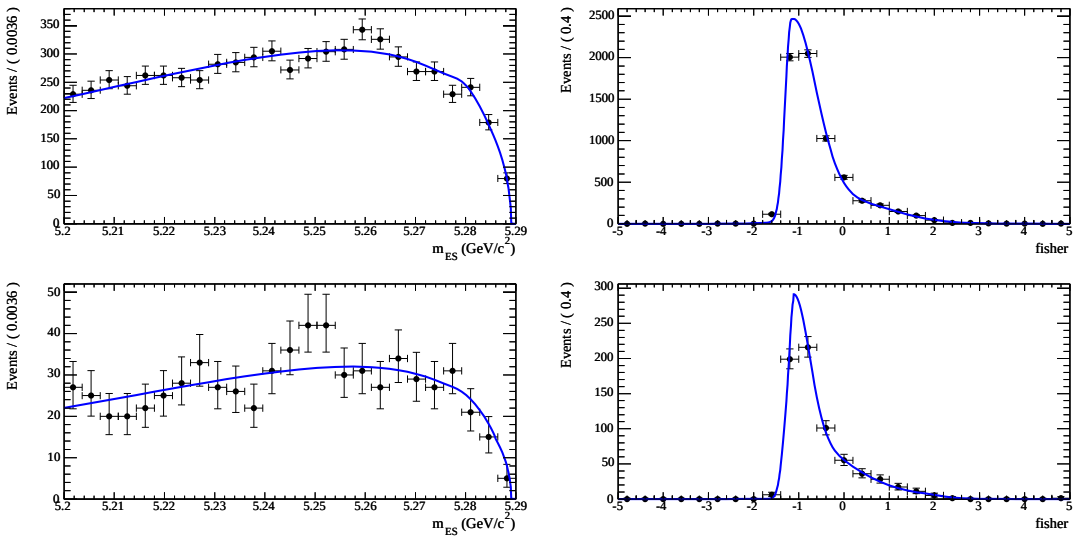

Figure 7.14: [$B \to DK^*$ decay channel] Projections of the 2D likelihood fit to the $m_{\rm ES}$ (left) and *Fisher* (right) variables performed on generic MC sample for $DK^*_{K\pi\pi}$ (top row) and $DK^*_{K^0_S\pi}$ (bottom row).

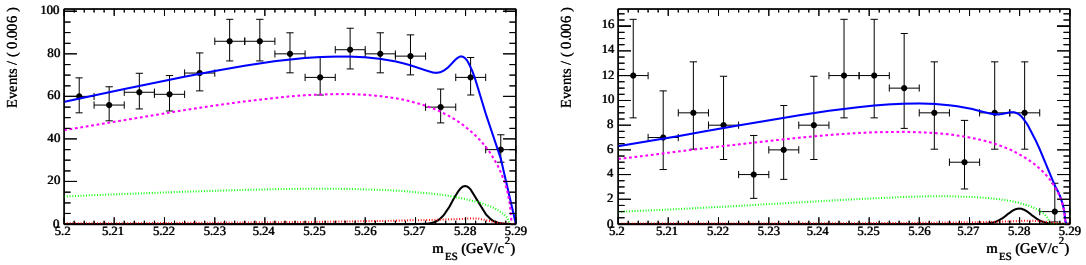

Figure 7.15: [$B \to DK^*$ decay channel] Projection of the 2D likelihood fit to the $m_{\rm ES}$ variable after having applied a cut on $Fisher > 0$. Blue line shows the result of the fit. Magenta, green, red and black lines show the results of the fit for continuum, $B\bar{B}$, peaking and signal components respectively. Plots for $DK^*_{K\pi\pi}$ (left), $DK^*_{K^0_S\pi}$ (right) decay channels are shown.

7.5 Branching Fraction Measurements and Sensitivity Studies

The number of signal events determined by the fit ($N_{\rm sig}$) is used to calculate the branching fraction using the following expression:

$$\mathcal{B}(B^+ \to D^+ K^0) = \frac{N_{\rm sig}}{N_{\rm B^+B^-} \cdot \epsilon_{\rm sig}} \cdot \frac{2}{\mathcal{B}_D \cdot \mathcal{B}_{K^0_S}}, \tag{7.3}$$

where $N_{\rm B^+B^-}$ is the total number of charged B mesons in the data sample (equal to a half of all $B\overline{B}$ pairs produced), $\mathcal{B}_D$ and $\mathcal{B}_{K^0_S}$ are the branching fraction for each D meson decay channel and for $K^0_S \to \pi^+\pi^-$ respectively [77], and $\epsilon_{\rm sig}$ is the reconstruction efficiency for each D decay channel evaluated on MC events. The expression for $\mathcal{B}(B^+ \to D^+ K^{*0})$ is obtained replacing $\mathcal{B}_{K^0_S}/2$ with branching fraction of $K^{*0} \to K^+\pi^-$, $\mathcal{B}_{K^{*0}}$.

Decay mode	$\mathcal{B}=5$	$\mathcal{B}$=0
	Mean error [95% range]	Mean error [95% range]
$B^+ \to D^+ K^0$		
$K\pi\pi$	$+3.3$ [2.7, 4.0] -3.0 [2.2, 3.6]	$+2.8$ [2.2, 3.6] -2.4 [1.6, 3.2]
$K\pi\pi\pi^0$	$+20$ [14, 25] -17 [10, 23]	$+19$ [13, 24] -17 [9.4, 22]
$K^0_S\pi$	$+12$ [7.3, 16] -8 [4.6, 14]	$+11$ [7.1, 16] -8 [4.5, 14]
$K^0_S\pi\pi^0$	$+14$ [8.9, 18] -12 [6.2, 16]	$+13$ [8.3, 17] -11 [5.6, 15]
combined	± 2.9 [2.1, 3.6]	± 2.5 [1.5, 3.2]
$B^+ \to D^+ K^{*0}$		
$K\pi\pi$	$+3.5$ [2.5, 4.0] -3.2 [1.8, 3.6]	$+3.3$ [2.5, 4.0] -2.8 [1.6, 3.8]
$K^0_S\pi$	$+15$ [9.8, 19] -11 [5.8, 16]	$+14$ [7.9, 17] -7.7 [3.8, 14]
combined	± 3.3 [2.1, 4.2]	± 3.0 [1.8, 3.9]

Table 7.16: Expected errors on the branching fractions from toy MC studies depending on the branching fractions generated. The errors obtained in case of $\mathcal{B}$=0 give the sensitivity of the analysis. The combined errors are obtained as results of likelihood combination per each toy (see text for details). All the numbers are given in units of 10^{-6}.

In the following we describe the tests of the procedure for extracting the branching fraction for a single channel and for the combination of the channels. We perform the tests both with toy MC experiments and with generic MC simulated events. We generate a large number of toy MC experiments (10000) with the amount of signal events corresponding to the branching fraction of 5×10^{-6} and the background events as indicated in Tables 7.8 and 7.9. The results on the errors obtained for a single channel and for their combination are reported in Table 7.16. In the same Table we list the results obtained for $\mathcal{B}(B^+ \to D^+ K^{(*)0})$ set to zero (namely, $N_{sig} = 0$).

These errors can be considered as the sensitivities for the different analyses. All these results are obtained by fitting the pull distributions using a Bifurcated Gaussian function. The final result will be obtained by combining the likelihoods for an individual channel to derive average branching fractions for the $\mathcal{B}(B^+ \to D^+ K^0)$ and $\mathcal{B}(B^+ \to D^+ K^{*0})$ decay modes. We test this procedure on toy MC experiments. Since the procedure is rather CPU-time consuming we generate "only" 1000 toy MC experiments. The pull distribution of the combined branching fraction is shown in Figure 7.16. The result of this test is satisfactory with the average value equals to 0.00 ± 0.03 and RMS equals 0.94 ± 0.02.

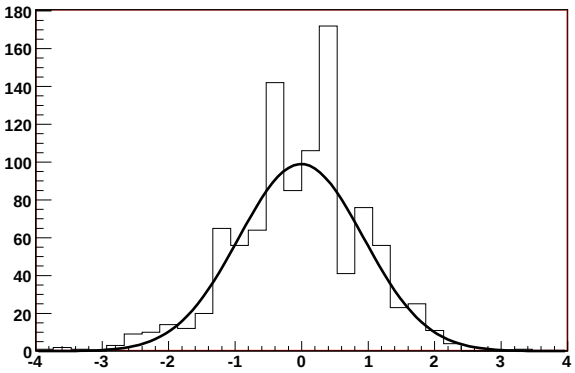

Figure 7.16: $[B^+ \to D^+ K^0]$ The distribution of the pull of combined BR for $B^+ \to D^+ K^0$ obtained after the each time the different likelihoods to get the results (mean and error) from the combined likelihood

We also determine the branching fraction performing the fit on generic MC sample. We obtain the following results:

$$\begin{aligned} BR_{DK_{K\pi\pi}} &= (15.0^{+3.7}_{-3.4}) \times 10^{-6}, \\ BR_{DK_{K\pi\pi\pi^0}} &= (37^{+23}_{-20}) \times 10^{-6}, \\ BR_{DK_{K_s\pi}} &= (16^{+15}_{-11}) \times 10^{-6}, \\ BR_{DK_{K_s\pi\pi^0}} &= (1.1^{+12}_{-9}) \times 10^{-6}. \end{aligned} \tag{7.4}$$

The likelihood scan of the combined result is shown in Figure 7.17 giving

$$BR_{B\to DK} = (14.7^{+3.6}_{-3.2}) \times 10^{-6}. \tag{7.5}$$

These results should be compared to the branching fraction 11×10^{-6} generated in generic Monte-Carlo sample.

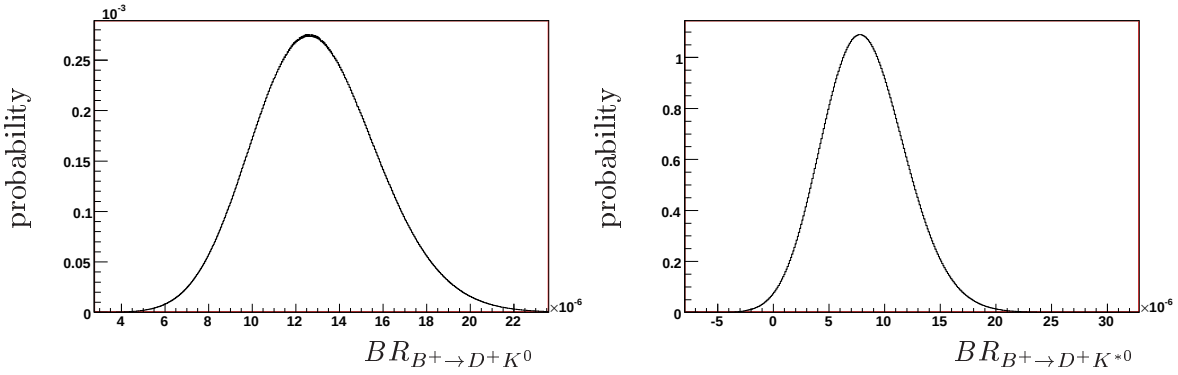

Figure 7.17: 1D likelihoods for combined BR obtained from the fit over MC generic sample of 426 fb^{-1} for $BR_{B^+\to D^+K^0}$ (left) and $BR_{B^+\to D^+K^{*0}}$ (right).

We perform the same test for the $B^+ \to D^+K^{*0}$ channel and get the following results:

$$\begin{aligned} BR_{DK^*_{K\pi\pi}} &= (8.2^{+4.0}_{-3.7}) \times 10^{-6}, \\ BR_{DK^*_{K_s\pi}} &= (3.9^{+15}_{-13}) \times 10^{-6}. \end{aligned} \tag{7.6}$$

The results from the combined likelihood (shown in Figure 7.17 is

$$BR_{B\to DK^*} = (7.6^{+3.8}_{-3.5}) \times 10^{-6}. \tag{7.7}$$

Also in this case the branching fraction was generated at $11 \cdot 10^{-6}$.

To test the procedure of setting the limit we perform the test on the generic MC sample removing signal events. We obtain the distributions given in Figure 7.18. If we exclude the negative part of the distributions and integrate the rest, the limits are $4.4 \cdot 10^{-6}$ for $B^+ \to D^+K^0$ and $2.8 \cdot 10^{-6}$ for $B^+ \to D^+K^{*0}$ at 90% probability.

7.6 Charmless Peaking $B\overline{B}$ Background

Charmless B decays may also contribute to the peaking background events. These decays can produce π and K mesons with characteristics similar to those of signal events without forming a real D meson. The charmless background is evaluated from data required to satisfy the criteria $1.774 < M_D < 1.84\,\mathrm{GeV}/c^2$ or $1.9 < M_D < 1.954\,\mathrm{GeV}/c^2$. The corresponding fits are shown in Figure 7.19, their results are shown in Table 7.17. The number of fitted events have to be rescaled according to the M_{D^+} range in the selected sample. Under the assumption that the charmless contributions are not sensibly different in the four D decay mode channels, the

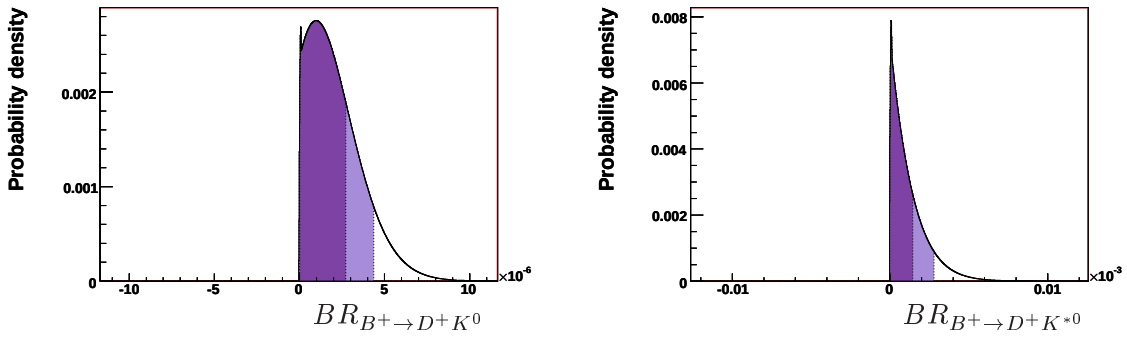

Figure 7.18: PDF for the combined branching fraction in case of no signal events in generic MC. Dark region corresponds to 68% probability region light color gives 90% probability region.

Decay	number of fitted charmless events ± error	rescaled events ± error
$DK_{K\pi\pi}$	-6.3 ± 6.7	-1.8 ± 1.8
$DK_{K\pi\pi\pi^0}$	19 ± 16	6.7 ± 5.6
$DK_{K^0_S\pi}$	-7.1 ± 5.6	-1.9 ± 1.5
$DK_{K^0_S\pi\pi^0}$	-9.2 ± 9.0	-2.5 ± 2.5
combination $B^+ \to D^+ K^0$		-1.7 ± 1.0
$DK^*_{K\pi\pi}$	-5.9 ± 17	-1.0 ± 2.9
$DK^*_{K^0_S\pi}$	-1.8 ± 7.3	-1.9 ± 1.5
combination $B^+ \to D^+ K^{*0}$		-0.7 ± 2.1

Table 7.17: Reconstructed number of charmless events per D decay mode and their combination

number of rescaled events can be combined. In this case, the contributions from charmless peaking events are found to be -1.7 ± 1.0 and -0.7 ± 2.1 after combination for $B^+ \to D^+ K^0$ and $B^+ \to D^+ K^{*0}$, respectively. The charmless peaking background contribution is estimated to be negligible and a systematic uncertainty is assigned to this assumption.

7.7 Results

7.7.1 Fit to the Data

The main results of the fit to the data are reported in Table 7.18, which gives the values of the fitted parameters for each D channel, the obtained branching fractions, and the combined ones. The background yields are close to those reported in Tables 7.12 and 7.13 and the errors obtained on the branching fractions are very compatible with the ones reported in Table 7.16. The leading

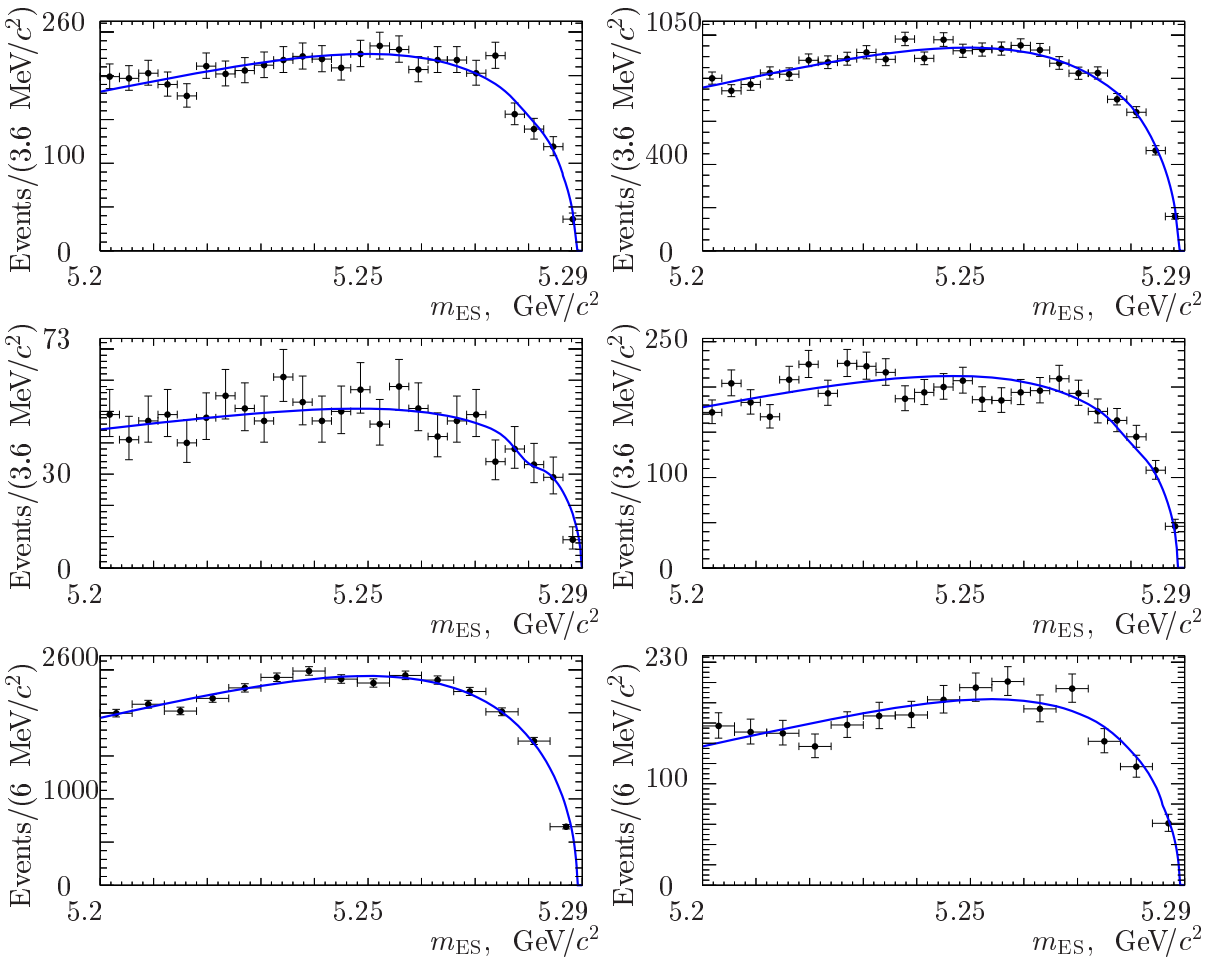

Figure 7.19: The resulting fit performed using events in the tails of the reconstructed D meson to search for possible charmless peaking background for the $DK_{K\pi\pi}$ (top left), the $DK_{K\pi\pi\pi^0}$ (top right), the $DK_{K^0_S\pi}$ (middle left), the $DK_{K^0_S\pi\pi^0}$ (middle right), the $DK^*_{K\pi\pi}$ (bottom left), and the $DK^*_{K^0_S\pi}$ (bottom right) decay modes. Dots with errors represent the on-peak data, blue lines gives the results of the fit.

contribution (as expected) is obtained from the $K\pi\pi$ mode. Likelihood fit projections of the $m_{\rm ES}$ and $\mathcal{F}$ distributions are shown in Figures 7.20 and 7.21. In Figure 7.22 we also show for illustrative purposes the fit projection for $m_{\rm ES}$, after applying a cut on $\mathcal{F} > 0$, to visually enhance any possible signal.

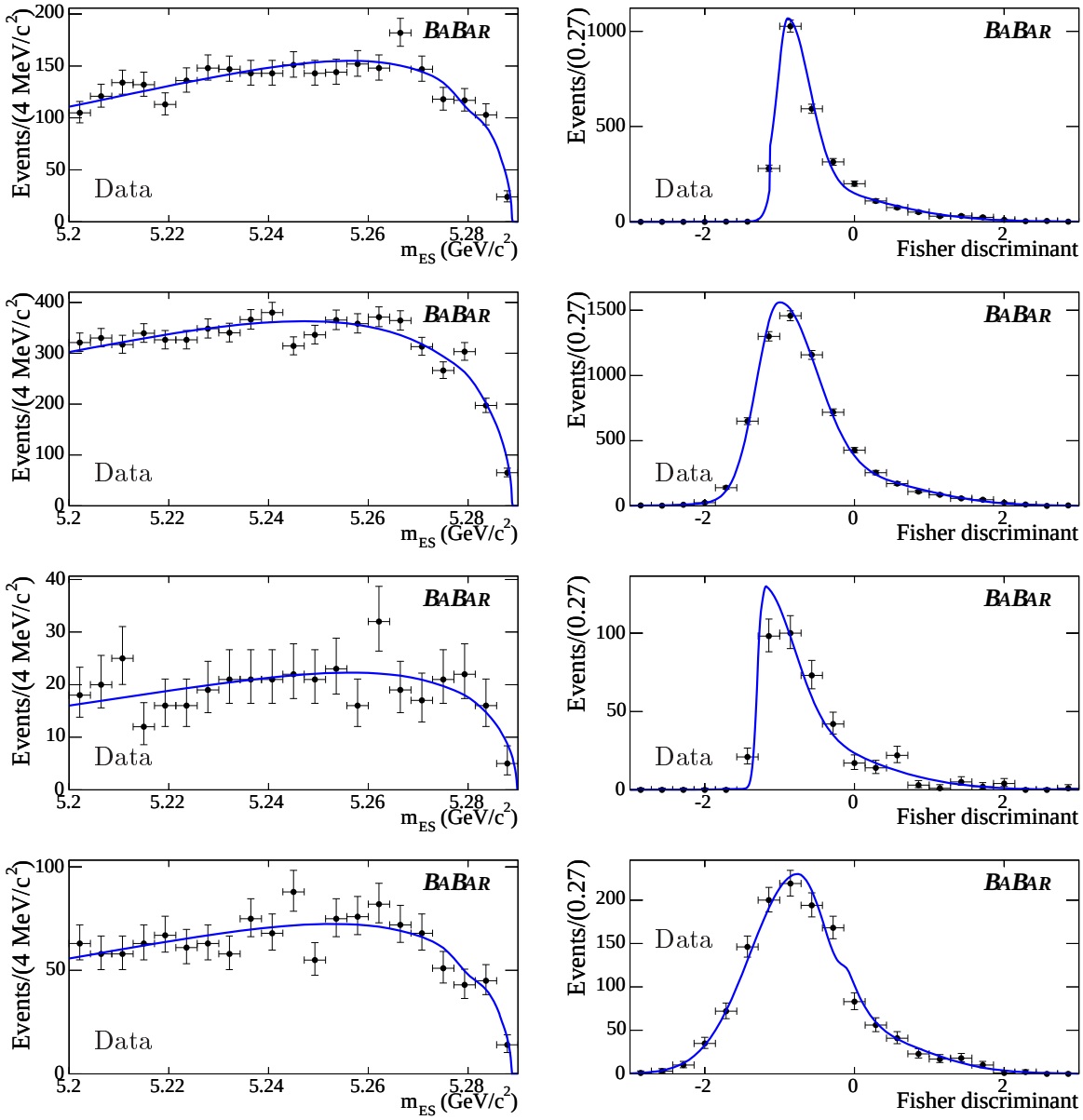

Figure 7.20: Projections of the 2D likelihood function onto the $m_{\rm ES}$ (left) and $\mathcal{F}$ (right) axes for $K\pi\pi$ (top row), $K\pi\pi\pi^0$ (2nd row), $K^0_S\pi$ (3rd row) and $K^0_S\pi\pi^0$ (4th row) for the $B^+ \to D^+ K^0_S$ mode. The data are indicated with black dots and error bars and the (blue) solid curve is the projection of the fit.

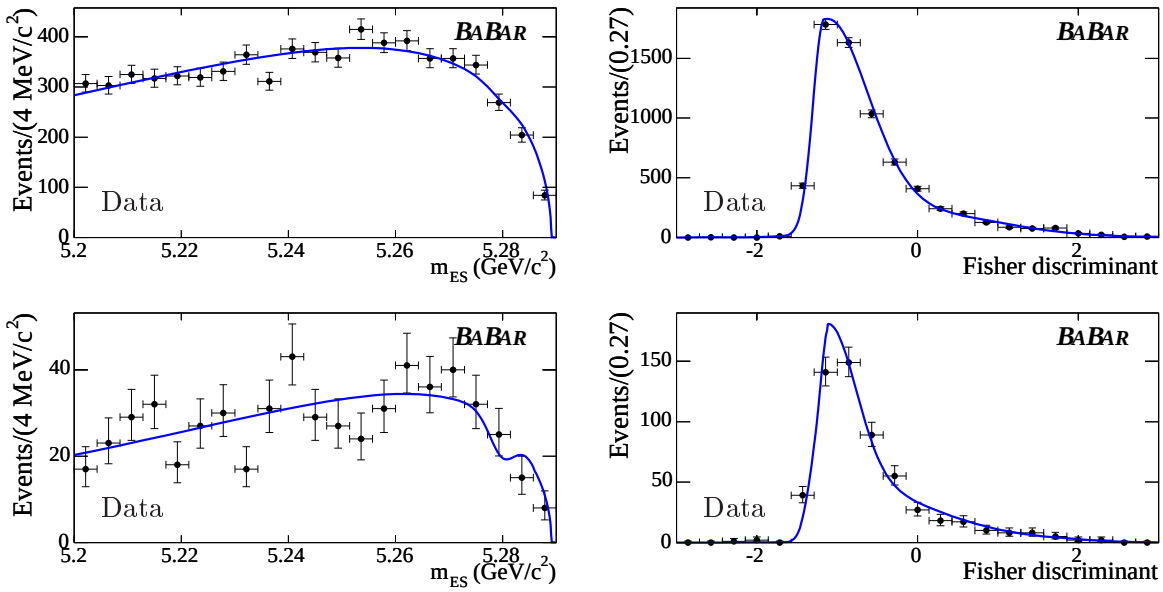

Figure 7.21: Projections of the 2D likelihood function onto the $m_{\rm ES}$ (left) and $\mathcal{F}$ (right) axes $K\pi\pi$ (top) and $K^0_S\pi$ (bottom) for the $B^+ \to D^+K^{*0}$ mode. The data are indicated with black dots and error bars and the (blue) solid curve is the projection of the fit.

The likelihood scan corresponding to results reported in Table 7.18 are shown in Figures 7.23 and 7.24.

Decay mode	$N_{\rm sig}$	$N_{\rm B\overline{B}}$	$N_{\rm cont}$	$\mathcal{B}$
$B^+ \to D^+ K^0$				
$K\pi\pi$	$-11.9 \,^{+\,6.7}_{-\,5.6}$	70 ± 27	2690 ± 57	$-4.2 \,^{+\,2.4}_{-\,2.0}$
$K\pi\pi\pi^0$	$10 \,^{+\,10}_{-\,9}$	111 ± 51	6516 ± 94	$20 \,^{+\,20}_{-\,17}$
$K^0_S\pi$	$0.6 \,^{+\,5.3}_{-\,4.5}$	20 ± 14	381 ± 23	$0.7 \,^{+\,15}_{-\,13}$
$K^0_S\pi\pi^0$	$-6.7 \,^{+\,4.5}_{-\,2.8}$	36 ± 22	1270 ± 41	$-14 \,^{+\,9.2}_{-\,6.2}$
combined	-	-	-	$-3.4 \,^{+\,2.2}_{-\,1.8}$
$B^+ \to D^+ K^{*0}$				
$K\pi\pi$	$-15.6 \,^{+\,8.7}_{-\,7.1}$	463 ± 63	6338 ± 98	$-5.0 \,^{+\,2.9}_{-\,2.1}$
$K^0_S\pi$	$-11.4 \,^{+\,3.5}_{-\,2.4}$	35 ± 15	547 ± 27	$-33 \,^{+\,10.2}_{-\,7.0}$
combined	-	-	-	$-5.3 \,^{+\,2.3}_{-\,2.0}$

Table 7.18: Branching fraction fit results in units of 10^{-6}, with statistical uncertainties. N_i are the yields of the fitted species, and $\mathcal{B}$ gives calculated branching fraction for each channel and their combination.

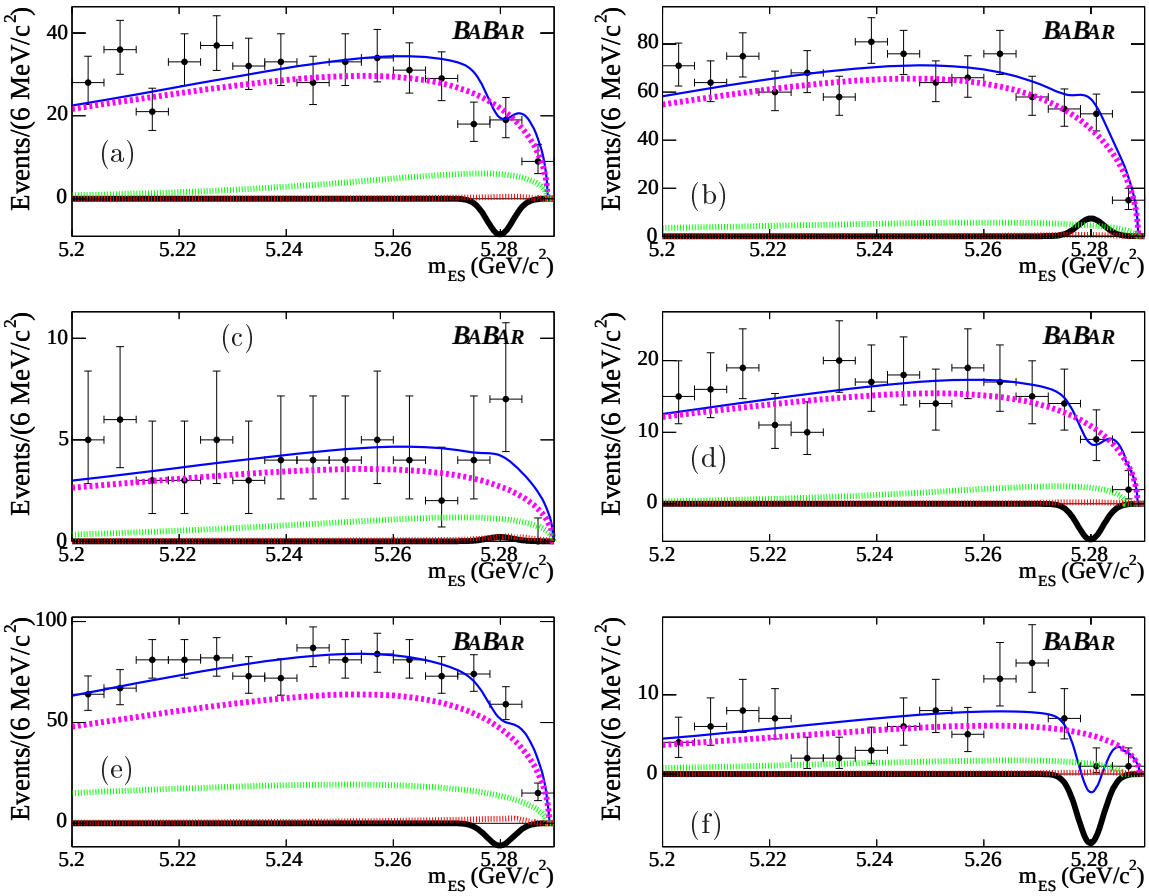

Figure 7.22: (color online) From top left to bottom right: $m_{\rm ES}$ projection for $K\pi\pi$ (a), $K\pi\pi\pi^0$ (b), $K^0_S\pi$ (c), and $K^0_S\pi\pi^0$ (d) for the $B^+ \to D^+K^0_S$ mode and $K\pi\pi$ (e) and $K^0_S\pi$ (f) for the $B^+ \to D^+K^{*0}$ modes. The data are indicated with black dots and error bars and the different fit components are shown: signal (black solid curve), combinatorial $B\overline{B}$ (green dotted), continuum (magenta dot-dashed) and $B\overline{B}$ peaking background (red dotted) and the blue solid curve is the projection of the fit. We require $\mathcal{F} > 0$ to visually enhance the signal component. Such a cut has an approximate efficiency of 70% for signal, while it rejects more than 80% of the continuum background.

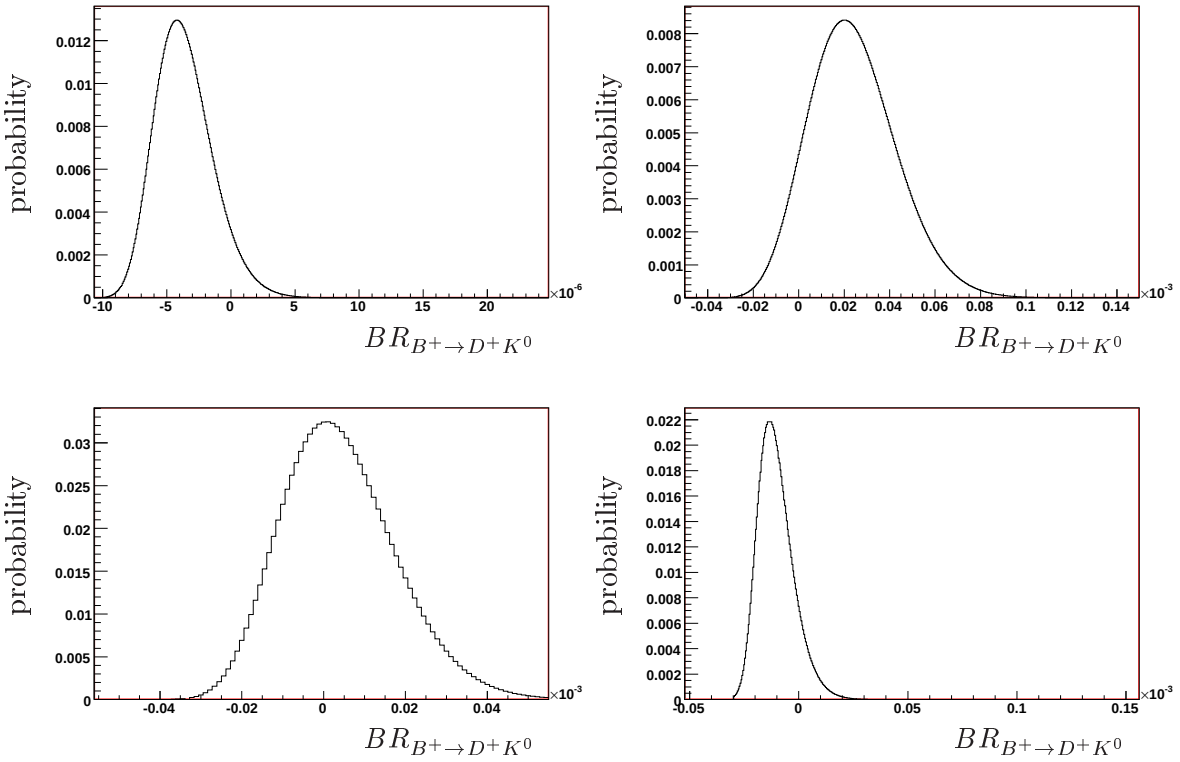

Figure 7.23: 1D likelihood for BR obtained from the fit on the onpeak data sample of 426 fb^{-1} for $DK_{K\pi\pi}$ (top left), $DK_{K\pi\pi\pi^0}$ (top right), $DK_{K^0_S\pi}$ (bottom left), $DK_{K^0_S\pi\pi^0}$ (bottom right).

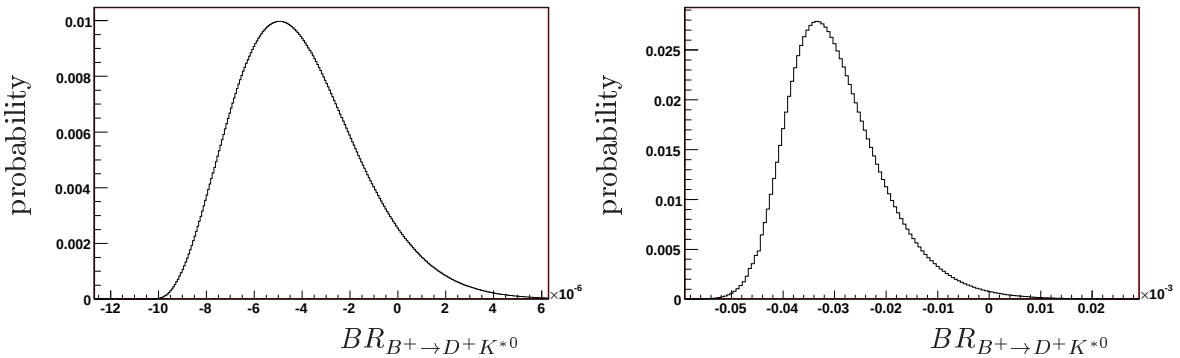

Figure 7.24: 1D likelihood for BR obtained from the fit on the onpeak data sample of 426 fb^{-1} for $DK^*_{K\pi\pi}$ (left), $DK^*_{K^0_S\pi}$ (right).

7.7.2 Fit to the $\overline{B}^0 \to D^+\pi^-$ and $\overline{B}^0 \to D^+\rho^-$ samples

Before discussing the systematic uncertainties evaluation we perform the analyses of the $\overline{B}^0 \to D^+\pi^-$ and $\overline{B}^0 \to D^+\rho^-$ decay modes. The interest of this study is that $\overline{B}^0 \to D^+\pi^-$ ($\overline{B}^0 \to D^+\rho^-$) is kinematically close decay channel to the $B^+ \to D^+K_S^0$ ($B^+ \to D^+K^{*0}$) and thus can be used to obtain the parameters of the $m_{\rm ES}$ and $\mathcal{F}$ distributions of the signal events.

We use generic MC sample to search for the possible sources of peaking background among $B\overline{B}$ events. The continuum, $B\overline{B}$, and peaking background event are parameterized following the same procedure as explained in Section 7.4.2.

For these two analyses the selection criteria corresponding to a particular D-decay channel is taken to be the same as for $B^+ \to D^+K_S^0$ and $B^+ \to D^+K^{*0}$. The list of the criteria can be seen in Table 7.7.

The fit to the on-peak data is performed on the part of the available dataset corresponding to 100 fb^{-1}. For this fit we leave floating the following parameters: N_{sig}, N_{cont}, $N_{B\bar{B}}$, shape of the Argus for the continuum and all the parameters of the signal distributions (i. e. 2 parameters for m_{ES} distribution (fitted by a Gaussian function) and 7 variables for *Fisher* distribution (Double bifurcated Gaussian function)).

The projections of the likelihood to the $m_{\rm ES}$ and Fisher are shown in Figure 7.25 (7.26) for $B^+ \to D^+K^0$ ($B^+ \to D^+K^{*0}$).

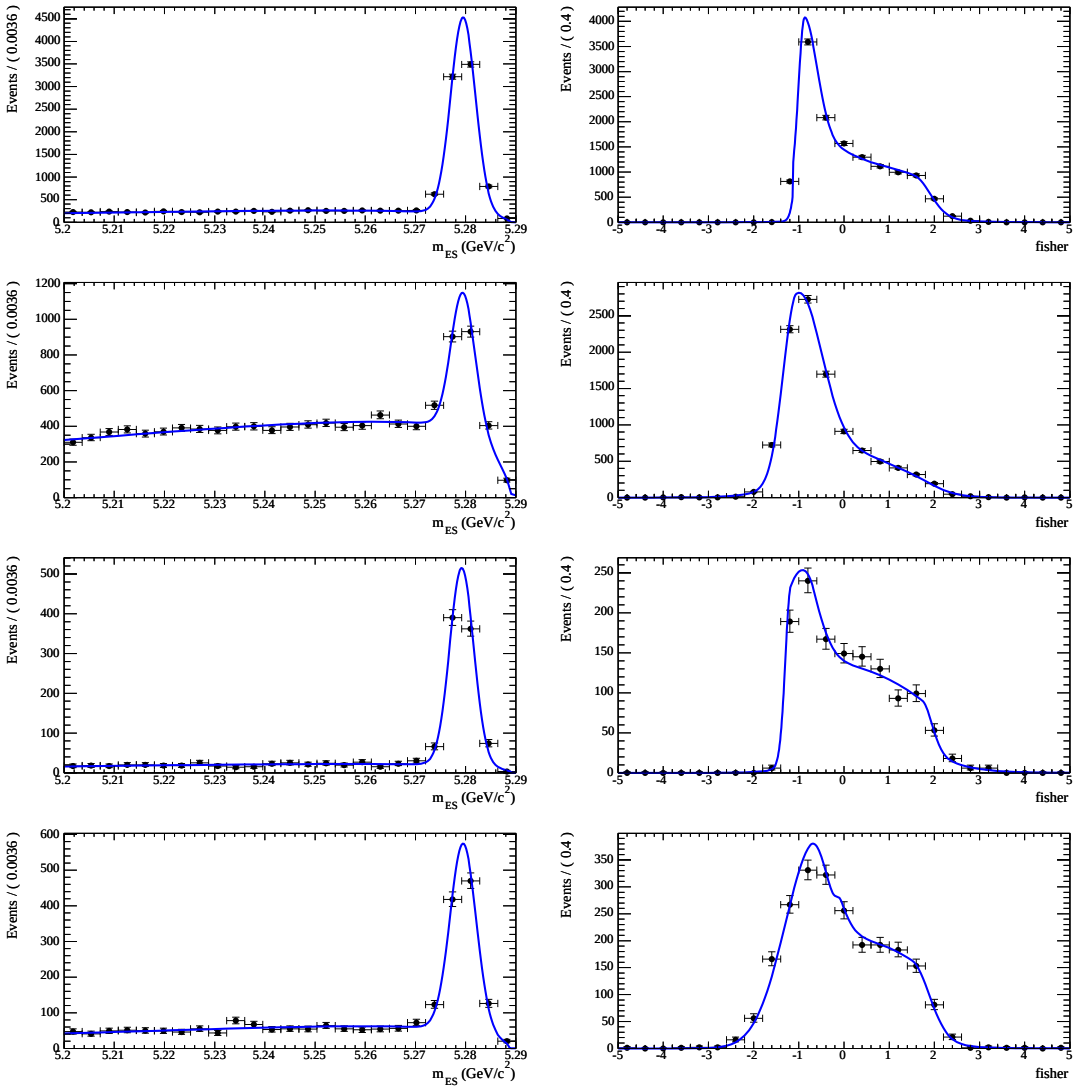

Figure 7.25: [The $\overline{B}^0 \to D^+\pi^-$ mode] Projections of the 2D likelihood to the $m_{\rm ES}$ (left) and Fisher (right) for the $D\pi_{K\pi\pi}$ (top row), $D\pi_{K\pi\pi\pi^0}$ (2nd row), $D\pi_{K^0_S\pi}$ (3rd row), and $D\pi_{K^0_S\pi}$ (right row).

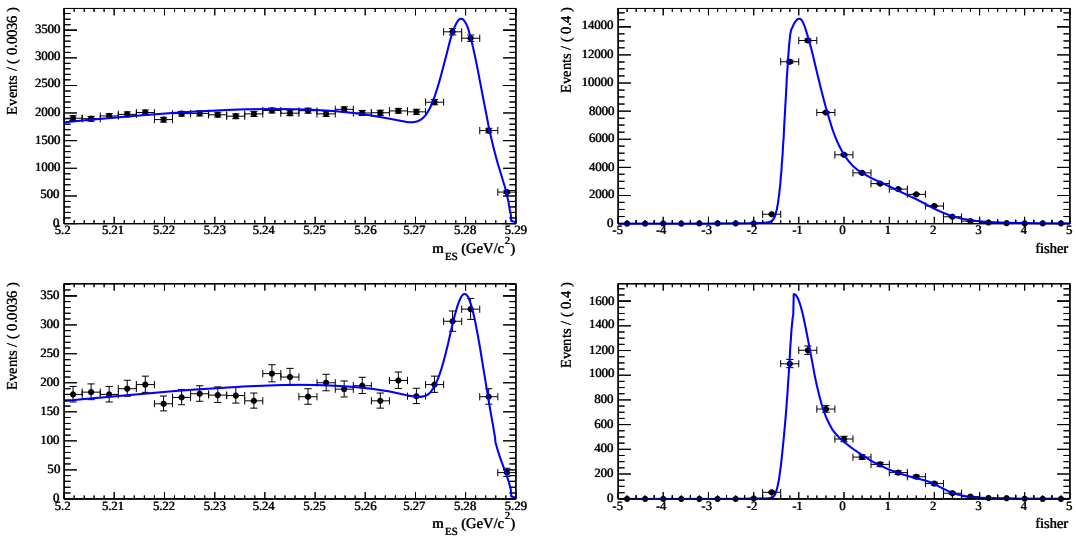

Figure 7.26: [The $\overline{B}^0 \to D^+\rho^-$ mode] Projections of the 2D likelihood to the $m_{\rm ES}$ (left) and Fisher (right). The fit is performed on the $D\rho_{K\pi\pi}$ (top), $D\rho_{K^0_S\pi}$ (bottom).

7.7.3 Systematic Error Evaluation

The systematic uncertainties on the fitted values for $\mathcal{B}$ can arise from the following sources:

- *The number of $B\overline{B}$ pairs* which was produced in the sample. This uncertainty is fixed to be 1.1% (according to the information from BbkLumi).

- *The uncertainty on the PDF parameterization.* All the parameters fixed in the fit are taken randomly from Gaussian distribution considering the correlations between different parameters then the new fit of a sample is performed. The operation is repeated 1000 times. The most probable values of the distributions are found corresponding to the central values for all parameters. The limits of 68% range obtained by integrating the distribution starting from the most probable value are taken to be the systematic error on the determination of N_{sig} (and BR).

- *Peaking background arising from $B\bar{B}$ events and charmless peaking background.* The number of peaking background events has been evaluated on simulated events. The different sources of identified peaking backgrounds were searched by scanning the generic MC sample after having all the selection criteria applied. The number of events coming from all identified sources is summed and fixed in the final fit (different depending on the channel). The error on determination of N_{peak} is coming from statistics and BR determination. The uncertainty in peaking is evaluated in the similar way we did for the uncertainty on the PDF shape. This uncertainty appeared to be very small. We assume that the uncertainty from the charmless peaking background does not exceed this magnitude.

- *The branching fraction of the D, K^0_S, K^{*0} mesons decays.* This source of systematic uncertainty is evaluated according to the errors of branching fractions taken from PDG 2008 [77].

- *The efficiency determination.* The error in this determination comes from two sources:

  - Uncertainty due to the limited signal Monte Carlo statistics used for the estimation of the reconstruction efficiency. The errors on $\epsilon_{\rm sig}$ are given in Tables 7.8 and 7.9.

  - Uncertainty on the reconstruction efficiency for charged tracks (1.3%), on the identification efficiency for a kaon (2%), K^0_S (1%) and π^0 (5%). In addition there could be an extra contribution to this uncertainty coming from the disagreement between data and MC distributions for all the variables used on the selection. The uncertainty on these variables have been obtained by comparing the distributions of events coming from MC for $B^+ \to D^+ K^0_S$ ($B^+ \to D^+ K^{*0}$) and data for $\overline{B}^0 \to D^+ \pi^+$ ($\overline{B}^0 \to D^+ \rho^-$)

Observable	smearing
M_D	2 MeV
ΔE	3 MeV
$M_{K^0_S}$	1 MeV
M_{K^*}	1 MeV
$\cos(\Theta_{B^+})$	0.01
M_{π^0}	1 MeV
P_{π^0}	5 MeV/c
E_{π^0}	1 MeV
$cos\Theta^{\rm H}_{K^{*0}}$	0.01
$\alpha_{K^0_S}$	10^{-9}

Table 7.19: The magnitude of smearing of observables.

applying the following selection criteria: $m_{\rm ES} > 5.27$ GeV/c^2 and $\mathcal{F} > 2$ to reduce to the background to a negligible level. To make the data and MC sample distributions agreeing the MC distributions are smeared by a Gaussian distribution. The width of this distributions is given in Table 7.19.

We perform the selection with the new smeared distribution and we always found variations of the efficiency of less then 4%. We decide to take an extra 4% uncertainty to be attributed to the data/MC agreement for the variables used in the selection criteria.

- *Data-MC difference.* We consider here the data/MC difference coming from the shape of the $m_{\rm ES}$ and *Fisher* for signal and background events.

  - *Continuum background.* We estimate this uncertainty using in the fit the PDF parameters obtained from off-peak data instead of the ones from continuum MC. In order to have enough statistics to fit the pdf we relax the cuts used for off-peak selection to a level of preselection. We verified on MC that the fitted parameters obtained with cuts at the preselection and final level are the same. The obtained difference gives the error on N_{sig} and corresponding BR.
  - $B\overline{B}$ *background.* We estimate this uncertainty leaving free in the fit all the parameters describing $B\bar{B}$ background. The corresponding difference gives the error on N_{sig} and subsequently to BR.
  - *Signal.* We use the sample of $B^0 \to D^-\pi^+$ and $B^+ \to D^+\rho^0$ to obtain from data the parameters for the signal PDFs respectively for $B^+ \to D^+K^0_S$ and $B^+ \to D^+K^{*0}$ as described in Section 7.7.2. Then we redo the fit with these parameters instead of those obtained from the MC signal. The corresponding difference in the N_{sig} obtained and

subsequently on BR is taken as a systematics error. We attribute this systematics error to the Data/MC difference on the PDF shape parameters. A detailed description of the analysis we performed on the control samples is given above.

The systematic uncertainties on the branching fractions are summarized in Table 7.20. All the uncertainties are considered to be uncorrelated and are treated separately for each channel.

7.7.4 Final Results

	$B^+ \to D^+ K^0$				$B^+ \to D^+ K^{*0}$	
	$K\pi\pi$	$K\pi\pi\pi^0$	$K^0_S\pi$	$K^0_S\pi\pi^0$	$K\pi\pi$	$K^0_S\pi$
PDF - MC	$^{+0.8}_{-0.8}$	$^{+6.2}_{-3.4}$	$^{+5.3}_{-4.4}$	$^{+7.3}_{-8.8}$	$^{+0.6}_{-0.9}$	$^{+3.1}_{-3.6}$
Peaking background	< 0.05	0.5	0.2	0.2	< 0.05	0.1
$\mathcal{B}$ errors	0.3	0.3	< 0.05	0.4	< 0.05	0.1
Data-MC PDF shapes:						
Continuum background	0.2	0.4	1.4	0.5	0.1	1.7
$B\overline{B}$ background	0.7	1.6	2.5	5.0	1.0	4.4
Signal	< 0.05	9.2	5.6	0.9	0.9	3.1
Efficiency error:						
Reconstruction efficiency (MC)	0.1	0.6	< 0.05	0.9	0.1	0.5
Data-MC	0.2	0.8	< 0.05	0.5	0.2	0.3
Combined	$^{+1.1}_{-1.3}$	$^{+11.3}_{-11.8}$	$^{+8.2}_{-9.3}$	$^{+9.0}_{-12.5}$	$^{+1.5}_{-1.8}$	$^{+6.4}_{-7.4}$

Table 7.20: Systematic errors on branching fractions for $B^+ \to D^+ K^0$ and $B^+ \to D^+ K^*$ decay channels. All quantities are given in units of 10^{-6}.

The final likelihood for each decay mode is obtained by convolving the likelihoods for the measured branching fractions with a Gaussian of width equal to the systematic uncertainty.

The final results including the total systematic uncertainty are

$$\begin{aligned} \mathcal{B}(B^+ \to D^+ K^0) &= (-3.8^{+2.5}_{-2.4}) \times 10^{-6}, \\ \mathcal{B}(B^+ \to D^+ K^{*0}) &= (-5.3 \pm 2.7) \times 10^{-6}. \end{aligned} \tag{7.8}$$

The corresponding likelihoods are shown in Figure 7.27.

Since the measurements for the branching fractions are not statistically significant, following a Bayesian approach and assuming a flat prior distribution for the branching fractions, we

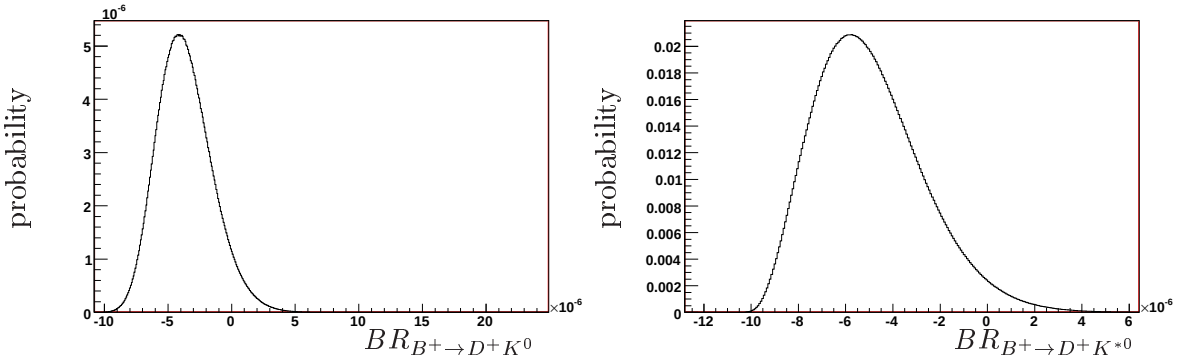

Figure 7.27: 1D likelihood for BR obtained from the fit to the data sample of 426 fb^{-1} for $B^+ \to D^+K^0$ (left) and $B^+ \to D^+K^{*0}$ (right).

integrate over the positive portion of the likelihood function to obtain the following upper limits at 90% probability:

$$\mathcal{B}(B^+ \to D^+K^0) < 2.9 \times 10^{-6},$$
$$\mathcal{B}(B^+ \to D^+K^{*0}) < 3.0 \times 10^{-6}.$$

The corresponding plots are shown in Figure 7.28. The limit on $\mathcal{B}(B^+ \to D^+K^0)$ updates the previous measurement [91]. The main improvements are coming from the updated strategy of the analysis (introduction of additional D^+ decay channel, likelihood fit technique) and the updated dataset.

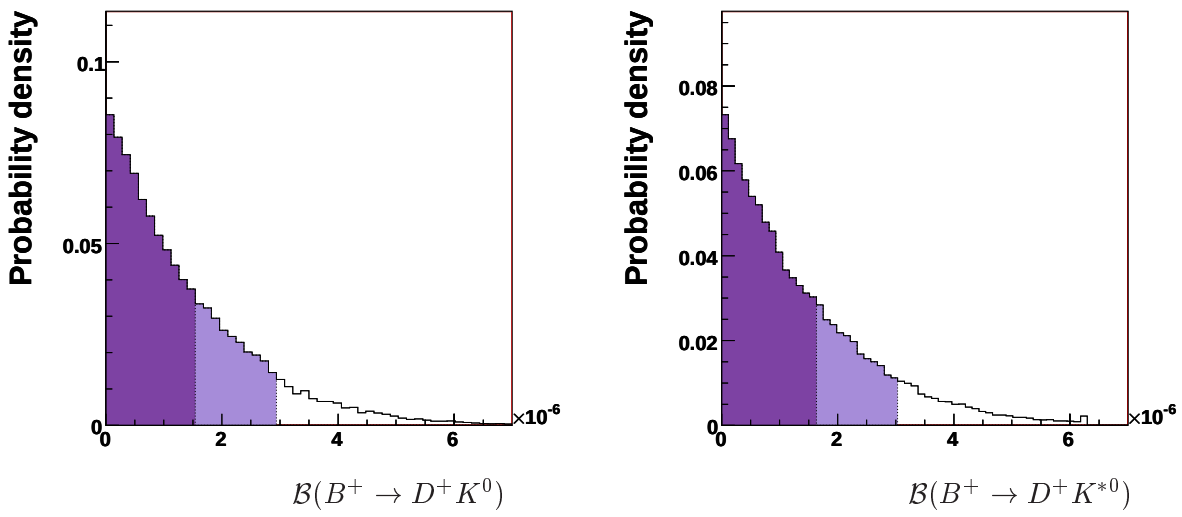

Figure 7.28: The limits obtained for the branching fractions of $B^+ \to D^+ K^0$ (left) and $B^+ \to D^+ K^{*0}$ (right). Dark (light) color corresponds to 68% (90%) probability region.

Chapter 8

The Search for the $b \to u$ transition in $B^+ \to D^0 K^+$ with $D^0 \to K^+\pi^-\pi^0$

In this Chapter, the analysis of the $B^+ \to D^0 K^+$ ($D^0 \to K^+\pi^-\pi^0$) channel is described. The channel is studied through the ADS method. The measurements of $R_{\rm ADS}$, $A_{\rm ADS}$, R^+, and R^- and the subsequent extraction of the parameters $r_{\rm B}$, γ, and $\delta_{\rm B}$ are presented. This analysis is performed on 428 fb^{-1} (471×10^6 $B\overline{B}$ pairs) of data collected with the *BABAR* detector, corresponding to the full data sample recorded at $\Upsilon(4S)$ center-of-mass energy.

8.1 Introduction to Analysis

8.1.1 Motivation

The ADS analysis is particularly suited to determine the ratio $r_{\rm B}$ (as discussed in Chapter 3). The precise knowledge of this ratio serves in improving the determination of γ from more precise method as the GGSZ analysis.

The most precise results for the $r_{\rm B}$ ratio can be obtained from the combination of different D decay channels. In this Chapter, we present the analysis using the $D^0 \to K^+\pi^-\pi^0$ decay channel. The analysis using the $D^0 \to K^+\pi^-$ decay channel was also performed by *BABAR* and published [64].

8.1.2 Previous Results on the $B^+ \to D^0 K^+$ with $D^0 \to K^+\pi^-\pi^0$ analysis

The *BABAR* experiment has published the first search for $b \to u$ transitions in $B^+ \to D^0 K^+$, with $D^0 \to K^\pm\pi^\mp\pi^0$ in [97]. This analysis had been performed on 205 fb^{-1} of on-resonance

data and had measured

$$R_{\rm ADS} = (12 \pm 12 \pm 9) \times 10^{-2}, \tag{8.1}$$

with $R_{\rm ADS}$ defined as the ratio between events with final state $K^-\pi^+\pi^0{}_D K^+$ and $K^+\pi^-\pi^0{}_D K^+$ (as described in Section 3).

The analysis presented in this thesis updates the previous one with improvement expected from the larger data sets used, new data selection criteria, and fit procedure, which are described in the following.

8.2 Selection and Background Characterization

8.2.1 Data Samples

In this analysis two decay modes are reconstructed:

- $B^- \to \overline{D}^0 K^-$, $\overline{D}^0 \to K^+\pi^-\pi^0$, which we call opposite sign signal mode (because kaons in the final state have opposite electric charge). The associated background will be named opposite sign background. The events composing the opposite sign sample come both from $b \to u$ and $b \to c$ mediated transition (see Chapter 3).
- $B^- \to D^0 K^-$, $D^0 \to K^-\pi^+\pi^0$, which we call same sign signal mode (because kaons in the final state have the same electric charge). The associated background will be named same sign background. The events in this sample are mainly coming from $b \to c$ mediated transitions followed by the CA D^0 decay (see Chapter 3).

In Table 8.1 the amount of data and MC used for the analysis, their cross sections, and equivalent luminosities are shown. Runs 1-6 of on-resonance data corresponding to 428 fb^{-1} and off-resonance data with approximate luminosity of 44.4 fb^{-1} are used.

8.2.2 Preselection Criteria

We use the following selection criteria:

- $E_\gamma > 70$ MeV (preselection on energy of photon candidates);
- $E_{\pi^0} > 200$ MeV (preselection on energy of π^0 candidates);
- $|M_{\pi^0} - M_{\pi^0,PDG}| < 0.03$ GeV/c^2 (preselection on mass of π^0 candidates);

Sample	Number of Events	Cross Section	Equivalent luminosity
On-resonance data	-	-	428 fb^{-1}
Off-resonance data	-	-	44.4 fb^{-1}
same sign signal	139K	61.5 fb	2.3 ab^{-1}
opposite sign signal	159K	0.9 fb	176 ab^{-1}
Generic B^+B^-	717M	0.55 nb	1305 fb^{-1}
Generic $B^0\overline{B}^0$	708M	0.55 nb	1289 fb^{-1}
Generic $c\overline{c}$	1128M	1.30 nb	868 fb^{-1}
Generic uds	1631M	2.09 nb	780 fb^{-1}

Table 8.1: Data and MC samples used for the analysis in terms of equivalent integrated luminosity and number of events. The luminosity of an opposite sign signal MC sample is estimated using $r_{\text{B}} = 0.1$ [17].

- $|M_{D^0} - M_{D^0,PDG}| < 0.04$ GeV/c^2 (preselection on mass of D^0's, the RMS for the D^0 mass distribution is of 0.016 GeV/c^2 for the signal mode);
- $|\Delta E| < 0.1$ GeV (the value of RMS for this variable is of 21 MeV for the signal mode);
- $m_{\text{ES}} > 5.2$ GeV/c^2 (with a shift of 20 MeV/c^2 for off-resonance data);
- $|p_\pi| > 0.15$ GeV/c (preselection on momentum of π^+ candidates);
- $|p_{\pi^0}| > 0.2$ GeV/c (preselection on momentum of π^0 candidates);
- $|p_K| > 0.2$ GeV/c (preselection on momentum of K^+ candidates);
- $|\Delta t| < 10$ ps (preselection on proper time difference calculated from the difference between the decay vertex z coordinates of the two B mesons in the event).

In the following, we refer to all selection criteria mentioned above as "preselection criteria". The D^0 masses are constrained to the PDG values [77] for the final B^+ fit.

8.2.3 Selection Criteria

The preselection criteria are followed by an optimization procedure which is applied on the remaining events. For the optimization procedure we use the criterion of maximizing the significance, given by the ratio $S = \frac{N_S}{\sqrt{N_S+N_B}}$, where N_S (N_B) is the number of signal (background) events in the opposite sign sample. The optimization is performed in the $m_{\text{ES}} > 5.27$ GeV/c^2 mass region (this is done in order to have the correct estimation of background contaminating the signal mass region). The same sign events are selected using a similar procedure.

All the numbers are rescaled to the data luminosity of 428 fb^{-1}. In order to estimate the signal MC sample luminosities, the branching fractions are taken from the PDG 2008 [77], CLEO-c collaboration [59], and the latest results of UTFit collaboration [17] In particular, we use $r_{\text{B}} = (0.10 \pm 0.02)$ and $r_{\text{D}} = (0.047 \pm 0.003)$.

Variables included in the selection criteria are summarized below:

- $|\Delta E|$: the beam-energy difference.
- M_{π^0}: the unconstrained mass of the π^0 from the D^0 decay products.
- δM: the difference between the fitted masses of D^0 mesons and π^0 mesons. The reason of using this cut is to take into account the correlation between the D^0 and π^0 masses for signal events (see Figure 8.1).

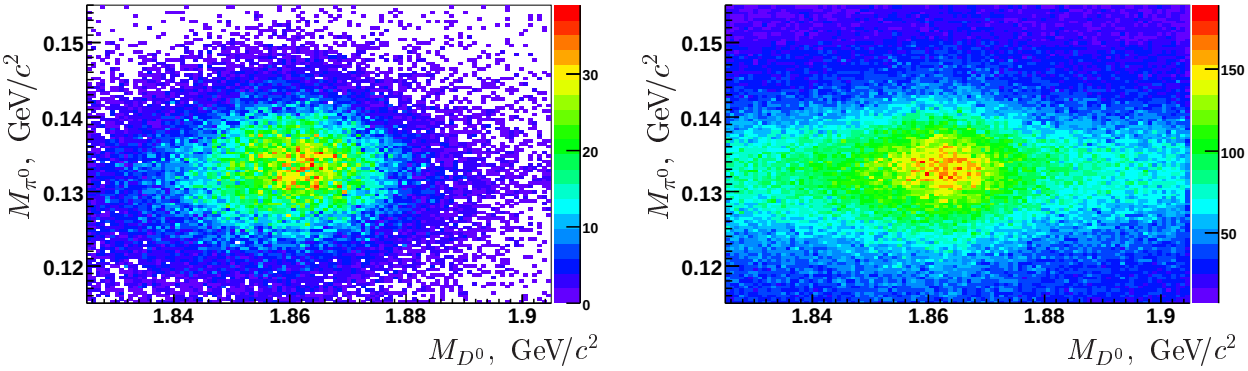

Figure 8.1: The distribution of the D^0 meson mass vs the π^0 meson mass for the opposite sign signal events (left) and $c\bar{c}$ opposite sign background (right) events.

- $\cos(\theta^B_{CM})$. The cosine of the polar angle of the B meson with respect to the beam axis (z) in the $\Upsilon(4S)$ center of mass frame.

Figure 8.2 shows the variation of the ratio S as a function of the cut on the variables: $|\Delta E|$, $|\delta M - \delta M_{\text{PDG}}|$, M_{π^0} and $\cos(\theta^B_{CM})$. The optimum cut corresponds to the value which maximizes S. We thus choose:

- $|\Delta E| < 23 MeV$.
- 0.119 GeV/c^2 $< M_{\pi^0} <$ 0.146 GeV/c^2.
- $|\delta M - \delta M_{PDG}| <$ 0.024 Gev/c^2.

- $|\cos\Theta^B_{cm}`| < 0.8$.

The distributions of the different components (signal and background) for these variables are shown in Figure 8.3.

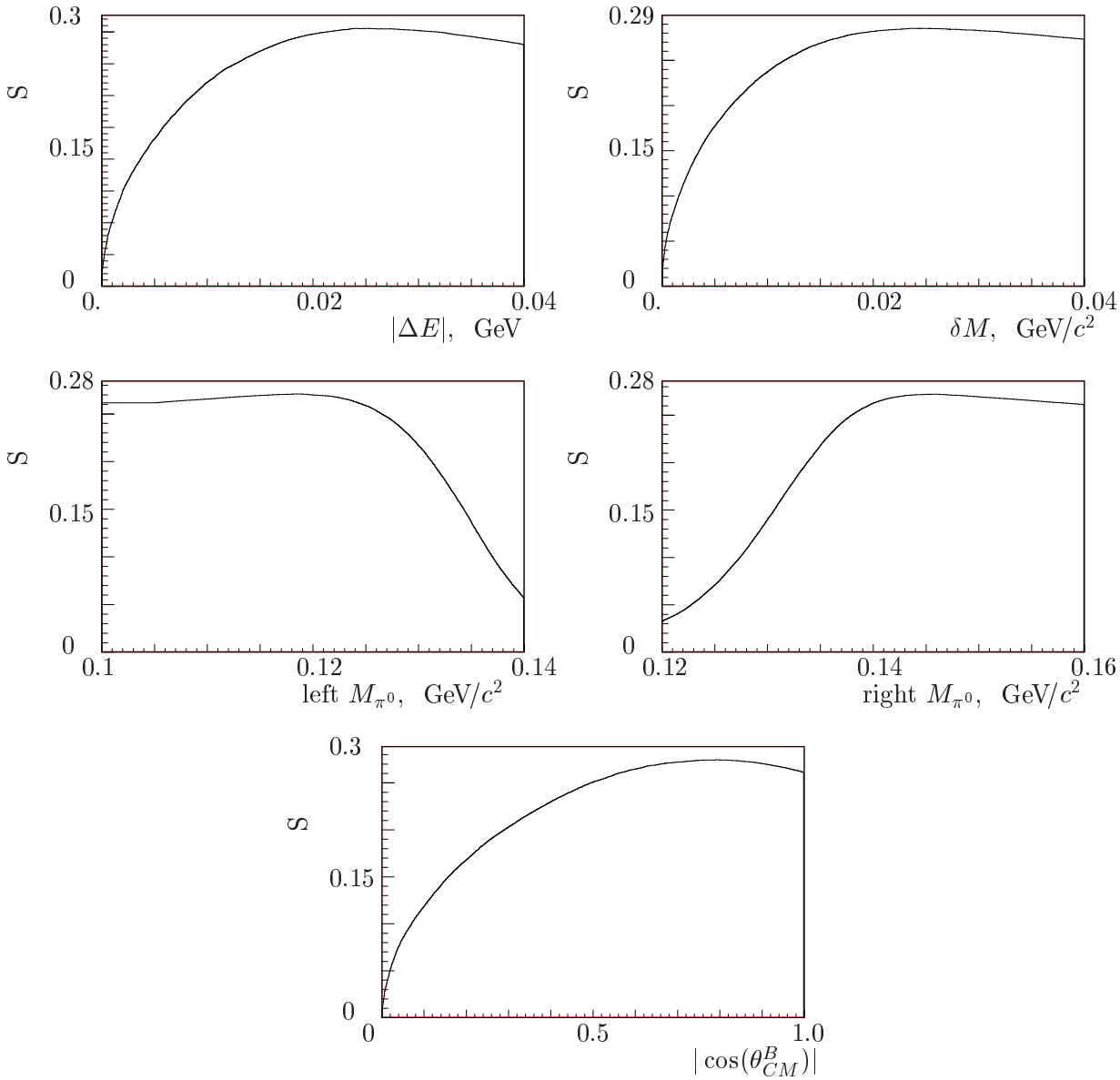

Figure 8.2: $S = \frac{N_S}{\sqrt{N_S+N_B}}$ as a function of the applied cut for $|\Delta E|$ (upper left), $|\delta M_D - \delta M_{\mathrm{PDG},D}|$ (upper right), M_{π^0} (lower cut) (middle left), M_{π^0} (higher cut) (middle right), and $|\cos(\theta^B_{CM})|$ (bottom). The smooth curve curve is the result of fine binning.

For the kaons coming from the B decay (named in the following "bachelor") and the kaon

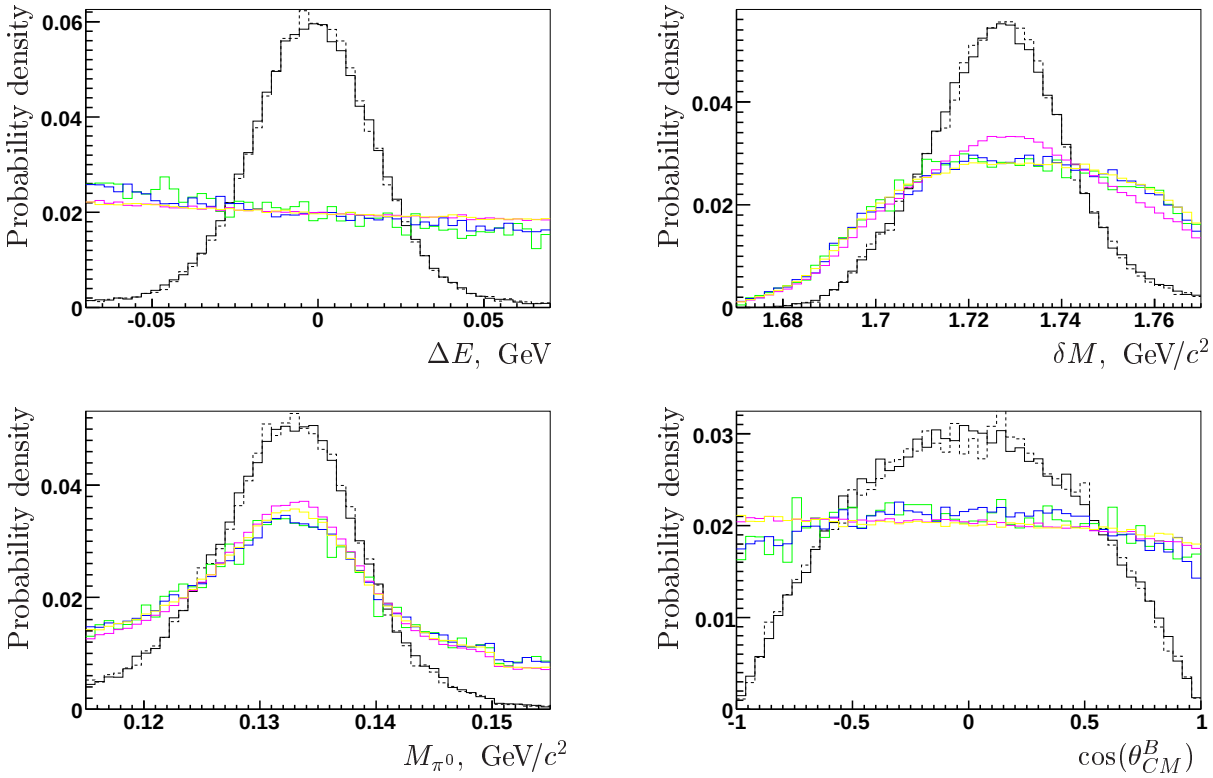

Figure 8.3: Distributions of ΔE (upper left), δM (upper right), M_{π^0} (bottom left), $\cos(\theta^B_{CM})$ (bottom right). The different components are indicated with different colors: $c\overline{c}$ (magenta), *uds* (yellow), $B^0\overline{B}^0$ (blue), B^+B^- (green), and signal (black). For signal opposite (same) sign distributions are shown with solid (dashed) lines.

from the D^0 decay we ask for a "tight" PID selection (see Chapter 6). This condition was introduced in order to distinguish the $B^+ \to D^0 K^+$ from the $B^+ \to D^0 \pi^+$ decay.

In Tables 8.2 and 8.3 we show the expected number of events for signal and different background categories and the value of significance S.

8.2.4 Peaking Background Studies

A special attention has been devoted to a possible source of peaking background within the $B\overline{B}$ background. Peaking background consists of processes leading to the same final state as for reconstructed signal. The $m_{\rm ES}$ and $\mathcal{F}$ (described below) distributions of these events are similar to those of the reconstructed signal.

The search for the peaking background is performed separately for same sign and opposite

	Selection criteria	opposite sign sample					
		signal	B^+B^-	B^0B^0	$c\bar{c}$	uds	S
1	preselection	79.2	13690	4763	304385	256273	0.10
2	$\lvert\Delta E\rvert < 23$ MeV	60.2	3429	1198	75923	63291	0.16
3	0.119 GeV/c^2 $< M_{\pi^0} <$ 0.146 GeV/c^2	56.5	2331	811	55274	45442	0.17
4	$\lvert\delta M - \delta M_{PDG}\rvert < 0.024$ Gev/c^2	49.6	1416	505	36537	27557	0.19
5	$\lvert\cos\Theta_{B_{cm}}\rvert < 0.8$	46.8	1177	413	29520	22178	0.20
6	K very tight	31.9	369	99	14712	6506	0.21
7	$\lvert M_{K^+K^-} - M_{PDG}\rvert > 20$ MeV/c^2	31.7	337	93	14592	6440	0.20
8	$m_{ES} > 5.27$ GeV/c^2	31.7	57	20	2006	1005	0.42
9	$Fisher > 0$	26.9	46	18	442	165	0.51

Table 8.2: [Opposite sign sample.] Cuts are optimized against background opposite sign MC events (lines 2-6). The last two cuts are given for illustration purposes only (see the discussion in the following sections).

	Selection criteria	same sign sample						
		signal	B^+B^-	B^0B^0	$c\bar{c}$	uds	$D\pi$	S
1	preselection	6190	22949	8180	206176	195072	16349	9
2	$\lvert\Delta E\rvert < 23MeV$	4720	5396	2015	51711	48243	3579	14
3	0.119 GeV/c^2 $< M_{\pi^0} <$ 0.146 GeV/c^2	4427	3646	1380	36832	34716	2850	15
4	$\lvert\delta M - \delta M_{PDG}\rvert < 0.024$ Gev/c^2	3895	2294	844	23621	21060	2266	17
5	$\lvert\cos\Theta_{B_{cm}}\rvert < 0.8$	3679	1933	698	19076	16884	2103	17
6	K tight	2500	340	121	4322	3146	176	24
7	$\lvert M_{K^+K^-} - M_{PDG}\rvert > 20$ MeV/c^2	2485	339	120	4303	3101	176	24
8	$m_{ES} > 5.27$ GeV/c^2	2482	134	44	582	451	159	40
9	$Fisher > 0$	2120	110	37	124	79	130	42

Table 8.3: [Same sign sample.] Cuts are optimized against background opposite sign MC events (lines 2-6). The last two cuts are given for illustration purposes only (see the discussion in the following sections)

sign events by scanning 1.3 ab^{-1} of the generic $B\overline{B}$ MC sample after final selection. Finally, we found a single peaking background contribution for same sign events associated to the $B^+ \to \overline{D}^0\pi^+$ with $\overline{D}^0 \to K^+\pi^-\pi^0$ decay modes ($D\pi$ in the following). For this channel π^+ coming from the B^+ meson is misidentified as K^+. We treat these events as a separate category in the fit.

We generate additional simulated events for this identified channel. The $m_{\rm ES}$ distribution for these events is shown in Figure 8.4.

Even if it has not been found by scanning procedure the $B^+ \to D^0\rho^+$ with $D^0 \to K^+K^-$

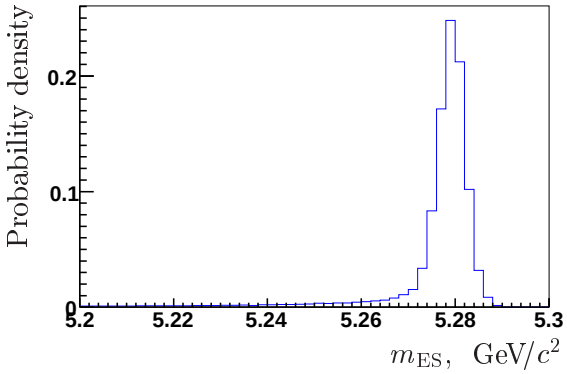

Figure 8.4: $m_{\rm ES}$ distribution for the $B^+ \to \overline{D}^0\pi^+$ events reconstructed in the same sign sample.

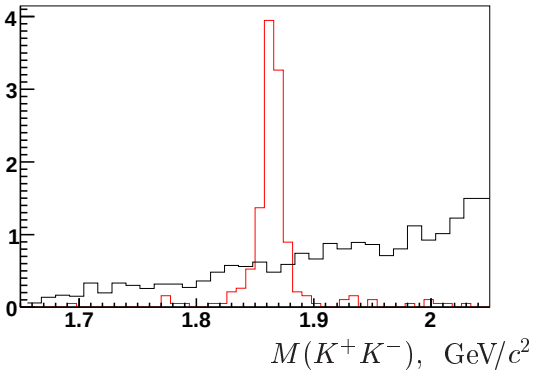

Figure 8.5: Invariant mass of K^+K^- for MC sample $B^+ \to D^0\rho^+$ with $D^0 \to K^+K^-$ normalized to the number of events expected (red histogram) and opposite sign signal events (black histogram) normalized to 10 times signal events yield.

decay mode can be a potential peaking background contributing to the opposite sign sample. The branching fraction of the process is approximately of 6×10^{-5}. Figure 8.5 shows the K^+K^- invariant mass ($M(K^+K^-)$) for the signal and $B^+ \to D^0\rho^+$ with $D^0 \to K^+K^-$ events. The last one clearly shows a peak at the D^0 mass. We request the following selection criteria: $|M(K^+K^-) - M_{D^0,PDG}| > 20$ MeV/c^2. The $m_{\rm ES}$ distributions for these events after preselection, selection cuts (but $M(K^+K^-)$) and adding this last are shown in Figure 8.6.

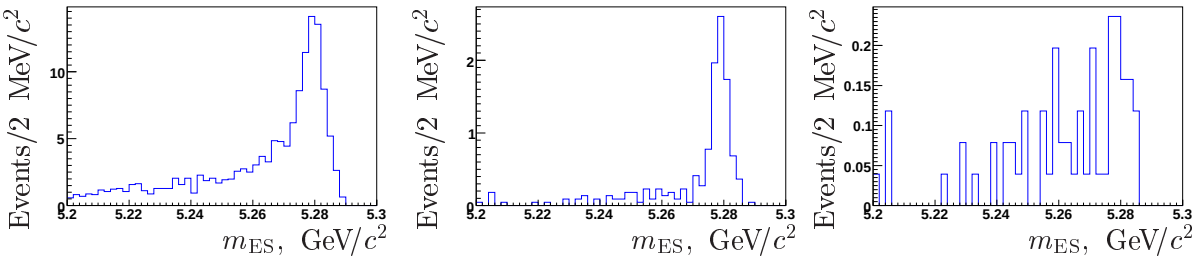

Figure 8.6: The $m_{\rm ES}$ distributions for $B^+ \to D^0\rho^+$ with $D^0 \to K^+K^-$ events after preselection (left), selection criteria (but $M(K^+K^-)$, central) and adding this last selection criterium (right).

The final sample contains 2.6 ± 0.1 events. The shape of the $m_{\rm ES}$ distribution shows that these events can be included in the generic $B\overline{B}$ background.

	opposite sign	same sign
events passing selection	20221	13260
of events with more than one candidate	226	179
misidentified events	94	94

Table 8.4: Number of simulated events with $m_{\rm ES} > 5.27$ GeV/c^2 for opposite sign and same sign sample passing all selection criteria, with multiple B candidates, and for which the incorrect B candidate was selected.

8.2.5 The Best Candidate Choice

In the case in which we have, after all the selection cuts, more than one B candidate in the same event, we choose the one that minimizes the quantity:

$$\chi^2(M_{D^0}) = \frac{(M_{D^0} - M_{D^0,PDG})^2}{\sigma^2_{D^0}}$$

where σ_{D^0} is the experimental resolution on Monte Carlo signal events for the reconstructed channel. In case the candidates have the same D^0 mass we choose the candidate with ΔE closest to zero.

The amount of events with multiple candidates after all the selection criteria (before the best candidate choice) as well as number of events where the wrong B candidate is selected are shown in Table 8.4.

8.2.6 Continuum Background Rejection

After applying all the selection criteria the most numerous background comes from the continuum events (see Tables 8.2 and 8.3). The Fisher discriminant (described in Section 6.6), $\mathcal{F}$, is constructed as a linear combination of observables with coefficients that are fitted to give the best discrimination between signal and continuum events. Six variables are included $|cos(\theta_{\rm thrust})|$, L_{10}, L_{12}, DOCA, $|\Delta t|$, and the distance between B and D vertices ($(B-D)_{dist}$), as discussed in Section 6.6.

The Fisher discriminant is constructed with signal and $q\overline{q}$ opposite sign MC events. The distributions of these variables are shown in Figures 8.7 and 8.8. In these Figures we also show the comparison between the off-resonance data and the MC for the continuum ($q\overline{q}$) events.

The Fisher discriminant used in the following is constructed as

$$\mathcal{F} = 0.56 + 0.14 \cdot L_{10} - 0.64 \cdot L_{12} + 0.1 \cdot |\Delta t| + 0.12 \cdot |\cos(\theta_{\rm thrust})| - 0.05 \cdot DOCA - 0.75 \cdot (B-D)_{dist}. \quad (8.2)$$

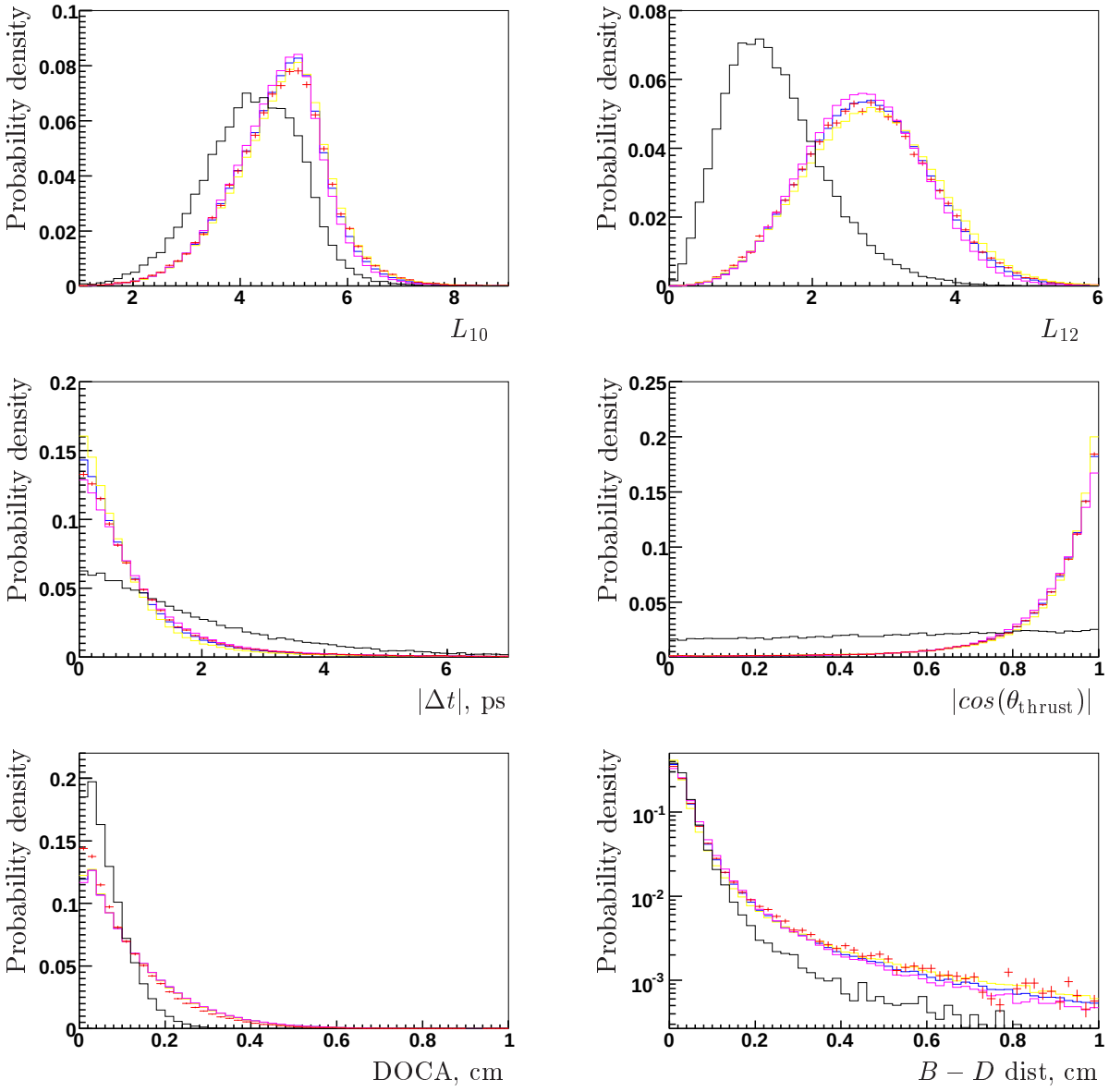

Figure 8.7: Distribution for *uds* MC (yellow), $c\bar{c}$ MC (magenta), a weighted sum of the two (blue), off-resonance data (red dots with errors), and signal (black) same sign events for the variables chosen to construct the Fisher discriminant. The variables are L_{10} (top left), L_{12} (top right), $|\Delta t|$ (middle left) $|\cos(\theta_{\rm thrust})|$ (middle right), DOCA (bottom left), and the distance between B and D vertices (bottom right).

The Fisher discriminant distributions for signal and continuum background events are shown in Figure 8.9.

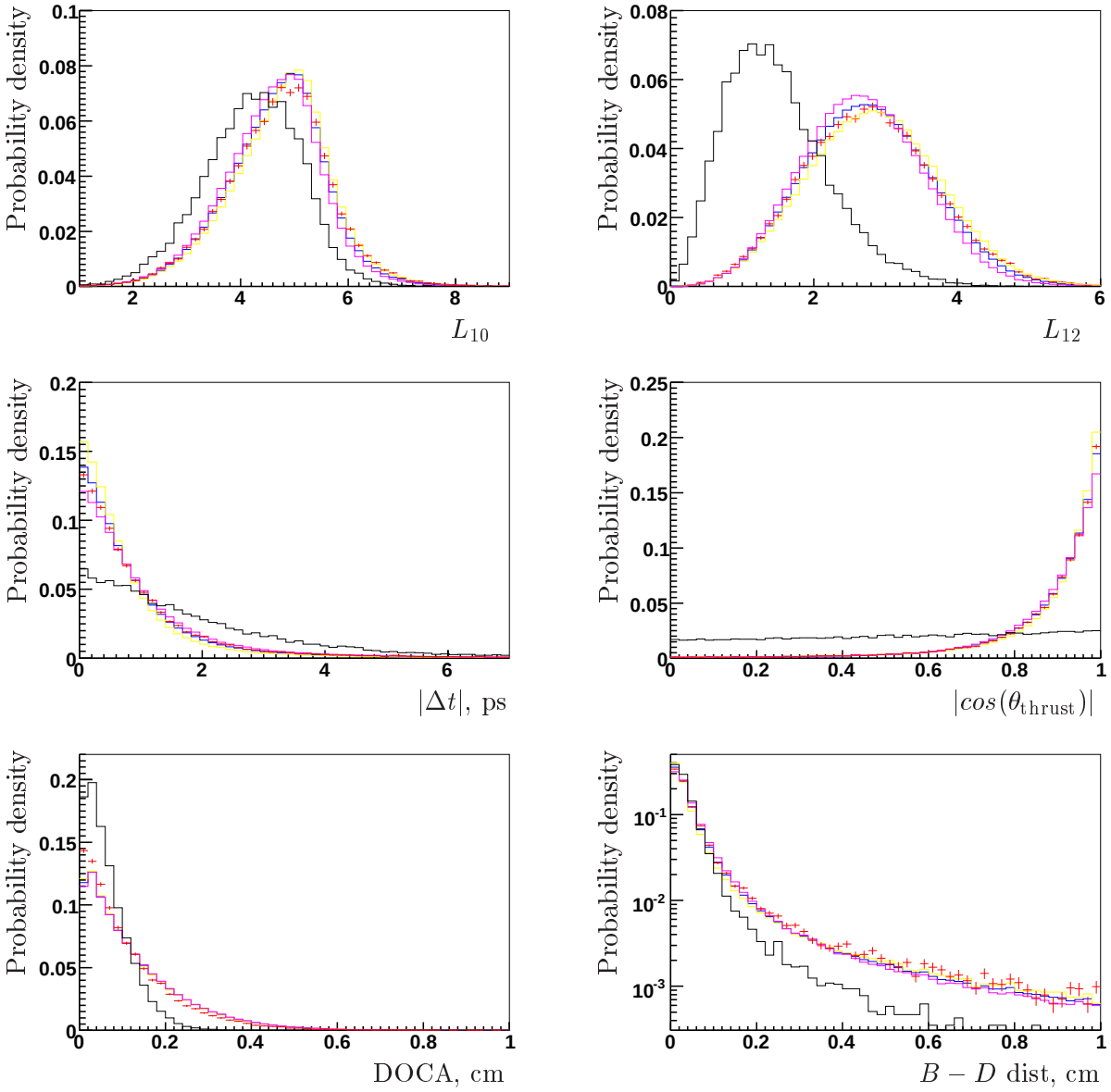

Figure 8.8: Distributions for *uds* MC (yellow), $c\bar{c}$ MC (magenta), a weighted sum of the two (blue), off-resonance data (red dots with errors) and signal (back) same sign events for the variables chosen to construct the Fisher discriminant The variables are L_{10} (top left), L_{12} (top right), $|\Delta t|$ (middle left) $|\cos(\theta_{\rm thrust})|$ (middle right), DOCA (bottom left), and the distance between B and D vertices (bottom right).

8.2.7 Crossfeed between Same Sign and Opposite Sign Events

The efficiency of reconstructing a same sign event as an opposite sign one (by exchanging the charged kaon with a charged pion in the final state for the D decay) has been checked on

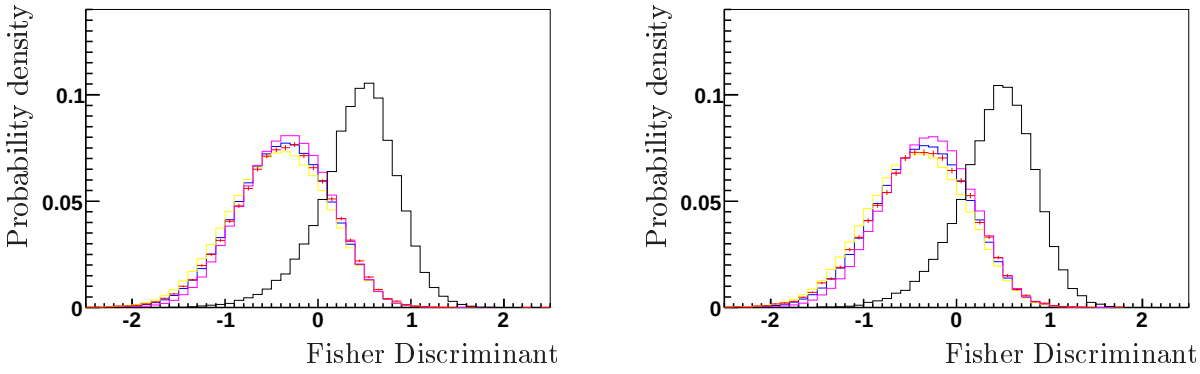

Figure 8.9: The $\mathcal{F}$ discriminant distribution for uds MC (yellow), $c\bar{c}$ MC (magenta), a weighted sum of the two (blue) and off-resonance data (red dots with errors) and signal (black) events. Left (right) plot shows the distributions for opposite (same) sign events.

simulated events. These are called cross-feed event with the associated crossfeed efficiency. Table 8.5 shows the reconstruction efficiency of the crossfeed selection.

	Cut name	Number of cross-feed events	cross-feed efficiency, 10^{-5}
1	preselection	37.77	145
2	$\|\Delta E\| < 23 MeV$	16.35	63
3	$0.119\ \text{GeV}/c^2 < M_{\pi^0} < 0.146\ \text{GeV}/c^2$	12.78	49
4	$\|\delta M - \delta M_{PDG}\| < 0.024\ \text{GeV}/c^2$	7.89	30
5	$\|\cos\Theta_{B_{cm}}\| < 0.8$	7.52	29
6	K tight	1.50	6
7	$\|M_{K^+K^-} - M_{PDG}\| > 20\ \text{MeV}/c^2$	1.47	6
8	$m_{\text{ES}} > 5.27\ \text{GeV}/c^2$	0.54	2
9	$Fisher > 0$	0.54	2

Table 8.5: The crossfeed efficiency and the associated number of the same sign MC events reconstructed as opposite sign events.

The crossfeed efficiency is extremely low ($\epsilon_{CF} = 2 \cdot 10^{-5}$) and only 0.5 ± 0.3 events are left in the final sample. The contribution of crossfeed events is taken into account in the systematic error evaluation.

8.2.8 Opposite Sign to Same Sign Efficiency Ratio

The efficiencies for same sign and opposite sign modes are estimated using events generated with a flat Dalitz distribution for $D^0 \to K^+\pi^-\pi^0$ decay. However, the same sign sample is mainly

constituted of $b \to c$ transition events with the neutral D decaying through Cabibbo allowed mode, while the opposite sign sample is composed of $b \to c$ transition events with the neutral D decaying through doubly-Cabibbo-suppressed mode and $b \to u$ transition events with the neutral D decaying through Cabibbo-allowed mode. Due to the fact that the Cabibbo-allowed and doubly-Cabibbo-suppressed neutral D decays are kinematically different, and hence have different distributions over the Dalitz plane, the selection efficiencies in same sign and opposite sign samples could be different.

The simulated events are reweighted according to the Dalitz distribution of Cabibbo Allowed (CA) or Doubly Cabibbo Suppressed (DCS) events as obtained by *BABAR* [98]. The efficiencies of the selection criteria calculated on CA or DCS reweighted events have been found compatible to the one obtained with a flat Dalitz distribution within 3%. An uncertainty of 3% on the ratio of the efficiency of opposite sign and same sign events is used in the systematics.

8.2.9 Comparison between Data and Simulated Events

In Figure 8.10 we show the distributions for data and MC events for $m_{\rm ES}$ and $\mathcal{F}$ variables in the $m_{\rm ES} < 5.27$ GeV/c^2 region. We find some excess of simulated events.

8.3 Maximum Likelihood Fit

8.3.1 Structure of the Fit Model

To perform a fit to the yield and to the $R_{\rm ADS}$ we perform an extended maximum likelihood fit to the set of variables: $\{m_{\rm ES}, \mathcal{F}\}$. We write the extended likelihood $\mathcal{L}$ as:

$$\mathcal{L} = \frac{e^{-N'}}{N!} \cdot N'^{N} \cdot \prod_{j=1}^{N} f(\mathbf{x}_j \mid \theta, N') \,,$$
$$\text{with } f(\mathbf{x} \mid \theta, N') = \frac{1}{N'} \left(\frac{R_{\rm ADS} N_{sig,total}}{1+R_{\rm ADS}} f_{sig,os}(\mathbf{x}|\theta_{\mathbf{sig,os}}) + \right.$$
$$\left. + \frac{N_{sig,total}}{1+R_{\rm ADS}} f_{sig,ss}(\mathbf{x}|\theta_{\mathbf{sig,ss}}) + \sum_i N_{B_i} f_{B_i}(\mathbf{x}|\theta) \right) ;$$

where $f_{sig,ss}(\mathbf{x}|\theta_{\mathbf{sig,ss}})$, $f_{sig,os}(\mathbf{x}|\theta_{\mathbf{sig,os}})$ and $f_{B_i}(\mathbf{x}|\theta)$ are the probability density functions (PDFs) of the hypothesis that the event is a same sign (opposite) sign signal or a background event (B_i are the different background categories used in the fit), respectively, N is the number of events in the selected sample, N' is the expectation value for the total number of events. The variables are indicated by the vector $\mathbf{x}$ and θ indicates a set of parameters. $N_{sig,total}$ is the total number of signal events, $R_{\rm ADS} = \frac{N_{sig,os}}{N_{sig,ss}}$, N_{B_i} is the total number of each background species events. For the opposite sign events the background comes from continuum and $B\overline{B}$. In addition to

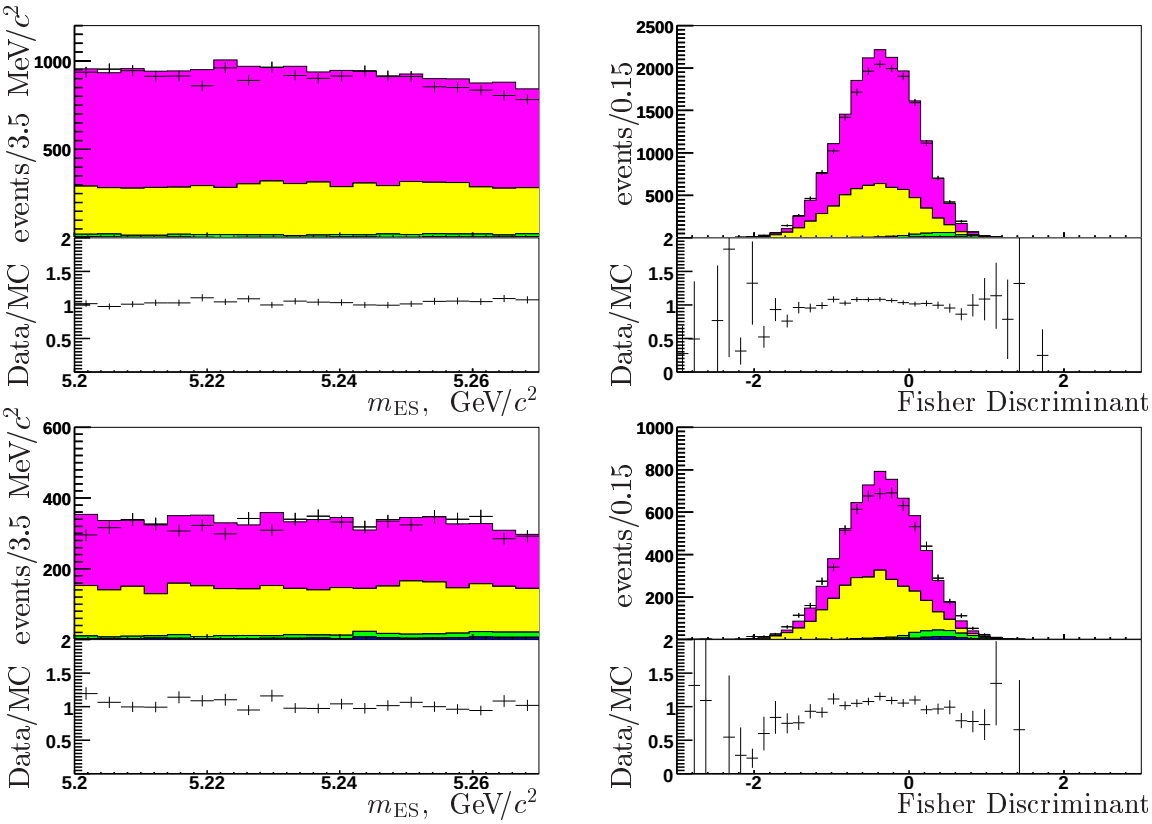

Figure 8.10: Data-MC comparison of the $m_{\rm ES}$ distribution (for $m_{\rm ES} < 5.27$ GeV/c^2), and Fisher for opposite sign (top row) and same sign (lower row) event sample. All the distributions are rescaled to the data luminosity (428 fb^{-1}). The black histogram represents the signal, blue, green, yellow and magenta show the B^+B^-, $B^0\bar{B}^0$, uds and $c\bar{c}$ background events, respectively. Dots with error bars are experimental data.

this, peaking backgrounds have to be considered when fitting the same sign events. Since the correlations among the variables are negligible, we write the PDF as the product of the 1-dimensional PDFs for the single variables. We use predefined forms of PDF in order to fit the variable distributions: Gaussian, asymmetric Gaussian, their combination, threshold [95] and Crystal ball (CB) functions [96]. The threshold function and the CB functions are defined in Chapter 6.

In case of the fit to the yields and to $R^\pm$ we use similar likelihood with

$$f^\pm(\mathbf{x} \mid \theta, N') = \frac{1}{N'} \left(\frac{R^\pm N^\pm_{sig,total}}{1+R^\pm} f^\pm_{sig,os}(\mathbf{x}|\theta_{\mathbf{sig,os}}) + \right. \\ \left. + \frac{N^\pm_{sig,total}}{1+R^\pm} f^\pm_{sig,ss}(\mathbf{x}|\theta_{\mathbf{sig,ss}}) + \sum_i N^\pm_{B_i} f^\pm_{B_i}(\mathbf{x}|\theta) \right), \tag{8.3}$$

where $^{\pm}$ symbol denotes the charge specific case.

The following parameters are left free in the fit:

- $N_{sig,total}$ total number of signal events (opposite and same sign) in the sample.
- $R_{\rm ADS}$ ratio of opposite to same sign events (or $R^{\pm}$ for the B^+ or B^- samples).
- $N_{BB,ss}$ and $N_{BB,os}$ number of opposite and same sign $B\bar{B}$ background events.
- $N_{cont,ss}$ and $N_{cont,os}$ number of opposite and same sign continuum background events.
- $c_{cont,ss}$ and $c_{cont,os}$ shape parameter of the threshold function parameterizing $m_{\rm ES}$ distribution for the opposite and same sign continuum background events.

The fit is performed in the region $(m_{\rm ES}, \mathcal{F})$ which is defined by 5.2 GeV/c^2 $< m_{\rm ES} <$ 5.3 GeV/c^2 and $-5. < \mathcal{F} < 5.$

8.4 PDF Parameterizations of the $m_{\rm ES}$ and $\mathcal{F}$ Distributions

In this section, we show the PDF parameterizations for signal and background events that are determined using Monte-Carlo samples listed in Table 8.1.

All the parameterizations discussed in this Section are summarized in Table 8.6. The details of the parameterization are explained in the following text.

fit component	opposite sign		same sign	
	$m_{\rm ES}$	$\mathcal{F}$	$m_{\rm ES}$	$\mathcal{F}$
signal	BG from $B \to D\pi$	DG from MC	same as os signal	same as os signal
$B\overline{B}$	CB from MC	DG from MC	CB from MC	DBG from MC
continuum	ARGUS from off-res	BG from off-res	same as os	same as os
$B\overline{B}$ peaking	-	-	same as os signal	same as os signal

Table 8.6: Functions used for the parameterization of signal and background events in the sample. BG stands for a Bifurcated Gaussian function, DBG stands for a Double Bifurcated Gaussian function, CB stands means Crystal Ball function. The parameterization is obtained from MC sample (marked as MC), off-resonance data sample (off-res), or from $B \to D\pi$ (see text for details). The coinciding parameterization are marked as "same as". "os" stands for opposite sign events.

8.4.1 PDF parameterization of Signal Events

Parameterization of the $m_{\rm ES}$ Distribution for Signal Events

The events reconstructed from $B^+ \to \overline{D}^0\pi^+$, $\overline{D}^0 \to K^+\pi^-\pi^0$ decay channel are kinematically close to the signal events ($B^+ \to \overline{D}^0 K^+$, $\overline{D}^0 \to K^+\pi^-\pi^0$) and can be used to get the parameterization of the $m_{\rm ES}$ distribution for these events directly from data. For that a full analysis of the $B^+ \to \overline{D}^0\pi^+$ decay channel with $\overline{D}^0 \to K^+\pi^-\pi^0$ is performed. This analysis is identical to the one performed for the signal sample but the reconstruction of a π meson instead of K meson accompanying the D meson in the B decay.

To perform this analysis we also search for the possible peaking background events in the $B^+ \to \overline{D}^0\pi^+$ with $\overline{D}^0 \to K^+\pi^-\pi^0$ in generic $B\overline{B}$ sample. The most important peaking background found is the signal events $B^+ \to \overline{D}^0 K^-$ with $\overline{D}^0 \to K^+\pi^-\pi^0$. For the aim of the analysis these events are included into the fit in the signal component. The parameterizations of other components are shown in Figure 8.11.

We perform the fit on the on-resonance data using a bifurcated Gaussian to parameterize the $m_{\rm ES}$ distribution for signal component with all the parameters left free in the fit. The results of the fit are shown in Figure 8.12.

The $m_{\rm ES}$ parameterization obtained from the $\overline{D}^0\pi^+$ data and $\overline{D}^0 K^+$ MC sample are shown in the Figure 8.13. The difference between the two parameterizations can be attributed to the DATA/MC incompatibility in the simulation of π^0 reconstruction distorting the D^0 mass and subsequently the $m_{\rm ES}$ distributions. In the final fit we use the parameters obtained from the $B^- \to D^0\pi^-$, $D^0 \to K^-\pi^+\pi^0$ sample.

Parameterization of the $\mathcal{F}$ Discriminant Distribution for Signal Events

The Fisher discriminant for opposite (same) sign events is parameterized with a double Gaussian. The distributions are shown in Figure 8.14. The distributions are rather similar and the parameters of the double Gaussian functions are found to be equal within the errors, a unique parameterization is used in the fit.

8.4.2 PDF parameterization for the $B\overline{B}$ background events

For the $B\overline{B}$ background events, the $m_{\rm ES}$ distribution is parameterized with a Crystal Ball function, while the Fisher discriminant is fitted using a double Gaussian (double bifurcated Gaussian) for opposite (same) sign events. The results of these fits are shown in Figure 8.15.

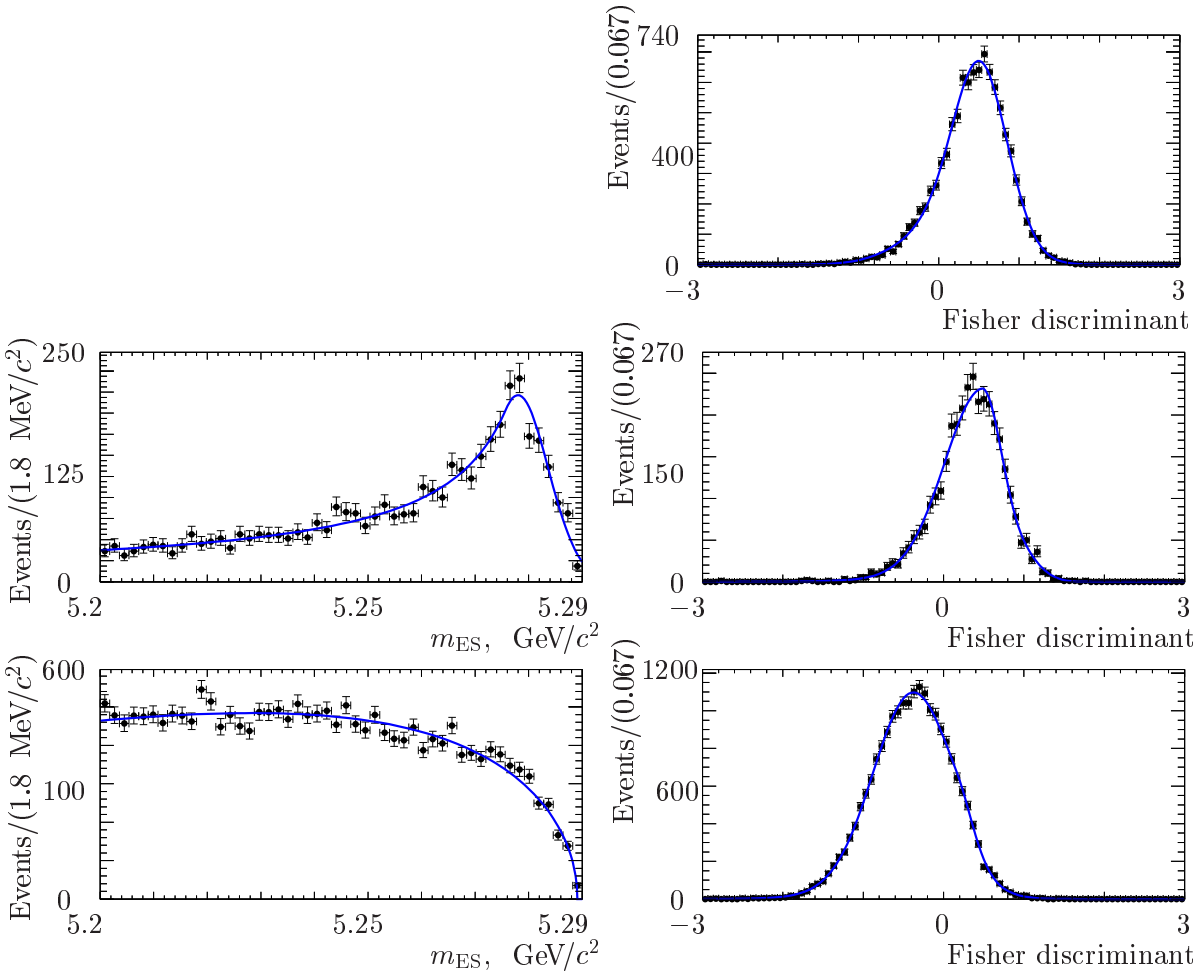

Figure 8.11: [$B^+ \to \overline{D}^0\pi^+$, $\overline{D}^0 \to K^+\pi^-\pi^0$ MC sample] $m_{\rm ES}$ and Fisher distributions from MC sample events. Left (right) plots show the $m_{\rm ES}$ ($\mathcal{F}$) distributions. From top to bottom row: signal, $B\overline{B}$ and continuum background events. The superimposed curves are the results of the fits.

8.4.3 PDF Parameterization for the Continuum Background Events

For the continuum background events, the $m_{\rm ES}$ distribution is parameterized with a threshold function and the Fisher discriminant distributions using a triple (double) Gaussian for opposite (same) sign events. The parameterizations of $m_{\rm ES}$ and Fisher for continuum events are shown in Figure 8.16.

Figures 8.17 show the $m_{\rm ES}$ and $\mathcal{F}$ distributions obtained from off-resonance data with superimposed fitted parameterizations as obtained from the MC samples.

We have also performed the parameterization of the off-resonance data. In this case we

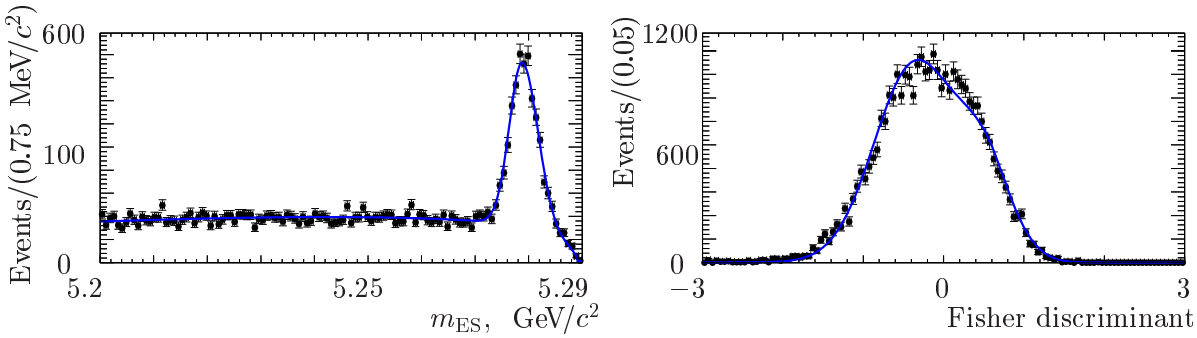

Figure 8.12: [$B^- \to D^0\pi^-$, $D^0 \to K^-\pi^+\pi^0$ data sample] Projections of the 2D likelihood fit of the $B^- \to D^0\pi^-$ with $D^0 \to K^-\pi^+\pi^0$ reconstructed sample to the m_{ES} (left) and $\mathcal{F}$(right) axes. The fit is performed with free m_{ES} signal PDF parameters but fixed parameters for the $\mathcal{F}$ distribution. The solid lines represent the fit.

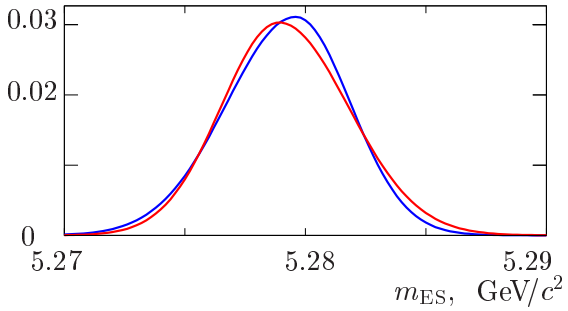

Figure 8.13: The parameterization of the m_{ES} signal distribution obtained from $D\pi$ data sample (red) and DK MC samples (blue). In both cases we use a bifurcated Gaussian functions.

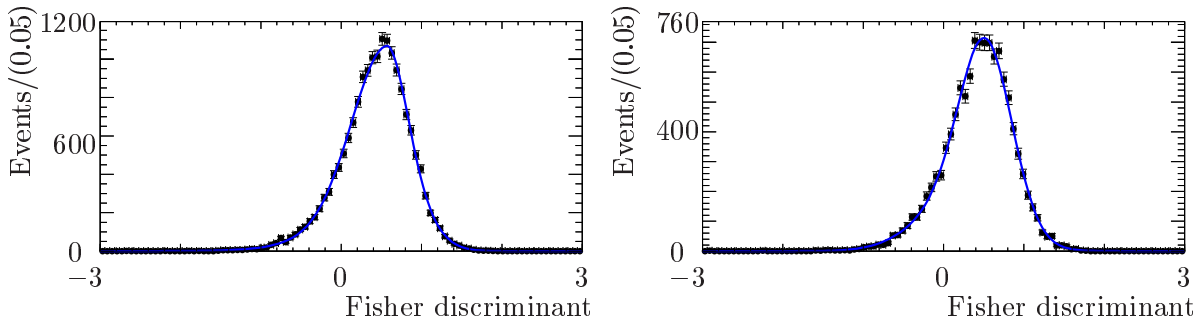

Figure 8.14: Fisher discriminant distributions for signal MC events. The left (right) plot are for opposite (same) sign event samples. The superimposed curves are the result of the fits.

have used a bifurcated Gaussian to parameterize the Fisher discriminant distribution. This parameterization is shown in Figure 8.18. In order to avoid possible statistical fluctuations

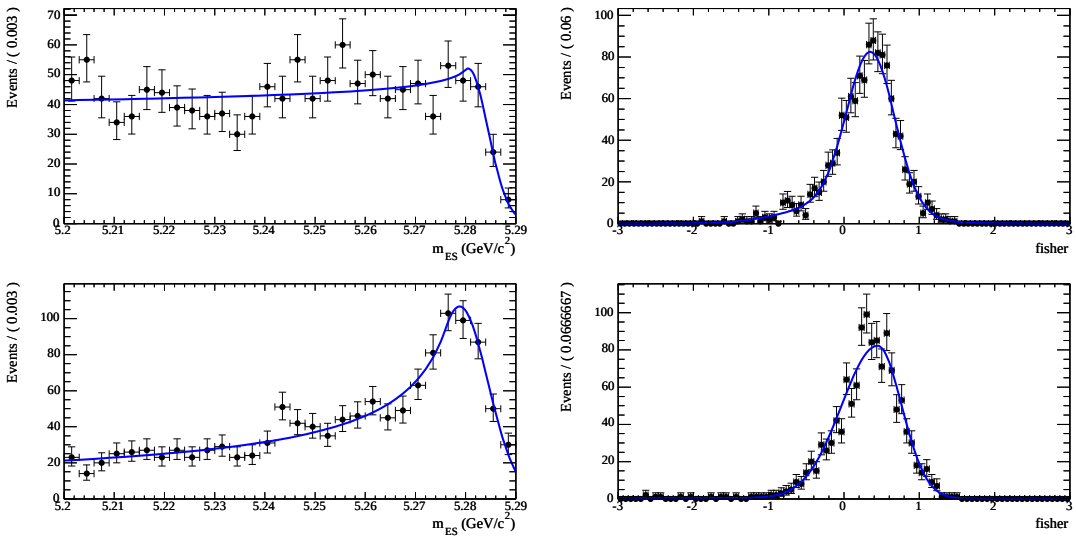

Figure 8.15: $m_{\rm ES}$ and Fisher discriminant distributions for $B\overline{B}$ events. Left (right) plots are for $m_{\rm ES}$ ($\mathcal{F}$) distributions. The upper (lower) row shows the distributions for opposite (same) sign events. The superimposed curves are the result of the fits.

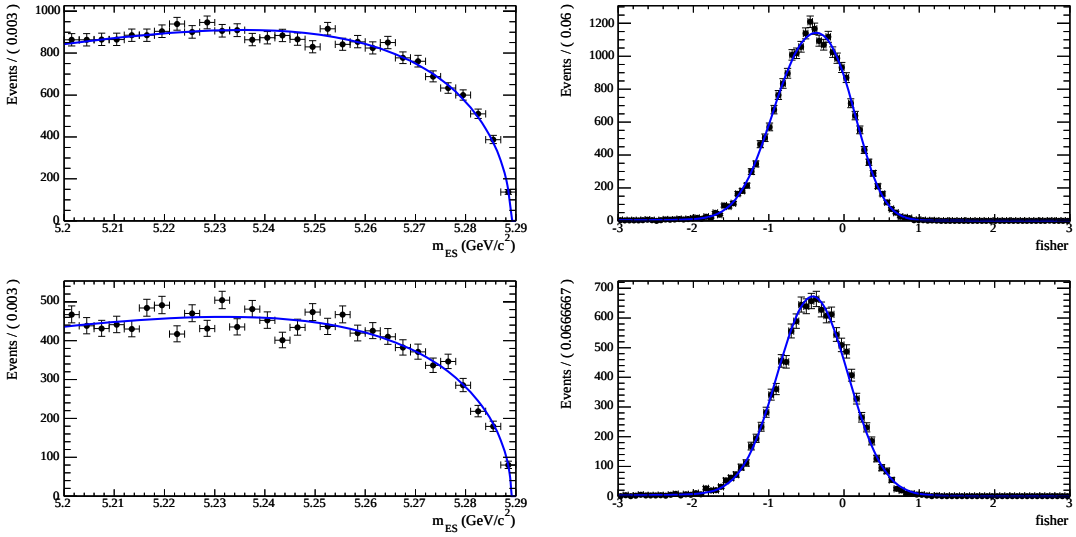

Figure 8.16: $m_{\rm ES}$ and Fisher distribution for continuum events. Left (right) plots show $m_{\rm ES}$ ($\mathcal{F}$) distributions. The upper (lower) row shows the distributions for opposite (same) sign events. The superimposed curves are the result of the fits.

we have also performed the fit to the data sample obtained without applying the selection criteria on δM, $\cos\Theta_{B_{cm}}$, and M_{π^0} (see Table 8.2). The $m_{\rm ES}$ and $\mathcal{F}$ distributions and their parameterizations are shown in Figure 8.19. Finally, in Figure 8.20 we compare the different

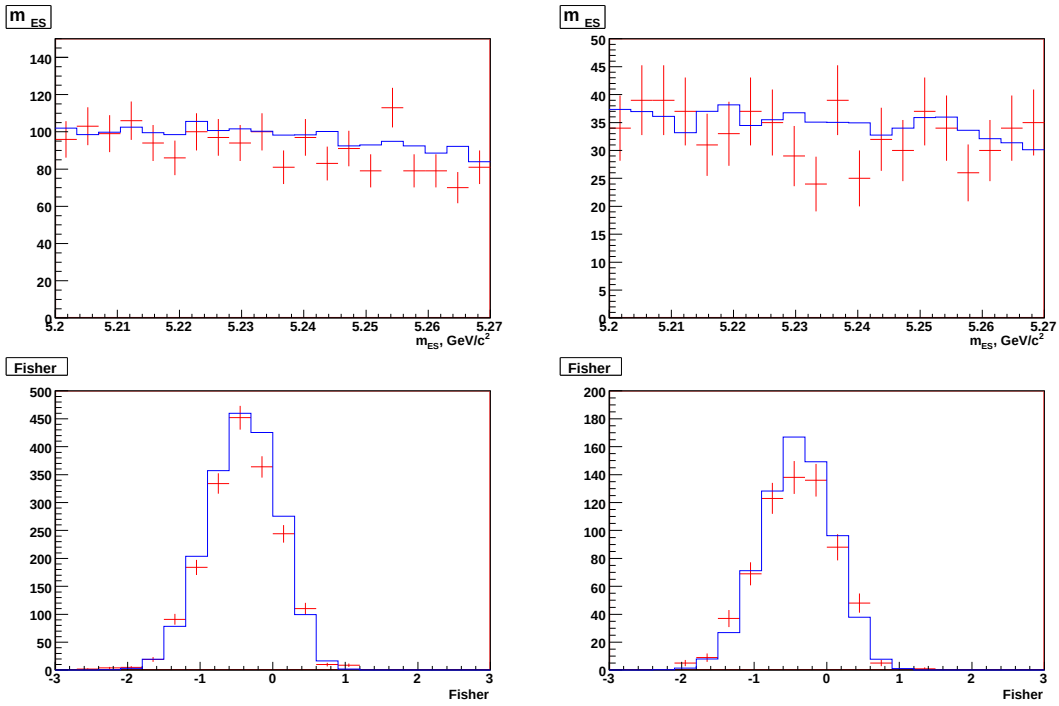

Figure 8.17: $m_{\rm ES}$ and Fisher distributions for continuum MC events (blue histogram) and off-resonance data (red dots with errors). Upper (lower) plots show the $m_{\rm ES}$ ($\mathcal{F}$) distributions. The plots on the left (right) column show the distribution for opposite (same) sign events. The plots are rescaled to the luminosity of the off-resonance data (44.4 fb^{-1}).

parameterizations obtained for $m_{\rm ES}$ and Fisher discriminant.

For the fit we decide to use the parameterization obtained from the fit to the same sign offpeak data for both same and opposite sign events.

8.4.4 PDF Parameterization for Peaking Background

The peaking background events are parameterized with the same parameterization as the one used for the signal events.

8.5 Fit Validation Studies

8.5.1 Fit Validation Using Parameterized Pseudo-experiments

In order to validate the fit model we perform 10000 pseudo-experiments (toy) with simulated events according to the fit model and using the PDF parameters obtained in previous Section.

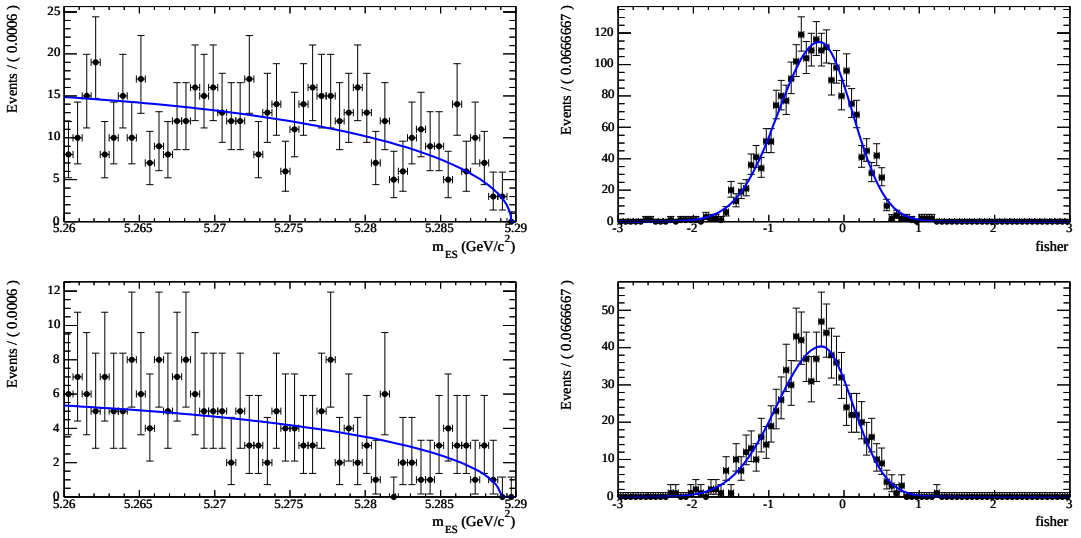

Figure 8.18: $m_{\rm ES}$ and Fisher distributions of the off-resonance events. Left (right) plots show the $m_{\rm ES}$ ($\mathcal{F}$) distributions. The upper (lower) row shows the distributions for opposite (same) sign channel. The overimposed curves are the result of the fit.

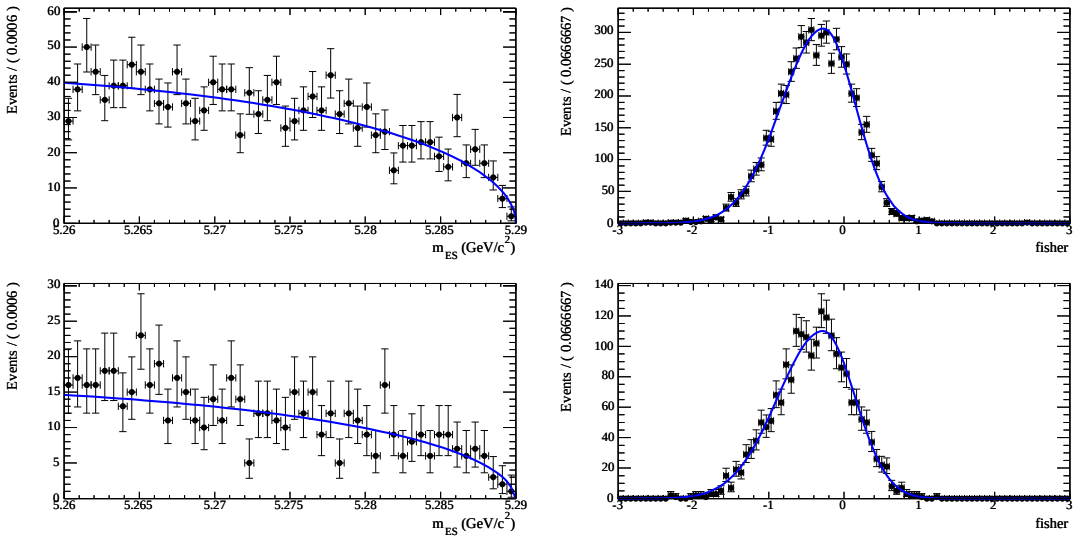

Figure 8.19: The $m_{\rm ES}$ and Fisher distributions of the off-resonance events before applying the selection criteria on δM, $\cos\Theta_{B_{cm}}$, and M_{π^0}. Left (right) plots show the $m_{\rm ES}$ ($\mathcal{F}$) distributions. The upper (lower) row shows the distributions for opposite (same) sign channel. The overimposed curves are the result of the fit.

The number of event for each species are generated according to the values reported in Tables 8.2 and 8.3.

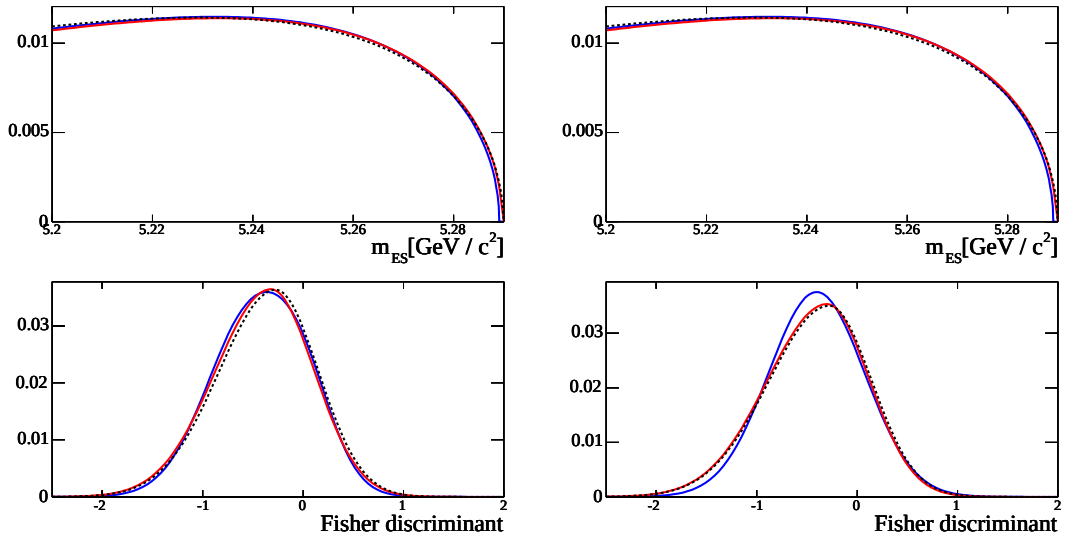

Figure 8.20: The comparison of the $m_{\rm ES}$ (top row) and Fisher discriminant (bottom row) parameterizations of continuum background component obtained from MC sample (blue), off-resonance final data sample (red), off-resonance data sample without applying the selection on δM, M_{π^0}, and ΔE (dashed black, see text for details). Left (right) plot shows the parameterization for opposite sign (os) events.

In Figures 8.21 and 8.22 we show the distribution of $R_{\rm ADS}$ and $N_{sig,total}$, their errors and pulls. The distributions for the fitted number of $B\overline{B}$ and continuum events are shown in Figure 8.23. The pull and asymmetric pull are described in Section 7.4.3.

We also test the sensitivity of our analysis by generating 10000 toys without opposite sign signal (i. e. $R_{\rm ADS} = 0$). The results of all the simulations are reported in Table 8.7.

$R_{\rm ADS}$ generated, 10^{-3}	error obtained, 10^{-3}	pull parameters	
		mean, 10^{-2}	$1-\sigma$, 10^{-2}
0	5.7 ± 0.7	-4.2 ± 1.0	1.0 ± 0.7
14.9	6.9 ± 0.4	-2.7 ± 1.0	1.0 ± 0.7
30	7.8 ± 0.5	-1.6 ± 1.0	1.8 ± 0.7

Table 8.7: The results of the studies on toy-MC experiments generated with different values of $R_{\rm ADS}$.

8.5.2 Fit Validation Using Fully Simulated Samples

We construct two almost independent samples of generic simulated events (with the amount of generic *uds* background MC available being the limiting factor) and perform the complete

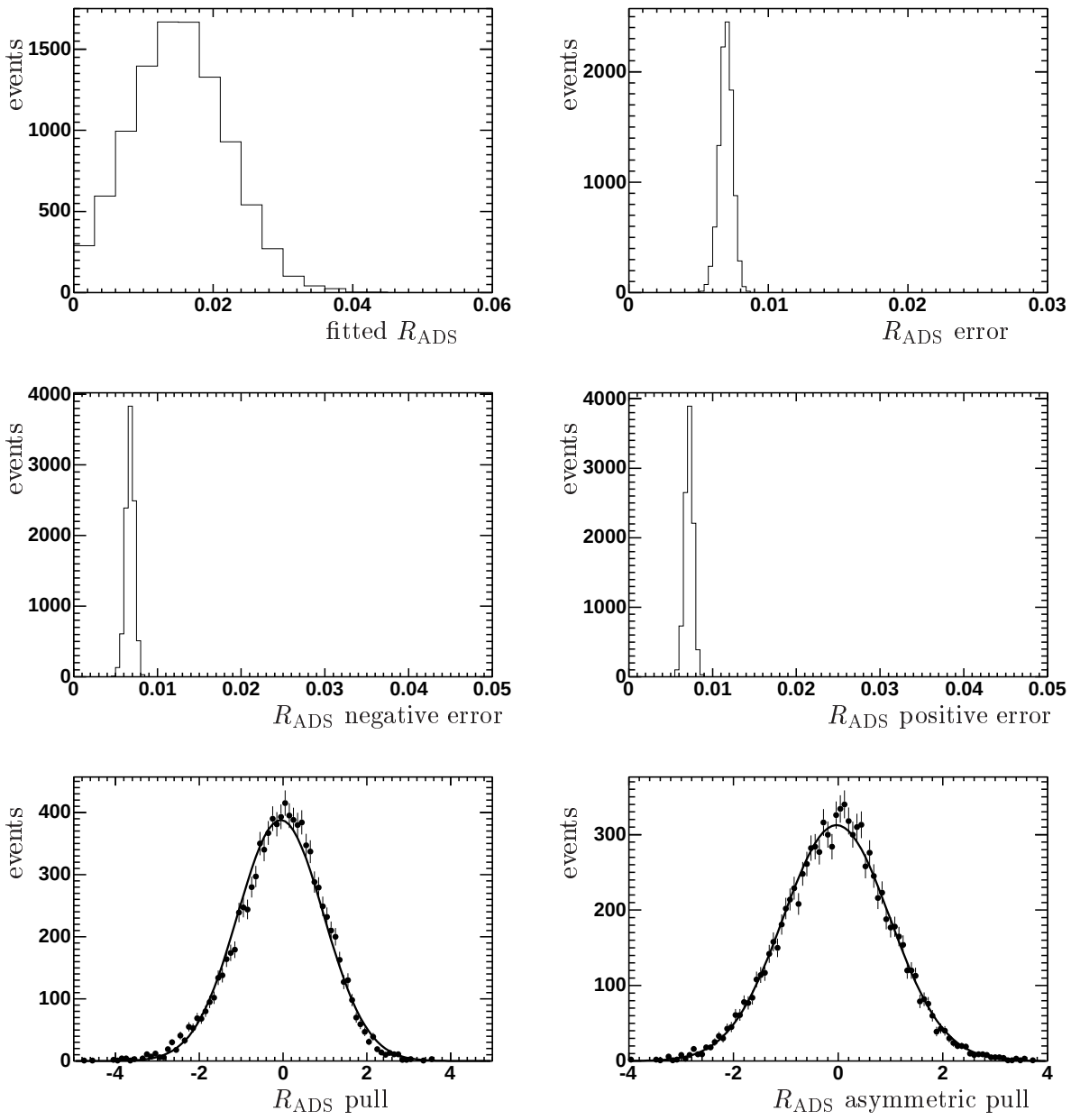

Figure 8.21: [$R_{\rm ADS} = 0.0149$] Distributions of the fitted value for $R_{\rm ADS}$ and its symmetric error (upper plots), its lower and higher errors (middle plots) and the symmetric and asymmetric pulls (lower plots) obtained from toy MC experiments with $R_{\rm ADS} = 0.0149$ (see details in the text).

analysis. The results of the fit are shown in Table 8.8. The generated value is $R_{\rm ADS} = 0.0149$. The resulting fits are shown in Figures 8.24 and 8.26. Figures 8.25 and 8.27 show the same distributions after having applied a cut on $\mathcal{F} > 0$ to visually enhance the signal.

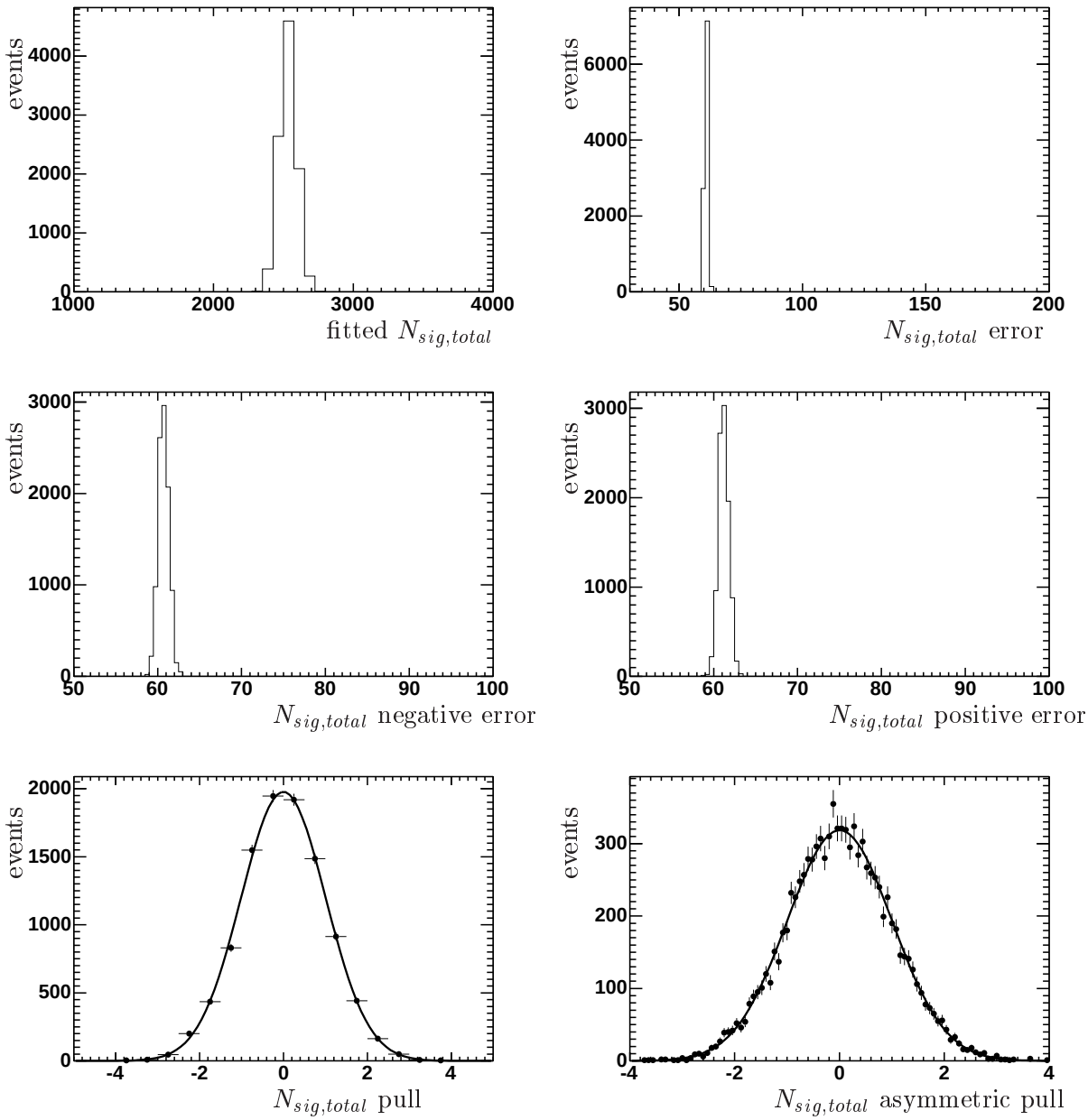

Figure 8.22: [$R_{\rm ADS} = 0.0149$] Distributions of the fitted value for $N_{sig,tot}$ and its symmetric error (upper plots), its lower and higher errors (middle plots) and the symmetric and asymmetric pulls (lower plots) obtained from toy MC experiments with $R_{\rm ADS} = 0.0149$ (see details in the text).

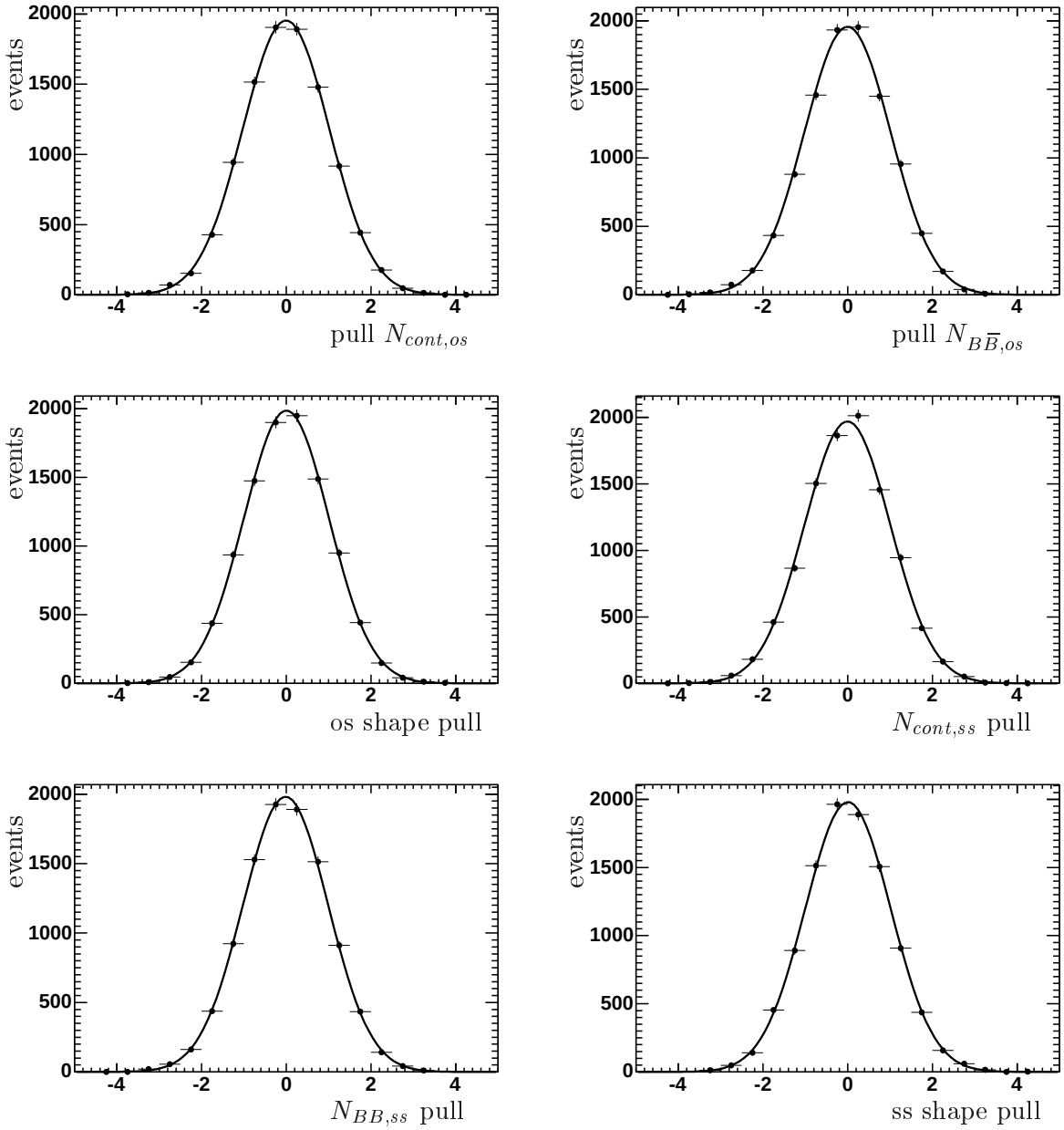

Figure 8.23: [$R_{\rm ADS} = 0.0149$] Pull distributions for opposite sign continuum (top left), opposite sign $B\bar{B}$ background (top right), $m_{\rm ES}$ shape of continuum opposite sign background variable (middle left), same sign continuum (middle right), same sign $B\bar{B}$ background (bottom left) and $m_{\rm ES}$ shape of continuum same sign background variable (bottom right) obtained from toy MC experiments with $R_{\rm ADS} = 0.0149$ (see details in the text).

Parameter	MC 1 fitted value ± error	MC 2 fitted value ± error	generated value
$R_{\rm ADS}$	$(29 \pm 7) \times 10^{-3}$	$(6 \pm 7) \times 10^{-3}$	14.6×10^{-3}
$N_{sig,total}$	2531 ± 61	2489 ± 61	2529
$N_{BB,os}$	320 ± 66	520 ± 65	467
$N_{cont,os}$	21326 ± 157	21179 ± 157	21229
$N_{peak,os}$ (fixed in the fit)	-	-	0
$N_{BB,ss}$	440 ± 61	384 ± 60	460
$N_{cont,ss}$	7520 ± 98	7561 ± 99	7468
$N_{peak,ss}$ (fixed in the fit)	-	-	176
Shape of Argus, opposite sign	-22.9 ± 0.8	-23.1 ± 1.0	
Shape of Argus, same sign	-21.0 ± 2.0	-24.0 ± 1.0	

Table 8.8: Results for the fit on generic MC samples of luminosity 428 fb^{-1}. We set $R_{\rm ADS} = 0.0149$

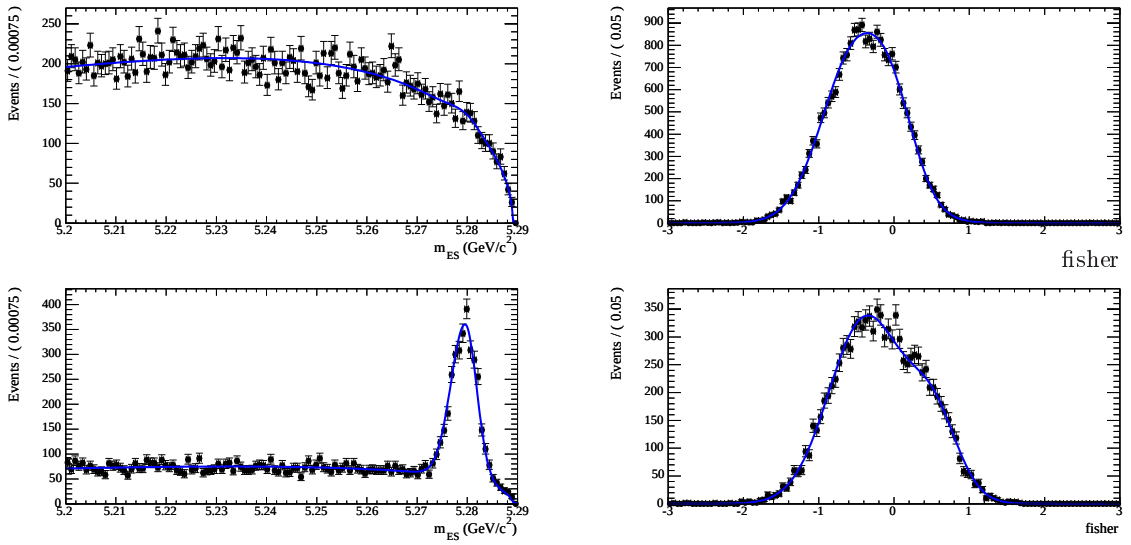

Figure 8.24: Projections of the 2D likelihood to the $m_{\rm ES}$ (left) and $\mathcal{F}$ (right) variables obtained by fitting to the Monte-Carlo generic sample (MC 1). The upper (lower) row displays the distributions for opposite (same) sign events.

We also performed the complete analysis using generic Monte-Carlo setting $R_{\rm ADS} = 0$. The results of the fit are indicated in the Table 8.9 and the likelihood projections are shown in Figures 8.28 and 8.30. In Figures 8.29 and 8.31 we also show the same distribution after having applied a cut on $\mathcal{F} > 0$ to visually enhance the signal.

The results of these fits are are in agreement with the generated values and are also in

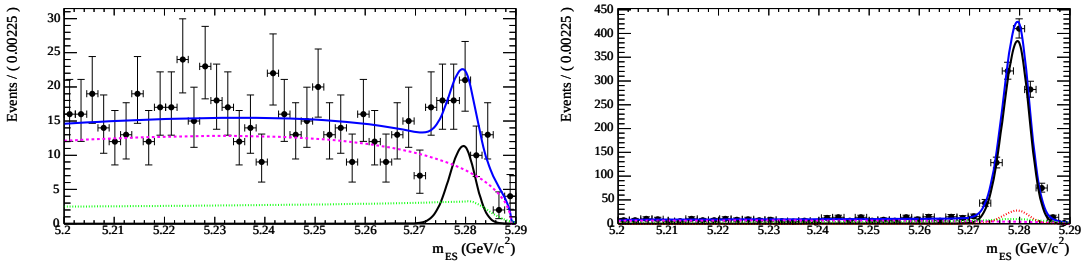

Figure 8.25: Projections of the 2D likelihood to the $m_{\rm ES}$ variable with a cut on $\mathcal{F} > 0$. Blue line shows the result of the fit of the Monte-Carlo generic sample (MC 1). Magenta, green, red and black lines show the results of the fit for continuum, $B\overline{B}$, same sign peaking $B\overline{B}$ background, and signal components respectively. The left (right) plots correspond to opposite sign (same sign) decay channels respectively.

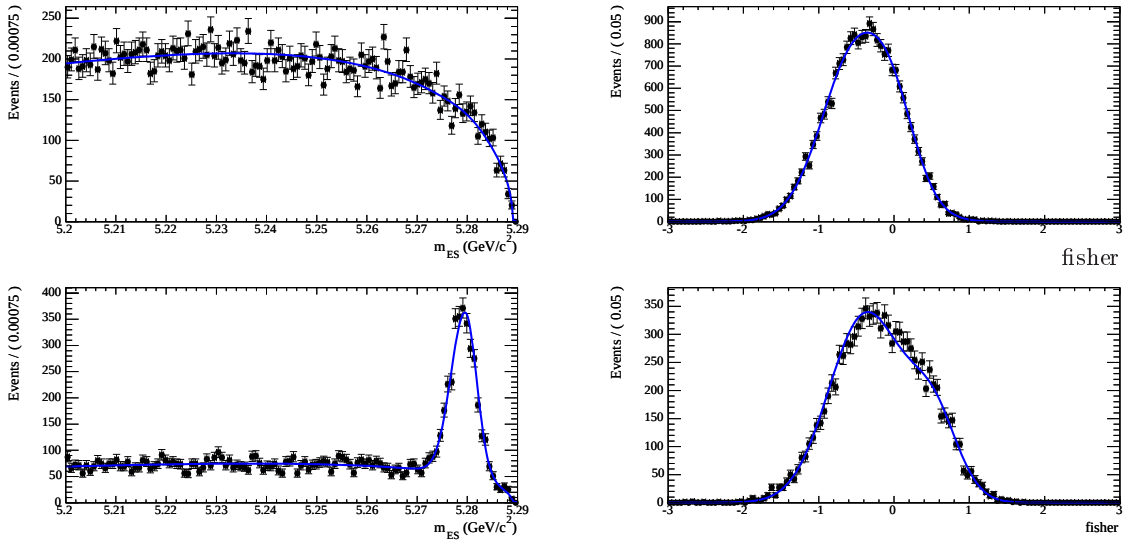

Figure 8.26: Projections of the 2D likelihood to the $m_{\rm ES}$ (left) and $\mathcal{F}$ (right) variables obtained by fitting to the Monte-Carlo generic sample (MC 2). The upper (lower) row displays the distributions for opposite (same) sign events.

agreement with those from to-MC experiments reported in Table 8.7.

We obtain the results on $R_{\rm ADS}$ by scanning the likelihood: The result of the scan are shown in Figure 8.32 and are:

$$\begin{aligned} R_{\rm ADS} &= 0.029^{+0.008}_{-0.007}\ (\text{fit } 0.029 \pm 0.007)\ \text{for MC1}, \\ R_{\rm ADS} &= 0.006^{+0.007}_{-0.006}\ (\text{fit } 0.006 \pm 0.007)\ \text{for MC2}. \end{aligned} \tag{8.4}$$

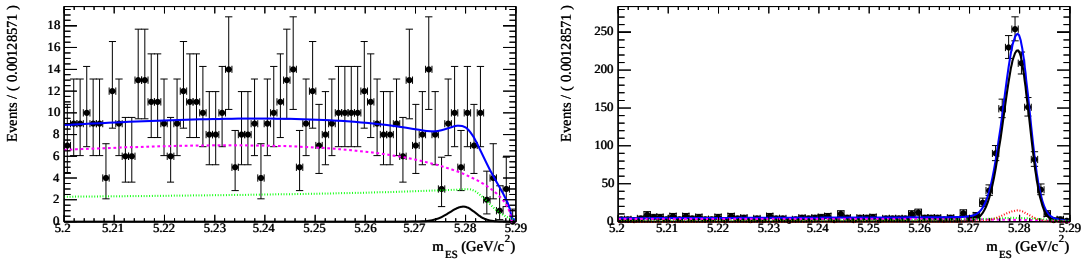

Figure 8.27: Projections of the 2D likelihood to the $m_{\rm ES}$ variable with a cut on $\mathcal{F} > 0$. Blue line shows the result of the fit of the Monte-Carlo generic sample (MC 2). Magenta, green, red and black lines show the results of the fit for continuum, $B\overline{B}$, same sign peaking $B\overline{B}$ background, and signal components respectively. The left (right) plots correspond to opposite sign (same sign) decay channels respectively.

Parameter	MC cocktail 1 fitted value ± error	MC cocktail 2 fitted value ± error	generated value
$R_{\rm ADS}$	$(9 \pm 6) \times 10^{-3}$	$(-9 \pm 5) \times 10^{-3}$	0.0
$N_{sig,total}$	2480 ± 60	2460 ± 60	2492
$N_{BB,os}$	330 ± 70	522 ± 67	468
$N_{cont,os}$	21300 ± 200	21178 ± 156	21220
$N_{BB,ss}$	440 ± 60	384 ± 60	460
$N_{cont,ss}$	7520 ± 90	7565 ± 100	7468
$N_{peak,os}$ (fixed in the fit)	-	-	0
$N_{peak,ss}$ (fixed in the fit)	-	-	176
Shape of Argus, opposite sign	-22.7 ± 0.8	-23.1 ± 0.8	
Shape of Argus, same sign	-22.0 ± 1.0	-24.0 ± 1.0	

Table 8.9: Results for the fit to the MC generic sample of luminosity 428 fb^{-1}. We set $R_{\rm ADS} = 0$.

8.5.3 Fit Validation for $R^{\pm}$ Variables

One can use R^+ and R^-, which were described in Section 3.1.2. The $R^{\pm}$ observables behave as $R_{\rm ADS}$, being the same quantity calculated separately for $B^{\pm}$ samples. Possible problems could come from a lack of signal statistics in the opposite sign sample.

We perform toy MC studies for $R^{\pm}$ observables, the resulting plots are shown in Figures 8.33. The pulls are satisfactory. The results from simulations for different values of $R^{\pm}$ are reported in Table 8.10.

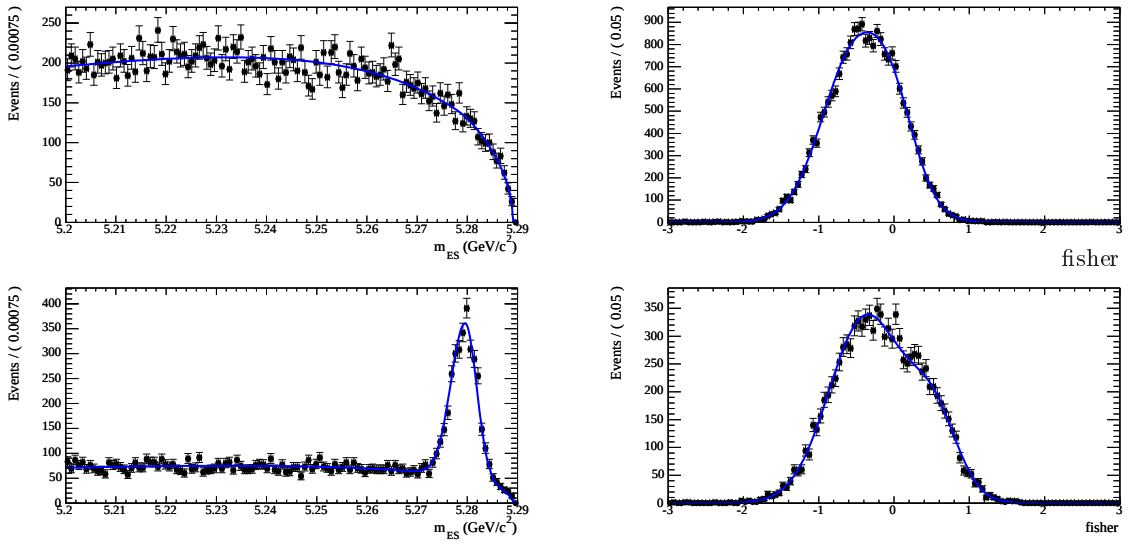

Figure 8.28: Projections of the 2D likelihood to the $m_{\rm ES}$ (left) and $\mathcal{F}$ (right) variables on Monte-Carlo cocktail (MC 1) with $R_{\rm ADS} = 0$. The upper row corresponds to opposite sign while the lower one corresponds to same sign decay channel.

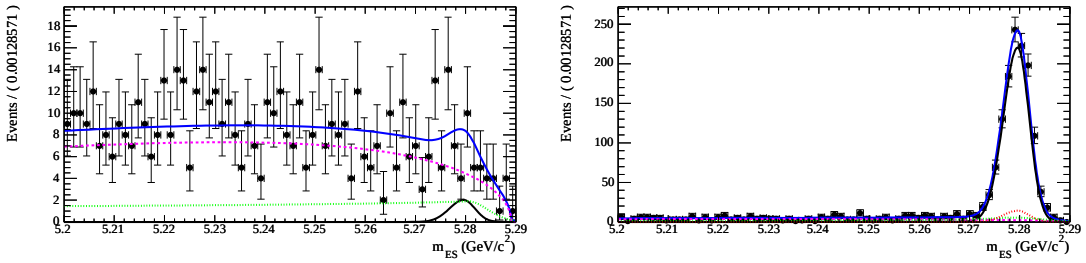

Figure 8.29: Projections of the 2D likelihood to the $m_{\rm ES}$ variable with a cut on $\mathcal{F} > 0$. Blue line shows the result of the fit of MC cocktail (MC 1). Magenta, green, red and black lines show the results of the fit for continuum, $B\overline{B}$, same sign peaking $B\overline{B}$ background, and signal components respectively. The rows correspond to opposite sign and same sign decay channels, respectively.

8.5.4 Charmless Peaking Background

The most important background contribution from the charmless B^+ meson decays is expected from the $B^+ \to K^+K^+\pi^-\pi^0$ decay channel. A close channel with $B^+ \to K^+K^+\pi^-$ was found to contribute to the background of $B^+ \to \{K^+\pi^-\}_D K^+$ analysis. The branching fraction of this channel have never been measured. Thus, in order not to depend on Monte-Carlo while evaluating this background we study that source using the data. We select the events in the tails of the D^0 mass distribution by cutting away the region with reconstructed D^0 meson mass

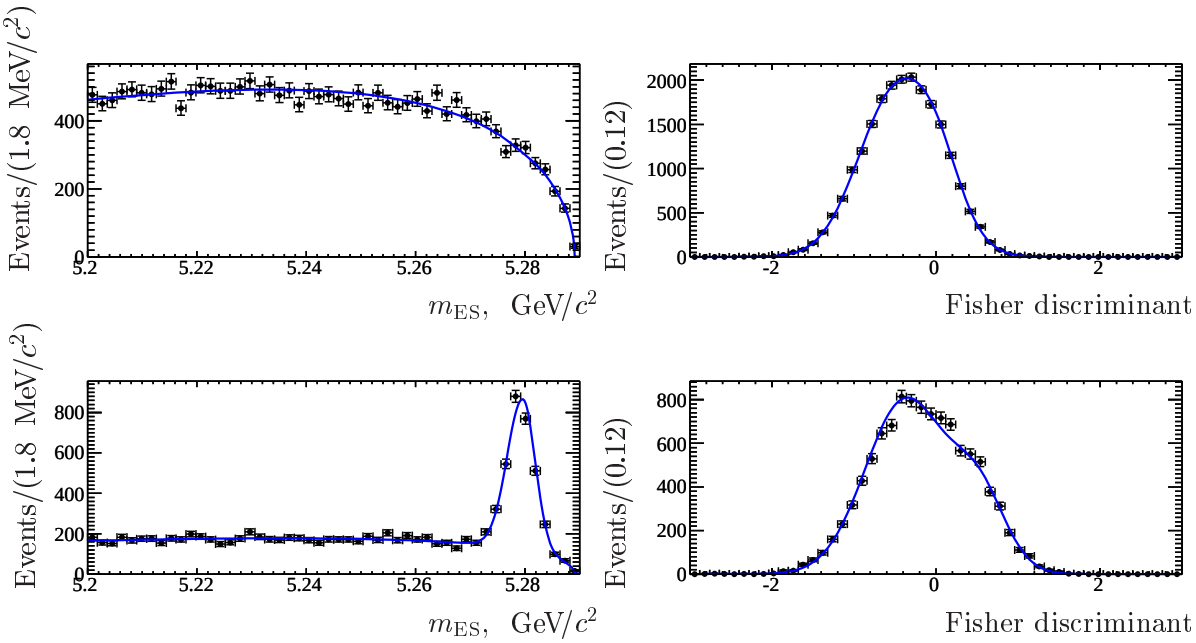

Figure 8.30: Projections of the 2D likelihood to the $m_{\rm ES}$ (left) and $\mathcal{F}$ (right) variables on Monte-Carlo cocktail (MC 2) with $R_{\rm ADS} = 0$. The upper row corresponds to opposite sign while the lower one corresponds to same sign decay channel.

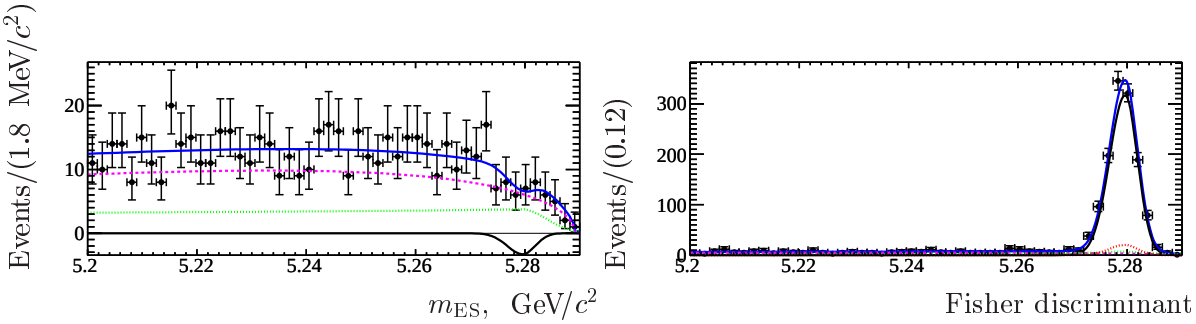

Figure 8.31: Projections of the 2D likelihood to the $m_{\rm ES}$ variable with a cut on $\mathcal{F} > 0$. Blue line shows the result of the fit of MC cocktail (MC 2). Magenta, green, red and black lines show the results of the fit for continuum, $B\overline{B}$, same sign peaking $B\overline{B}$ background, and signal components respectively. The rows correspond to opposite sign and same sign event samples, respectively.

less then 40 MeV from the nominal D^0 mass (i.e. taking only $1.904 < M_{D^0} < 2.000$ GeV/c^2 or $1.700 < M_{D^0} < 1.824$ GeV/c^2). These sample is treated in the same manner as real data, i. e. $m_{\rm ES}$ and Fisher variables are put into the likelihood after having applied all the cuts (the details of the fit model can be found in the following sections). The resulting plots for the fit projections to $m_{\rm ES}$ and $\mathcal{F}$ planes are shown in Figure 8.34. The number of fitted events have to be rescaled

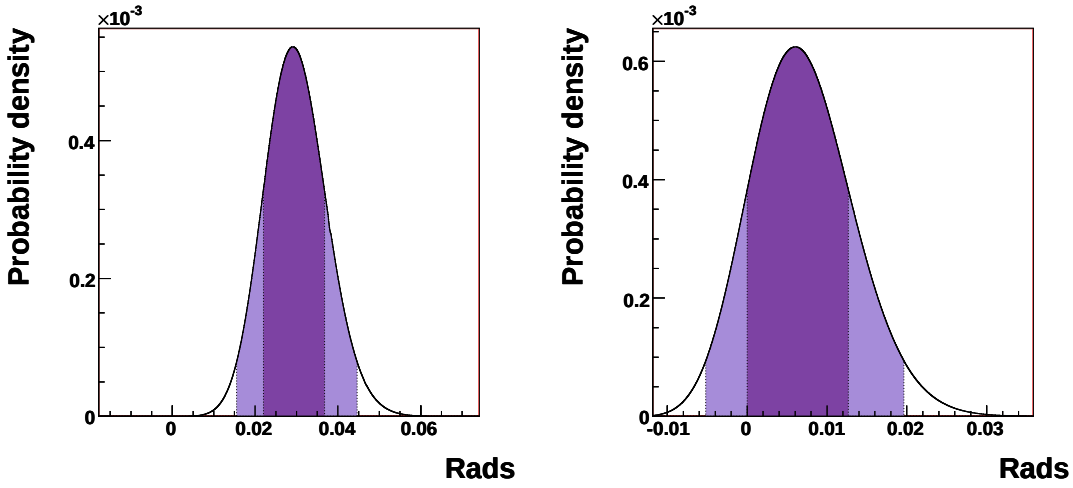

Figure 8.32: 1D likelihoods for $R_{\rm ADS}$ obtained from the scan procedure over MC generic sample of 428 fb^{-1} (MC 1 (left) and MC 2 (right)) generated with $R_{\rm ADS} = 0.0149$. The dark and light shaded zones represent the 68% and 95% probability regions, respectively.

$R^{\pm}$ generated, 10^{-3}	error obtained, 10^{-3}	pull parameters	
		mean, 10^{-2}	$1-\sigma$, 10^{-2}
0	8.3 ± 1.0	-8.2 ± 1.1	5.7 ± 0.8
7	9.0 ± 1.1	-6.9 ± 1.0	4.0 ± 0.7
12	9.6 ± 1.0	-5.9 ± 1.0	3.8 ± 0.7
30	11.1 ± 1.0	-2.4 ± 1.0	1.0 ± 0.7

Table 8.10: Errors expected for the $R^{\pm}$ ratios depending on the value of $R^{\pm}$.

according to the M_{D^0} range in the selected sample. The contributions from charmless peaking events are found to be compatible with zero being equal to -15 ± 9 for opposite sign channel and 3 ± 13 for same sign channel. The number should be compared with 176 events expected in the $B^+ \to D^0\pi^+$ channel for the same sign case. The results of this search are included in the systematic error evaluation from the peaking background.

8.6 Fit Results on Data

8.6.1 Results on $R_{\rm ADS}$

The fit to data is performed on the 428 fb^{-1} on-resonance data sample. The distributions are shown in Figure 8.35. We also show the same distributions after having applied a criteria on

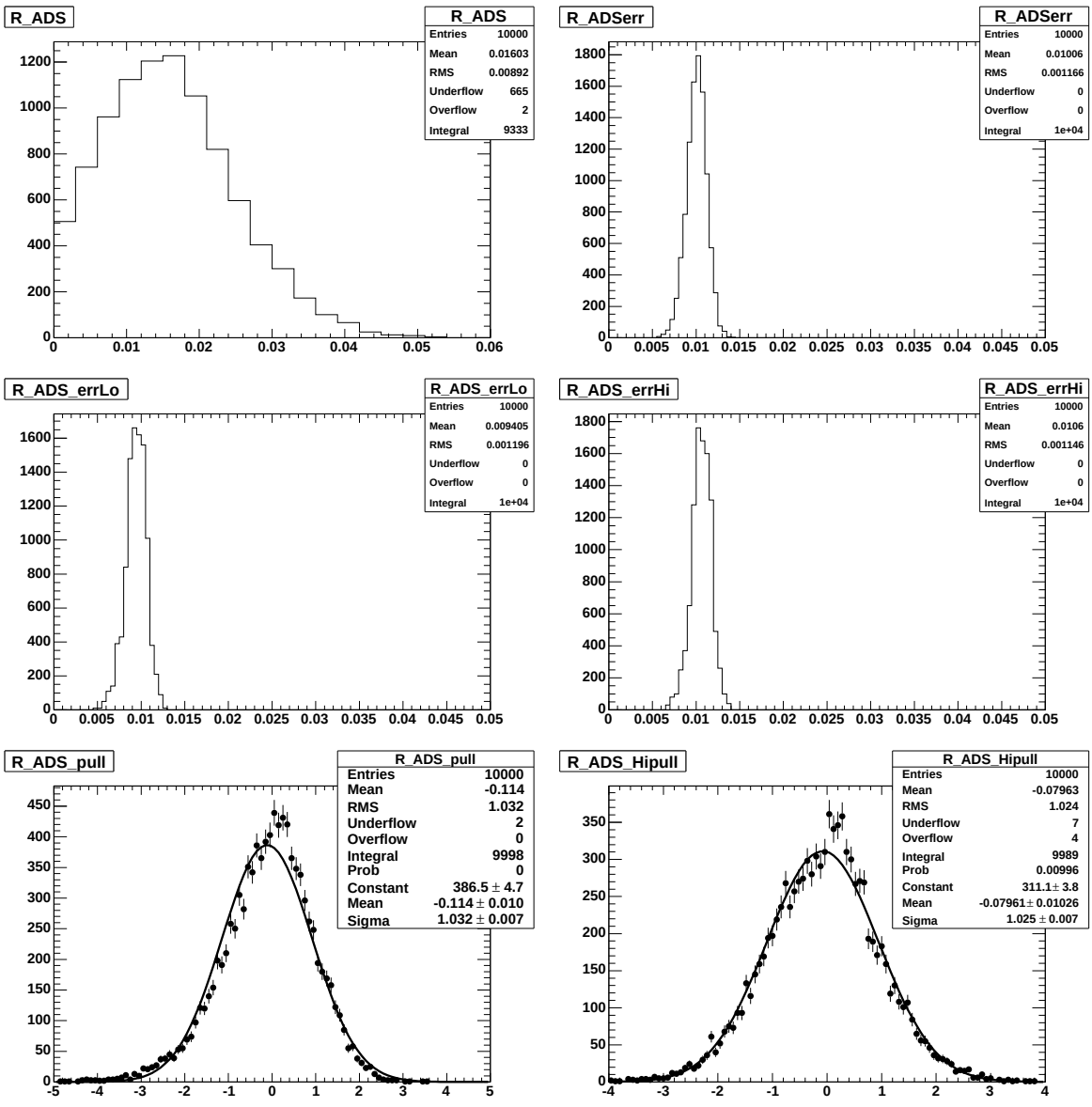

Figure 8.33: [R^+ fit]. Distributions of the fitted value for R^+ and its symmetric error (upper plots), its lower and higher errors (middle plots) and the symmetric and asymmetric pulls (lower plots) obtained from the toy MC described in the text.

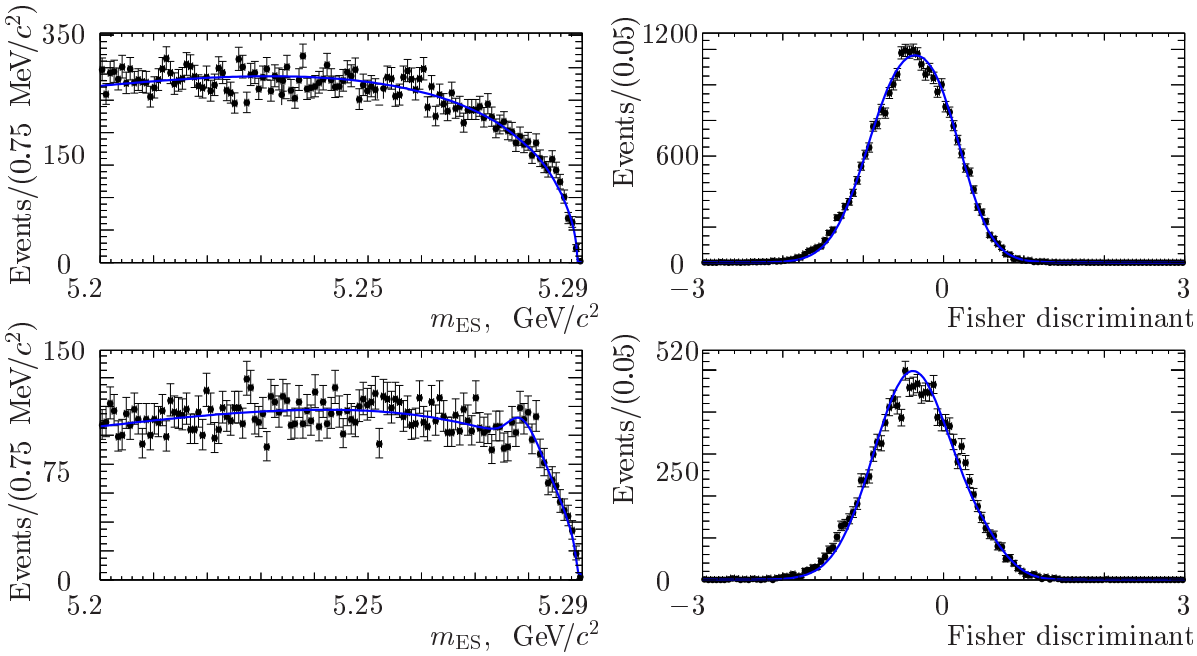

Figure 8.34: Projections of the 2D likelihood to the $m_{\rm ES}$ (left) and $\mathcal{F}$ (right) variables on the tails of the reconstructed D^0 meson in order to search for possible charmless peaking backgrounds. The plots on the upper (lower) row corresponds to opposite (same) sign events sample.

$\mathcal{F} > 0$ to visually enhance signal (Figure 8.36). The likelihood scan is shown in Figure 8.37 and all the numerical results of the fit are shown in Table 8.11. The fit gives:

$$R_{\rm ADS} = \left(8.9^{+8.2}_{-7.4}\ (\mathsf{stat.})\right) \times 10^{-3}. \tag{8.5}$$

The evaluation of the systematic errors is performed in Section 8.7.

8.6.2 Results on $R^{\pm}$

The same procedure has been followed to fit separately the B^+ and B^- samples. The $m_{\rm ES}$ and $\mathcal{F}$ fitted distributions are shown in Figures 8.38 and 8.39. The plots with enhanced $\mathcal{F} > 0$ to visually enhance the signal are shown in Figures 8.40 and 8.41.

The scan for R^+ and R^- are shown in Figure 8.42 with the result:

$$R^+ = \left(5.0^{+12.8}_{-11.0}\ (\mathsf{stat.})\pm\right) \times 10^{-3}, \tag{8.6}$$

$$R^- = \left(13.2^{+12.8}_{-10.9}\ (\mathsf{stat.})\right) \times 10^{-3}. \tag{8.7}$$

and all the results for the fits are reported in Table 8.12.

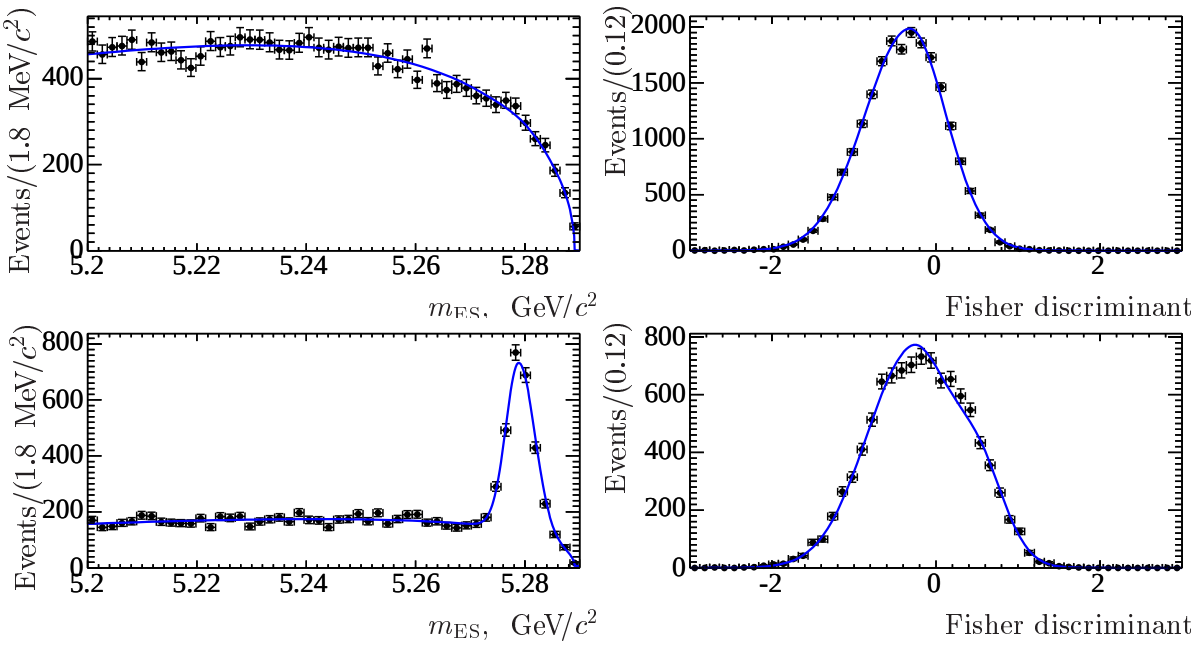

Figure 8.35: Projections of the 2D likelihood to the $m_{\rm ES}$ (left) and $\mathcal{F}$ (right) variables obtained from the fit to data. The plots in the upper row correspond to the opposite sign sample, while the ones in the lower row correspond to the same sign sample.

Parameter	$R_{\rm ADS}$ fit results
$R_{\rm ADS}$	$(9.0 \pm 7.8) \times 10^{-3}$
$N_{sig,total}$	2008 ± 57
$N_{BB,os}$	402 ± 65
$N_{cont,os}$	20329 ± 154
$N_{peak,os}$ (fixed in the fit)	0
$N_{BB,ss}$	644 ± 62
$N_{cont,ss}$	7201 ± 97
$N_{peak,ss}$ (fixed in the fit)	176
Shape of Argus, opposite sign	-21.7 ± 0.7
Shape of Argus, ss	-25.3 ± 1.4

Table 8.11: Results for the fit to the on-peak data resonance.

8.7 Systematic Uncertainties

We first make an evaluation of the systematic uncertainties on the generic MC sample. The systematic uncertainties can arise from the following sources:

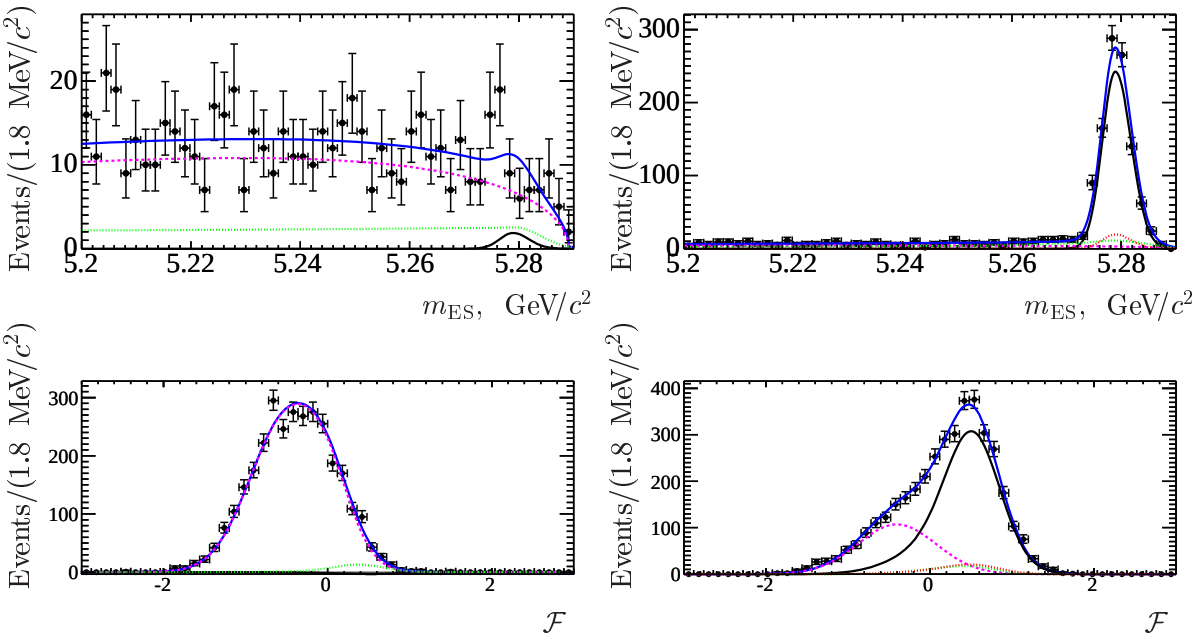

Figure 8.36: Projections of the 2D likelihood to the $m_{\rm ES}$ variable with a cut on $\mathcal{F} > 0$ (top row) and to the $\mathcal{F}$ variable with a cut on $m_{\rm ES} > 5.27$ GeV/c^2. Blue line shows the result of the fit to on-peak data. Magenta, green, red and black lines show the results of the fit for continuum, $B\overline{B}$, same sign peaking $B\overline{B}$ background, and signal components respectively. The left (right) plots correspond to opposite (same) sign samples.

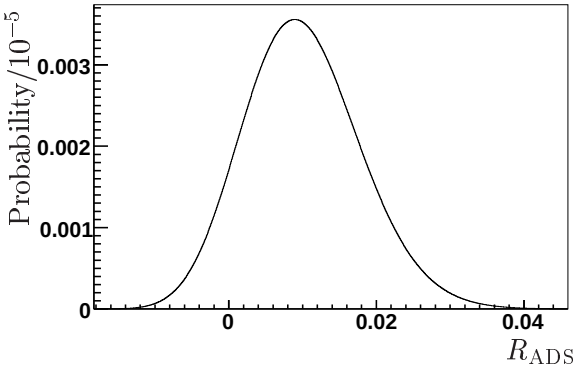

Figure 8.37: Likelihood scan for $R_{\rm ADS}$ obtained from the fit to on-resonance data sample.

- *The number of $B\overline{B}$ pairs* which was produced in the sample. This uncertainty is fixed to be 0.6 % (according to the information from *BABAR* luminosity monitor).

- *The uncertainty on the PDF parameterization.* All the parameters fixed in the fit are taken randomly from a Gaussian distribution considering the correlations between different parameters. The operation is repeated 1000 times. The most probable value of the

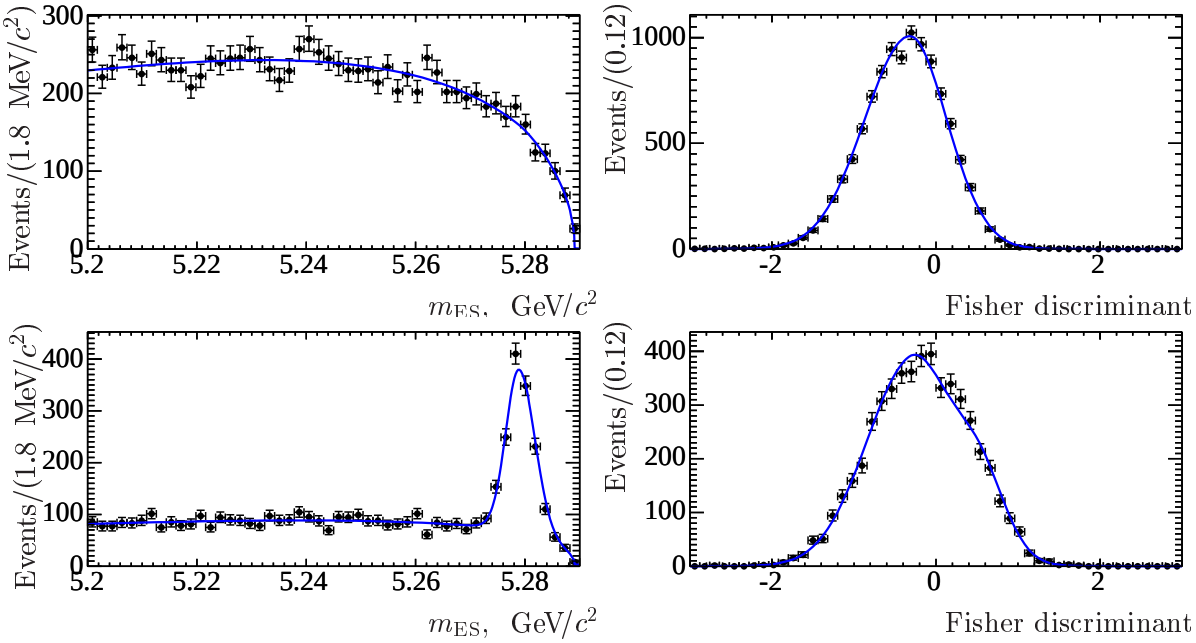

Figure 8.38: Projections of the 2D likelihood to the $m_{\rm ES}$ (left) and $\mathcal{F}$ (right) variables obtained from the fit to the B^+ data sample. The plots in the upper (lower) row correspond to opposite (same) sign.

Parameter	R^+ fit results	R^- fit results
$R_{\rm ADS}$	$(5.0 \pm 12.1) \times 10^{-3}$	$(13.4 \pm 11.8) \times 10^{-3}$
$N_{sig,total}$	961 ± 41	876 ± 39
$N_{BB,os}$	305 ± 52	121 ± 37
$N_{cont,os}$	10290 ± 111	10017 ± 105
$N_{peak,os}$ (fixed in the fit)	0	0
$N_{BB,ss}$	315 ± 44	330 ± 44
$N_{cont,ss}$	3657 ± 69	3537 ± 68
$N_{peak,ss}$ (fixed in the fit)	88	88
Shape of Argus, os	-22.8 ± 1.1	-20.6 ± 1.1
Shape of Argus, ss	-24 ± 2	-26 ± 2

Table 8.12: Results of fits to the B^+ and B^- data samples separately.

distribution corresponds to the value of the fitted $R_{\rm ADS}$. The limits of 68% range obtained by integrating the distribution starting from the most probable value are taken to be the systematic error on the determination of $R_{\rm ADS}$ from the uncertainties on the PDF parameterization. This uncertainty dominates for all three observables measured.

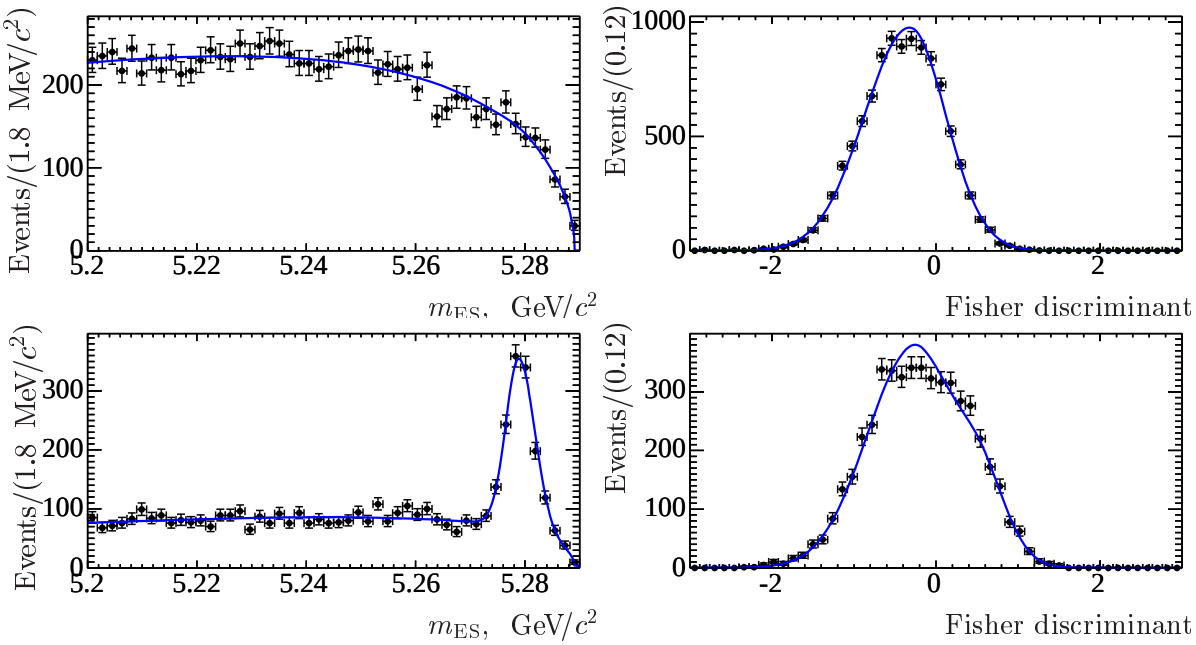

Figure 8.39: Projections of the 2D likelihood to the $m_{\rm ES}$ (left) and $\mathcal{F}$ (right) variables obtained from the fit to the B^- data sample. The plots in the upper (lower) row correspond to opposite (same) sign.

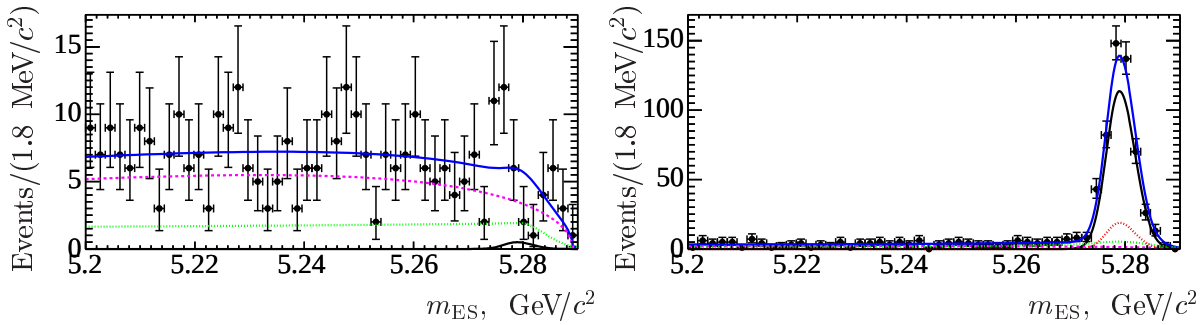

Figure 8.40: Projections of the 2D likelihood to the $m_{\rm ES}$ variables obtained from the fit to the B^+ data sample applying the criteria $\mathcal{F} > 0$. Blue line shows the result of the fit to on-peak data. Magenta, green, red and black lines show the results of the fit for continuum, $B\overline{B}$, same sign peaking $B\overline{B}$ background, and signal components, respectively. The left (right) plots correspond to opposite (same) sign sample, respectively.

- *Peaking background arising from $B\bar{B}$ events.* The number of peaking background events is fixed in the final fit. The error on determination of $N_{ss,peak}$ is coming from MC available statistics and BR determination and results in 176 ± 14. The uncertainty in peaking background is evaluated in the similar way we did for the uncertainty on the PDF shape. We assume that the uncertainty from the charmless peaking background does not exceed

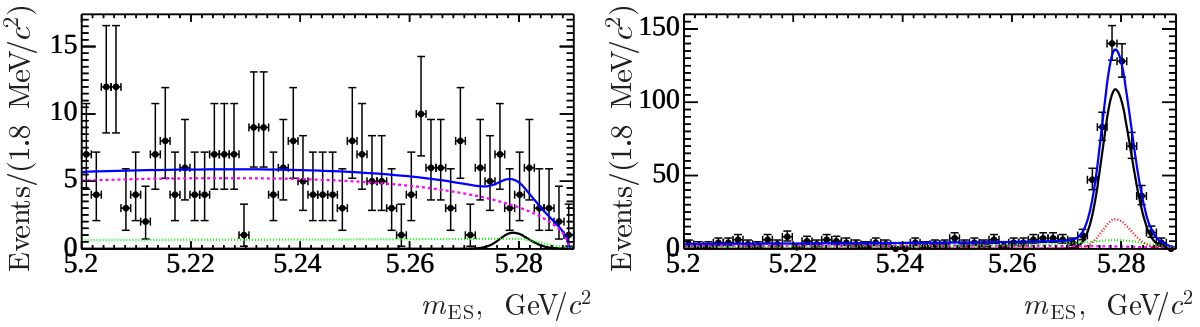

Figure 8.41: Projections of the 2D likelihood to the $m_{\rm ES}$ variables obtained from the fit to the B^- data sample applying the criteria $\mathcal{F} > 0$. Blue line shows the result of the fit to on-peak data. Magenta, green, red and black lines show the results of the fit for continuum, $B\overline{B}$, same sign peaking $B\overline{B}$ background, and signal components, respectively. The left (right) plots correspond to opposite (same) sign sample, respectively.

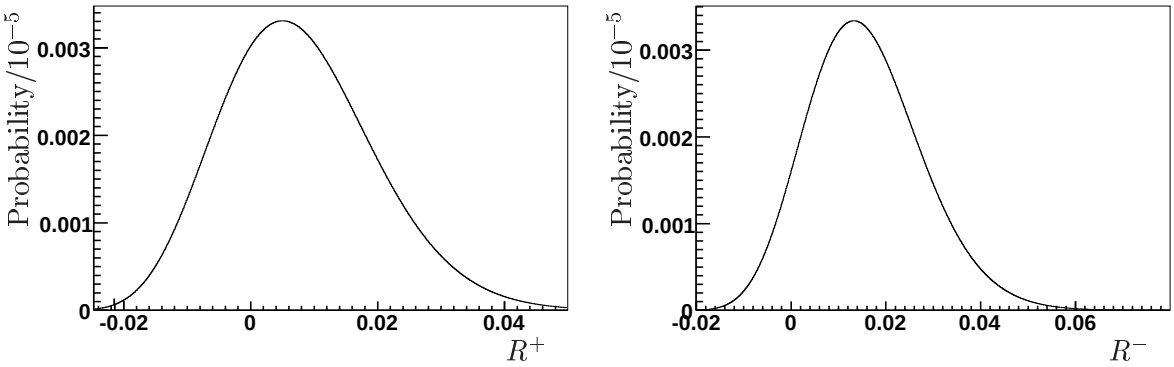

Figure 8.42: Probability distribution for R^+ (left) and R^- (right) obtained from the fit to the B^+ and B^- data samples separately.

the magnitude of the error coming from $B\overline{B}$ events containing a D meson in decay chain.

- *Crossfeed between same sign and opposite sign events.* In sec. 8.2.7, the efficiency of the cross-feed between opposite sign and same sign events, ϵ_{CF}, has been evaluated. The associated systematic uncertainty on $R_{\rm ADS}$ is calculated according to the following expression:

$$R_{\rm ADS} = \frac{N_{os} \pm N_{ss} \cdot \epsilon_{CF}}{N_{ss} \pm N_{os} \cdot \epsilon_{CF}} \sim \frac{N_{os}}{N_{ss}} \pm \epsilon_{CF}. \tag{8.8}$$

- *Efficiency ratio for same sign and opposite sign events.* As explained in section 8.2.8, it has been verified that the efficiencies for same sign and opposite sign events are the same within a precision of 3%. We hence assign as systematic error on $R_{\rm ADS}$, the variation of $R_{\rm ADS}$ fitted values obtained assuming the efficiencies ratio to be 1.03 and 0.97.

Source	$R_{\rm ADS}$ error	R^+ error	R^- error
PDF error	24.0	37.0	21
Peaking background	4.0	6.0	6.0
$\mathcal{B}$ errors	4.3	2.4	6.1
Crossfeed	2.9	1.6	4.2
Efficiency ratio	1.0	$< 1.$	1.0
Combined error	24.9	37.6	23.1

Table 8.13: Absolute systematic errors for $R_{\rm ADS}$ in units of 10^{-4}.

The evaluation of systematic errors performed on the data sample for $R_{\rm ADS}$, R^+, and R^- is summarized in the Table 8.13.

8.7.1 Final Results

The final result for $R_{\rm ADS}$ ratio is:

$$R_{\rm ADS} = \left(8.9^{+8.2}_{-7.4}\ (\mathsf{stat.}) \pm 2.5\ (\mathsf{syst.})\right) \times 10^{-3}. \tag{8.9}$$

The final results for $R^{\pm}$ ratios are:

$$R^+ = \left(5.0^{+12.8}_{-11.0}\ (\mathsf{stat.}) \pm 3.8\ (\mathsf{syst.})\right) \times 10^{-3}, \tag{8.10}$$

$$R^- = \left(13.2^{+12.8}_{-10.9}\ (\mathsf{stat.}) \pm 2.3\ (\mathsf{syst.})\right) \times 10^{-3}. \tag{8.11}$$

These results are close to the expected values, as calculated from the world averages. The improvement comparing to a previous analysis [97] is achieved due to several factors, the main being the larger dataset analyzed and improved analysis strategy. The results for R^+ and R^- are obtained for the first time.

Chapter 9

Phenomenological Impact of the Measurements

In this Chapter, the phenomenological impact of the measurements performed in this thesis is presented. We first describe the determination of $r_{\rm B}$, γ, and $\delta_{\rm B}$ obtained with the ADS analysis that was discussed in Chapter 8 and the combination with other available measurements. In the second part we show the impact of the results on search for the $B^+ \to D^+ K^{(*)0}$ to the prediction of the $r_{\rm B}$ values

9.1 The Impact of the ADS Analysis

In this Section, we present the extraction procedure of the γ, $r_{\rm B}$, and $\delta_{\rm B}$ variables from the measurements of the $R_{\rm ADS}$, R^+, and R^- ratios.

The procedure is first validated using toy-MC experiments and finally applied to the results obtained on data. The analyses used are $B^+ \to D^0 K^+$ with $D^0 \to K^-\pi^+$ (referred as $K\pi$ analysis) and with $D^0 \to K^-\pi^+\pi^0$ ($K\pi\pi^0$ analysis) and their combination.

For the extraction procedure we use the formula derived in Section 3.1.2:

$$\begin{aligned} R_{\rm ADS} &= r_{\rm B}^2 + r_{\rm D}^2 + 2 r_{\rm B} r_{\rm D} k_{\rm D} \cos\gamma \cos\delta, \\ R^+ &= r_{\rm B}^2 + r_{\rm D}^2 + 2 r_{\rm B} r_{\rm D} k_{\rm D} \cos(\gamma + \delta), \\ R^- &= r_{\rm B}^2 + r_{\rm D}^2 + 2 r_{\rm B} r_{\rm D} k_{\rm D} \cos(\gamma - \delta), \\ A_{\rm ADS} &= \frac{R^- - R^+}{R^- - R^+}, \end{aligned} \tag{9.1}$$

with $\delta = \delta_{\rm B} + \delta_D$. The parameters $r_{\rm D}$, $\delta_{\rm D}$, and $k_{\rm D}$ ($r_{\rm B}$ and $\delta_{\rm B}$) depend on the D (B) meson decay channel.

9.1.1 r_B, γ, and δ_B Extraction Using Toy MC Experiments

We follow a Bayesian approach extracting r_D, δ_D, k_D, R_{ADS}, R^+, and R^- according to their experimental distributions. We use flat distributions for r_B, $[0; 0.3]$, γ, $[0°; 360°]$, and δ_B, $[0°; 360°]$. The distributions for r_D, R_{ADS}, R^+, and R^- are taken to be Gaussian, while the 2D experimental likelihood from the CLEO-c experiment [59] is used for δ_D and k_D. The likelihood for A_{ADS} is recalculated from the R^+ and R^-using Bayesian approach.

The central value of R_{ADS}(or $R^\pm$) are chosen according to the values of $\{r_B; \gamma; \delta_B\}$ and $\{r_D; \delta_D; k_D\}$ shown in Table 9.1.

observable	r_B	γ	δ_B	r_D	δ_D	k_D
value	0.1	74°	126°	0.047	47°	0.83

Table 9.1: The central values of the observables used to generate the toy MC.

The results of the extraction are shown Table 9.2. From this table one can conclude that the two methods of extraction (either from $\{R_{ADS}; A_{ADS}\}$ or from $\{R^+; R^-\}$) give comparable precision. In order not to depend on the possible correlations between R_{ADS} and A_{ADS} we decide to use the extraction from $\{R^+; R^-\}$ in the following.

We also show the r_B probability distribution (Figure 9.1) and 2D likelihood for $\{\delta_B; \gamma\}$ (Figure 9.2) with the errors expected for the $K\pi\pi^0$ analysis and the plots obtained by combining the $K\pi\pi^0$ and $K\pi$ analyses. The errors listed correspond to the 68% probability regions and are consistent with the generated one.

Decay chain	Fitted variable	r_B	95% prob. range
$D \to K\pi$	$R_{ADS}(K\pi) = (1.55 \pm 0.63) \times 10^{-2}$, $A_{ADS}(R^+, R^-)$	$0.11^{+0.04}_{-0.05}$	$[0.0117, 0.1796]$
$D \to K\pi$	$R^+(K\pi) = (2.3 \pm 0.9) \times 10^{-2}$, $R^-(K\pi) = (0.76 \pm 0.7) \times 10^{-2}$	$0.10^{+0.04}_{-0.05}$	$[0.0024, 0.166]$
$D \to K\pi\pi^0$	$R_{ADS}(K\pi\pi^0) = (0.94 \pm 0.63) \times 10^{-2}$, $A_{ADS}(R^+, R^-)$	$0.07^{+0.04}_{-0.06}$	$[0, 0.1396]$
$D \to K\pi\pi^0$	$R^+(K\pi\pi^0) = (0.7 \pm 0.9) \times 10^{-2}$, $R^-(K\pi\pi^0) = (1.2 \pm 0.95) \times 10^{-2}$	$0.07^{+0.04}_{-0.05}$	$[0, 0.1377]$
combination	R_{ADS}, $A_{ADS}(R^+, R^-)$	$0.08^{+0.03}_{-0.03}$	$[0.0167, 0.1338]$
combination	R^+, R^-	$0.08^{+0.03}_{-0.03}$	$[0.0108, 0.1286]$

Table 9.2: r_B measurements extracted from different fitting variables and analyses.

The distributions obtained for r_B are not of Gaussian shape (while R_{ADS}, R^+, and R^- are described by a Gaussian distribution), in particular the tail for the low values of r_B comes from the functional dependence $R_{ADS} \sim r_B^2$ and accounts for the fact that we cannot exclude $r_B = 0$ with higher probability for r_B than we exclude $R_{ADS} = 0$. Another reason of non-gaussianity of the r_B distribution is coming from the presence of the $r_B$ambiguity(see test for 50 ab^{-1}).

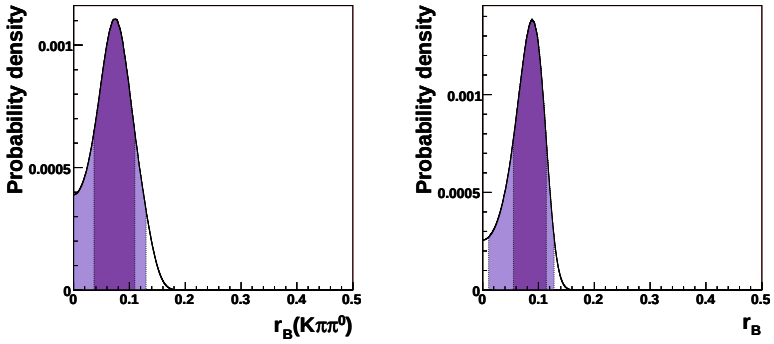

Figure 9.1: The results of the $r_{\rm B}$ extraction from $R^{\pm}$ observables for the $K\pi\pi^0$ analysis (left) and its combination with the $K\pi$ analysis (right) using the toy MC. The dark and light shaded zones represent the 68% and 95% probability regions, respectively. The generated value is $r_{\rm B} = 0.1$

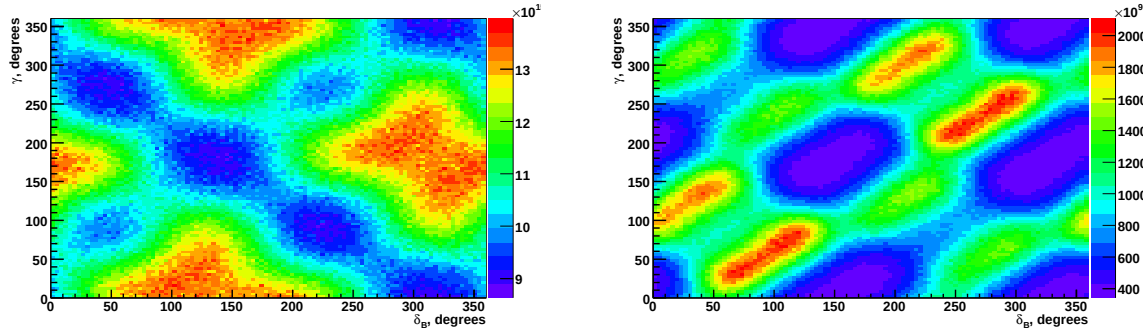

Figure 9.2: The extracted 2D likelihood $\{\delta_{\rm B}; \gamma\}$ using toy MC and for the errors foreseen for the $K\pi\pi^0$ analysis (left) and its combination with the $K\pi$ analysis (right). The generated values are $\{\gamma; \delta_{\rm B}\} = \{74^\circ; 114^\circ\}$.

We test the importance of the measurements of $r_{\rm D}$, $\delta_{\rm D}$, and $k_{\rm D}$ in the precision of the $r_{\rm B}$ determination. Figure 9.3 shows the evolution of the error on $r_{\rm B}$ for the combination of two channels in different configurations:

- no measurements of $\delta_{\rm D}$ and $k_{\rm D}$. $r_{\rm D}$, R^+, and R^- errors are scaled with square root of luminosity;
- measurements of $\delta_{\rm D}$ and $k_{\rm D}$ are taken from the likelihoods of CLEO-c collaboration. $r_{\rm D}$, R^+, and R^- errors are scaled with square root of luminosity;
- values of $\delta_{\rm D}$ and $k_{\rm D}$ are fixed to central values given by CLEO-c collaboration. $r_{\rm D}$, R^+, and R^- errors are scaled with square root of luminosity.

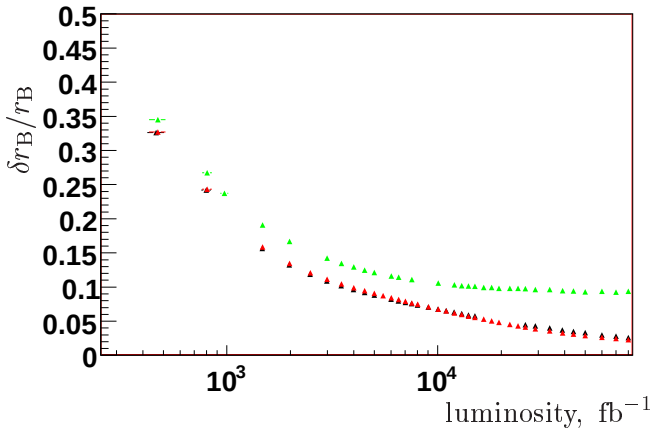

Figure 9.3: The relative RMS of the r_B extraction as a function of luminosity (see text for details). The green triangles correspond to the result without δ_D and k_D measurements, black (red) triangles correspond to the use of the δ_D and k_D with the present (no) errors.

It can be noted that the variation of the errors shows that the measurements in charm sector are important to get the present uncertainty but the improvements on these measurements will not impact the precision on r_B.

The extraction procedure is tested using statistics equivalent to 50 ab^{-1} (which is the projected integrated luminosity of the SuperB experiment). The resulting probability distributions for r_B in case of the $K\pi$, $K\pi\pi^0$, and the combination of the two are presented in Figures 9.4. The r_B distributions extracted from a single channel have several most probable values. This ambiguity is coming from the fact that r_B is reconstructed with other 2 unknowns: δ_B and γ. When we combine $K\pi$ and $K\pi\pi^0$ the ambiguity disappears and only the r_B value corresponding to the generated one is present. Using the $K\pi$ and $K\pi\pi^0$ analyses r_B can be measured with the precision of 5%. Figure 9.5 shows the result of the γ extraction for the case of using (or not using) δ_D and k_D.

9.1.2 The r_B and γ Extraction from Data

Following the procedure described in Section 9.1.1, we used the results obtained in Chapter 8 ($R^+(K\pi\pi^0) = \left(5.0^{+12.8}_{-11.0}\ (\text{stat.}) \pm 3.8\ (\text{syst.})\right) \times 10^{-3}, R^-(K\pi\pi^0) = \left(13.2^{+12.8}_{-10.9}\ (\text{stat.}) \pm 2.3\ (\text{syst.})\right) \times 10^{-3}$). We extract r_B from the $K\pi\pi^0$ analysis:

$$\begin{aligned} &r_B(K\pi\pi^0) = 0.078^{+0.033}_{-0.063}, \\ &r_B(K\pi\pi^0) \in [0, 0.138] \text{ at } 90\% \text{ probability}\ . \end{aligned} \tag{9.2}$$

This leads to the upper limit of:

$$r_B\ < 0.14 \text{ (at } 90\% \text{ probability)}. \tag{9.3}$$

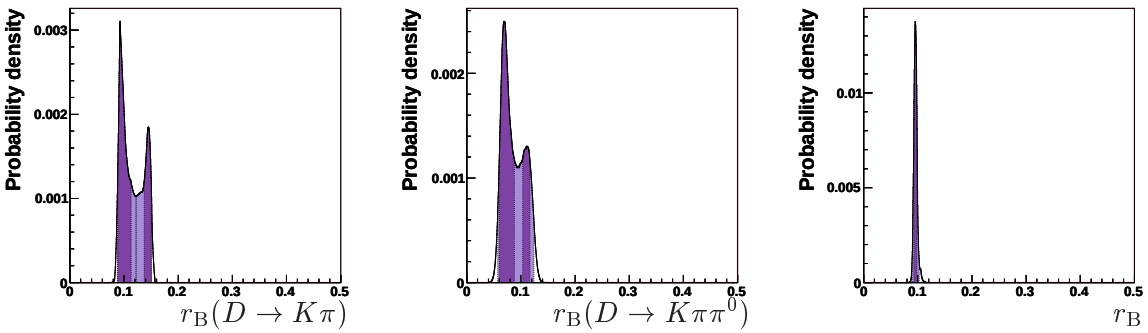

Figure 9.4: [50 ab^{-1}] The probability distributions for r_B for the $K\pi$ (left) and $K\pi\pi^0$ (central), and the combination of the two analyses (right). The dark and light shaded zones represent the 68% and 95% probability regions, respectively. The generated value is $r_B = 0.096$

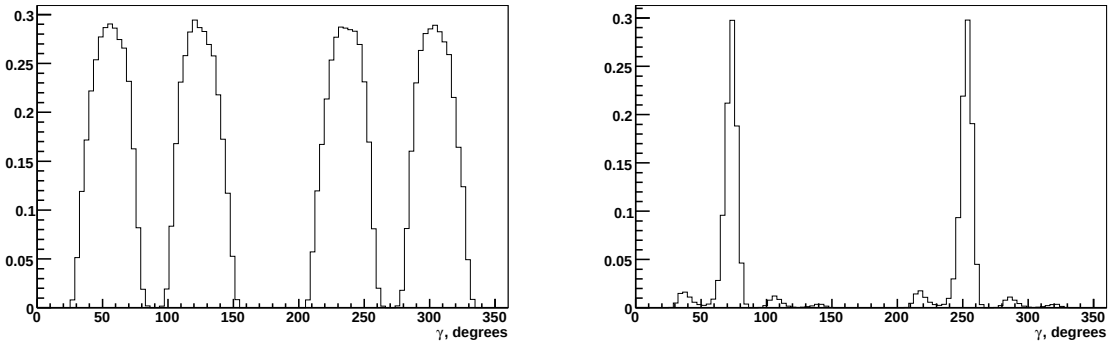

Figure 9.5: [50 ab^{-1}] The probability distributions for γ extracted from the combination of $K\pi$ and $K\pi\pi^0$ analyses. The extraction is performed in case of no δ_D and k_D measurements (left) and using δ_D, k_D (right). The generated value is $\gamma = 74^\circ$

The probability distribution is shown in Figure 9.6.

For the $B^+ \to D^0 K^+$ with $D^0 \to K^+\pi^-$ analysis we use:

$$\begin{aligned} R^+(K\pi) &= \left(21.9 \pm 9.0\ (\text{stat.})^{+2.0}_{-2.6}\ (\text{syst.})\right) \times 10^{-3}, \\ R^-(K\pi) &= \left(1.7^{\pm}5.9\ (\text{stat.}) \pm 1.8\ (\text{syst.})\right) \times 10^{-3} \end{aligned} \tag{9.4}$$

and obtain the following results:

$$\begin{aligned} &r_B(K\pi) = 0.087^{+0.032}_{-0.057}, \\ &r_B(K\pi) \in [0, 0.128]\ (\text{at } 90\%\ \text{probability}). \end{aligned} \tag{9.5}$$

That can be compared to the output of the frequentist approach, as quoted in [64]:

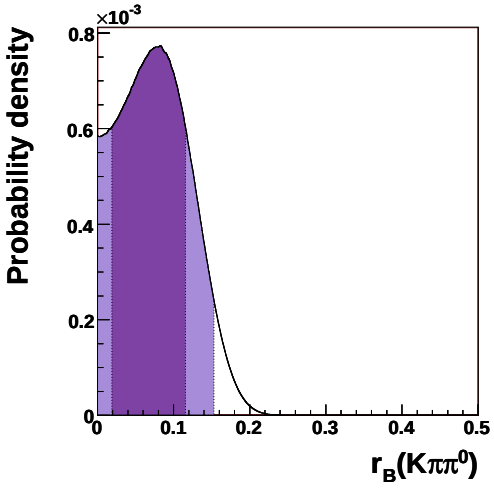

Figure 9.6: Probability distribution for r_{B} obtained using the result of the $B^+ \to D^0 K^+$ with $D^0 \to K^+\pi^-\pi^0$ analysis presented in this thesis.

$$\begin{aligned} &r_{\mathrm{B}}(K\pi,\ \text{freq.}) = 0.095^{+0.051}_{-0.041}, \\ &r_{\mathrm{B}}(K\pi) \in [0, 0.167] \text{ at (90\% confidence level).} \end{aligned} \tag{9.6}$$

When combining the two analysis both r_{B} and γ can be obtained. The probability density functions obtained combining the $K\pi\pi^0$ and the $K\pi$ analyses are shown in Figure 9.7, which leads to a result:

$$\begin{aligned} &r_{\mathrm{B}}(comb.) = 0.083^{+0.028}_{-0.043}, \\ &r_{\mathrm{B}}(comb.) \in [0.009, 0.119] \text{ at (90\% probability).} \end{aligned} \tag{9.7}$$

For γ we receive two possibilities different by modulus 180°:

$$\gamma(\text{comb.}) = 86^{\circ}{}^{+51^{\circ}}_{-45^{\circ}} \bmod \pi \tag{9.8}$$

This result includes the ambiguities discussed in Section 3.1.2.

9.2 The DK System Description

The $B \to DK$ decays can be described in terms of only four amplitudes $|\bar{T}|$, $|\bar{C}|$, $|C|$, $|A|$, and their relative phases $\phi_{\bar{C}}$, ϕ_C, and ϕ_A (see Chapter 4 for definitions and discussions). The

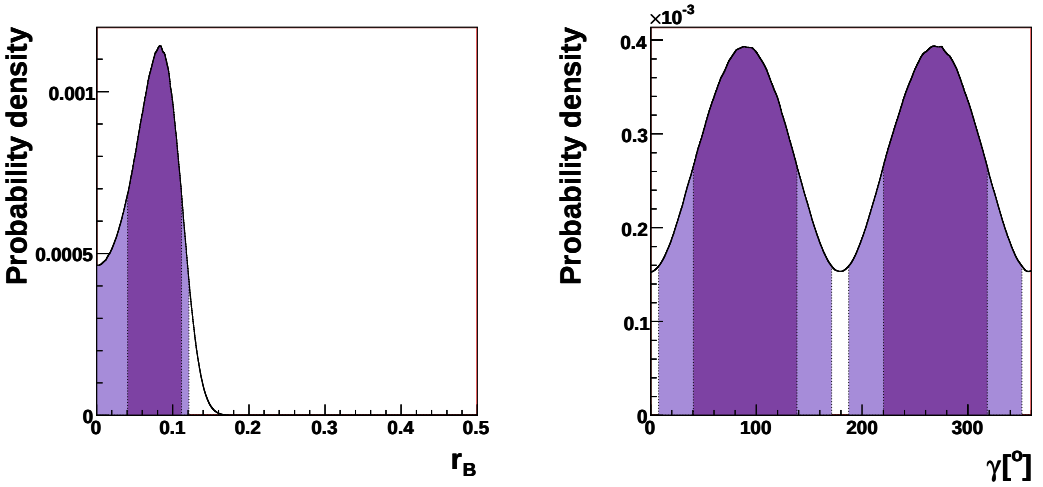

Figure 9.7: Probability distribution for $r_{\rm B}$ (left) and γ (right) obtained from the combination of the $K\pi\pi^0$ and $K\pi$ analyses.

resulting system is formed of six equations and have six unknowns.

$$
\begin{aligned}
\mathcal{B}(B^+ \to \overline{D}^0 K^+) &= (|\bar{T}|^2 + |\bar{C}|^2 + 2|\bar{T}||\bar{C}|\cos(\phi_{\bar{C}})), \\
\mathcal{B}(B^0 \to D^- K^+) &= |\bar{T}|^2, \\
\mathcal{B}(B^0 \to \overline{D}^0 K^0) &= |\bar{C}|^2, \\
\mathcal{B}(B^+ \to D^+ K^0) &= |A|^2; \\
\left(r_{\rm B}^+\right)^2 &= \frac{|C|^2 + |A|^2 + 2|C||A|\cos(\phi_C - \phi_A)}{|\bar{T}|^2 + |\bar{C}|^2 + 2|\bar{T}||\bar{C}|\cos(\phi_{\bar{C}})}, \\
\left(r_{\rm B}^0\right)^2 &= \frac{|C|^2}{|\bar{C}|^2},
\end{aligned}
\tag{9.9}
$$

The observables in the left-hand side of the system are taken from PDG [77] (for equations 1-3), from the measurements made in this thesis (equation 4), and from the results obtained by UTfit collaboration [17] (equations 5 and 6). For equation 6 the result presented in this thesis in this paragraph is also used.

The aim of the study presented here is to determine the unknowns and/or improving the precision on the observables using the relations exposed in Equations 9.9. Also in case of the absence of same of the six measurements, this system can give predictions for the values of missing observables.

The results for the DK and DK^* systems are discussed in the corresponding sections.

9.2.1 The $B \to DK^*$ Decay Mode System

For the $B \to DK^*$ decays we have the information of all six observables including the likelihood for the $\mathcal{B}(B^+ \to D^+K^{*0})$ presented in this thesis. The results are reported in Table 9.3. The input and output probability distributions are shown in Figures 9.8 and 9.9, respectively.

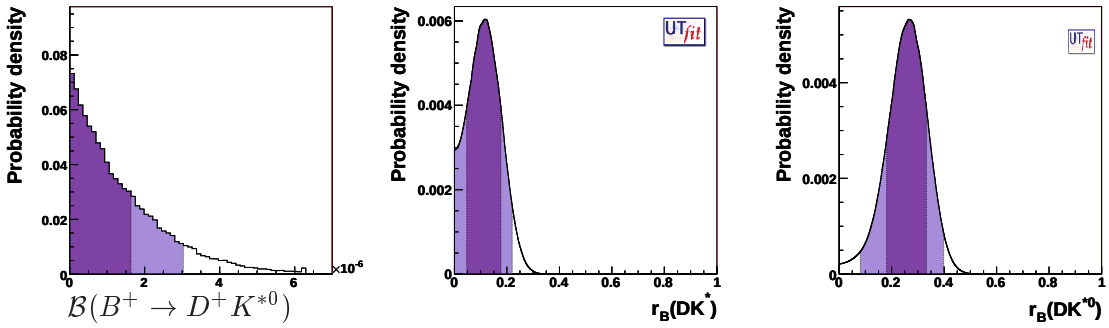

Figure 9.8: [The $B \to DK^*$ mode system] The likelihoods used as inputs to system of Equations 9.9 for the $B \to DK^*$ modes: $\mathcal{B}(B^+ \to D^+K^{*0})$, $r_{\rm B}^+$, $r_{\rm B}^0$.

Measurement	input	output
$\mathcal{B}(B^+ \to \overline{D}^0 K^{*+})$	$(5.3 \pm 0.4) \times 10^{-4}$	$(5.3 \pm 0.4) \times 10^{-4}$
$\mathcal{B}(B^0 \to D^- K^{*+})$	$(4.5 \pm 0.7) \times 10^{-4}$	$(4.4 \pm 0.7) \times 10^{-4}$
$\mathcal{B}(B^0 \to \overline{D}^0 K^{*0})$	$(4.2 \pm 0.6) \times 10^{-5}$	$(4.2 \pm 0.6) \times 10^{-5}$
$\mathcal{B}(B^+ \to D^+ K^{*0})$	$< 3 \times 10^{-6*}$ (@90% prob.)	$< 3 \times 10^{-6}$ (@90% prob.)
$r_B^+(DK^*)$	$0.13 \pm 0.09^*$	0.08 ± 0.03
$r_B^0(DK^*)$	$0.26 \pm 0.08^*$	0.27 ± 0.08

Table 9.3: Results obtained using Equations 9.9 for the $B \to DK^*$ decay mode system. In the second column we list the values used as inputs whereas in the third column we show the results. Asterisk marks that the likelihood is used as an input for this observable.

An important result is the improvement of a factor about three on the precision for the $r_{\rm B}^+(DK^*)$ determination. This improvement is due to the use of the correlations between $r_{\rm B}^+$ and $r_{\rm B}^0$ as shown in Equation 4.21.

Another interesting result that can be obtained from this system is the probability of the $\frac{|A|}{|C|}$. In fact the measurements of $r_{\rm B}^0(DK^*)$ gives access to $|C|$ whereas the analysis presented in Chapter 7 of this thesis allows to set a limit on the amplitude $|A|$. We can thus express this limit as:

$$\frac{|A|}{|C|} < 0.6 \text{ @90\% probability} \tag{9.10}$$

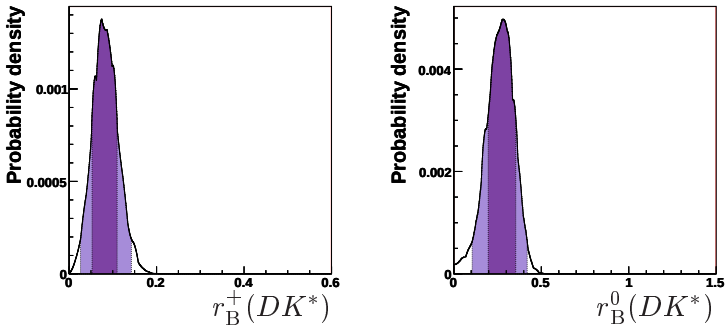

Figure 9.9: [The $B \to DK^*$ decay mode system] The pdfs for $r_{\rm B}^{+}(DK^*)$ and $r_{\rm B}^{0}(DK^*)$ obtained using the measurements in the $B \to DK^*$ system.

9.2.2 The $B \to DK$ Decay Mode System

For this system we do not dispose of the measurement of $r_{\rm B}^0(DK)$. The use of System 9.9 allows to predict the value of $r_{\rm B}^0$. The probability distributions of $\mathcal{B}(B^+ \to D^+K^0)$ and $r_{\rm B}^+$ are shown in Figure 9.10. The likelihood of the $\mathcal{B}(B^+ \to D^+K^0)$ is obtained in this thesis. For $r_{\rm B}^+$ we use all the available measurements including the one obtained in this thesis (Chapter 8).

The results of the analysis are shown in Table 9.4.

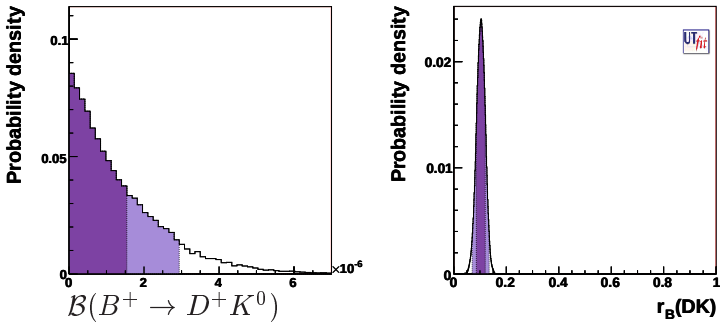

Figure 9.10: [The $B \to DK$ decay mode system] The likelihoods used as inputs for Equations 9.9 in the $B \to DK$ decay mode: $\mathcal{B}(B^+ \to D^+K^0)$, $r_{\rm B}^+$.

We found the value of $r_{\rm B}^0 = 0.27 \pm 0.09$. The corresponding pdf is shown in Figure 9.11. This large value is similar to the one measured in the DK^* system (0.27 ± 0.08). This prediction can be used as an input for the time-dependent analysis of $B^0 \to D^0K^0$ decay aiming the extraction of $2\beta + \gamma$.

Measurement	input	output
$\mathcal{B}(B^+ \to \overline{D}^0K^+)$	$(3.7 \pm 0.3) \times 10^{-4}$	$(3.6 \pm 0.3) \times 10^{-4}$
$\mathcal{B}(B^0 \to D^-K^+)$	$(2.0 \pm 0.6) \times 10^{-4}$	$(2.0 \pm 0.5) \times 10^{-4}$
$\mathcal{B}(B^0 \to \overline{D}^0K^0)$	$(5.2 \pm 0.7) \times 10^{-5}$	$(5.2 \pm 0.7) \times 10^{-5}$
$\mathcal{B}(B^+ \to D^+K^0)$	$< 2.9 \times 10^{-6}$ (@90% prob.)*	$< 3 \times 10^{-6}$ (@90% prob.)
r_B^+	0.10 ± 0.02*	0.10 ± 0.02
r_B^0	—	0.27 ± 0.09

Table 9.4: Results obtained using Equations 9.9 for the $B \to DK$ decay mode system. In the second column we list the values used as inputs whereas in the third column we show the results. Asterisk marks that the likelihood is used as an input for this variable.

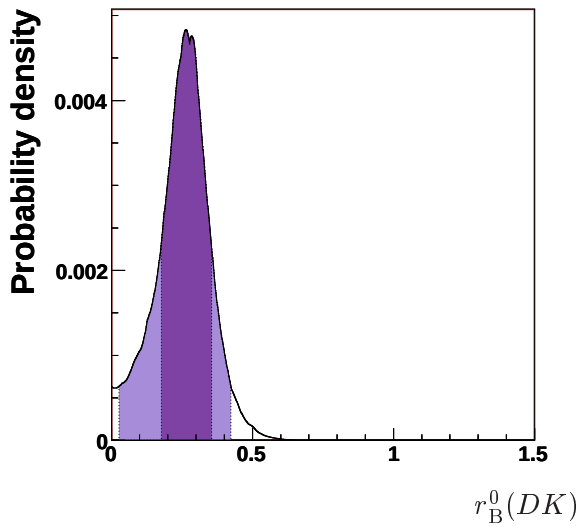

Figure 9.11: [The $B \to DK$ decay mode system] The likelihood of $r_B^0(DK)$ obtained using all the measurements available on the $B \to DK$ system.

Chapter 10

Conclusions

The first analysis presented in this thesis is the search for the rare V_{ub} mediated decay $B^+ \to D^+ K^{(*)0}$. This decay modes are particularly interesting since they are expected to be dominated by weak annihilation processes.

The search for $B^+ \to D^+ K^0$ is done by reconstructing the D^+ meson decaying into $K^-\pi^+\pi^+$, $K^-\pi^+\pi^+\pi^0$, $K^0_S\pi^+$, and $K^0_S\pi^+\pi^0$. No signal is found in 426 fb^{-1} and we obtain the upper limit of

$$\mathcal{B}(B^+ \to D^+ K^0) < 2.9 \times 10^{-6} \text{ at } 90\% \text{ probability.} \tag{10.1}$$

This result updates the previous *BABAR* result of 5.0×10^{-6}.

The decay of $B^+ \to D^+ K^{*0}$ is searched for the first time looking at D^+ decaying into $K^-\pi^+\pi^+$ and $K^0_S\pi^+$ final states. Also for this mode no signal is found and we obtain

$$\mathcal{B}(B^+ \to D^+ K^{*0}) < 3 \times 10^{-6} \text{ at } 90\% \text{ probability.} \tag{10.2}$$

We also presented the analysis of the $B^+ \to D^0(\overline{D}^0)K^+$, $D^0(\overline{D}^0) \to K^+\pi^-\pi^0$ decay modes analyzed through the ADS method. The results we obtained are expressed in terms of the ratio $R_{\rm ADS}$,

$$R_{\rm ADS} = \left(8.9^{+8.2}_{-7.4}\ (\text{stat.}) \pm 2.5\ (\text{syst.})\right) \times 10^{-3}, \tag{10.3}$$

or of the R^+, R^-ratios separately for B^+ and B^- samples:

$$\begin{aligned} R^+ &= \left(5.0^{+12.8}_{-11.0}\ (\text{stat.}) \pm 3.8\ (\text{syst.})\right) \times 10^{-3}, \\ R^- &= \left(13.2^{+12.8}_{-10.9}\ (\text{stat.}) \pm 2.4\ (\text{syst.})\right) \times 10^{-3}. \end{aligned} \tag{10.4}$$

By using only this analysis no information of γ can be extracted and an upper limit on the ratio $r_{\rm B}$ is obtained to be

$$r_{\rm B} < 0.14 \text{ at } 90\% \text{ probability.} \tag{10.5}$$

If this analysis is combined with an analysis of another D^0 final state ($D^0 \to K\pi$) one obtains

$$r_{\rm B} \ = 0.083^{+0.028}_{-0.043} \tag{10.6}$$

and

$$\gamma(comb.) = 86^{\circ}{}^{+51^{\circ}}_{-45^{\circ}} \text{ with } \pi \text{ ambiguity.} \tag{10.7}$$

The $B \to DK$ or $B \to DK^*$ decay systems can be described in terms of four amplitudes and two phase differences. In general, six observables can be used to constrain these amplitudes and phases: four branching fractions and $r_{\rm B}$ for the charged and neutral modes.

In case of the $B \to DK^*$ system all the observables have been measured, which allows to close the system. The limit on $\mathcal{B}(B^+ \to D^+ K^{*0})$ can be converted into

$$\frac{|A|}{|C|} < 0.6 \text{ at } 90\% \text{ probability.} \tag{10.8}$$

Another important result is the improvement of the of the precision of the $r_{\rm B}$ ratio for the charged mode. The final result gives

$$r_{\rm B}^{+}(DK^*) = 0.08 \pm 0.03. \tag{10.9}$$

For the $B \to DK$ system the situation is different since the measurement of $r_{\rm B}^{0}(DK)$ is lacking. This ratio can be predicted using the results on $r_{\rm B}^{+}(DK)$ and $\mathcal{B}(B^+ \to D^+ K^0)$ obtained in this thesis:

$$r_{\rm B}^{0}(DK) = 0.27 \pm 0.09. \tag{10.10}$$

The prediction of $r_{\rm B}^{0}(DK)$ can be used as an input for the time dependent analysis of $B^0 \to D^0 K^0$ decay aiming to the extraction of $2\beta + \gamma$.

Bibliography

[1] A. Noether Nachr. d. König. Gesellsch. d. Wiss. zu Göttingen, Math-phys. Klasse (1918) 235.

[2] S. L. Glashow, Nucl. Phys. **22**, (1961) 579; S. Weinberg, Phys. Rev. Lett. **19** (1967) 1264; A. Salam Proceedings of the 8th Nobel Symposium, ed. N. Swartholm, Almquist and Wiksells, Stockholm (1968); Gell-Mann Phys. Lett. **8**, 214 (1964); Zweig, CERN Preprint 8182/TH401 (1964).

[3] N. Cabibbo, Phys. Rev. Lett. **10** (1963) 531; M. Kobayashi and T. Maskawa Prog. Theor. Phys. **49** (1973) 652.

[4] See, for example, Joanne L. Hewett *et al.,*The Discovery potential of a Super B Factory, Proceedings, SLAC Workshops, Stanford, USA, 2003, SLAC-R-709

[5] J. H. Christenson, J. W. Cronin, V. L. Fitch, and R. Turlay, Phys. Rev. Lett. 13 (1964) 138.

[6] B. Aubert *et al.,*(*BABAR*Collaboration), Phys Rev Lett **87** (2001) 091801.

[7] I. Bigi and A. Sanda *CP violation.* Cambridge University Press (1999).

[8] L. L. Chan and W. L. Keung, Phys. Rev. Lett. **53** (1984) 1802.

[9] L. Wolfenstein, Phys. Rev. Lett. **51** (1983) 1945.

[10] A. J. Buras, M. E. Lautenbacher and G. Ostermaier, Phys. Rev. D **50** (1994) 3433.

[11] T. Inami and C. S. Lim, Prog. Theor. Phys. **65**, 297 (1981) [Erratum-ibid. **65**, 1772 (1981)].

[12] A. J. Buras, M. Jasmin and P. H. Weisz, Nucl. Phys. **B347** (1990) 491.

[13] T. T. E. Group *et al.,*. [CDF Collaboration], arXiv:0803.1683 [hep-ex].

[14] C. Jarlskog, Phys. Rev. Lett. **55**, (1985) 1039.

[15] method is described in Eur.Phys.J.C **41** 1,2005, results in Moriond 2010 (?). The most recent update can be found in http://ckmfitter.in2p3.fr/ .

[16] G. DAgostini, CERN Report 9903.

[17] method is described in M. Ciuchini *et al.*,, JHEP **0107** (2001) 013. Updated results on the web page http://www.utfit.org.

[18] E. Barberio *et al.* [Heavy Flavor Averaging Group], arXiv:0808.1297. The update can be found in the http://www.slac.stanford.edu/xorg/hfag/index.html.

[19] S. Pruvot, M. H. Schune, V. Sordini and A. Stocchi, arXiv:hep-ph/0703292.

[20] B. Aubert *et al.* [BABAR Collaboration], Phys. Rev. D **66**, 032003 (2002).

[21] B. Aubert *et al.* [BABAR Collaboration], Phys. Rev. D **77**, 111102 (2008).

[22] K. Abe *et al.* [BELLE Collaboration], Phys. Rev. D **73**, 051106 (2006).

[23] T. Aaltonen *et al.* [CDF Collaboration], Phys. Rev. D **81**, 031105 (2010).

[24] B. Aubert *et al.* [BABAR Collaboration], Phys. Rev. D **78**, 092002 (2008).

[25] K. Abe *et al.* [BELLE Collaboration], Phys. Rev. D **73**, 051106 (2006).

[26] B. Aubert *et al.* [BaBar Collaboration], Phys. Rev. D **80**, 092001 (2009).

[27] B. Aubert *et al.* [BaBar Collaboration], EPS 2009 preliminary.

[28] Y. Horii *et al.* [Belle Collaboration], Phys. Rev. D **78**, 071901 (2008).

[29] B. Aubert *et al.* [BaBar Collaboration], Phys. Rev. D **80**, 092001 (2009).

[30] P. del Amo Sanchez *et al.* [The BABAR Collaboration], arXiv:1005.1096 [hep-ex].

[31] A. Poluektov *et al.* [Belle Collaboration], Phys. Rev. D **73**, 112009 (2006).

[32] A. Poluektov *et al.* arXiv:1003.3360 [hep-ex].

[33] B. Aubert *et al.* [BABAR Collaboration], Phys. Rev. D **79**, 072003 (2009).

[34] B. Aubert *et al.* [BaBar Collaboration], Phys. Rev. Lett. **99**, 251801 (2007).

[35] *PEP II - An Asymmetric B Factory, Conceptual Design Report*, SLAC-418, LBL-5379 (1993).

[36] B. Aubert *et al., BABAR* Collaboration, Nucl. Instr. and Methods A **479**, 1 (2002).

[37] P.F. Harrison, ed. *et al.*,, *BABAR* Collaboration, *The BABAR physics book: Physics at an asymmetric B factory.*, SLAC-R-0504 (1998).

[38] B. Aubert *et al.*,*BABAR* Collaboration, *The First Year of the BABAR experiment at PEP-II*, BABAR-CONF-00/17, Contribution to XXX^{th} International Conference of High Energy Physics, Osaka (Japan) (2000).

[39] C. Bozzi *et al.*,Nucl. Instr. and Method A **453**, 78 (2000).

[40] V. Re *et al.*,Nucl. Instr. and Method A **511**, 1 (2003).

[41] G. Sciolla *et al.*,Nucl. Instr. and Method A **419**, 310 (1998).

[42] M. H. Kelsey *et al.*,Nucl. Instr. and Method A **536**, 206 (2004).

[43] I. Adam *et al.*,IEEE Trans. Nucl. Sci. 45, 657 (1998).

[44] I. Adam *et al.*,SLAC-PUB-8783 (2001).

[45] B. Lewandowski *et al.*,Nucl. Instr. and Method A **494**, 302 (2002).

[46] F. Anulli *et al.*,Nucl. Instr. and Method A **409**, 542 (1998).

[47] J. E. Duboscq *et al.*,, CLEO Collaboration, Phys. Rev. Lett. **76**, 3898 (1996).

[48] J. L. Goity and W. Roberts, Phys. Rev. D **51**, 3459 (1995).

[49] P. Billior, Nucl. Instr. and Method A **225**, 225 (1984).

[50] http://www.slac.stanford.edu/BFROOT/www/Physics/Tools/Pid/Selectors/r22a/selectors.html and http://www.slac.stanford.edu/BFROOT/www/Physics/Tools/Pid/Selectors/r24a/selectors.html .

[51] T. Brandt, *"Likelihood based electron identification"*, *BABAR* analysis document 391.

—

M. Bona *et al.*, arXiv:0709.0451 [hep-ex].

[52] M. Gronau and D. London, Phys. Lett. B **253**, 483 (1991).

[53] M. Gronau and D. Wyler, Phys. Lett. B **265**, 172 (1991).

[54] D. Atwood, I. Dunietz and A. Soni, Phys. Rev. Lett. **78**, 3257 (1997) [arXiv:hep-ph/9612433].

[55] D. Atwood, I. Dunietz and A. Soni, Phys. Rev. D **63**, 036005 (2001) [arXiv:hep-ph/0008090].

[56] A. Giri, Y. Grossman, A. Soffer and J. Zupan, Phys. Rev. D **68**, 054018 (2003) [arXiv:hep-ph/0303187].

[57] X. C. Tian et al. (Belle Collab.), Phys. Rev. Lett. 95, 231801 (2005).

[58] B. Aubert *et al.,*(*BABAR* Collab.), Phys. Rev. Lett. 103, 211801.

[59] N. Lowrey et al. CLEO Collaboration Phys. Rev. D **80**, 031105(R) (2009).

[60] M. Gronau, D. Wyler, Phys. Rev. Lett. B **253** (1991) 483; M. Gronau, D. London, Phys. Rev. Lett. B **265** (1991) 172.

[61] I. Dunietz, Phys. Rev. Lett. B **270** (1991) 75; Phys. Rev. Lett. D **52** (1995) 3048; D. Atwood, I. Dunietz and A. Soni, Phys. Rev. Lett. **78**, 3257 (1997).

[62] A. Giri, Y. Grossman, A. Soffer and J. Zupan, Phys. Rev. D **68** (2003) 054018.

[63] B. Aubert *et al.,*(*BABAR* Collab.), Phys. Rev. D **80** (2009) 031102.

[64] *BABAR* collab, to be published in Phys. Rev. **D**.

[65] Y. Horii *et al.,*(Belle Collab.) Phys. Rev. D **78** (2008) 071901.

[66] F. J. Ronga *et al.,*, (Belle Collaboration), Phys. Rev. D **73** (2006) 092003.

[67] B. Aubert *et al.,*(*BABAR* Collab.), Phys. Rev. D **73** (2006) 111101.

[68] B. Aubert *et al.,*(*BABAR* Collab.), Phys. Rev. D **77** (2008) 071102

[69] I. Dunitz, Phys. Lett. B **427** (1998) 179.

[70] G. Eilam *et al.,*, Phys. Rev. Lett. **74**, 4984 (1995); Bediaga *et al.,*, Phys. Rev. Lett. **81**, 4067 (1998). Blanco *et al.,*, Phys. Rev. Lett. **86**, 2720 (2001).

[71] M. Gronau et J. L. Rosner, Phys.Lett. B **572** (2003) 43.

[72] B. Aubert *et al.* [*BABAR*Collaboration], Phys. Rev. D **76**, 052002 (2007); B. Aubert *et al.* [*BABAR*Collaboration], Phys. Rev. D **77**, 011107 (2008); K. Ikado *et al.*, Phys. Rev. Lett. **97**, 251802 (2006).

[73] V. Sordini, M. Pierini, L. Silvestrini, and A. Stocchi in Proceedings of 3rd Workshop on the Unitarity Triangle CKM 2005, San Diego, California, 15-18 Mar 2005, p. 24 [arXiv:hep-ph/0603019].

[74] G. Buchalla, A. J. Buras, and M. E. Lautenbacher, Rev. Mod. Phys. **68** (1996) 1125.

[75] V. Sordini, PhD Thesis, LAL 08-59, Juin 2008.

[76] A. J. Buras and L. Silvestrini Nucl. Phys. B **569** (2000) 3.

[77] C. Amsler *et al.,*. (Particle Data Group), Phys. Lett. B **667**, 1 (2008) and 2009 partial update for the 2010 edition.

[78] P. Billoir. Track Fitting with Multiple Scattering: A New Method. Nucl. Instr. Meth., A **225** (1984) 352.

[79] R.A. Fisher, Annals Eugenics **7**, 179 (1936).

[80] For the list of PID selectors see

[81] http://tmva.sourceforge.net/

[82] F. James and M. Roos Comput. Phys. Commun. **10** (1975) 343.

[83] D. J. Lange, Nucl. Instrum. Meth. A **462** (2001) 152.

[84] T. Sjöstrand, Comput. Phys. Commun, **82** (1994) 74.

[85] S. Agostinelli *et al.,*, Nucl. Instrum. Meth. A **506** (2003) 250.

[86] A. J. Buras and L. Silvestrini, Nucl. Phys. B **569**, 3 (2000).

[87] B. Blok, M. Gronau, and J.L. Rosner, Phys. Rev. Lett. **78** 3999 (1997).

[88] Charge conjugation is implied throughout this paper.

[89] P. F. Harrison, J. Phys. G: Nucl. Part. Phys. **28**, (2002) 2679.

[90] M. Gronau and D. London, Phys. Lett. B **253**, (1991) 483.

[91] B. Aubert et al. (*BABAR* Collaboration), Phys. Rev. D **72**, 011102 (2005).

[92] D. Lange et al. "A B Flavour tagging algorithm for CP violation measurements with the BABAR experiment". BABAR Analysis Document 1025. Unpublished.

[93] G. Cowan. *Statistical Data Analysis* Oxford University Press, 1998.

[94] R. Barlow. *Statistics: A Guide to the Use of Statistical Methods in the Physical Sciences* Wiley, 1989.

[95] H. Albrecht *et al.,*. (ARGUS Collaboration), Z. Phys. C **48**, 543 (1990).

[96] J. E. Gaiser, Ph.D. thesis, Stanford University [SLAC-R-255] (1982).

[97] B. Aubert *et al.* [The BABAR Collaboration], Phys. Rev. D **76** (2007) 111101.

[98] B. Aubert *et al.* [BABAR Collaboration], Phys. Rev. Lett. **97**, 221803 (2006) [arXiv:hep-ex/0608006].

Appendix A

Additional Information on the Search for Rare $B^+ \to D^+ K^{(*)0}$ Decays

In this Chapter some additional information to search for rare $B^+ \to D^+ K^{(*)0}$ decays is presented. This information is crucial for the analysis, but presenting it in main text would harden the reading.

A.1 Observable Distributions

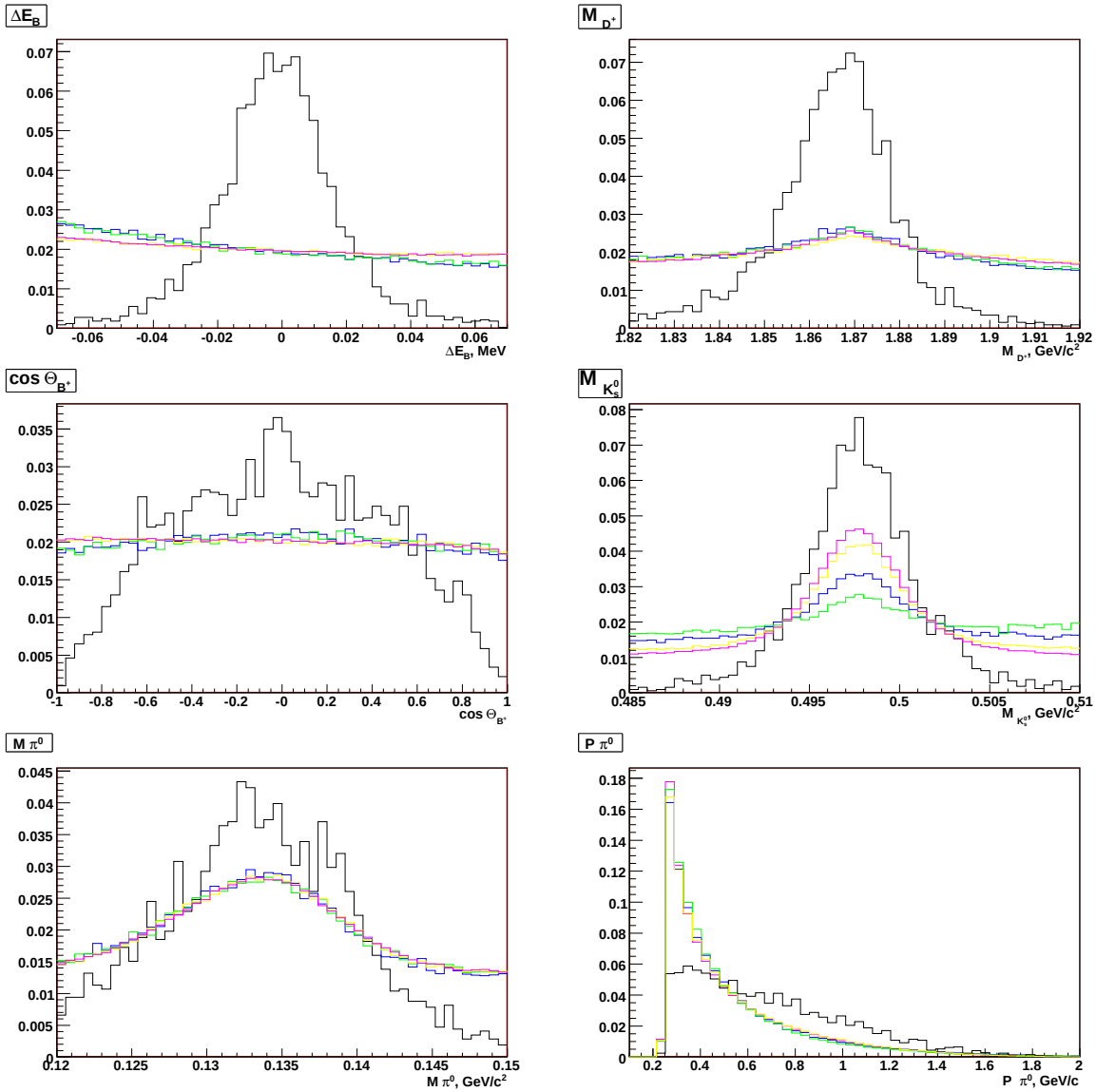

Figure A.1: [$DK_{K\pi\pi\pi^0}$ decay channel] Variable distributions for ΔE (upper left), M_D (upper right), $\cos(\Theta_{B^+})$ (middle left), $M_{K^0_S}$ (middle right), M_{π^0} (bottom left) and P_{π^0} (bottom right). The color codes for histogram corresponds to $c\overline{c}$ background MC magenta, *uds* background MC yellow, $B^0\overline{B}^0$ background MC blue, B^+B^- background MC green, black histograms are for signal MC.

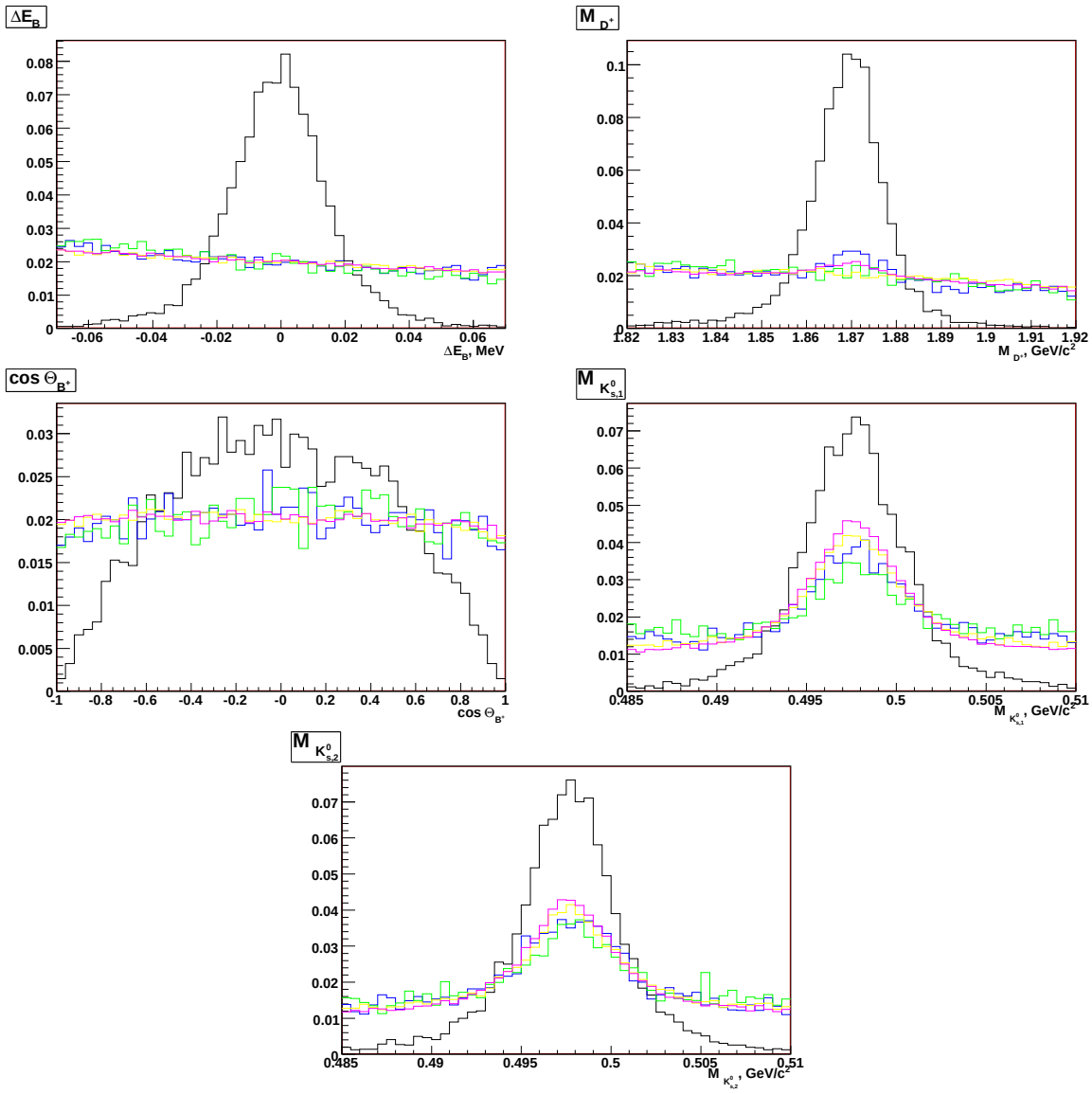

Figure A.2: [$DK^0_S\pi$ decay channel] Variable distributions for ΔE (upper left), M_D (upper right), $\cos(\Theta_{B^+})$ (middle left), $M_{K^0_S,B}$ (middle right) and $M_{K^0_S,D}$ (bottom). The color codes for histogram corresponds to $c\overline{c}$ background MC magenta, uds background MC yellow, $B^0\overline{B}^0$ background MC blue, B^+B^- background MC green, black histograms are for signal MC.

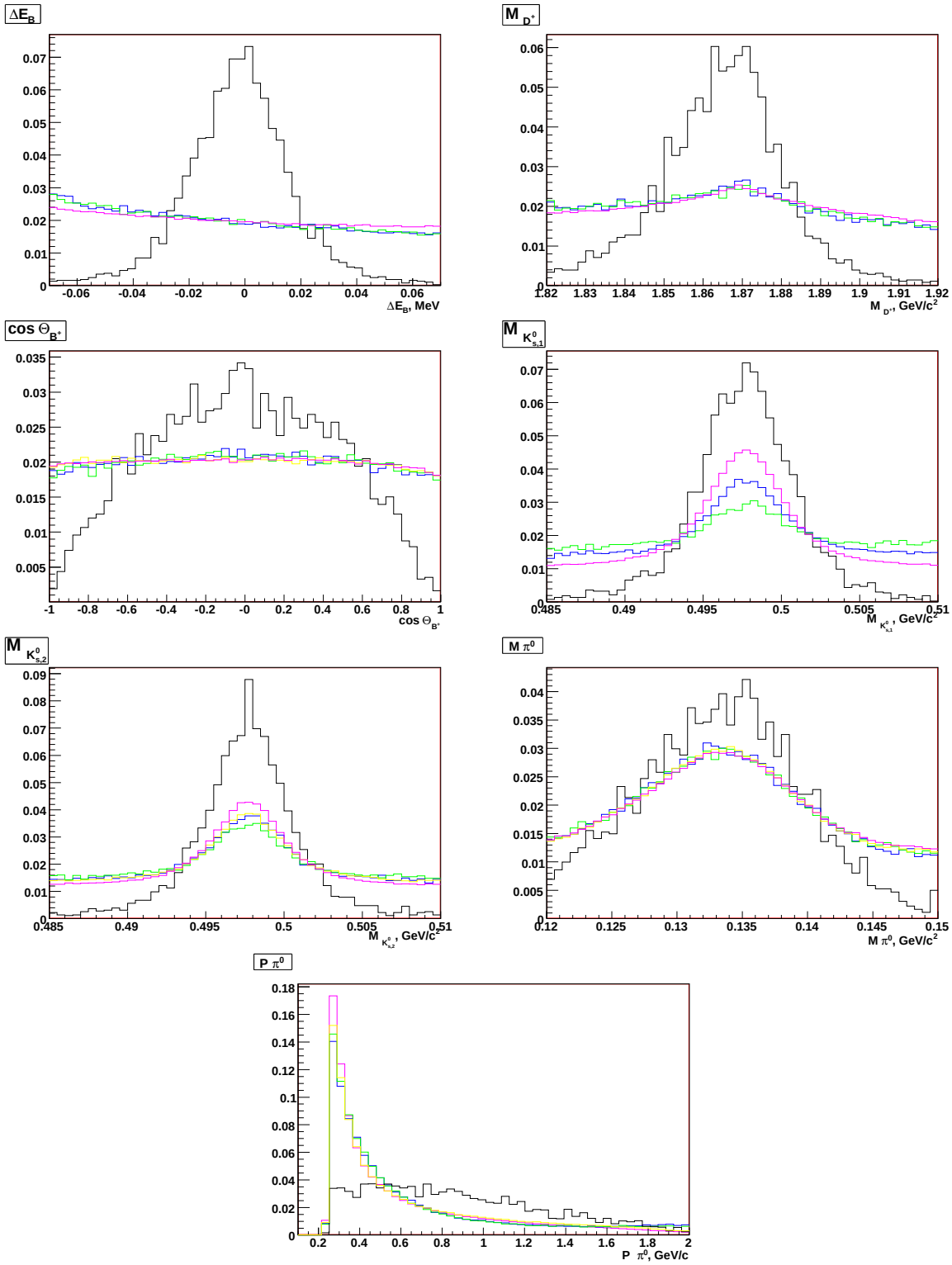

Figure A.3: [$DK_{K^0_S\pi\pi^0}$ decay channel] Variable distributions for ΔE (upper left), M_D (upper right), $\cos(\Theta_{B^+})$ (upper middle left), $M_{K^0_S,B}$ (upper middle right), $M_{K^0_S,2}$ (lower middle left), M_{π^0} (lower middle right) and P_{π^0} (bottom). The color codes for histogram corresponds to $c\bar{c}$ background MC magenta, *uds* background MC yellow, $B^0\overline{B}^0$ background MC blue, B^+B^- background MC green, black histograms are for signal MC.

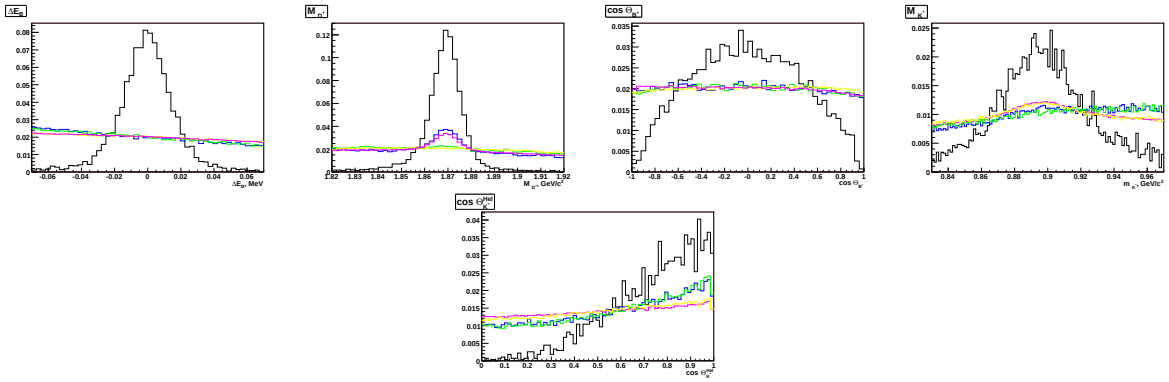

Figure A.4: [$DK^*_{K\pi\pi}$ decay channel] Variable distributions for ΔE, M_D, $\cos(\Theta_{B^+})$, and $M_{K^{*0}}$ (top row, respectively) and $|\cos(\Theta^{Hel}_{K^*})|$ (bottom). The color codes for histogram corresponds to $c\overline{c}$ background MC magenta, *uds* background MC yellow, $B^0\overline{B}^0$ background MC blue, B^+B^- background MC green, black histograms are for signal MC.

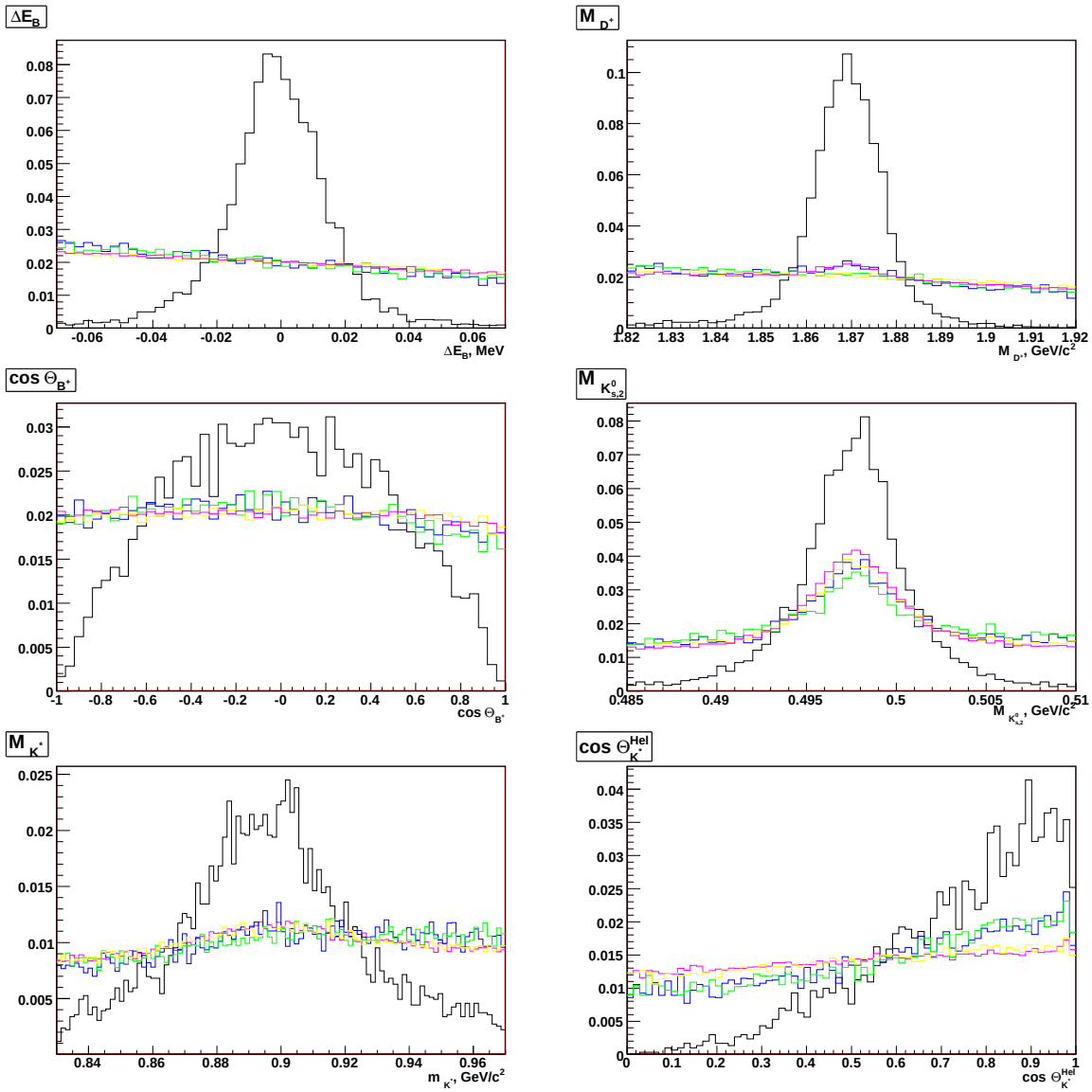

Figure A.5: [$DK^*_{K^0_S\pi}$ decay channel] Variable distributions for ΔE (upper left), M_D (upper right), $\cos(\Theta_{B^+})$ (middle left), $M_{K^0_S,D}$ (middle right), $M_{K^{*0}}$ (bottom left) and $|\cos(\Theta^{Hel}_{K^*})|$ (bottom). The color codes for histogram corresponds to $c\overline{c}$ background MC magenta, uds background MC yellow, $B^0\overline{B}^0$ background MC blue, B^+B^- background MC green, black histograms are for signal MC.

A.2 Global Event Variables

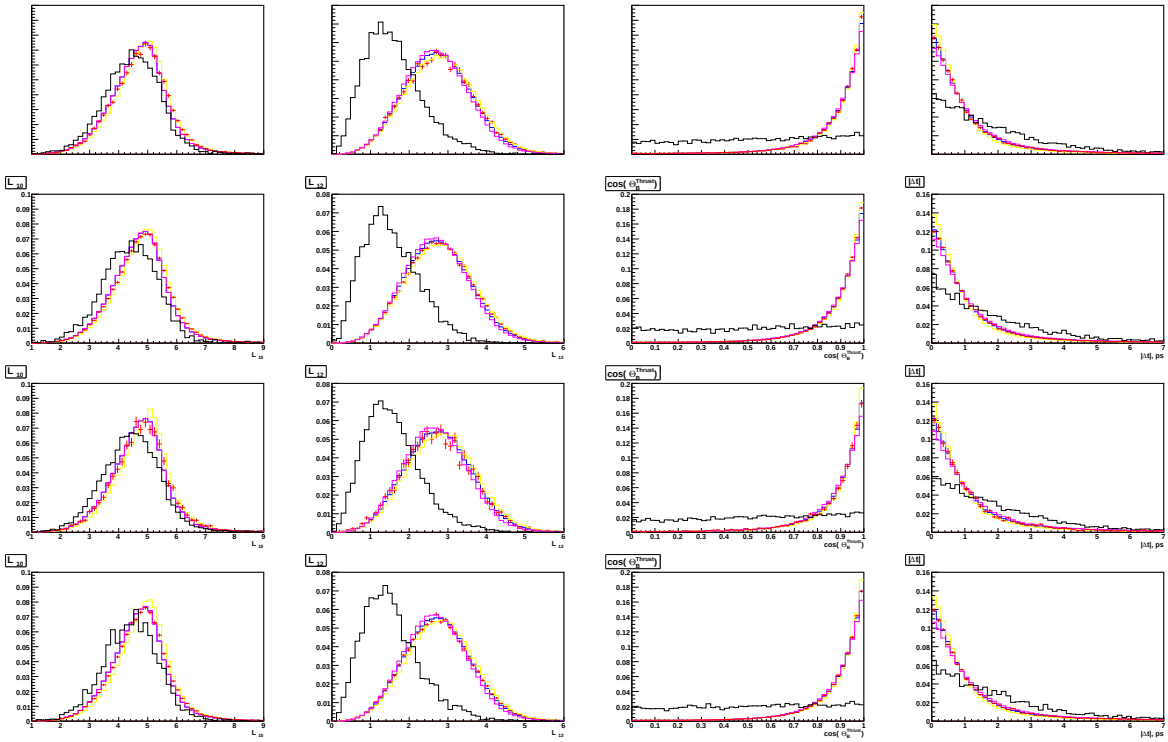

Figure A.6: $[B \to DK]$. Comparison between *uds* MC (yellow), $c\overline{c}$ MC (magenta), a weighted sum of the two (blue), off-resonance data for the variables (red dots with errors) and signal MC (black) chosen to construct the Fisher discriminant. The variables are from left to right: L_{10}, L_{12}, $|cos(\theta_{thrust})|$, and $|\Delta t|$. The rows are for the $DK_{K\pi\pi}$, $DK_{K\pi\pi\pi^0}$, $DK_{K^0_S\pi}$, $DK_{K^0_S\pi\pi^0}$, respectively.

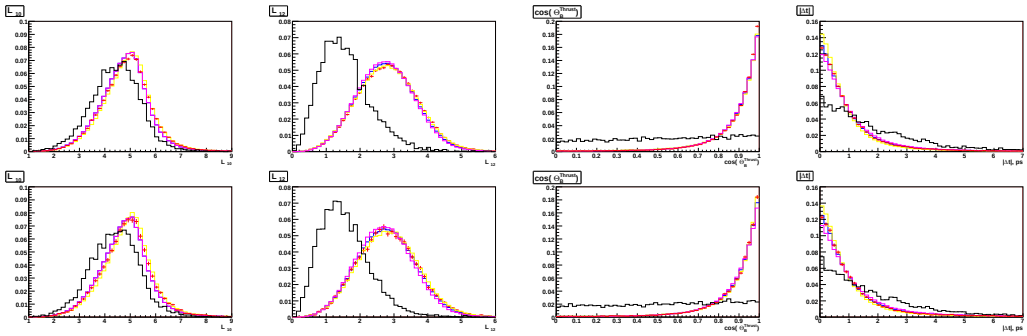

Figure A.7: $[B \to DK]$. Comparison between *uds* MC (yellow), $c\overline{c}$ MC (magenta), a weighted sum of the two (blue), off-resonance data for the variables (red dots with errors) and signal MC (black) chosen to construct the Fisher discriminant. The variables are from left to right: L_{10}, L_{12}, $|cos(\theta_{thrust})|$, and $|\Delta t|$. The rows are for the $DK^*_{K\pi\pi}$ and $DK^*_{K^0_S\pi}$, respectively.

A.3 Peaking background Studies

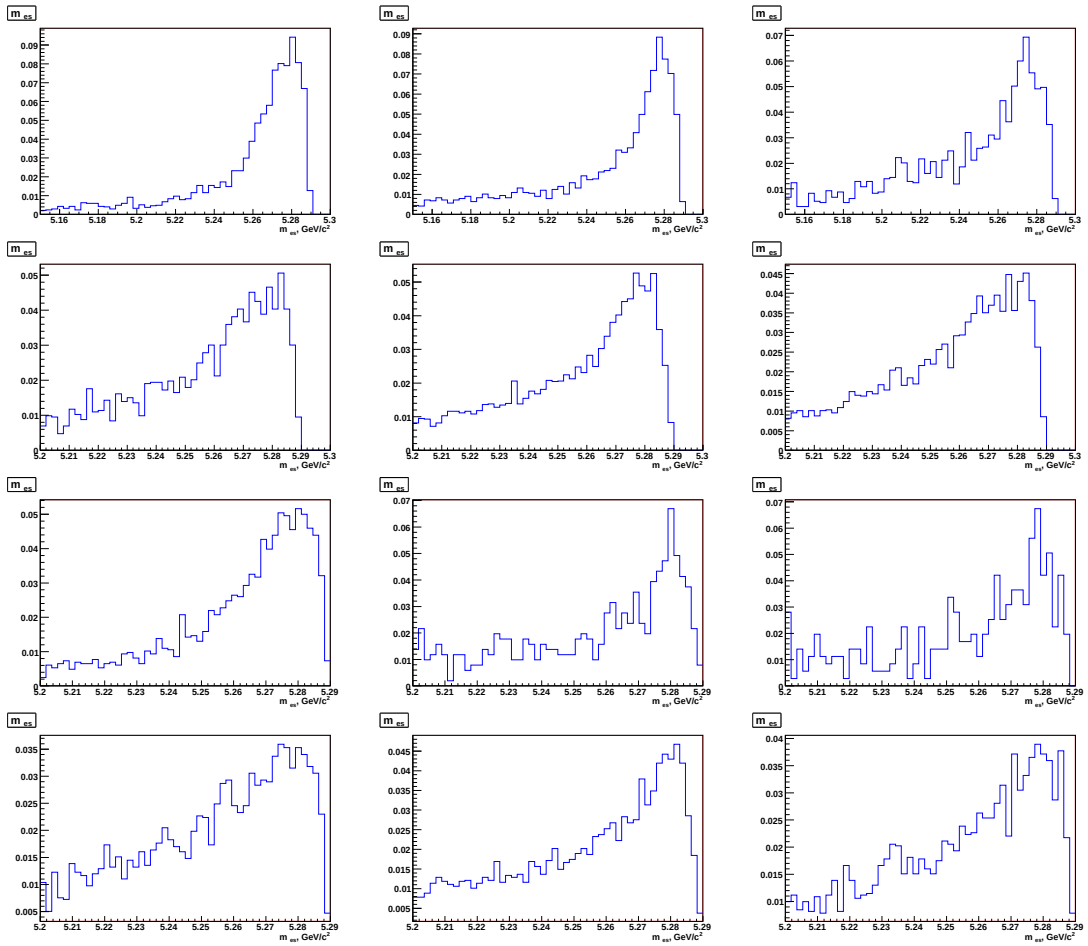

Figure A.8: $[B \to DK]$. $m_{\rm ES}$ distributions for the identified samples of peaking backgrounds: $D\rho$ (left), $\overline{D}^0 K^0$ (center) and $\overline{D}^{*0} K^0$ (right) for the $DK_{K\pi\pi}$ (top row), the $DK_{K\pi\pi\pi^0}$ (second row), the $DK_{K^0_S\pi}$ (third row), and $DK_{K\pi\pi\pi^0}$ (fourth row) modes.

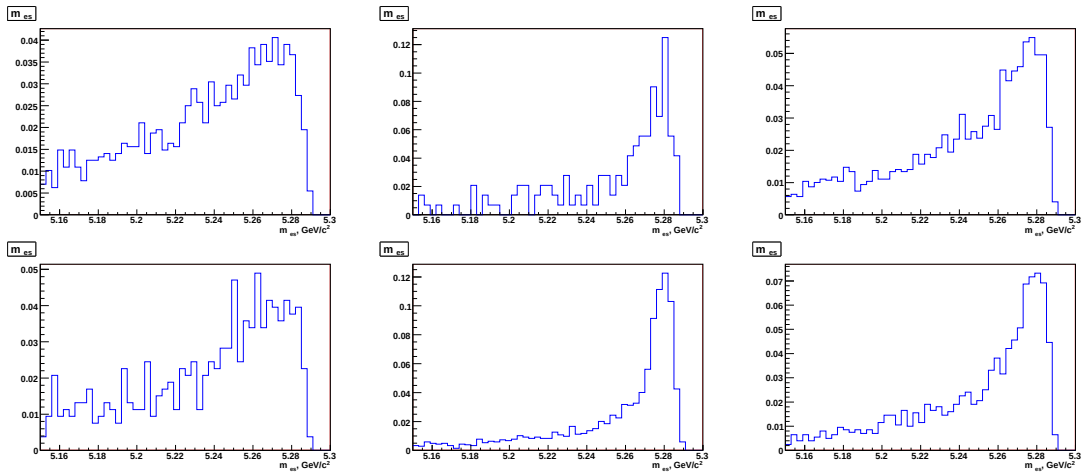

Figure A.9: $[B \to DK^*]$. $m_{\rm ES}$ distributions for the identified samples of peaking backgrounds: $D\rho$ (left), Da_1 (center) and DK^* (right) for the $DK^*_{K\pi\pi}$ (top row) and the $DK^*_{K^0_S\pi}$ (bottom row).

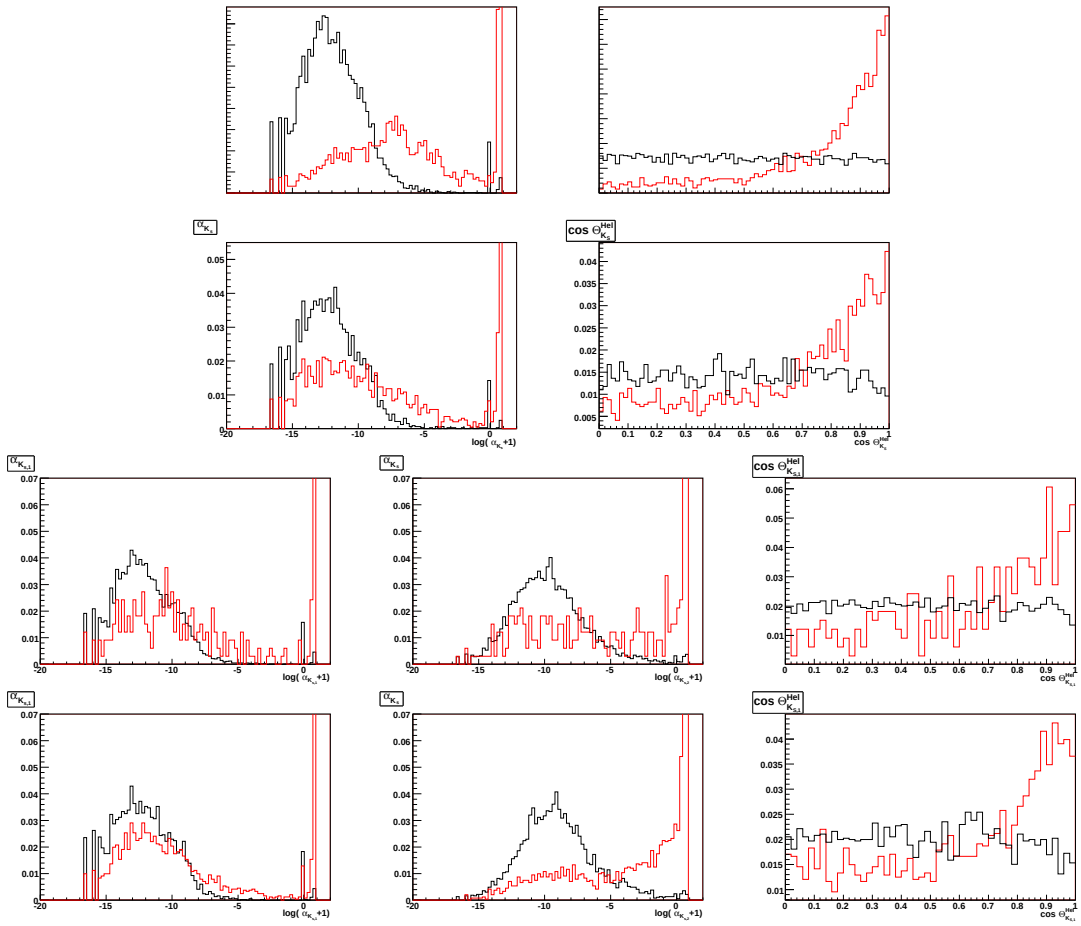

Figure A.10: [$B^+ \to DK$ mode]. Distributions for signal and peaking $B\overline{B}$ background samples for $|cos\Theta^{Hel}_{K^0_S}|$ (left plot), $\log(\alpha_{K^0_S}(B^+)+1)$ (central plot), and $\log(\alpha_{K^0_S}(D^+)+1)$ (right plot, if applicable) for the $DK_{K\pi\pi}$ (top row), the $DK_{K\pi\pi\pi^0}$ (second row), the $DK_{K^0_S\pi}$ (third row), and $DK_{K\pi\pi\pi^0}$ (fourth row) modes. Black and red histograms represent the signal and the peaking $B\overline{B}$ background respectively.

A.4 Comparison between data and simulated events

In Figures A.11 and A.12 the agreement between data and MC for $m_{\rm ES}$ and Fisher variables is shown. The disagreement between the Data and Monte-Carlo is only in normalization but not in shapes. Since we leave the yields free in the fit we consider that this disagreement is not very important in our analysis. The difference in shape is taken into account in the systematics.

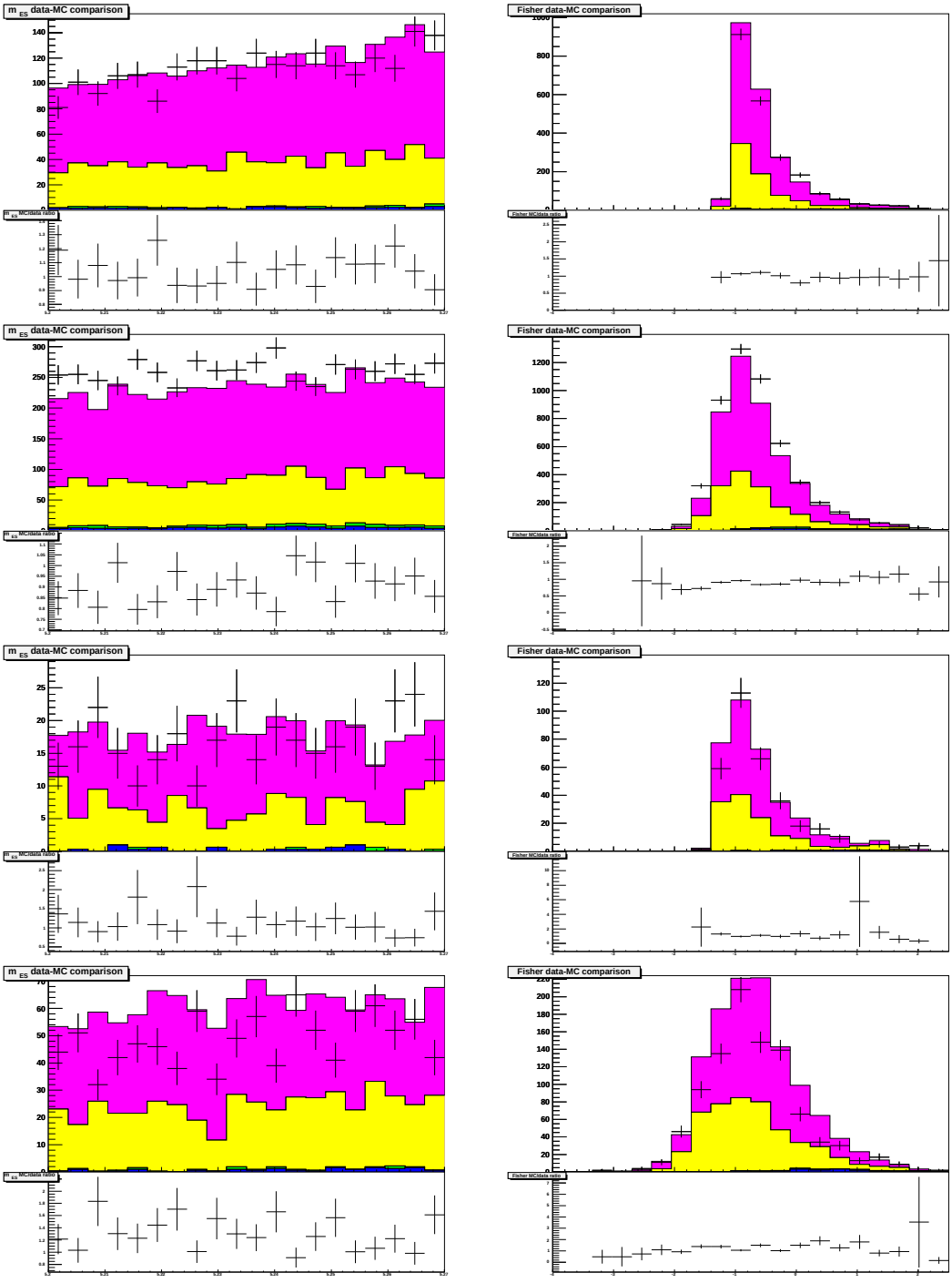

Figure A.11: Data-MC comparison of the m_{ES} distribution (for $m_{\rm ES} < 5.27$ GeV/c^2), and Fisher for $DK_{K\pi\pi}$ (top row), $DK_{K\pi\pi\pi^0}$ (second row), $DK_{K^0_S\pi}$ (third row), and $DK_{K\pi\pi\pi^0}$ (fourth row) decay channels. All the distributions are scaled to the data luminosity (425 fb^{-1}). The black histogram represents the signal, blue, green, yellow and magenta are the contributions from B^+B^-, $B^0\overline{B}^0$, *uds* and $c\overline{c}$ background respectively. Dots with error bars are experimental points.

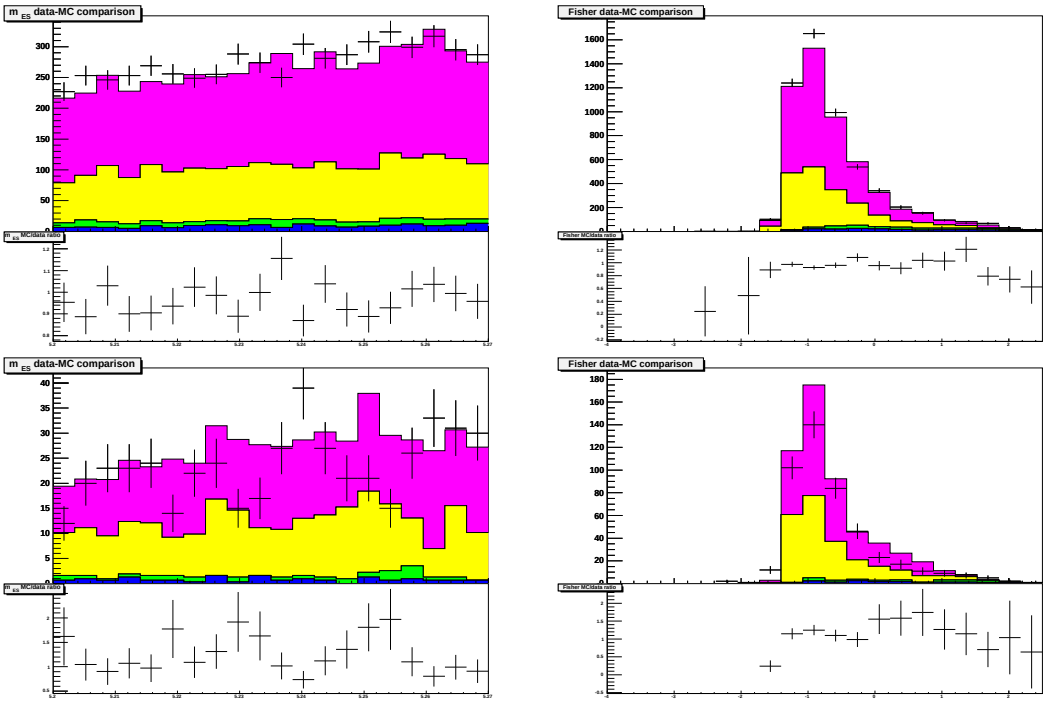

Figure A.12: Data-MC comparison of the m_{ES} distribution (for $m_{\rm ES} < 5.27$ GeV/c^2), and Fisher for $DK^*_{K\pi\pi}$ (top row) and $DK^*_{K^0_S\pi}$ (bottom row) decay channels. All the distributions are scaled to the data luminosity (425 fb^{-1}). The black histogram represents the signal, blue, green, yellow and magenta are the contributions from B^+B^-, $B^0\overline{B}^0$, uds and $c\overline{c}$ background respectively. Dots with error bars are experimental points.

A.5 Parameterizations

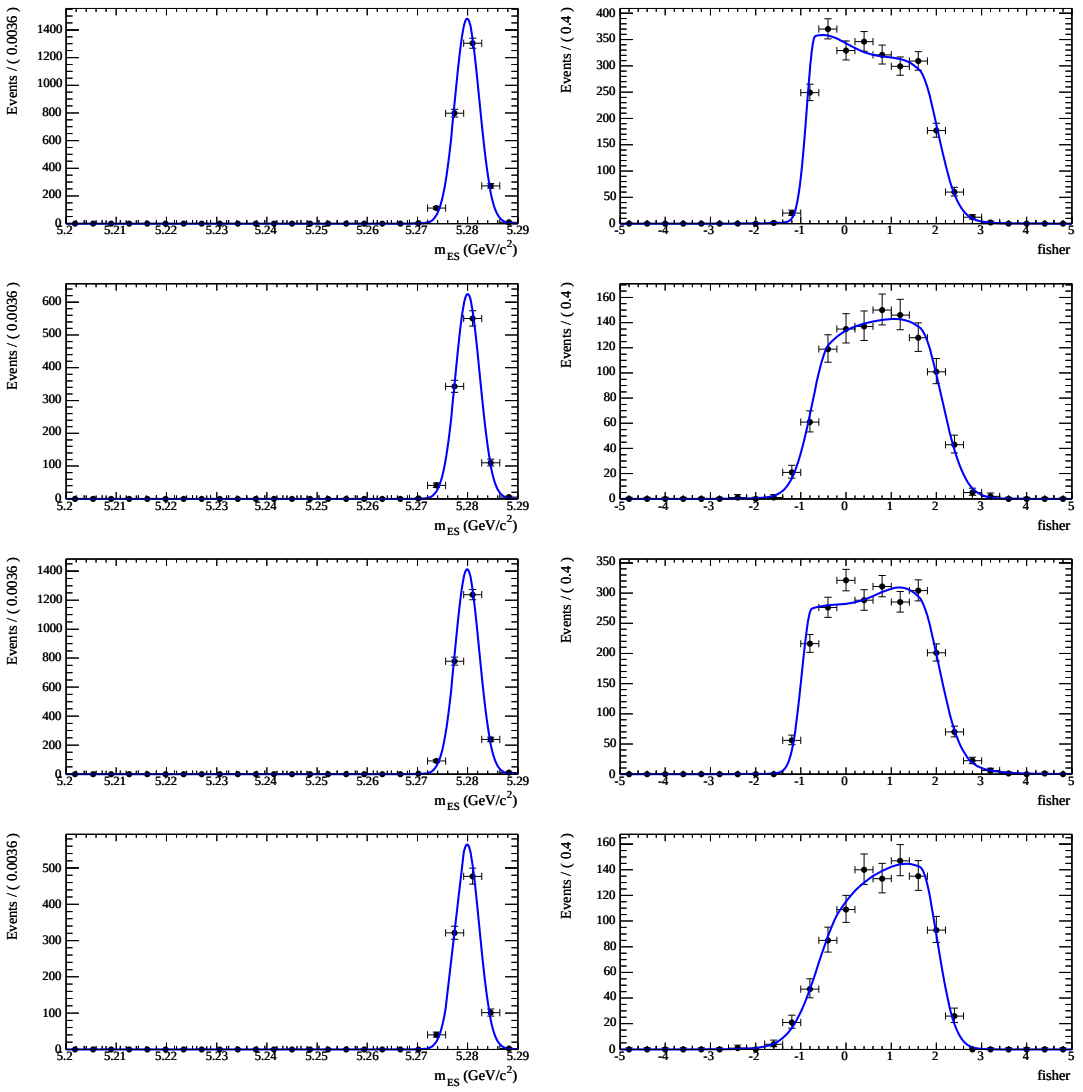

Figure A.13: $m_{\rm ES}$ and Fisher distribution for signal MC events. Left plots are for $m_{\rm ES}$ distributions, right plots show Fisher distributions. The upper line is for $DK_{K\pi\pi}$ channel, next lines are for $DK_{K\pi\pi\pi^0}$, $DK_{K^0_S\pi}$, $DK_{K^0_S\pi\pi^0}$ channels respectively. The overimposed curve is the result of the fit.

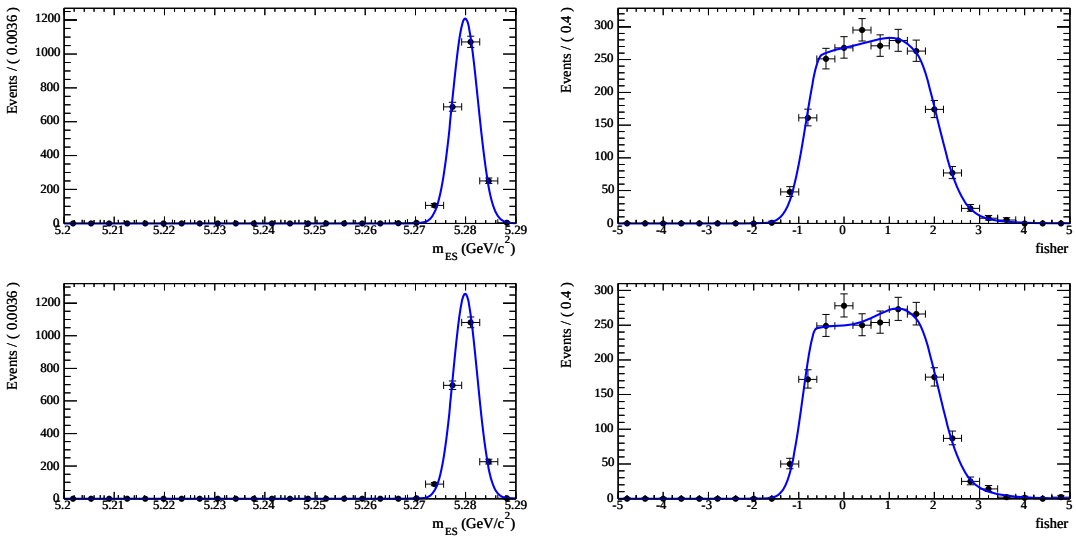

Figure A.14: $m_{\rm ES}$ and Fisher distribution for signal MC events. Left plots are for m_{ES} distributions, right plots show Fisher distributions. The upper line is for $DK^*_{K\pi\pi}$ channel, the lower one is for $DK^*_{K^0_S\pi}$ channel. The overimposed curve is the result of the fit.

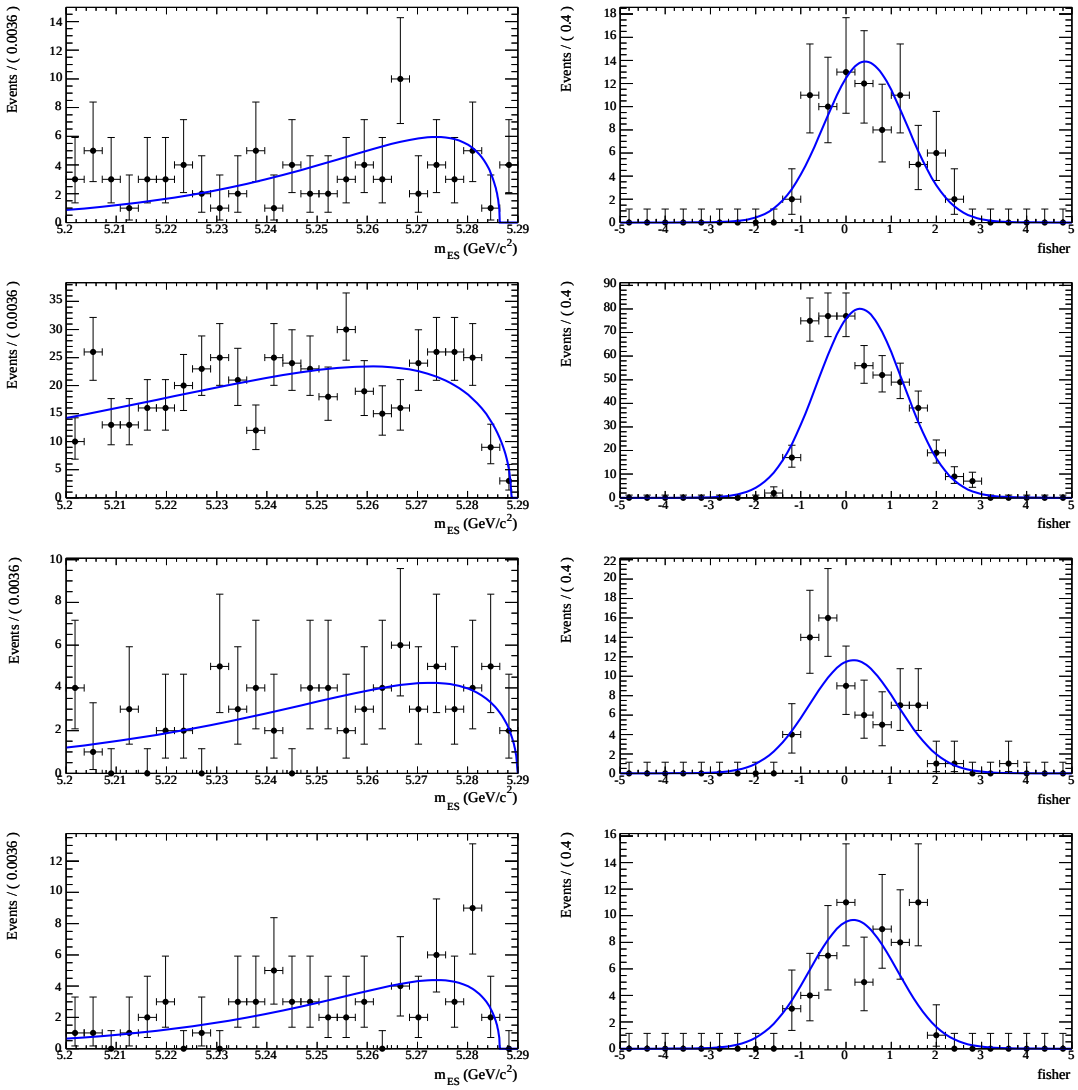

Figure A.15: $[B \to DK]$ $m_{\rm ES}$ and Fisher distribution for $B\overline{B}$ MC events. Left plots are for $m_{\rm ES}$ distributions, right plots show Fisher distributions. The upper line is for $DK_{K\pi\pi}$ channel, next lines are for $DK_{K\pi\pi\pi^0}$, $DK_{K^0_S\pi}$, $DK_{K^0_S\pi\pi^0}$ channels, respectively. The overimposed curve is the result of the fit.

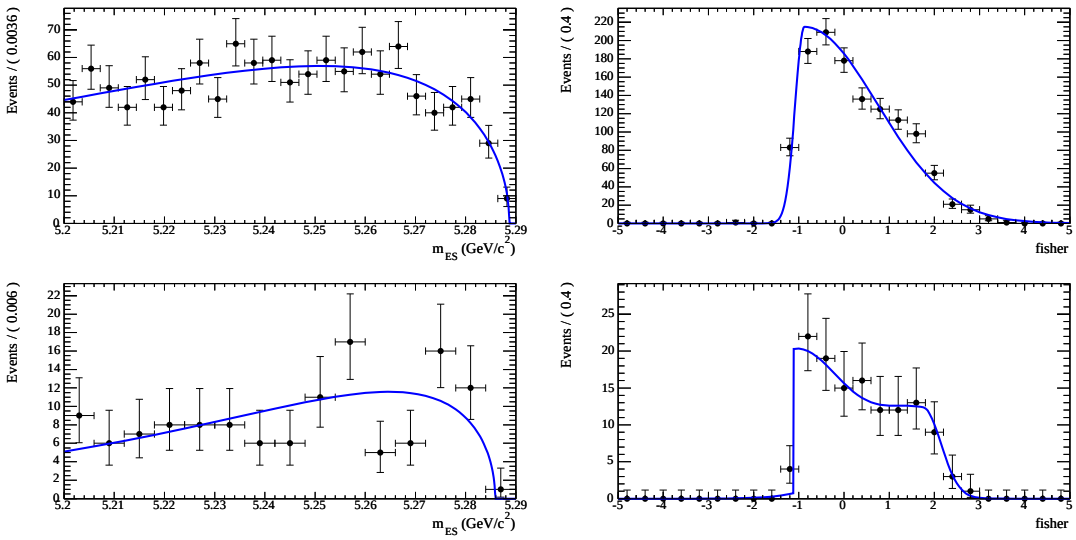

Figure A.16: $[B \to DK]$ $m_{\rm ES}$ and Fisher distribution for $B\overline{B}$ MC events. Left plots are for $m_{\rm ES}$ distributions, right plots show Fisher distributions. The upper line is for $DK^*_{K\pi\pi}$ channel, the lower line is for $DK^*_{K^0_S\pi}$ channel, respectively. The overimposed curve is the result of the fit.

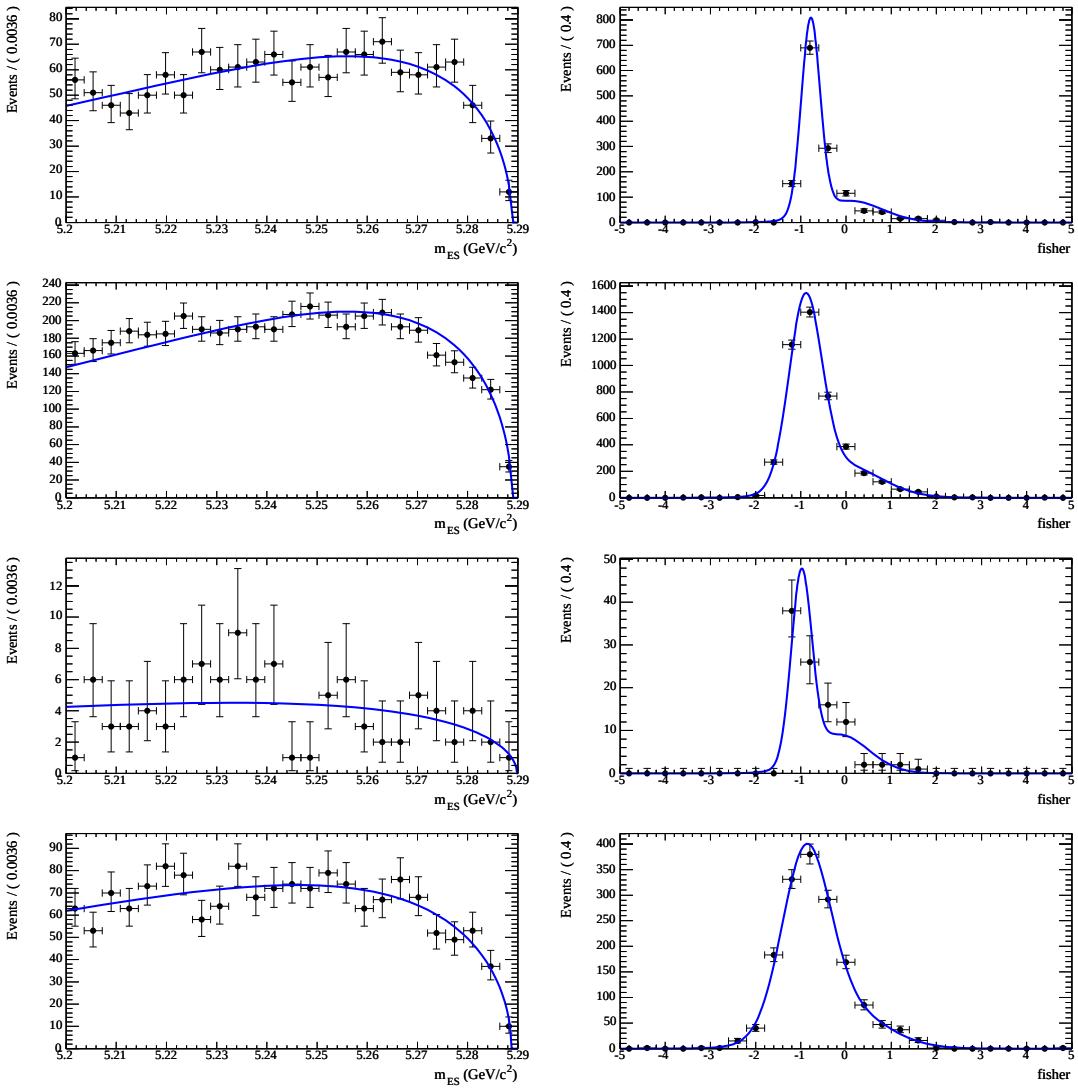

Figure A.17: $m_{\rm ES}$ and Fisher distribution for continuum MC events. Left plots are for $m_{\rm ES}$ distributions, right plots show Fisher distributions. The upper line is for $DK_{K\pi\pi}$ channel, next lines are for $DK_{K\pi\pi\pi^0}$, $DK_{K^0_S\pi}$, $DK_{K^0_S\pi\pi^0}$ channels respectively. The overimposed curve is the result of the fit.

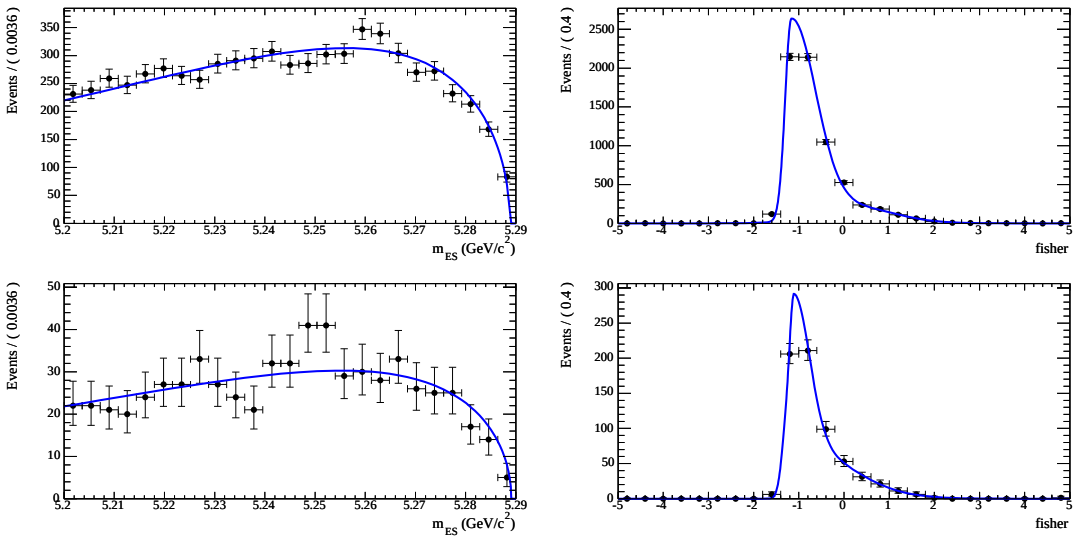

Figure A.18: $m_{\rm ES}$ and Fisher distribution for continuum MC events. Left plots are for $m_{\rm ES}$ distributions, right plots show Fisher distributions. The upper line is for $DK^*_{K\pi\pi}$ channel, next line is for $DK^*_{K^0_S\pi}$ channel. The overimposed curve is the result of the fit.

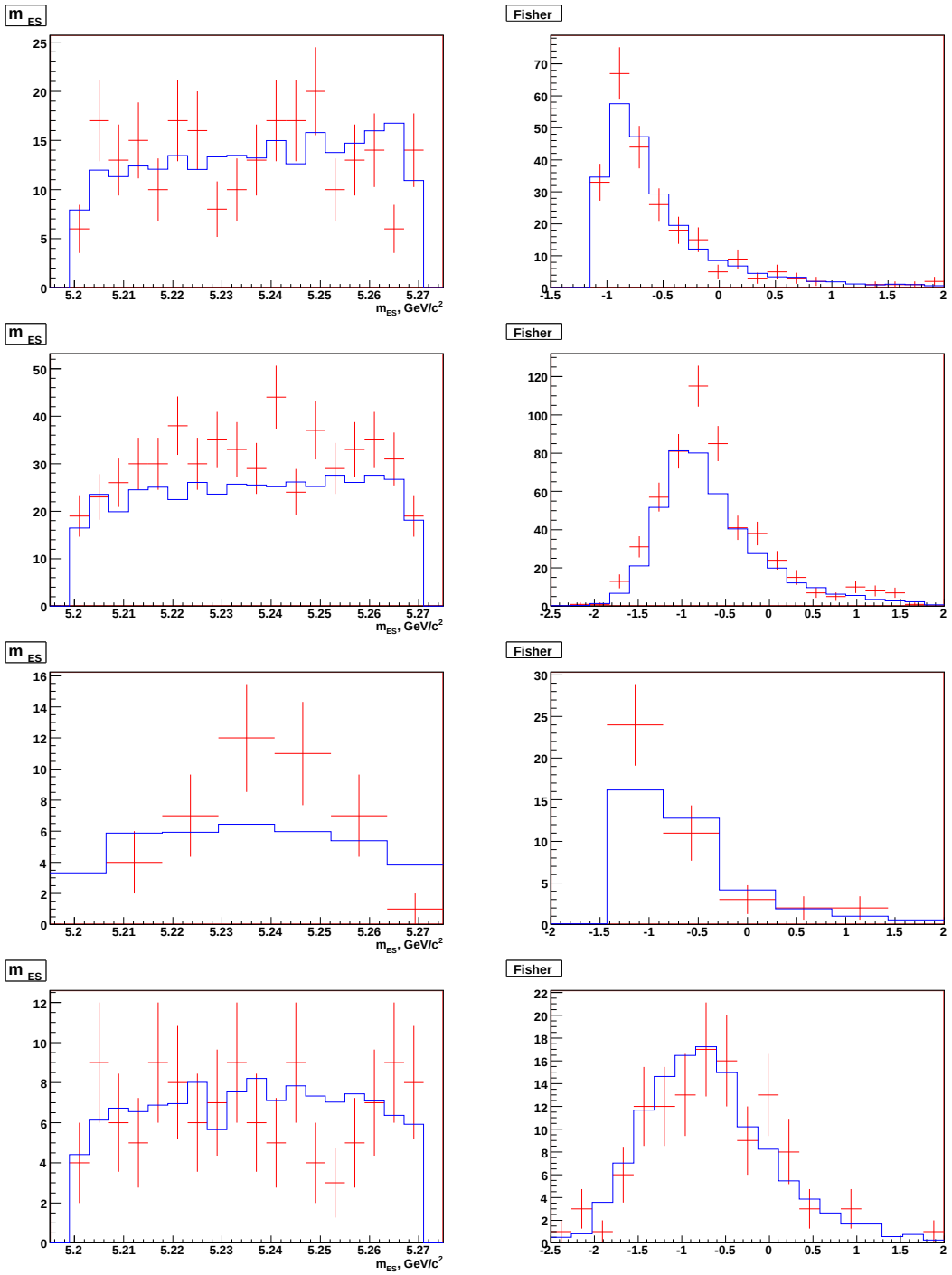

Figure A.19: $m_{\rm ES}$ and Fisher distribution for continuum cocktail MC events (blue histogram) and offpeak data (red dots with errors). Left figures are for $m_{\rm ES}$ distributions, right figures show Fisher distributions. The plots on the upper row are for $DK_{K\pi\pi}$ channel, in the following lines we show $DK_{K\pi\pi\pi^0}$, $DK_{K^0_S\pi}$, $DK_{K^0_S\pi\pi^0}$ channels respectively. The plots are rescaled to the luminosity of offpeak data (44 fb^{-1}).

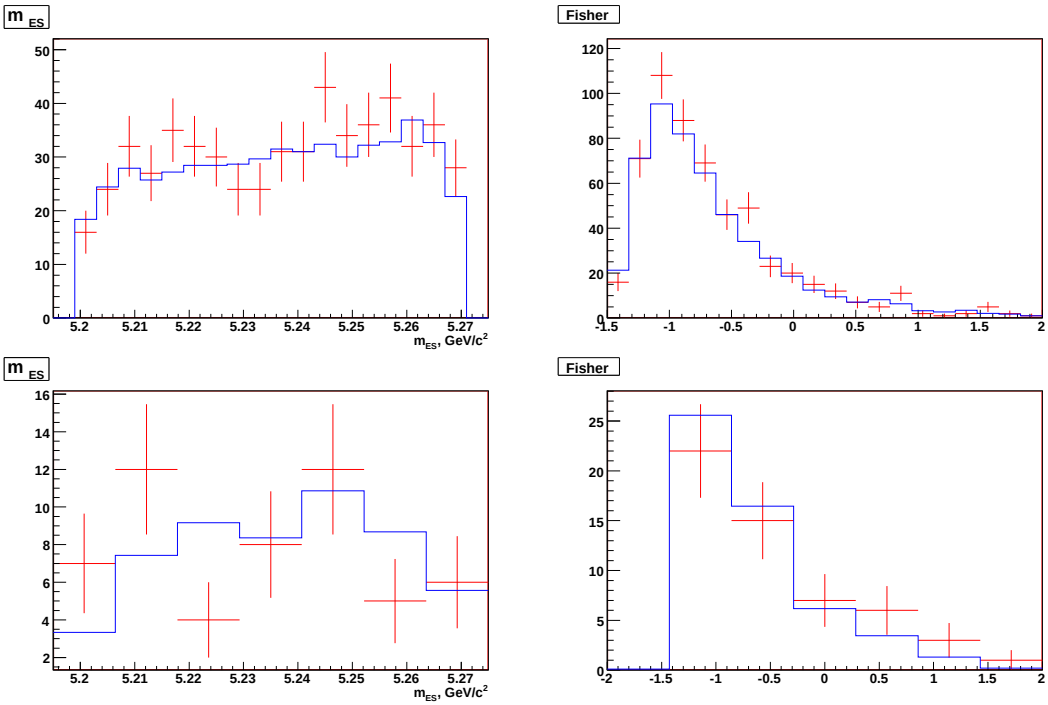

Figure A.20: $m_{\rm ES}$ and Fisher distribution for continuum cocktail MC events (blue histogram) and offpeak data (red dots with errors). Left figures are for $m_{\rm ES}$ distributions, right figures show Fisher distributions. The plots on the upper row are for $DK^*_{K\pi\pi}$ channel, in the following line we show $DK^*_{K^0_S\pi}$ channel. The plots are rescaled to the luminosity of offpeak data (44 fb^{-1}).

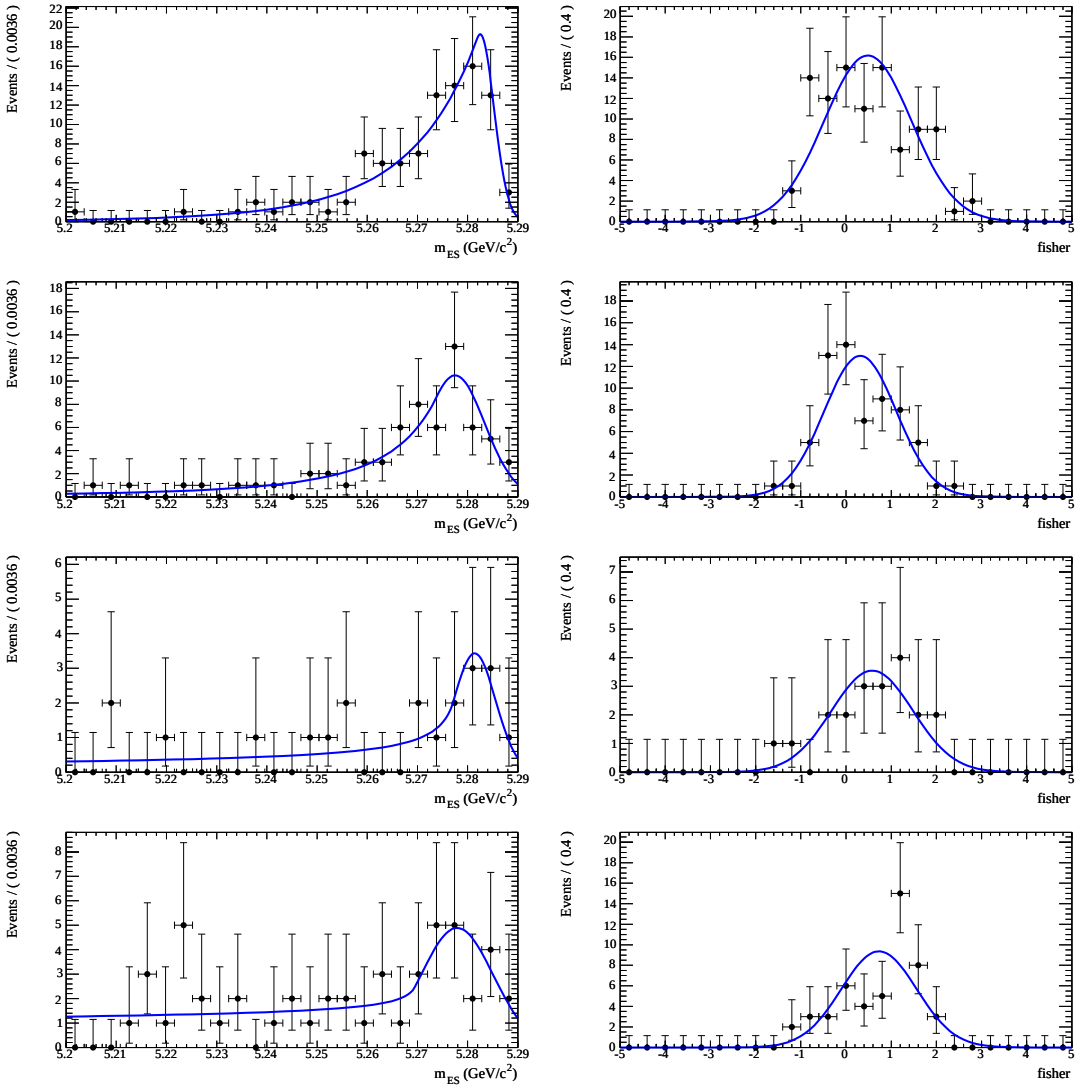

Figure A.21: $m_{\rm ES}$ and Fisher distribution for peaking MC events. Left plots are for $m_{\rm ES}$ distributions, right plots show Fisher distributions. The upper line is for $DK_{K\pi\pi}$ channel, next lines are for $DK_{K\pi\pi\pi^0}$, $DK_{K^0_S\pi}$, $DK_{K^0_S\pi\pi^0}$ channels respectively. The overimposed curve is the result of the fit.

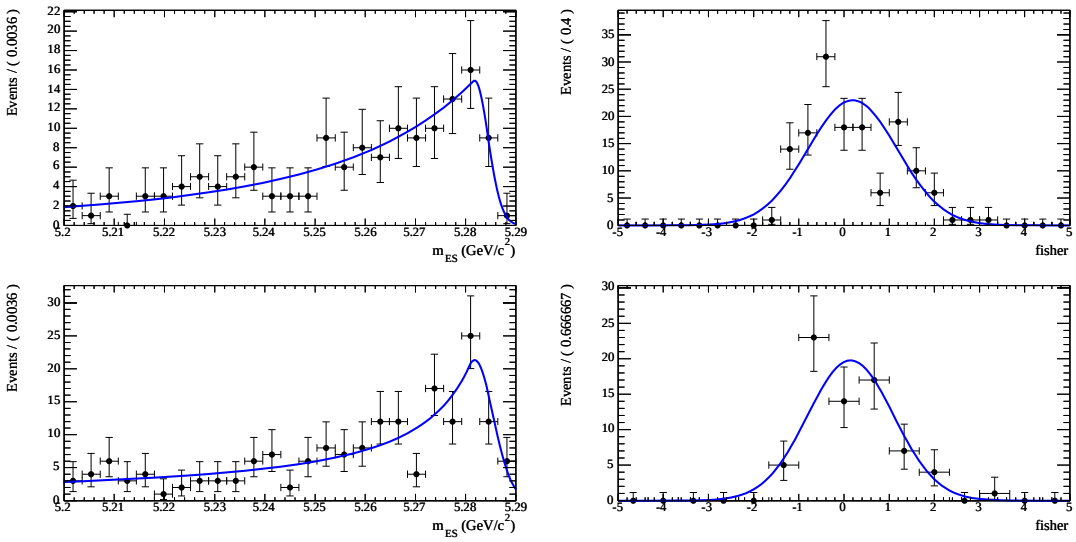

Figure A.22: $m_{\rm ES}$ and Fisher distribution for peaking MC events. Left plots are for $m_{\rm ES}$ distributions, right plots show Fisher distributions. The upper line is for $DK^*_{K\pi\pi}$ channel, next lines is for $DK^*_{K^0_S\pi}$ channel. The overimposed curve is the result of the fit.

A.6 Control Sample Parameterizations

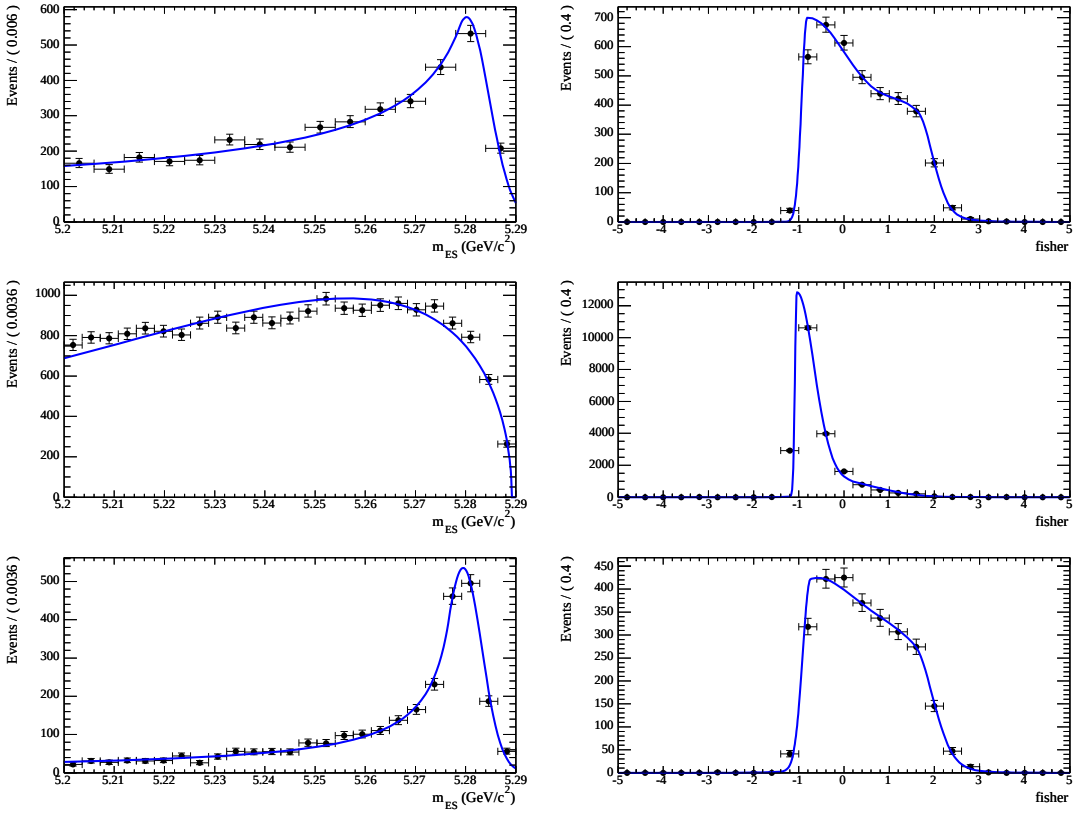

Figure A.23: [Control sample for $DK_{K\pi\pi}$] The parameterization of the m_{ES} (left column) and Fisher (right column) distributions for $B\bar{B}$ background (top row), continuum one (middle row) and peaking background (bottom). The channels contributing to peaking are: $B^- \to D^0\rho^-, D^0 \to K\pi\pi^0$; $B^- \to D^0\pi^-, D^0 \to K\pi\pi^0$; $B^- \to D^0K^-, D^0 \to K\pi\pi^0$; $B^0 \to D^-\rho^+, D^- \to K\pi\pi$; $B^0 \to D^-K^+, D^- \to K\pi\pi$; $B^0 \to D^{*-}\pi^+, D^{*-} \to D^-X, D^- \to K\pi\pi$.

Acknowledgements

In the beginning, I would like to thank Laboratoire de Accélérateur Linéaire and Universté Paris Sud 11 (and, in particular, Guy Wormser and Achille Stocchi) for support that made it possible to accomplish this thesis. The time I had in the lab was really very exciting and gave me a feeling of what the big science is like.

My supervisor, Achille Stocchi, deserves the very warm words for inspiring me to start in this field and continuous attention to my scientific and non-scientific problems. Thank you very much for that, Achille!

I also would like to thank the rapporteurs, Jean-Pierre Lees and Stéphane Monteil, who were ready to read this thesis, their advices were really helpful in understanding some aspects of this work. The contribution of Emi Kou and Adrian Bevan as members of jury cannot be overestimated.

Many thanks to the group of BaBar-LAL: Anne-Marie, Achille, Patrick, Michel, Nicolas, Guy, and Bogdan (also Joao, Wenfeng, Justine, and Viola, who were a part of the group before). I learned a lot from them, their involvement in my work was really big. Special thanks go to Anne-Marie and Nicolas for their advices during this time. Here, I also would like to thank people from the LHCb-LAL, superB-LAL and Théorie-LAL groups, their advices and discussion influenced this work amazingly, thank you Emi, Marie-Hélène, Andrey, Aurélien, Leonid, Alejandro, Benoît and many others (somehow all working in the same building).

Thanks to many other BaBarians who have helped me along the way, in particular: Giovanni, Vincent, Eli, Simon, Pablo and all the other people on BABAR from around the world, whom I have had the pleasure to meet and work with.

I also want to thank the members of the UTfit group that I joined not long ago, but enjoyed being collaborator to such people: Maurizio, Marcella, Marco, Vincenzo, Luca, and Achille (I promise to learn Italian).

Coming to a supporters' part I want to thank first of all my parents and other members of

my family for a complete understanding during these years. Despite the distance between us I constantly felt your support to all my initiatives. I hope to see you more often in the coming years.

Paris community of high-energy doctorant(e)s was always encouraging. So thanks to Andrey (especially for Sunday lunches in the lab), Leonid (for Ukranian jokes), Wen Bin (for delicious Chinese restaurants), Aurélien (and Véronique, for representing France in this international society), Viktor (for plov), Pietro (for parties and beer), Michelle (for a wee bit of Scotish in my English), João (for perfect dinners in Bourg-la-Reine), Bogdan (for helping me to fight with non-English phone calls), Simon (for sharing SLAC experience with me). (I have written in brackets the first things I remembered about you, but there are much more).

Lots of thanks to my friends around the world, who partly became virtual, but yet very close. Julia (from Hamburg), thanks for being always open for commenting all the questions in my life, Sasha (from Frankfurt-Main), thanks for the support especially in the beginning, Anton (wherever you are now), thanks for often visits and interesting discussions, Ksenia (New-York), thanks for a constant will to visit me in this faraway place, Natasha (Saint-Petersburg), thanks for the support in the last part of this thesis (really, the hardest one) and making me remember that penguins are actually birds, I would not do without you. Thanks to all other friends, that kept in touch during these years: Nastya L., Nastya G., Ira, Kirill, Vika, Polina, Dima, Misha, Zhenja, Sasha and many others.

This thesis was really supported by all the people mentioned above and many others who deserve to be mentioned but somehow disappeared from the list. Thanks to all of you!